INVERSE GRADING IN GRANULAR FLOW

THÈSE N° 2287 (2000)

PRÉSENTÉE AU DÉPARTEMENT DE GÉNIE CIVIL

ÉCOLE POLYTECHNIQUE FÉDÉRALE DE LAUSANNE

POUR L'OBTENTION DU GRADE DE DOCTEUR ÈS SCIENCES TECHNIQUES

PAR

Martin KERN

Diplom-Physiker, Universität Bayreuth, Allemagne
de nationalité allemande

acceptée sur proposition du jury:

Prof. L. Vulliet, directeur de thèse
Dr W. Ammann, rapporteur
Prof. F. Descoeudres, rapporteur
Prof. J. Peinke, rapporteur

Lausanne, EPFL
2000

Contents

Abstract

The current work concerns with the parametrical dependencies of inverse grading in granular flows from material properties of individual particles involved in the flow. The investigations were initiated and motivated by the search for an explanation of the function principle of the avalanche airbag, which prevents a skier from going under in a flowing avalanche.

The functionality of the avalanche airbag cannot be understood in the frame of the classical hydrodynamical avalanche models: the hydrostatic buoyancy caused by the avalanche airbag is not sufficient to keep a skier on the surface of a flowing avalanche. Starting from this motivation, a short phenomenological and historical overview over snow avalanches and the development of the avalanche airbag is given.

Existing field observations and laboratory experiments are described to outline the occurrence and main features of granular flows. It is discussed, how far these observations and experiments indicate specific properties of granular flows such as inverse grading.

Mathematical modelling of avalanches or granular flows can easily be adjusted to the specific investigated problems and does not consume as much property as physical modelling in laboratory experiments does. Different classes of mathematical and numerical models of avalanches and granular flows are reported with respect to the question how far they allow qualitative or quantitative insight into the nature of inverse grading.

Comparing continuum dynamic avalanche models, analytic models of granular flow and discrete element models (DEM), it can be seen that DEMs are well suited for the investigation of inverse grading. According to the type

of the granular flow which has to be investigated, either the hard sphere or the soft sphere type of DEM is the appropriate description for the flow. Quasistatic granular flows, which are dominated by multiparticle interactions over longer durations are described by soft sphere models. For rapid granular flows, hard sphere models are the appropriate approach. In this case, it is assumed, that the flow is dominated by instantaneous binary contacts which extend over time intervals that can be neglected compared to the time intervals of free particle motion.

In the current work, snow avalanches are considered as rapid flows. According to this, a hard sphere DEM was used for the investigation of inverse grading in granular flow. In the used model, binary collisions of particles are parametrized by the particle elasticities e and b in longitudinal and transversal direction and by the Coulomb coefficient μ of the colliding particles. The model can reproduce the effect of inverse grading in a defined range of particle material parameters. Therefore, the global flow and segregational behaviour of the granular flow can be considered to depend from the interaction behaviour of individual particles. The longitudinal restitution coefficient e, which describes the particle elasticity in longitudinal direction, seems to be the parameter, which influences the flow- and segregational behaviour most strongly.

It is tried to establish a link between the model results and continuum dynamic granular flow models by searching for a constitutive relation between stress and strain in the model flow. However, a unique relation could not be found, probably because the model flow fails to meet some principle requirements for the derivation of stress tensors in granular flows.

On the other hand, the method of stochastic analysis could successfully be applied to the model flow data: the time series of the vertical position of individual particles are apparently noisy and have Markov properties. This allows to derive deterministic, particle size dependent segregational dynamics of one single particle from its time series of vertical position. The fixed points of these dynamics for large particles lie in upper flow layers, where the fixed points of smaller particles are situated near the bottom.

The results of the investigations in the frame of the numerical DEMs are

compared with field observations and with results of laboratory measurements of the longitudinal restitution coefficient e of snow. Field measurements of mean snow lump size profiles correspond qualitatively to the particle size profiles obtained from the numerical simulations.

The measured value of $e \approx 0.1...0.3$ for snow differs significantly from the value of $e \approx 0.8$, which is necessary to obtain granular model flows which are exhibiting inverse grading. This difference can be explained by the fact that snow flow avalanche dynamics also incorporate particle interactions extended in time, for which the numerical hard sphere model cannot account.

Conceptually, this work spans an arc from the application of the avalanche airbag to an explanation of the typical granular flow behaviour or inverse grading in the frame of a numerical hard sphere approach.

Résumé

Le présent travail traite de la dépendance paramétrique de la ségrégation inverse lors d'un flux granulaire par rapport aux propriétés matérielles des particules individuelles présentes dans le flux. De telles études ont été motivées par la recherche d'une explication concernant le principe de fonctionnement du sac airbag, qui évite tout enfouissement sous la neige du skieur en cas d'avalanche.

Le fonctionnement du sac airbag ne peut être expliqué correctement avec les modèles hydrodynamiques d'avalanches classiques, pour lesquels la poussée hydrostatique causée par le ballon est trop faible pour maintenir le skieur à la surface de l'avalanche. Dans un premier temps, une courte présentation du phénomène et de l'historique des avalanches ainsi que du développement des sacs airbag est présentée.

Le déclenchement et les caractéristiques des flux granulaires sont analysés par des observations de terrain ainsi que par des expérimentations en laboratoire. Il sera discuté des possibilités de description, grâce aux observations de terrain et aux expérimentations en laboratoire, des flux granulaires et en particulier de la ségrégation inverse.

La modélisation mathématique d'avalanches ou de flux granulaires peut aisément être ajustée à un problème spécifique et requiert moins de coûts que des expérimentations en laboratoire ou des modélisations physiques. Un certain nombre de modélisations mathématiques et numériques seront présentées en précisant jusqu'où celles-ci permettent d'analyser quantitativement et qualitativement la nature de l'effet de ségrégation inverse.

La comparaison de modèles dynamiques d'avalanches, de modèles analy-

tiques de flux granulaires et de modèles d'éléments discrets (DEM) montre que les modèles d'éléments discrets sont les plus appropriés dans l'étude de la ségrégation inversée.

En fonction du type de flux granulaire à étudier, la variante à sphères rigides ou celle à sphères souples du DEM sont utilisées. Les flux granulaires quasi statiques, qui sont dominés par des interactions entre les particules pendant de longues périodes, sont décrits par les modèles à sphères souples. Pour ce qui est des flux granulaires rapides, le modèle à sphères rigides constitue la meilleure approche. Dans ce cas, il est supposé que le flux est dominé par des contacts binaires instantanés sur un intervalle de temps qui peut être négligé par rapport aux intervalles de temps de mouvements libres des particules.

Dans ce travail, les avalanches étant considérées comme des flux rapides, le modèle DEM à sphères rigides a donc été utilisé afin d'étudier la ségrégation inverse dans un flux granulaire. Dans le modèle utilisé, les collisions binaires entre les particules sont paramétrées par les élasticités longitudinales et transversales des particules, respectivement e et b, ainsi que par le coefficient de friction de Coulomb μ des surfaces des particules. Le développement de ce modèle ainsi que les méthodes d'analyses statistiques seront décrites. Le modèle peut reproduire l'effet de ségrégation inverse pour un certain type de paramètres concernant les caractéristiques des particules. Par conséquent, le flux granulaire et le comportement de ségrégation peuvent être considérés comme dépendant du comportement d'interactions entre les particules.

Le coefficient longitudinal de restitution e, qui décrit l'élasticité longitudinale de la particule, semble être le paramètre qui influence le plus le flux et la ségrégation.

Une corrélation sera recherchée entre les résultats des modélisations et les modèles de la dynamiques des milieux continus de flux granulaires en recherchant une relation constitutive entre pressions et déformations du modèle de flux. Aucune relation ne fut cependant trouvée, ce qui s'explique certainement par le fait que le modèle de flux ne permet pas de respecter certains principes au niveau de la dérivation du tenseur de contraintes dans un flux granulaire.

A l'inverse, la méthode d'analyse stochastique fut utilisée avec succès sur les données du modèle de flux. Il apparaît que le signal dépendant du temps des positions verticales des particules comporte du bruit et possède les propriétés de Markov. Ceci permet la description déterministe de la dynamique de ségrégation pour chaque particule libre à partir du signal dépendant du temps de la position verticale. Les points fixes de la dynamique des grosses particules se situent essentiellement dans les couches supérieures du flux, ceux des petites particules se trouvent au contraire près du fond.

Les résultats des études des modèles numériques DEM sont ensuite comparés à des observations de terrain et à des expérimentations en laboratoire. La répartition verticale de la taille moyenne des blocs de neige déterminée sur le terrain se corrèle bien avec la répartition obtenue grâce aux modèles numériques.

La valeur mesurée sur le terrain de $e \approx 0.1...0.3$ pour la neige est assez éloignée de la valeur $e = 0.8$, qu'il est nécessaire d'obtenir afin de pouvoir décrire un flux granulaire avec ségrégation inverse. Cette différence s'explique par le fait qu'une avalanche réelle incorpore les interactions des particules pendant une longue période, ce que le modèle numérique à sphères rigides ne peut simuler.

D'un point de vue conceptuel, ce travail relie donc les applications concrètes du sac airbag dans une avalanche à l'explication de l'effet de ségrégation inverse lors d'un flux granulaire typique grâce aux simulations numériques.

Zusammenfassung

Die vorliegende Arbeit befasst sich mit der parametrischen Abhängigkeit der inversen Segregation in granularen Strömungen von den Materialeigenschaften der individuellen an der Strömung beteiligten Partikel.

Ausgangspunkt und Motivation der Untersuchungen war die Frage nach dem Wirkungsprinzip des Lawinenairbags, der seinen Träger davor bewahren soll, in einer fliessenden Lawine unterzugehen. Im Rahmen der klassischen hydrodynamischen Lawinenmodelle lässt sich die Wirksamkeit des Lawinenballons nicht verstehen, da der durch den Ballon bewirkte hydrostatische Auftrieb zu gering ist, um einen Skifahrer an der Oberfläche der Lawine zu halten. Von dieser Motivation ausgehend, wird eine kurze phänomenologische und historische Einführung in Schneelawinen und in die Entwicklung des Lawinenballons gegeben.

Vorkommen und Eigenschaften granularer Strömungen werden anhand von Beobachtungen und Laborexperimenten erläutert. Die Möglichkeiten, mit Hilfe dieser Beobachtungen und Experimente spezifische Eigenschaften granularer Strömungen wie die inverse Segregation zu erklären, werden diskutiert.

Mathematische Modellierungen bieten bei der Untersuchung spezifischer Fragestellungen grosse Flexibilität bei geringem materiellen Aufwand. Verschiedene Klassen mathematischer und numerischer Modelle für Lawinen bzw. granulare Strömungen werden bezüglich der Frage diskutiert, inwiefern sie qualitativ oder quantitativ Einsicht in die Natur des Effekts der inversen Segregation erlauben. Aus dem Vergleich kontinuumsmechanischer Lawinenmodelle, analytischer Modelle für granulare Strömungen, sowie Diskrete-

Element-Modelle (DEM) ergibt sich, dass die DEM zur Beschreibung der gegebenen Fragestellung am besten geeignet sind. Je nach Fliesscharakteristik der interessierenden granularen Strömung ist entweder die soft-sphere oder hard-sphere Variante der DEMs die geeignete Beschreibung: Quasistatische granulare Strömungen, in denen längerdauernde Kontakte mehrerer Partikel vorherrschen, lassen sich besser mit dem soft-sphere Ansatz beschreiben, während schnelle granulare Strömungen besser mit dem hard-sphere Ansatz zu beschreiben sind: Hier wird angenommen, dass die Strömung von Zweierstössen dominiert wird, deren zeitliche Dauer gegenüber der Zeit der freien Bewegung der Partikel vernachlässigt werden kann.

Die Ausbildung der inversen Segregation wird im Rahmen eines hard-sphere-DEM untersucht, in dem die Zweierstösse individueller Partikel durch deren Elastizitätseigenschaften e und b in longitudinaler bzw. in transversaler Richtung sowie durch die Coulombreibung μ der Partikeloberflächen parametrisiert sind. Die Entwicklung des Modells sowie der Routinen zur statistischen Auswertung wird beschrieben. Das Modell ist in der Lage, in einem bestimmten Parameterbereich der individuellen Partikeleigenschaften den Effekt der inversen Segregation zu reproduzieren: das Fliess- und Segregationsverhalten der granularen Strömung wird also durch das Wechselwirkungsverhalten der individuellen Partikel bestimmt. Dabei scheint der die Elastizität in longitudinaler Richtung bestimmende longitudinale Restitutionskoeffizient e der das Fliess- und Segregationsverhalten am stärksten beeinflussende Parameter zu sein.

Die Modellierungsergebnisse werden im Hinblick auf einen Bezug zu kontinuumsmechanischen Granulatmodellen untersucht. Ein eindeutiges Konstitutivverhalten der granularen Modellströmungen lässt sich allerdings nicht feststellen.

Demgegenüber erweist sich die Anwendung der Methode der stochastischen Analyse als sehr erfolgreich: Es zeigt sich, dass die Zeitserien der Vertikalpositionen einzelner Partikel Markov-Eigenschaften besitzen. Unter dieser Voraussetzung lassen sich deterministische Beschreibungen der Segregationsdynamik für einzelne Partikel ableiten, die signifikant grössenabhängig sind: Die Fixpunkte der Dynamik liegen für grössere Partikel in höheren Strö-

mungsschichten als für kleinere Partikel.

Die Untersuchungen im Rahmen des numerischen DEM werden mit Feldbeobachtungen und Laborversuchen verglichen. Feldmessungen von Profilen der mittleren Schneebrockengrössen stimmen qualitativ mit den Grössenprofilen aus den numerischen Simulationen überein. Die Diskrepanz zwischen den gemessenen und den in den Modellierungen zur Erzeugung der inversen Segregation erforderlichen longitudinalen Restitionskoeffizienten von $e \approx 0.1...0.3$ (gemessen) und $e = 0.8$ (modelliert) lassen sich aus der Tatsache erklären, dass in einer realen Schneelawine auch längerdauernde Wechselwirkungen zwischen Partikeln vorkommen, die vom verwendeten numerischen Modell nicht berücksichtigt wurden.

Insgesamt spannt die vorliegende Arbeit einen Bogen von der konkreten Anwendung des Lawinenballons in einer Schneelawine bis hin zur Erklärung des für granulare Strömung typischen Effekts der inversen Segregation. (Für ein vertieftes Verständnis von Schneelawinen und der durch sie verursachten Gefahren wird die Beschreibung der Lawinendynamik durch Aspekte granularer Dynamik von Bedeutung sein.)

Abstract

Scopo di questo lavoro è l'analisi della dipendenza parametrica tra la segregazione inversa all'interno di un flusso granulare e le proprietà del materiale con cui sono costituite le singole particelle coinvolte nel flusso stesso. Questa ricerca è stata motivata dall'esigenza di dare una spiegazione al principio di funzionamento dell'airbag da valanga, mezzo attraverso il quale lo sciatore, coinvolto in una valanga densa, viene mantenuto a galla.

La funzionalità dell'airbag da valanga non puo' essere spiegata tramite l'utilizzo dei classici modelli idrodinamici finora utilizzati per lo studio della dinamica delle valanghe, in quanto, la spinta idrostatica esercitata sull'airbag non è sufficiente per mantenere a galla uno sciatore. Viene data una breve sintesi storico scientifica del fenomeno valanghe e sullo sviluppo dell'airbag.

Le osservazioni di eventi reali ed esperimenti di laboratorio sono utilizzati per sottolineare le principali caratteristiche di un flusso granulare. Viene discusso quanto a fondo queste osservazioni e questi esperimenti possano aiutare ad individuare particolari proprietà dei moti granulari quali ad esempio la segregazione inversa.

I modelli matematici di simulazione delle valanghe o dei moti granulari possono facilmente essere adattati a problemi specifici e non richiedono grossi investimenti di capitali come invece richiesti dagli esperimenti di laboratorio. Vengono riportati differenti classi di modelli numerici e matematici per la simulazione di valanghe e moti granulari, allo scopo di verificare la loro adattabilità qualitativa e quantitativa al fenomeno della segregazione inversa.

La comparazione tra modelli dinamici di tipo continuo, modelli di simu-

lazione di moti granulari e "discrete element models" (DEM) dimostra che questi ultimi sono quelli che meglio riproducono le osservazioni sulla sedimentazione inversa. L'utilizzo di questo tipo di modelli dà una appropriata descrizione del moto sia quando questo viene riprodotto con l'utilizzo di "hard sphere" DEM o "soft sphere" DEM, in accordo con il tipo di moto che si vuole riprodurre. Moti granulari quasi-statici, dominati da fenomeni di iterazione tra le singole particelle di lunga durata, possono essere accuratamente descritti tramite l'utilizzo di modelli "soft sphere" mentre per moti granulari rapidi i modelli di tipo "hard sphere" sembrano rappresentare il miglior approccio. In questo caso viene assunto che il moto sia dominato da contatti binari istantanei la cui durata è trascurabile se confrontata con l'intervallo di tempo del moto delle particelle.

In questo lavoro, le valanghe vengono considerate come un moto di tipo rapido e quindi, per investigare il fenomeno della sedimentazione inversa, è stato utilizzato un modello di tipo "hard sphere" DEM. In questo modello la collisione binaria tra le particelle è parametrizzata in funzione delle elasticità longitudinale e e trasversale b delle particelle e in funzione del coefficiente μ di Coulomb relativo alle particelle che collidono. Il modello può riprodurre l'effetto della sedimentazione inversa per un definito range di parametri relativi ai materiali con cui sono costituite le particelle. Viene assunto che, sia il moto, che il processo di segregazione delle particelle dipendono dal processo di iterazione delle singole particelle. Il coefficiente di restituzione longitudinale e, che descrive l'elasticità delle particelle in direzione longitudinale, sembra essere il parametro che influenza maggiormente questi due processi.

Si è cercato di stabilire un collegamento tra i risultati del modello e i modelli continui di simulazione del moto granulare cercando una relazione costitutiva per descrivere la relazione tra tensione e deformazione . Risulta evidente che non può essere determinata una relazione univoca probabilmente perchè il modello di moto non possiede alcuni requisiti necessari per la derivazione dei tensori di tensione nel flusso granulare.

D'altro canto il metodo di analisi stocastica pu essere applicato con successo ai risultati del modello. Dal punto di vista deterministico, la dinamica di segregazione delle singole particelle, dipendente dalla dimensione delle

stesse, pu essere determinata dalle serie temporali riportanti la posizione verticale delle singole particelle. Queste serie sono apparentemente disturbate da un "rumore" e hanno le proprietà di Markov. I punti fissi della dinamica sono localizzati nello strato di moto superficiale per le particelle di grosse dimensioni e vicini alla superficie basale per le particelle di minori dimensioni.

I risultati dell'analisi, ottenuti con i modelli di tipo DEM, sono comparati alle osservazioni di eventi reli e agli esperimenti di laboratorio atti alla determinazione del coefficiente di restituzione elastica e della neve. Le misure in campo relative ai profili di distribuzione delle dimensioni delle particelle corrispondono qualitativamente alle dimensioni delle particelle ottenute dalla simulazione numerica.

La differenza valori misurati $e \approx 0.1...0.3$, corrispondente alla neve, e $e = 0.8$, utilizzato allo scopo di ottenere un modello di flusso granulare in grado di riprodurre il fenomeno della segregazione inversa, può essere spiegata dal fatto che la dinamica delle valanghe dense considera anche gli impatti tra le particelle aventi lunga durata, cosa che non pu essere riprodotta con l'ausilio di modelli del tipo "hard sphere".

Concettualmente questo lavoro crea un collegamento tra l'applicazione dell' airbag da valanga con la spiegazione del tipico comportamento dei moti granulari, o segregazione inversa, tramite l'utilizzo di un approccio numerico del tipo "hard sphere".

Chapter 1

Introduction

Similar to a mountain tour, the reading of a scientific documentation needs information about the destination and the way to reach it. Both will be provided here to prepare a kind of tour of the current work. Firstly, the "destination" will be fixed by defining the subject of the current work. A "route description" will then be provided. This description starts with a more narrative sketch of the train of thought and is supplemented by a short synopsis of each chapter of the work.

1.1 Subject of the work

This work is concerned with the effect of inverse grading in granular flows: when granular materials consisting of different-sized particles flow under the influence of gravity, they may unmix in such a way that the larger particles move to the upper, smaller ones to the lower layers of the flow.

The main goal of this work is to understand the dependency of this effect on material parameters of the granular material in the frame of a simple computational model of granular flow. These investigations have been motivated by the use of inverse grading as a function principle of the avalanche airbag, which helps to prevent skiers to be buried by a flowing avalanche.

The documentation of the train of thought leading from this real application to a rather abstract numerical model investigation is the other objective at

which this work is aimed.

1.2 Train of Thought

It is said that a scientific report has to tell a story, which allows the reader to participate in the motivation and evolution of the thoughts underlying the reported work. The story of the current work spans a wide arc from the avalanche airbag against the background of the attempt to reduce the number of avalanche fatalities to the analysis of inverse segregation in the frame of a simple numerical model of granular flow.

So the story of this work begins with the history of human struggle against the natural hazard of snow avalanches. The avalanche airbag, which helps to prevent skiers from being buried by a flowing avalanche, fits well into this tradition.

The avalanche airbag or avalanche balloon, respectively, consists of an ordinary hiking backpack, which contains a pressured air cartridge, which can fill two balloons with a total volume of 150l within 1-2 seconds. In the unreleased state, the balloons are folded up into the side bags of the backpack. They can be released by a release grip in case of being caught by an avalanche.

The function principle of the avalanche airbag could not be understood in the frame of "classical" avalanche science. A skier's density even with inflated avalanche airbags is higher than the density of the surrounding flowing avalanche snow. Therefore hydrostatic buoyancy within an avalanche, which is assumed to be a continuous fluid-like medium, does not provide a satisfactory explanation of the functioning of the avalanche airbag.

The fact that a flowing snow avalanche does not entirely behave like a flowing fluid, has become established in the more recent avalanche dynamics models: the flow behaviour is also determined by the interaction of discrete particles such as snow blocks or -lumps of which an avalanche consists. It is tried to take this granular-like flow behaviour into account by special forms of the constitutive laws which are elements of continuum mechanical avalanche

models and relate deformations to stresses whithin the flowing snow.

The function principle of the avalanche airbag is based on a special feature of granular flows. Mixtures of different-sized granular material moving under the influence of gravity are unmixing in such a way that larger particles are moving to the top of the flow, whereas the smaller ones are sinking down to lower flow layers. This unmixing behaviour is termed "inverse grading" or "inverse segregation".

Aspects of granular flow including inverse grading can be observed in geomechanical processes such as rockfalls or avalanches, in industrial processing, where mixing of different-sized granular material causes problems and, of course, in laboratory experiments. To the reader, inverse grading also might be present from childhood observations of dry and wet gravity currents occuring during fascinating sandbox games...

Turning back from the sandbox to severe science, there are two principle ways of mathematical approach to granular flows.

Analytical approaches provide the advantage of a comprehensive formal understanding of the physical processes involved in the overall flow behaviour. The analytical descriptions of granular flows are formally very similar to the kinetic gas theory. Due to the large number of necessary assumptions, the range of flow and material parameters, for which such descriptions are valid, is rather limited and therefore analytical descriptions of granular flows are not so well suited for the treatment of practical problems.

Micromecanical modelling uses to trace the motions of all individual particles which participate in the flow and their mutual interactions by collisions including friction and deformation. By doing so, it is possible to simulate flows of granular materials over a wide range of material properties and boundary conditions. As such models deal with individual particles, they are termed "discrete element models" or, shortly, DEMs. For reasons of computational efficiency, in most numerical discrete element models the granular material is assumed to consist of spherical particles.

In the frame of the current work, a discrete element model of a granular flow of different-sized inelastic frictional spheres is developed. The investigations

of the model are concerned with the dependencies of the granular flow behaviour and, especially, the inverse segregational behaviour on the material properties of the spheres forming the model flow. It was found, that only for a limited range of combinations of particle inelasticity and frictional properties, stable model flows could develop which displayed the effect of inverse grading.

Now one may wonder about the relation of those abstract numerical investigations and the function principle of an avalanche airbag in a flowing snow avalanche, which for sure involves much more physical processes than can be represented by a simple sphere model. In fact, laboratory measurements of collisional inelasticity of snow performed in the course of this work indicate that the mechanical properties of snow do not correspond to the properties of the spheres in the numerical model, which finally caused the model flow to exhibit inverse grading.

But even from the very simple sphere model, principle insights could be extracted concerning the relation of different particle material properties and the evolution of different overall flow behaviour. Depending on the choice of particle material parameters, also the onset or breakdown of segregational flow behaviour could be observed. Comparing the size distribution profiles of snow lumps in snow flow avalanche debris with numerically obtained particle size profiles, one can state good qualitative correspondence: in each case, the large particles are situated on the top and the smaller ones in the lower layers of the flow.

At this point, the story of the avalanche balloon and its relation to modelling of inverse grading in a discrete element model comes to a preliminary end. But it continues in joining avalanche dynamics and concepts of granular dynamics and hopefully will provide improvement of our understanding of the inner structure of avalanche flows and therewith an improvement of avalanche hazard mapping - as a further step in the human struggle against the natural hazard of avalanches.

1.3 Synopsis of Chapters

After the introduction provided in the current Chapter 1, Chapters 2-4 are concerned with the practical and theoretical background of this work. The numerical and experimental investigations performed in the frame of this work are described in Chapters 5, 6 and 7. The results are summarized in Chapter 8.

Chapter 2 gives an introduction into the subject of the work from the point of view of avalanche science. After a short historical sketch of human dealing with avalanches, a characterisation of snow avalanches is given and the recent development and testing work on the avalanche balloon is reported. Inverse grading is introduced as the function principle of the avalanche airbag and then explained as a generic feature of granular flows which occur in geomechanical processes as well as in industrial processing.

Chapter 3 provides examples of field observations and laboratory investigations on the nature of granular flow, where, in the case of laboratory work the stress lies on the relation of methodology and observed properties.

Chapter 4 is concerned with mathematical modelling of avalanches and granular flows with respect to the question as of how far the reported mathematical models are appropriate descriptions of the granular segregational behaviour displayed by the avalanche airbag. Avalanche flow models of increasing complexity are reported. Though the more elaborate ones also use aspects of granular flow behaviour to describe the constitutive behaviour of flowing avalanche snow, these "classical" avalanche flow models cannot account for the specific granular flow behaviour. An analytical approach to granular flow, which is formally similar to kinetic gas theory, is sketched. This approach is leading to a continuum mechanical formulation of constitutive and flow behaviour. The characteristic features of numerical soft sphere and hard sphere discrete particle models are explained, their ranges of validity are discussed and examples of their application are given. Finally, two analytical approaches - one of continuum gas dynamical type, the other one employing geometrical and statistical considerations - are reported. Of all considered flow models, the numerical discrete particle models seem to

be most appropriate for a systematic parametrical investigation of inverse grading.

Chapter 5 is an outline of the numerical part of the present work. It consists of the description of the development of a 3D hard sphere model of multidisperse granular flow and of the analysis of the model results. After introducing the main features of the model, the numerical implementation of the model and of statistical evaluation routines for the interpretation of the model output is explained. Time averaged flow quantities, such as velocity or particle size profiles, are used to characterize dependencies of the model flow behaviour on material parameters of the spherical particles forming the model flow and from initial and boundary conditions. The parametrical dependency of the formation of inverse grading in the flow is of special interest. An attempt to extract continuum constitutive behaviour from the model flow is reported as well as the stochastic analysis of single particle elevation dynamics, which allows to extract a deterministic description of the segregational dynamics of single particles from their elevation time series.

Chapter 6 is dedicated to field observations and experimental investigations supplementing the numerical work. Firstly, the qualitative observation of inverse grading in the debris of snow flow avalanches is reported. Subsequently, the investigation of the dependency of segregational behaviour of large bodies in snow avalanches on their geometrical form by a field experiment is decribed. In order to relate the numerical model to real snow avalanche flow, the inelastic behaviour of colliding snow balls is investigated in a laboratory experiment. Numerical results of particle size profiles are compared to the results of a quantitative analysis of snow lump size profiles in the debris of a wet snow flow avalanche. A comparison of the inelastic behaviour of snow balls measured in laboratory experiments to the particle inelasticity assumed in the frame of the numerical model confirms the assessment that one has to abstract from real snow avalanche dynamics to obtain a granular flow model which is able to reproduce the effect of inverse grading.

Chapter 7, finally, summarizes the results of this work and comes to the conclusion that the rather abstract hard sphere model is able to reproduce

the effect of inverse grading and that there is need for further work to account for the granular nature of snow avalanche flow in a more realistic way.

Chapter 2

Snow avalanches and granular flow

The current work has been motivated by the attempt to understand the functionality of the avalanche airbag in flowing snow avalanches. In some sense, the experimental investigations of this device can be regarded as embedded in the history of human struggle against the natural hazard of snow avalanches.

In the course of this work, the term "avalanche balloon" is used synonymously with "avalanche airbag".

From the experimental observations, it turned out that the buoyant behaviour of the avalanche airbag could not be explained by hydrostatic buoyancay related to a description of avalanches as continuum fluids. Inclusion of granular aspects of avalanche flow provides a reasonable explanation of the functionality of the avalanche airbag device: the effect of inverse grading was believed to be responsible for the fact, that skiers wearing an inflated avalanche airbag can stay near the surface of a flowing avalanche.

To enlighten this train of thought leading from the avalanche airbag to inverse grading, Section 2.1 firstly provides a sketch of the history of human perception of avalanches. Subsequently, Section 2.2 gives an outline of the avalanche characterisation which is commonly in operational use. The history of invention and experimental investigation of the avalanche airbag is

reported in section 2.3. Section 2.4, finally, is concerned with the basic features of granular flows: after explaining the effect of inverse grading, some examples for the importance of granular flows in geological context and industrial procesing are given.

2.1 Brief history of snow avalanches

The word "avalanche" probably originates from the latin word "labare" for sliding down, as quoted by Ammann et al. (1997) and Oppenheim (1974). In the Raeto-Romance speech area the item "lavina" is known , where the french or english word "avalanche" probably evolved from "valanze" which is related to the french word "val" or "vallèe" for valley. The german word "Lawine" has replaced the former old german words "Lauwine", "Lauine", "Lavine" or "Lowine".

The history of human reception of avalanches is documented in numerous literature, which will not be reviewed here. At this point, we will confine to a short insight, in which the interesting transition from the numinous, mystic picture of avalanches in former times to a more rational, naturalistic approach to the phenomenon from the age of enlightenment until nowadays is observable.

The problems, Hannibal had during his crossing of the Alps in the year 218 before Christ, are historically well documented. Also the loss of people and property of Hannibal's army is reported by the chronicler Italicus, quoted by Ammann et al. (1997).

In the middle ages, people avoided the alpine mountain regions which they believed to be inhabited by ghosts and dangerous fabulous creatures. Avalanches were looked upon as demonic and weird supernatural forces.

For example, one of the first extensive descriptions of an avalanche incident origins from Rudolf, the abbot of St. Troud, who is quoted by Oppenheim (1974). He narrates from a pilgrimage over the Grand St. Bernard Pass in 1228, when the local guides were caught by an avalanche, while the pilgrims were praying for shelter on their journey in the church of St. Rémy.

Though also describing dragons and fabulous creatures which were said to have been seen in the southern valleys of Grisons, Johann Jakob Scheuchzer in 1706 described serveral avalanches, their origins and first means of avalanche shelter and rescue. He also wrote down a first historical listing of several avalanche events.

Until the beginning of the 19th century, however, avalanches were looked upon as large snow balls, which cause large destructions when rolling down a slope. In David Herrlisberger's "Topographie der Eydgenossenschaft" a picture can be found (see fig. 2.1) which is explained as follows:

"Snow lumps are rolled together to large balls, which plunge down from the highest, jagged mountains into the valleys and depths with tremendous and awful rattle and hum"

In 1863, finally, a more naturalistic point of view was formulated by Bernhard Studer commenting the Herrlisberger picture:

"Nobody ever has seen avalanches with enclosed houses, trees and people falling through the air like little globes."

Some decades later, avalanches were emotionlessly seen as a physical phenomenon and employed as an effective killing machine in the mountain battles of World War I between Italian and Austrian troops. The number of soldiers killed by avalanches which were artificially released by mines and shells exploding above the front lines, exceeded the number of soldiers killed by direct action and is estimated to ly in the range from 40,000 to 60,000.

With growing settlement of the Alps and evolving alpinism in the 19th century, the number of fatalities due to avalanches increased and forced people thinking about possibilities of avalanche prevention and rescue of people buried by avalanches.

Ludwig Gramminger, one of the pioneers of the mountain rescue service in the Alps, reports several rescue actions in the 20- and 30 years, where people buried by avalanches could only be recovered dead (see Gramminger (1986)). In this early times of mountain rescue service, there were no searching devices available except to the avalanche rope. Also the employment of avalanche dogs was not in common use, if one omits Barry, the legendary

Figure 2.1: *Illustration of an avalanche from 1754. The avalanche is depicted as a large snow ball carrying trees and houses.*

first avalanche dog at the Grand St. Bernard pass, who is told to have saved up to 40 people buried by avalanches more than 200 years ago. Gramminger reports the first avalanche rescue action employing a dog in the year 1945. As Tschirky et al. (2000) state, most avalanche victims are dead when recovered by professional rescue teams and the immediate help by companions has the greatest chances of success. The radio tracker systems introduced in the seventies were a step to more likely success of rescue by companions. The best rescue method, however, is to avoid avalanche burial by being cautious. The avalanche airbag, which was developed in the years from 1975, can prevent persons caught by an avalanche from being buried.

2.2 Types of snow avalanches

2.2.1 Morphological avalanche classification

A simple consistent method of characterizing avalanches is of advantage for comparison of avalanche data from different areas or different weather conditions, respectively. Several avalanche sizing systems have been suggested in the US by Perla & Martinelli (1976), in Japan by Shoda (1965) and Shimizu (1967) or, in Switzerland, by Quervain (1975) and Foehn et al. (1977).

An international system for classifying observable features of avalanche events, which has been published by the UNESCO (1981), has two parts: The genetic part of the classification system refers to processes and conditions causing avalanches or being responsible for their effects, while the morphological part deals with directly observable properties helping to classify the type of the regarded avalanche.

Only the morphological part of the system is operationally used and has not been adopted verbatim by any country. It is used more as a guideline, what to record or to observe, than as an obligatory regulation. The system takes into account three zones: the origin, the transition regime and the runout of the avalanche. Table 2.1 shows the morphological part of the international classifying system.

The avalanches regarded in the current work (see Sections 6.1.1 and 6.1.2)are

Table 2.1: *Morphological part of international avalanche classifying system. Table taken from UNESCO (1981).*

Zone	Criterion	Alternative Characteristics, and Code	Denominations
Zone of origin	**A** Manner of starting	**A1** Starting from a point (loose snow avalanche)	**A2** Starting from a line (slab avalanche)
		A3 Soft	**A4** Hard
	B Position of sliding surface	**B1** Within snow cover (surface layer avalanche)	**B2** New snow fracture
		B3 Old snow fracture	**B4** On the ground (full depth avalanche)
	C Liquid water in snow	**C1** Absent (dry snow avalanche)	**C2** Present (wet snow avalanche)
Zone of transition	**D** Path form	**D1** Path on open slope (unconfined avalanche)	**D2** Path in gulley or channel (channeled avalanche)
	E Form of movement	**E1** Snow dust cloud (powder avalanche)	**E2** Flowing along the ground (flow avalanche)
Zone of deposition	**F** Surface roughness of deposit	**F1** Coarse (coarse deposit)	**F2** Angular blocks
		F3 Rounded clods	**F4** Fine (fine deposit)
	G Liquid water in snow debris at time of deposition	**G1** Absent (dry avalanche deposit)	**G2** Present (wet avalanche deposit)
	H Contamination of deposit	**H1** No apparent contamination (clean avalanche)	**H2** Contamination present (contaminated avalanche)
		H3 Rock, debris, soil	**H4** Branches, trees
		H5 Debris of structures	

mostly typical "skier avalanches", which are small or mid-sized dry or wet slab avalanches which evolve to flow avalanches on slopes. This kind of avalanches fits to the categories A2, B1, C1 or C2, D1, E2 and H1 of table 2.1. The wet snow flow avalanche examined in Sections 6.1.1 and 6.3.1 belongs to the categories A2, B1, C2, D2, E2, H2.

2.2.2 Common avalanche classification

More commonly known classifications of avalanches can be found in literature concerning practical aspects of avalanches for tourists and mountain professionals. Here we refer to some popular examples of avalanche literature and the references therein and give a characterisation of snow avalanches mainly following Mc Clung & Schaerer (1993). Characterisations of avalanches can, for example, also be found in Salm (1982), Munter (1991) or Munter (1997).

In the following, a common classification of avalanches into 5 types is given. The avalanche types which are most dangerous to skiers and mountaineers are the loose snow and, especially, the snow slab avalanches. Powder snow, slush and ice avalanche can be of more catastrophic nature and may cause large loss of lives and property.

2.2.3 Loose snow avalanches

Loose snow avalanches are composed of loose snow with little or no cohesion. They start at a single point and spread out in a triangle as they are moving down the slope. The triangular pattern forms as snow is pushed down the slope and entrained by the avalanche. Loose snow avalanches form near the surface of the (loose) snow cover on initiation. After start, subsurface snow maybe swept away. Loose snow avalanches usually remain small.

2.2.4 Snow slab avalanches

Slab avalanches are more dangerous to skiers than loose snow avalanches. They are initiated by failure of weak layers within the snow cover. An ap-

proximately rectangular block of snow is cut out by propagation of fractures in the snow.

Failure of snow cover occurs, when the downslope component of gravity force appproaches the shear resistance of a weak layer of the snow cover. At failure, the snow has absorbed the maximum load it can bear. If deformed slowly in shear, snow can fail without fracture. (Snow deformation without fracture is known as snow creep.)

Fracture is defined as catastrophic failure of snow. The neccessary requirements for fracture are:

- the shear stress in the weak layer must approach the shear strength.
- the relative velocity v_{cr} of a snow layer against the weak layer must be high enough. For example, it must exceed v_{cr} >1 mm min^{-1}. This reqirement can be satisfied by deformation imposed by skiers on the snow cover above the weak layer or by shear waves caused by explosives.

Snow slab avalanches can be subdivided into dry and wet snow slab avalanches. A dry, wind packed snow cover, which fulfils the above reqirements, usually forms dry slab avalanches. Wet snow slabs are caused by

- additional loading by new precipitation (rain)
- changes of buried weak layer due to water intrusion
- water lubrication of a sliding surface in the snowpack.

2.2.5 Powder avalanches

Bozhinsky & Losev (1998) describe the formation of a powder snow avalanche as follows: "If a dry snow slab releases in the starting zone, the snow, while in fast motion, rapidly scatters into minute powdry particles as a result of numerous collisions of blocks and fragments of snow as well as by friction. The pulverized snow forms a snow cloud which rises above the flowing

avalanche body making it inaccessible for direct observation. In this manner, a powder avalanche forms." Another generation mechanism of powder avalanches is provided by dry snow flow avalanches falling down over terrain walls. The snow falling down is suspended into the air and forms a powder cloud. The cloud of a powder avalanche can reach considerable velocities and cause vast damages on forests and property.

2.2.6 Ice avalanches

Ice avalanches are caused by the calving of ice masses or séracs from a glacier flowing over a steep slope or cliff band. An ice avalanche consists of ice chunks which move like rocks in rockfalls and a powder cloud which travels further than the rest of the ice avalanche but with less destructive force. As ice avalanches usually are released by glacier motion or earthquakes, their release is fairly independent from current weather or snow conditions.

Very large ice avalanches form an own class of ice avalanches. They evolve by braking off of a large piece from a glacier forming a flow with landslide--like behaviour. These large ice avalanches are significantly larger than ice avalanches emerging from glacier calving and consist of up to $10^6 m^3$ of ice. For example, the Allalin disaster ice avalanche from August 30, 1965 in the Swiss Fee valley, which caused 88 fatalities, had a volume of approximately 10^6 m^3 (see Schild (1967)).

2.2.7 Slush avalanches

Slush avalanches are most likely in high latitudes as, for example, in Northern Norway or in the Brooks Range, Alaska. They occur due to the sudden onset of snow melt or heavy rainfall in spring and in most cases there exists depth hoar at the base of the snow cover. Other characteristic features of slush avalanches are:

- slope of starting zone in the range from 5° to 40°, but rarely over 25° - 30°.
- snowpack is partially or totally saturated with water.

- release is often associated with a bed surface which is impermeable for water.

The release mechanism comprises the reduced snow cohesion due to presence of water and a substantial reduction of the friction coefficient of snow by the hydrostatic pressure of the water contained in the snowpack. Densities of slush avalanches can exceed 1000 kgm^{-3} due to earth and rock material entrained at the base of the slush flow.

Considering the avalanche types listed above, one can suppose that the flowing debris of slab avalanches and ice avalanches can, to some degree, be described as a granular flow consisting of discrete particles: the snow slab is breaking into numerous snow blocks and particles (wet snow avalanches can even form snowballs) and also ice chunks of an ice avalanche can be identified as granular particles.

2.3 Motivation of presented work - the avalanche airbag

The avalanche airbag is a device which helps skiers who are caught by an avalanche to stay near the surface of the flowing avalanche so that they have better chances to survive the accident. The device consists of a backpack with integrated release and filling system for two balloons with a total volume of 150 l, which are folded up into the side bags of the backpack. Figures 2.2 and 2.3 show the inflating of the balloons and the inflated airbag system, respectively.

If caught by an avalanche, one has to pull a grip attached to the left strap of the backpack. By doing so, an explosive charge inside the grip is released and the shock wave produced by the explosion propagates through a pressure tube to a cartridge and hits a spike into the cartridge stopper. The cartridge contains nitrogen at a pressure of 350 bar. The nitrogen escapes the opened cartridge at high velocities entraining the surrounding air through valves by the Venturi effect. The balloons are filled with $\frac{1}{3}$ of nitrogene from the cartridge and $\frac{2}{3}$ of surrounding air. This filling mechanism also works if the

Figure 2.2: *Avalanche balloons at beginning (upper picture) and at end (lower picture) of inflation. In this side view, one can observe one of the balloons inflating and growing out of one side bag of the avalanche airbag backpack. Note that the skiers in the background have only moved a short distance during the complete inflation of the balloons. Photographs by André Roth, SFISAR.*

Figure 2.3: *Front view of a skier wearing an avalanche balloon backback with inflated balloons. Photograph by Martin Popp, MPG.*

backpack is totally buried by (avalanching) snow or if the backpack has been wetted and then frozen at -35°C. The filling of the balloons takes about 1-2 seconds.

In an earlier stage of development, the avalanche balloon device consisted of a single balloon of 150 l volume and a mechanical releasing system for opening of the pressure cartridge.

As the avalanche balloon system proved its effectiveness in various field experiments and real avalanche incidents, the question arose which physical mechanism could be responsible for the forces keeping the balloon at the avalanche surface. Knowledge of the physical reason for the effectiveness of the airbag was supposed to support useful hints for optimizing the device.

At this point, it maybe interesting to have a look at the history of the development of the avalanche balloon system and on how the current work was initiated and influenced by this practical problem.

The legend of the invention

The avalanche balloon was invented in the seventies by Josef Hohenester, a forester living in Reichenhall, Bavaria. There exists a nice little legend on how he got the basic idea for the development of the avalanche balloon.

In his leisure time, Joseph Hohenester was a passionate hunter. Pursuing his hobby also in wintertimes, he was sometimes caught by an avalanche. It is told that there he made the observation, that each time he was wearing a chamois over his shoulder, he was not buried by the avalanche and could easily free himself. Since most skiers do not have a chamois over their shoulder when going outside in winter, Hohenester thought about how to take advantage of the "chamois effect" by a compact transportable device for skiers. This is the legend of the invention of the avalanche airbag device. Josef Hohenester is still alive...

A brief history of development and research

From 1975 to 1979, Hohenester performed various tests with balloons of different sizes attached to crash test dummies and other test bodies in the Zugspitze ski area. These tests are reported in Hohenester (1979). In this early state of development, the avalanche balloon simply consisted of air filled balloons closely attached to test bodies by some straps. Water filled plastic canisters of 75 kg weight were used as test bodies. In the course of 17 experiments, the balloon volumes were varied in the range from 60 l to 500 l.

In all tests, which were performed under dry slab or powder snow avalanche conditions, the balloons were visible on the avalanche debris surface after the avalanches had stopped and the test bodies were only partly buried. The motion of the test bodies with the balloons during flowing in the avalanche was characterized as "bopping" with alternatingly being covered by snow and being visible on the surface of the flowing avalanche.

A test was also performed in spring 1978 at the Zugspitze ski area by an independent institution, the "Allianz Zentrum für Technik" belonging to

a German insurance company. This test performed by Wolff et al. (1978) confirmed the effectiveness of the balloons. The two test bodies and the 75 kg crash test dummy were only partly buried and the balloons were widely visible on the avalanche debris. These results encouraged the test staff to strongly recommend the further development of the avalanche balloon device.

In spring of 1980, the Canadian mountain rescue service performed a test of the prototype balloons in the Lake Louise ski area, which is reported by Irving (1980). Three dummies of 75 kg weight were constructed from spruce. Two of them were equipped with balloons of 110 l or 280 l volume, respectively. Also this test confirmed the "bopping motion" of the dummies with balloons in the flowing avalanche as well as the dummies with balloon to be found at the surface of the avalanche debris after standstill of the avalanche

In 1979, a bavarian engineer, Peter Aschauer, purchased the patent of the ballon and began developing a device usable for skiers. As Aschauer (2000) states, the essential engineering problem, that had to be solved, was how to inflate the balloon quickly in case of being caught by an avalanche. In 1982, Aschauer and Hohenester presented the first prototype of an avalanche balloon which could be filled within 1.5 seconds employing the Venturi effect. As the pressure cartridges were filled with carbon dioxide, the device was not licenced by the TÜV, the German authority for safety of any technical device. Carbon dioxide freezes at temperatures below -20° C, but the device specifications required it to work at temperatures down to -35°C. For this reason, the complete device had to be developed again, so that finally in 1985, the first commercial avalanche airbag device entered the market. From then on, the avalanche balloon device was continuously improved until it ended up at the current state of a unrestrictedly usable skiing backpack with the integrated balloon device consisting of two 75 l balloons and a filling system.

In the ninteties, some more small qualitative tests of the avalanche airbag were performed (each with one dummy and one balloon) and reported in alpine magazines. In the winter of 1994/95, a large systematic test of the

effectiveness of the avalanche airbag was performed by the Swiss Federal Institute for Snow and Avalanche Research as reported by Tschirky et al. (1995) and Tschirky et al. (1996).

In this extensive field experiment in March 1995, 7 pairs of dummies were placed in an avalanche slope, one dummy of of each pair being equipped with an avalanche airbag. One of the airbags was already inflated, the others could be released by radio control. Stiff, sand- filled showcase puppets were used as dummies. They were wearing complete skiing clothes and skiing equipment and their weight was ranging between 65 and 85 kg. The downslope dislocation between the dummy pairs placed in the slope was approximately 30 m.

An avalanche was artificially released in the slope and the avalanche balloons were released by radio control when the dummies were caught by the avalanche.

After the avalanche had come to rest, all inflated balloons were visible at the surface of the avalanche debris. One of the ballons had not been inflated due to technical failure, another was only partly inflated. Four of the dummies with avalanche balloon were totally buried, i.e. their heads were covered with snow. But as the balloons were clearly visible, they could immediately been located and dug out. Another dummy was not buried and lying on the surface of the avalanche debris as shown in Figure 2.4.

Figure 2.4: *Dummy with inflated avalanche balloon lying on the surface of the debris of an artificially released avalanche*

On the other hand, six of the dummies without balloon were totally buried and four of them had to be searched for by tranceiver device. The test could be interpreted as a proof of the effectiveness of the avalanche balloon. Even if it does not prevent from burial, the avalanche balloon is an easily locatable marker which helps to immediately find the buried person wearing it.

Furthermore, the data collected by Tschirky (2000) from actual avalanche accidents with people involved wearing an avalanche balloon system since 1991, supports the above statement.

Until April 2000, there have been 25 known avalanche incidents involving people wearing an avalanche airbag. From the 40 persons wearing an avalanche balloon, 32 could inflate it in time. There were two technical malfunction and the other six cases of not inflated balloons were caused by human failure. (This is a weak point of the avalanche airbag: In the extreme stress situation of being caught by an avalanche, one has to release the balloon by manually pulling the release grip. Therefore, quick release must be practised !)

From the 32 persons with inflated balloon, 16 were not buried, 11 partly buried (their head was not covered with snow) and 5 totally buried (their head and thorax were covered with snow). But also in these cases (except one), the balloon was widely visible on the avalanche debris surface, so that the buried persons could immediately be located and dug out. One of the totally buried persons died, for also the balloons were totally buried. The person had already been fixed by avalanche snow before being buried by subsequent avalanche snow. The avalanche airbag is only effective in *flowing* avalanches. Regarding the fact that Tschirky et al. (2000) assume a mortality of 13 percent of all people involved in avalanche accidents, the recorded accident data is nevertheless an encouraging indication to the avalanche balloon being an effective safety device.

The physical mechanism

When starting his investigations, Joseph Hohenester calculated the balloon volumes from the hydrostatic buoyancy, which was necessary to keep a skier

"swimming" on the surface of an avalanche, which was regarded to behave like a fluid continuum. But as the necessary balloon volumes determined in the field experiments appeared to be much less than the ones calculated from the hydrostatic assumption, Hohenester (1979) stated:

"As the test series finished now shows, these calculations were wrong. Obviously, the static buoyancy is widely exceeded by the buoyancy caused by the avalanche dynamics."

Also the observations made in the frame of the Canadian tests were interpreted as dynamic effects in spite of static buoyancy by Irving (1980):

"It appeared that as long as there was forward motion, or the body not cemented in, the balloons would bring the dummies to the surface."

In the frame of the tests of the avalanche airbags in winter 94/95, the idea evolved that "inverse grading" in granular flows could be the physical mechanism responsible for the effectiveness of the avalanche airbag (see Tschirky et al. (1995)).

From this point of view, a flowing avalanche had to be regarded as a granular material moving under the influence of gravity, which shows the effect of unmixing or inverse grading: larger particles are more likely to be found near the surface, where the smaller ones tend to accumulate near the bottom of the flow. This effect is termed "inverse grading" or "inverse segregation", respectively. Interpreting a skier with inflated avalanche balloon as a large particle, the effectiveness of the balloon could qualitatively be understood.

The question underlying this current work is, whether the inverse grading effect explains the observation that large particles with densities exceeding the surrounding mean flow density ride on the top of the flow. If so, how does the effect depend on particle properties such as size and material type.

2.4 Granular flows: phenomenology and occurence

In this Section, the occurence of granular flow behaviour in the fields of geosciences and industrial processing will be enlightened.

Firstly, the term *granular flow* should be defined: Granular flow denotes the collective motion of individual particles of *granular material.* The term granular material refers to mixtures made up of discrete solid particles which are dispersed in a fluid phase. Granular materials can occur as suspensions, pastes and slurries, or, on the other hand, as dry powders or grains. Some common examples are sand, pharmaceuticals, Muesli, ceramic powders, ore, pack ice, avalanche snow... Typical solid concentrations are quite high in situations of flow or yielding of such granular materials, where the solid particles are closely adjacent or in contact with each other. Though the interstitial fluid may contribute to some extent to flow behaviour of granular materials, the essential mechanics of granular motion is governed by interaction between the distinct solid particles.

Questions of principle interest concerning the nature of granular flow arise as well as practical problems when regarding the fields of occurence of granular flows. A typical feature of granular flow showing up in industrial processing problems as well as in the geomechanical context is the effect of inverse segregation or inverse grading.

2.4.1 The phenomenon of inverse grading

If a material mass consisting of individual particles which differ in size, shape, density, surface character or other properties, is shaken or deformed by shearing motion in the presence of gravity, *segregation* or *grading* can occur: particles having similar properties are collecting together in a part of the system.

The distinction between *normal* and *inverse* grading stems from the geological context and accounts for underwater sedimentation and for sedimentation on land, respectively. Normal segregation occurs in beds of rivers or lakes. Finer particles are found in the upper layers of the sediment and coarse ones are lower down. This is due to different sedimentation velocities of different sized particles in water. The smaller the radius r of a particle is, the smaller is its sedimentation velocity v_{sed}: $v_{sed} \sim r^2$. Accordingly, if a mass of granular mass is discharged into water, the large particles reach the

ground first, whereas the smaller ones sink down slower and therefore reach the bed last on top of the sediments.

The opposite layering can be found in the sediments or debris of geomechanical granular flows on land. The term *inverse* grading denotes a layering, where the large particles are more likely to be found in higher layers and the smaller ones accumulate near the bottom. Figure 2.4.1 illustrates the generic structure of sediments generated by normal and inverse grading, respecticvely.

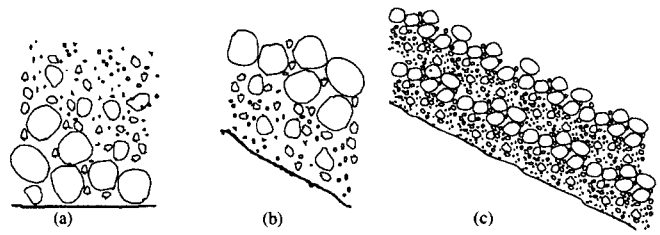

Figure 2.5: *Examples of sediment structures formed by a) normal sedimentation, b) granular flow and c) subsequent sequences of granular flow. Figure taken from Vulliet et al. (2000).*

Jaeger et al. (1996) define "inverse grading" as "unmixing behaviour" which occurs in vibrated or sheared systems of different sized granular particles. The separation of larger particles towards to the top of the system happens unindependently of their density. In vertical shaken containers, inverse grading is directly linked to convection systems developing in the shaken granular material. Large particles are entrained by the upward flow but they are too large to be entrained by the downward flow along the container walls.

Attempts to understand inverse segregation in sheared granular flows first have been made by Bagnold (1954) who explains the buoyant forces acting on larger particles by shearing deformation decreasing with flow height. So the lower parts of the large particles encounter more collisions of other (small) particles than the upper part. This imbalance of powers forces the large particles to rise to higher flow layers. A sophisticated qualitative decription by the effects of "random sieving" and "squeeze expulsion" has been

established by Savage & Lun (1988). Smaller particles are falling through randomly occuring voids in the fluctuating granular flow, and large ones are squeezed out into higher flow layers by imbalance of powers for which, however, a consistent quantitative description is still missing.

From the thermodynamical point of view, inverse grading is an example of simple mechanical systems displaying nonequilibrium, counterintuitive behaviour. As Rosato et al. (1987) point out, in an equilibrium system, a large particle put into a container with small particles should move down to the bottom of the container to minimize the total potential energy of the system. Intuitively, one would interpret shaking or shearing of the granular material as a method to help the system to find a stable equilibrium state. The fact, that the system proceeds from an equilibrium state (large particles at the bottom) towards to a non-equilibrium metastable state (large particles at the top) is rather surprising from the intuitive point of view.

2.4.2 Granular flows in geosciences

In the geomechanical context, granular flows occur in the form of rockfalls, landslides or debris flows.

During rockfalls, rock material is dislodged on steep slopes, accelerates down the slope, reaches a maximum velocity and decelerates with decreasing angle of bed and finally comes to rest due to bed friction. The remarkable mobility of large rockfalls is reflected by the fact that the ratio of total vertical fall height and horizontal travel distance is size dependent and decreases with the total volume of the rock material for rockfalls with a total volume greater than $10^6 m^3$, as outlined, for example, by Hsü (1978). One attempt to explain the high mobility and the fluid like behaviour of such flows in terms of granular dynamics has been made by Dent (1986), who explains the reduced surface friction by a thin layer of rapidly fluctuating particles beneath a densely packed overburden mass.

Debris flows consist of discrete solid particles of rock, soil and organic material in a fluid like matrix (see e.g. Iverson & Denlinger (1987) and Iverson (1997)). Debris motion is characterized by complex interaction of fluids and

solids, which is difficult to describe in a comprehensive quantitative physical theory. As first stated by Bagnold (1954), with increasing solid particle concentration and flow deformation rate, particle-particle interactions gain increasing influence on the debris flow behaviour. Thus also debris flow features as their high mobility and their ability to carry large stones are related to their partial granular nature by Davies (1985), who, on the other hand, also discusses pore fluid pressure and substantial shear strength of the debris material as possible mechanisms underlying the observed behaviour.

The applicability of granular flow description to gravity currents like rockfalls and debris flows is used by Lorig et al. (1995) to apply numerical discrete element modelling (see sect 4.4) to geomechanical gravity current problems.

2.4.3 Granular flows in industrial processing

The industrial processing of granular material is of great economical importance. For example, Ennis (1997) states that the value of the US industrial output affected by processing of particulate materials is about one trillion US $. Though of such great economical importance, research on granular material dynamics is of more principle nature which, from the point of view of industrial application, is far away from real technical problems. For this reason, Ennis (1997) and Adams (1997) state the need for research in granular mechanics and development of numerical methods that are able to deal with real industrial scale powder and granular material processing problems. From the point of view of industrial particulate matter processing, an interdisciplinary approach is demanded.

Practical problems with granular flow arise, for example, by silo quakes or other shock phenomena, which may cause silos to collapse. For this reason, silos and similar equipment are the industrial structures which are, by some orders of magnitude, the most endangered to collapse. The reason for such catastrophic events lies in the fact that forces exerted by flowing granular material are fluctuating by many orders of magnitude. These problems have been outlined together with an extensive compilation of related computer simulations in the review article by Herrmann & Luding (1998).

Another field of problems in industrial powder and granulate material proceeding comes up, if mixtures of different sized granular particles are used. If such mixtures are shaken, jostled or subjected to shearing motion, the larger particles rise to the top due to the effect of inverse grading. On one hand, this effect is appreciated and used to sort mixtures of different sized granular particles. This is done by devices as pinched sluices, Humphrey spirals or Reichert cones which make use of the effect of inverse grading of sheared granular material moving down a slope. As Jaeger et al. (1996) point out, this is of importance in the fields of powder metallurgy, pharmaceuticals or glass and paint industries.

On the other hand, Williams (1986) discusses inverse grading as difficulty in achieving homogeneous mixtures of different sized particulate matters. Unmixing by inverse grading can be avoided by choosing an appropriate mixer type and by reducing particle size differences of the materials that should be mixed or, finally, by reducing the absolute particle size. For example, no segregation occurs, if the particle sizes are smaller than 30 μm for materials with bulk densities in the range of 2000 to 3000 kgm^{-3}.

If particles of one component are very small, say smaller than about 5μm, mixing occurs by coating of the larger particles and no segregation occurs. Figure 2.4.3 shows some examples of common mixer types.

2.5 Conclusion

The aim of this chapter was to provide the wider background of the current work which is embedded in the fields of snow avalanche and granular flow research. Though originally treated in the frame of classical avalanche science, a comprehensive understanding of the functionality of the avalanche airbag must take into account the effect of inverse grading displayed by flowing granular media.

Granular flow is of great importance in the fields of industrial processing and geomechanics. As the work on the avalanche balloon showed, also avalanche dynamics are influenced by granular flow behaviour.

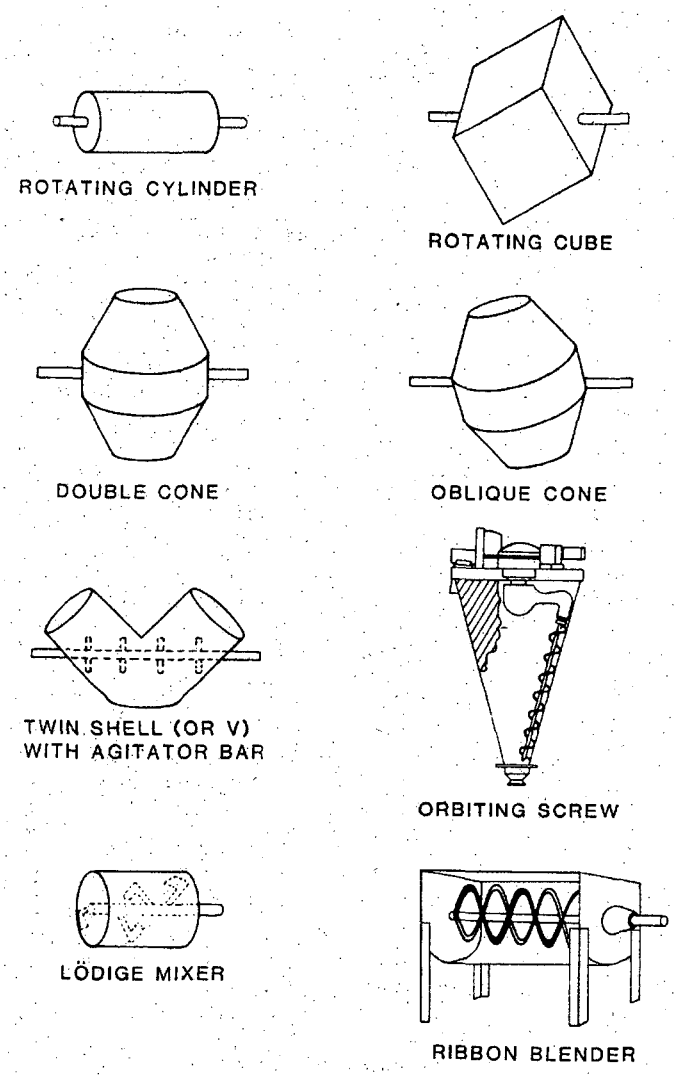

Figure 2.6: *Some common types of particle mixers. Figure taken from Williams (1986).*

Chapter 3

Empirical and experimental findings

This chapter is concerned with field observations on natural granular flows such as debris flows or snow flow avalanches and with physical modelling of granular aspects of avalanche and debris flow in laboratory experiments.

Firstly, some examples of field observations of rockfalls and snow avalanches displaying granular behaviour are given in Section 3.1. Some aspects of the behaviour exhibited by these phenomena cannot entirely be explained in terms of continuum flow laws. For example, the fact that runout distances of large avalanches or rockfalls are much longer than predicted by the continuum theories, give rise to the assumption that granular dynamics contributes to the flow behaviour. The effect of inverse grading can be observed in natural debris flows and snow avalanches.

Section 3.2 is concerned with laboratory experiments on granular chute flows. As field observations cannot easily be reproduced and therefore do not allow systematic investigations of parametrical dependencies of avalanche or debris flow, it is tried to simulate the main features of the flow by physical modelling in laboratory experiments which are designed to optimally capture the desired aspect of flow behaviour. Though there have been many experiments on granular flow behaviour in cylindrical flow geometry, we here confine to chute flow experiments, which are more similar to naturally oc-

curing avalanche flows. This confinement is also motivated by the initial question of the current work to find an explanation for the functionality of the avalanche airbag in rapid downslope avalanche motion. According to this, the further interest is focused on free surface flow of granular materials which is experimentally represented by chute experiments.

3.1 Field observations

This section provides examples of field observations on debris flows, rockfalls and snow avalanches which are related to granular flow properties with (some) respect to inverse grading.

3.1.1 Mud- and debris- flows and rockfalls

Debris flows and rockfalls are investigated and classified by numerous aspects as geological environment, geomechanical release mechanism, extent, geometry and stratification of the deposit. Here, we want to stress the observations which are related to the granular nature of the considered flows. Debris flows are made up from many discrete solid blocks and fragments generated by a rockfall.

A comprehensive collection of descriptions and data of known rockfalls in the western hemisphere and their interpretation from the geological and geomechanical point of view is provided by Voight (1978).

The almost classical example of observation of rockfalls is the description of the Elm Rockfall in Switzerland, september 10, 1881 by Heim (1882). Albert Heim defined the mean slope of a rockfall event as ratio of total vertical heigt difference H and total horizontal displacement or runout distance L during a rockfall event and related the so defined "Fahrböschung" α_f to an apparent friction coefficient μ_{ap} of the regarded rockfall and subsequent debris flow: $\tan\alpha_f = \mu_{ap} = \frac{H}{L}$, where μ_{ap} denotes the apparent friction coefficient of the rockfall.

Heim (1932) stressed the fact that the observed debris masses did not slide but flow and identified the colliding interaction between the discrete blocks

Table 3.1: *Relation of apparent friction μ_{ap} to the size of rockfall mass. Table after Heim (1932) taken from Hsü (1978).*

Rockfall	Apparent friction coefficient $\mu_{ap} = \frac{H}{L}$	Fahrböschung α_f [degree]	Volume of displaced mass [$10^6 m^3$]
Airolo	0.65	33	0.50
Monbiel	0.42	23	0.75
Elm	0.29	16	10
Frank	0.25	14	30
Goldau	0.21	12	30-40
Kandertal	0.19	11	140
Flims	0.14	8	12'000

and particles as mechanism dominating the flow. Regarding deposits of historical rockfalls in Switzerland, he observed that the apparent friction coefficient is decreasing with increasing volumes for rock fall volumes larger than 0.5×10^6 m^3 and he postulated a lubrication mechanism, which he first related to lubrication by mud. Later on, he attributed the decrease of friction to a tixotropy-like behaviour of large rockfalls, which is synonymous to the term "fluidisation" of granular material, which is commonly used to explain the large runout distances of large rockfalls and avalanches. Table 3.1 shows apparent friction coefficients of historical rockfall events determined by Heim (1932).

Albert Heim had thus intuitively developed the idea, that special features of debris flows as long runout distances might originate from the granular nature of such flows.

A comprehensive explanation of the long runout distances of large gravity currents is still missing, although many attempts of explanation listed by Savage (1993) have been made. However, it seems clear, that the high mobility of large rockfalls and debris flows is related to their granular flow nature.

Another typical feature of granular flows displayed by debris flows is inverse segregation. According to Iverson & Denlinger (1987), inverse segregation

is generally regarded as diagnostic of sediment deposited by debris flow or other sedimentary gravity currents. Though not always explicitly related to inverse grading, Voight (1978) provides several descriptions of debris flow or landslide deposits whith extraordinarily large blocks or boulders on the debris surface.

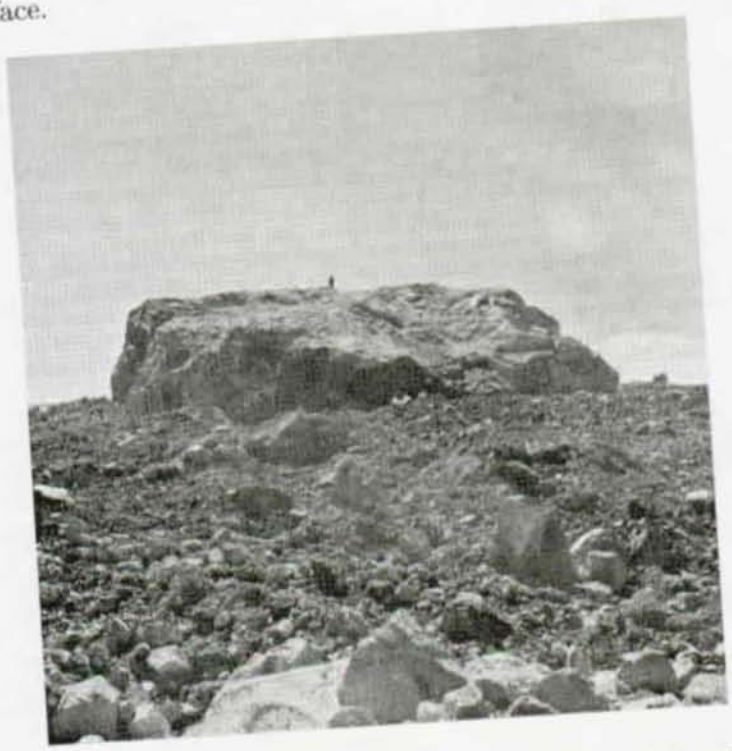

Figure 3.1: *Large block at the surface of rock avalanche debris. Size of block 40×50m, weight approximately 45,000 tons. Picture taken from Fahnestock (1978).*

3.1.2 Snow avalanches

Snow flow avalanches usually do not form a homogeneous continuum flow, but they consist of many different sized snow lumps or even snow balls, which can be observed in the debris of snow flow avalanches, as outlined in Section 6.1.1. Snow lumps are characterized by more or less sharp edges and are generated by subsequent breaking of a initial dry snow slab. In wet snow avalanches, snow balls form by rolling granulation, as explained by Nohguchi et al. (1997). For an example of such snow balls formed by

wet snow avalanches, see Figure 6.10. The investigation of depth profiles of snow lump size reported in Section 6.1.1 resulted in particle size profiles, which aretypical for inverse grading: Larger snow balls are predominant in the upper layers of the investigated debris, smaller ones are more likely to be found near the ground.

Though these observations have been concerned with the granular structure of snow avalanche debris at rest, they give a hint that the dynamics of snow flow avalanches is of granular nature. A direct proof of this assumption is not quite straightforward.

Measurements related to the structure of snow avalanches in motion have been performed by Dent et al. (1997) and Schaer & Issler (2000).

In the first case, velocity measurements using the optical correlation method were performed in small snow flow avalanches at a natural avalanche path in 0.01, 0.05, 0.09, 0.13, 0.17 and 0.19 m flow depth. The measured flow velocity increases from 0 to 3-4 ms^{-1} within the lowest, 0.01 m deep layer of the avalanche flow. The rate of shear in this thin flow layer is one order of magnitude higher than in the flow above. The highly active bottom flow layer of the avalanche is responsible for the avalanche speed. An attempt to understand the mechanisms behind has been made by Dent (1986) and Dent (1993): the avalanche is interpreted as a rapidly sheared and fluctuating layer of granular material with a large, slowly deforming overburden load.

Schaer & Issler (2000) performed high frequency pressure measurements in large scale avalanches by placing piezo electric pressure sensors with 0.1 m diameter on a round mast in the upper runout zone of a large avalanche track. The sensors were placed at heights of 0.9, 2.1, 3.0, 3.9, 7 and 19 m. The existence of the so-called saltation layer of discrete snow particles bouncing on the compact snow flow layer could be proved this way. Particle sizes from 1 to 50 cm diameter could be identified and velocity distribution functions of different size classes of particles were obtained.

The saltation layer could be characterized as a rapid, dilute granular flow of discrete particles: there was zero pressure measured between the single particle impacts on the sensor. The time evolution of the pressure in deeper

snow flow layers was characterized by a steady offset pressure overlayed by a fluctuating signal, which is hoped to provide granular flow properties, which then could be interpreted as direct proof of the granular nature of snow flow avalanches.

3.2 Laboratory experiments

In the following, an overview over experiments on granular model avalanches, which have been performed on laboratory chutes, is provided. The experiments are, on one hand, concerned with aspects of granular flow, which can be described in the frame of fluid dynamics, and, on the other hand, they deal with the inner dynamical structure of granular model or snow avalanches. Experiments performed with granular model avalanches have the advantage of being reproducable and provide the possibility to vary specific parameters of the experimental flow such as initial and boundary conditions, particle size and material properties.

Recent chute experiments dealing with granular model avalanches are enumerated. For each experiment, the experimental setup is briefly described as well as the theoretical motivation of the experiment.

3.2.1 Flow of cohesionless granular material

Savage (1979) performed chute experiments on 2-dimensional chute flow of cohesionless granular material to investigate the dependency of the flow behaviour on the roughness of the chute bottom.

Preliminary experiment

A first experiment performed by Savage was dealing with cohesionless granular material and made use of an aluminium girder with double-T profile with a lenght of 6.1 m and an inner width of 18 cm as a rectangular flow channel. The inclination of this channel could be varied between 18° and 23°. One side of the aluminium girder was roughened by gluing sand on the

aluminium surface, the aluminium surface of the other side was left smooth. By turning the girder, the bottom roughness of the channel could be varied. Glass spheres with a diameter of (0.50 $\pm$ 0.09) mm were used as granular material in the preliminary experiments.

The preliminary experiments were mainly dealing with the dependency of global flow behavior on bottom roughness of the channel. The flow was recorded perpendicularly to the flow direction by a 16 mm film camera with 64 frames per second. Flow velocity was measured by determining the displacement of coloured spheres in the flow between single frames. By doing this, surface velocity profiles in flow direction and perpendicular to flow direction could be obtained. While in the channel with smooth aluminium bottom and wall surfaces a rectangular uniform flow profile evolved, the roughened bottom and wall surfaces caused an arched flow profile and secondary flows. Furthermore, a dependency of flow height from bottom roughness was observed which was not influenced by upstream distortion (stagnation) of the flow.

Two-dimensional flow behaviour

In another experiment, Savage (1979) investigated the two- dimensional flow behaviour by determination of vertical velocity profiles at different downslope positions of the flow.

The chute employed for measurement of two-dimensional flow behaviour is shown in Figure 3.2. It had a length of 1.22 m, a width of 3.86 cm and its inclination was variable from 30° to 90°. The side walls of the chute were transparent for visual observations, the bottom was covered with nopped rubber gum to model bottom roughness. The granular material consisted of polystyrene spheres with a mean diameter of 1.2 mm and a density of 103 kgm^{-3}. The outflow of the granular material from a supply bin was regulated by a wooden plate with holes of different diameters.

Extensive measurements of downslope flow velocity profiles were performed in each 10 vertical positions at three downslope flow positions. For the velocity measurements, the method of cross correlation of reflexivity measure-

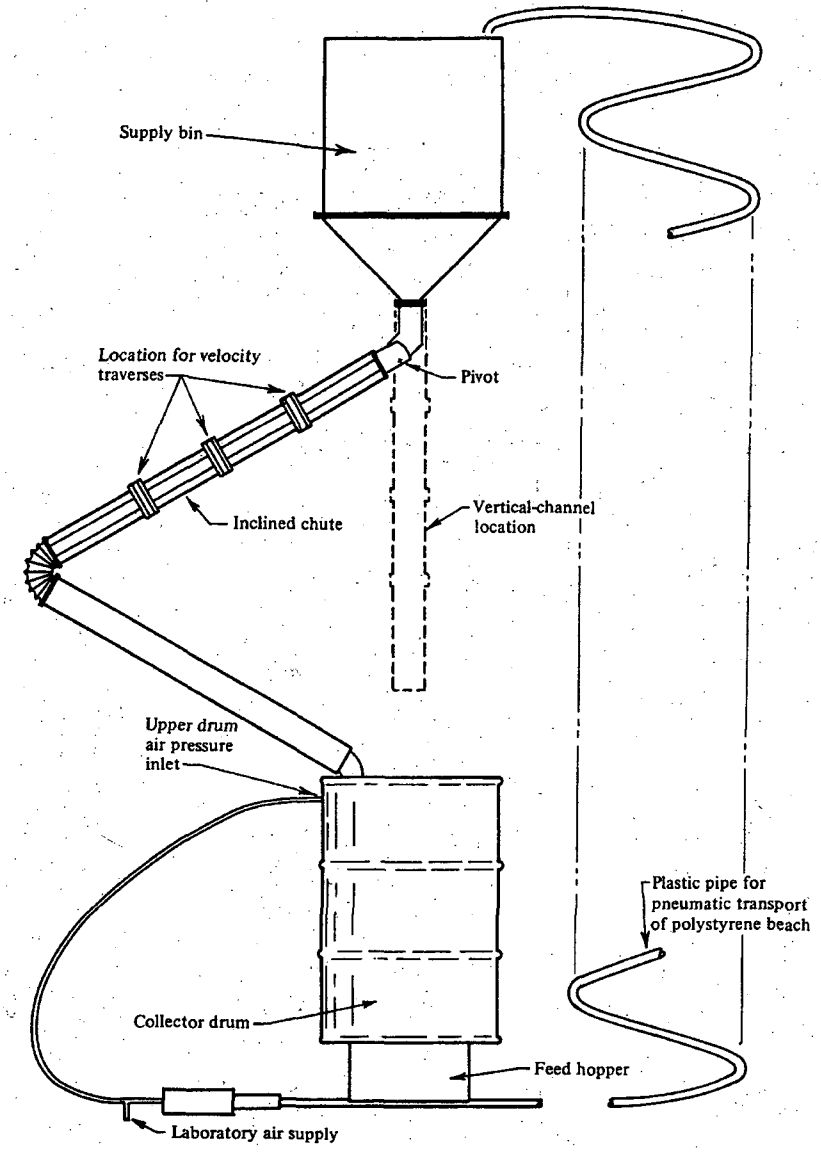

Figure 3.2: *Sketch of setup of inclined chute experiment. Figure taken from Savage (1979).*

ments was employed, which is extensively explained in Dent et al. (1997).

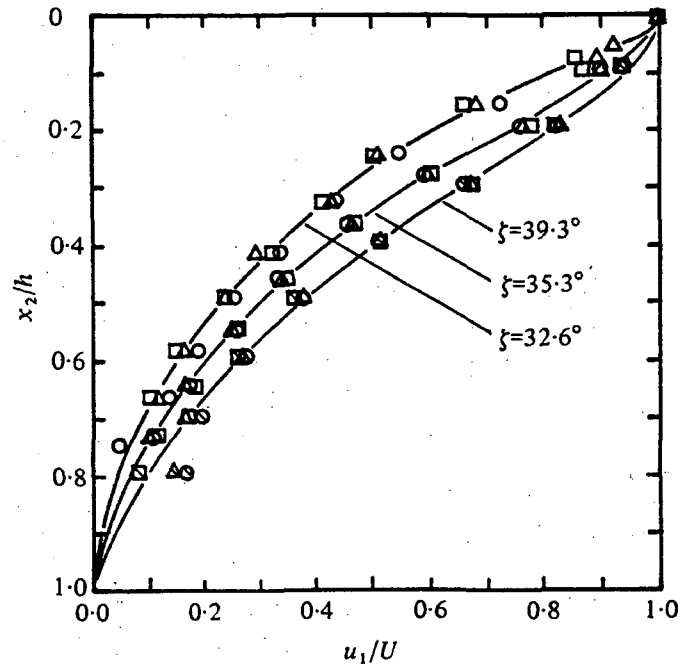

Figure 3.3: *Non-dimensional profiles of downslope flow velocity u_1/U against normalized flow depth x_2/h, where U is the surface flow velocity and h the flow depth. Profiles at different downslope positions for different chute inclinations ζ are shown. Circles, triangles and squares denote donslope positions at 33.0, 63.5 and 94.0 cm from entry of the chute. Figure taken from Savage (1979).*

Profile shapes were observed with respect to chute inclination, flow density (or material flow, respectively) and downslope position, as shown in Figure 3.3. The measured profiles were compared to profiles obtained from a continuum mechanical model based on the derivation of a constitutive law for cohesionless granular material. As the experimental conditions were close to the simplifying assumptions underlying the theoretical description of the granular material, there was satisfactory agreement between experimentally observed and theoretically derived velocity profiles.

3.2.2 Measurement of inverse segregation

The experimental setup for measurement of inverse grading used by Savage & Lun (1988) consisted of a 1 m long, 7.5 cm wide chute with an inclination of 26° - 28° with roughened bottom and smooth glass walls. At the downslope end of the chute there were splitter plates parallel to the chute, which collected the particles of different flow layers in separate collector bins. The granular material used in the experiment consisted of a homogeneous binary mixture of larger and smaller polystyrene spheres with a density of 1095 kgm^{-3}. The spheres had diameters of 1.6 mm and 0.94 mm, respectively. The experimental setup is shown in Figure 3.4.

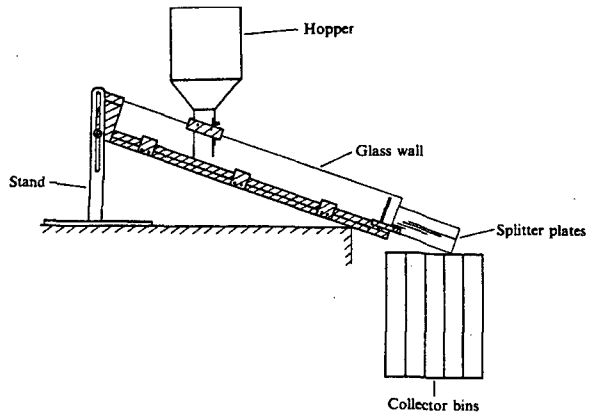

Figure 3.4: *Experimental setup for measurement of inverse grading on an inclined chute. Figure taken from Savage & Lun (1988).*

The segregation of the initially homogeneous binary mixture in flow direction was observed by placing the splitter plates at different downslope flow directions. The degree of segregation was determined by counting of the large and small particles in the collector bins related to different flow heights defined by the splitter plates.

The concentration profiles of large and small particles at different downslope flow positions were compared to theoretical predictions (see fig. 3.5). The theoretical background underlying the above experiment comprises simple geometrical and mechanical considerations ("random sieving and squeeze expulsion") embedded in a statistical formulation. This theoretical model

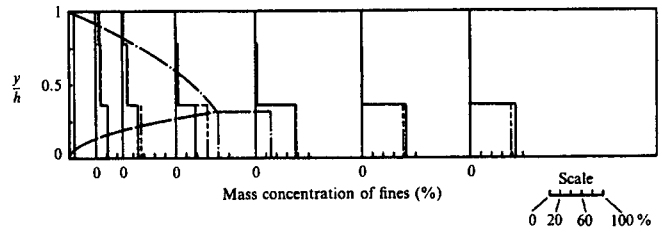

Figure 3.5: *Concentration profiles of fine particles at different downslope positions. The curved lines are the theoretically obtained lines of zero or hundred percent concentration of fine particles. Figure taken from Savage & Lun (1988).*

approach will be reported in section 4.5.2, a qualitative demonstration in the frame of the current work is provided in section 5.18.

3.2.3 Laterally confined granular avalanches

The experimental setup and work are described as well as the underlying theory of depth averaged evolution equations in Savage & Hutter (1991), Hutter & Koch (1991), Greve et al. (1993a) and Hutter et al. (1995).

A model for initially stationary granular material along a rough inclined track was checked employing a chute with a 1.4 m long inclined and a 1.7 m long runout part. The chute was 10 cm wide and confined by transparent glass walls with a metric scale for qualitative and quantitative visual observations. The bottom roughness of the chute could be varied by employing either PVC, drawing- or sand paper as floor material.

Lense-shaped vestolene-particles with approximate dimensions of (2.5 $\times$ 4.0) mm and a particle density of 950 kgm^{-3} were used as granular material. Glass spheres with a diameter of 3 mm and a bulk density of 1730 kgm^{-3} were employed as alternative material.

By opening a shutter, a defined mass (either 1, 2, 3 or 4 kg) of granular material was released and the evolution of the avalanche shape was recorded by photograph or video takes with 6 or 24 frames per second, respectively.

The evolution of the avalanche shape was observed with respect to granular material properties, slope angle of chute, total mass of released material

and bottom roughness. The avalanche shape was characterized by the time evolution of its front- and rear edge positions, as shown in Figure 3.6.

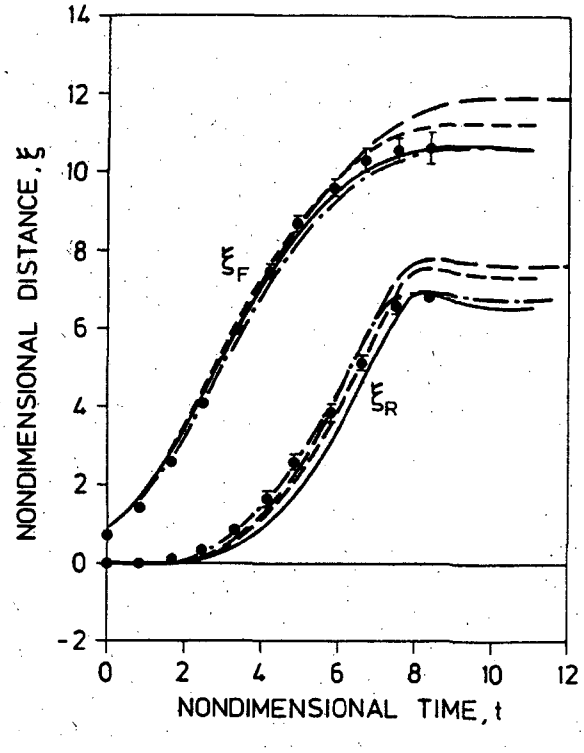

Figure 3.6: *Experimentally measured and theoretically predicted dimensionless leading and trailing edge positions ξ_F and ξ_R for a granular pile consistig of 1 kg of vestolen particles moving on a 50° inclined chute. Figure taken from Savage & Hutter (1991).*

The experiment was also performed employing an exponentially curved chute and a chute with a concavely curved section.

The model checked by the above experimental setup is based on depth averaged field equations for mass and momentum balance from which partial differential equations for (depth averaged) downslope velocity and for evolution of flow depth were derived. The parameters joining these equations are the bed friction angle of the chute and the internal friction angle of the granular material, respectively.

3.2.4 Two-dimensional spreading of unconstrained granular model avalanches

Various experiments were performed by Lang et al. (1989) and Koch et al. (1994) on a 5 m long and 2 m wide chute (see fig. 3.7) to investigate the two- dimensional evolution of a unconstrained granular model avalanche. The inclination of a 2 m long part of the chute could be varied from 20° to 60°, where the transition part of the chute connecting the inclined with the horizontal part was curved. The chute surface consisted of safety glass or, for modelling of bottom roughness, of sandpaper with 120 grains per cm^2. Used granular materials had typical sizes in the range from 2 mm to 5 mm and were consisting of glass and quartz spheres or marble gravel.

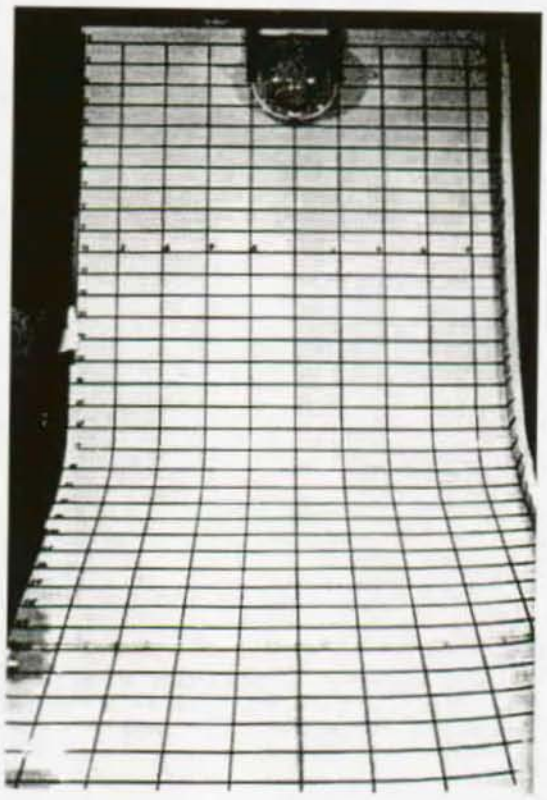

Figure 3.7: *Front view of experimental chute. Width = 2 m, length = 5m, grid spacing 200 mm × 100 mm. Picture taken from Lang et al. (1989).*

The experiments were performed to check theoretical predictions on granular

flow on rough, curved beds by Greve et al. (1993b) and Hutter (1996).

Approximately 20 kg of granular material were released by instantly lifting a half sphere shaped reservoir. Considering dependencies from material properties, slope inclination and bottom roughness, the evolution of the shape of the released granular material was recorded by a motor-driven wide-angle photo camera taking 10-15 frames per second.

Experimental results were compared with similarity solutions of a two dimensional continuum mechanical model of unconfined granular flow, described in Savage & Hutter (1991).

3.2.5 Chute experiment on single particle dynamics

Dippel et al. (1996)(a), and Dippel et al. (1996)(b) experimentally investigated the interaction of one single particle with the rough surface of an inclined plane instead of the global dynamics of a multiparticle flow. Theoretical considerations of the single particle problem can be found in Bideau et al. (1996) and Dippel et al. (1997). By confining on the behaviour of one single particle, an insight in the principle mechanism of motion of single particles forming a granular flow was achieved. Against this background, the evolution of friction by interaction of a particle with the rough plane was of special interest.

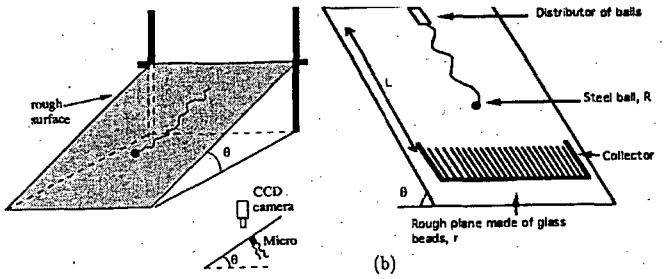

Figure 3.8: *Principle sketch of experimental setup for measurement of single particle dynamics down a rough inclined chute. Figure taken from Dippel et al. (1997).*

The experimental setup consisted of a 2 m long and 1 m wide chute with variable inclination and rough surface as depicted in Figure 3.8. The sur-

face roughness could be varied by different materials as sand or little glass spheres, which were fixed onto the chute surface by contact paper. The governing parameter of the experiment is the ratio $\mathcal{R} = \frac{r}{R}$ of particle radius r and the typical radius R of the bottom roughness. Furthermore, the longitudinal coefficient of restitution e_n for the particle collisions with the bottom influences the particle motion. It is defined as ratio $e_n = \frac{v_n'}{v_n}$ of the longitudinal velocity component of the particle (with respect to the rough bottom surface it is colliding with) after and before collision and thus gives a measure for the inelasticity of the collision process. The motion of single steel or plastic spheres with different roughness ratios $\mathcal{R}$ was investigated. The spheres were put onto the chute with defined start velocities at defined place by a computer-controlled particle distributor.

The particle motion was recorded by a video camera perpendicular to the chute, while collisions of the particle with the bumps on the bottom were recorded by a microphone, which was connected with an amplifier and a spectrum analyzer. Particle velocities were determined by light barriers at the side of the chute and the lateral displacement of the particles was observed by placing 70 collector bins at the lower end of the chute.

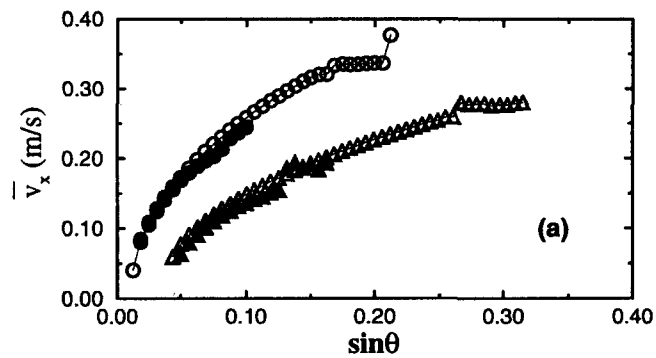

Figure 3.9: *Dependency of steady terminal downslope velocity $\bar{v}_x$ on slope angle θ, roughness ratio $\mathcal{R}$ and restitution coefficient e_n of the particle. Triangles refer to $\mathcal{R}$=1.75, circles to $\mathcal{R}$=3.0. Open symplols correspond to e_n=0.3, closed symbols to e_n = 0.8. Figure taken from Dippel et al. (1997).*

As a result of the experiments, there could be observed a terminal steady velocity of the particles which is dependent from the chute inclination and

from the roughness ratio $\mathcal{R}$ but not from the initial particle velocity (see fig 3.9). This behaviour could be reproduced by a analytical geometrical analysis as well as by numerical molecular dynamics simulation, as outlined in the two papers of Dippel et al. (1996).

3.2.6 Chute experiment with fluidized snow and ice as granular material

In a cold laboratory, chute experiments with fluidized snow were performed by Nishimura (1990) at a temperature of -15°C. Fluidized snow is a suspension of snow in air, where both components are in motion. Snow was kept in fluidized state in a reservoir with 0.9 m diameter, in which 3 arms were rotating with 1 Hz. Within one second, 5-7 kg of fluidized snow were put onto the chute. The snow used in the experiment was natural granular snow with a mean grain diameter of 0.59 mm.

The experimental chute sketched in Figure 3.10 was 5.4 m long and 8 cm wide and its inclination could be varied between 30° and 45°. The chute had transparent side walls and the chute's bottom roughness could be adjusted by employing different materials as PVC-foil, sand or snow.

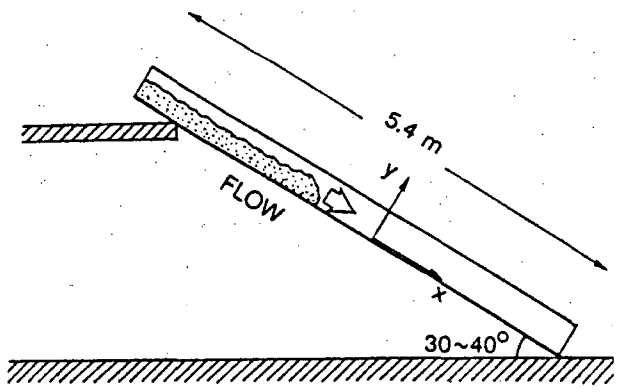

Figure 3.10: *Experimental setup for chute flows of ice spheres. Figure taken from Nishimura et al. (1993).*

The flow of the fluidized snow was recorded through the transparent side wall

of the chute by a high-speed video camera with 200 frames per second. By evaluation of the video takes, velocity profiles and flow depth as a function of downslope position were obtained. Density fluctuations of the flowing snow were accessible by capacitance measurements in 10 mm and 35 mm flow height.

As fluidized snow is, at first approximation, behaving like a fluid, the experiment could be used to validate avalanche flow models based upon laws of motion of continuous fluid-like media. Furthermore, the experiment provided valuable measurements of the viscosity of fluidized snow.

The experimental setup described above was also used by Nishimura et al. (1993) for the investigation of the behaviour of a granular avalanche consisting of little ice spheres with a mean diameter of (2.9±0.3) mm.

The experiments were performed at temperatures in the range of -30°C to 0°C. In the region of the chute, where the flow of the granular ice avalanche had adjusted to a stationary state, velocity and density profiles were obtained by evaluation of high-speed (200 fr/s) video recordings. An example of measured velocity profiles is shown in Figure 3.11.

The flow properties were investigated as function of material properties of the ice spheres, which could be varied using their temperature dependency. Furthermore, the influence of bottom roughness of the chute on the ice sphere flow was considered.

For rough chute bottoms, mean flow densities and velocities in the vicinity of the bottom were observed to be lower than in the other flow regions. Velocity fluctuations in downslope direction were stronger than in lateral and vertical direction. Furthermore, fluctuations are more evolved in flow regions with lower mean density, i.e. in the vicinity of the flow surface as well as in the vicinity of the chute bottom.

3.2.7 Physical modelling of avalanche shape

To verify theoretical results concerning similarity properties of granular avalanches, Nohguchi (1997) used a 2 m long chute with semicircular cross-section and a variable inclination of 30° to 50° (see also Nohguchi & Nishimura

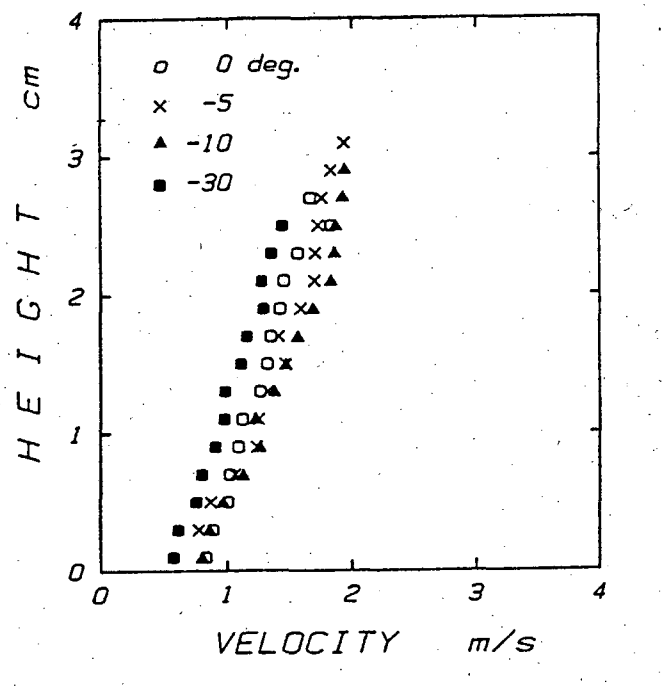

Figure 3.11: *Temperature dependency of ice sphere flow velocity profiles at a chute inclination of 30°. Figure taken from Nishimura et al. (1993).*

(1996)). The width (i.e. the diameter of the cross sectional semicircle) was varied between 50, 75, 100, 125 and 150 mm. The model granular material consisted of polystyrene foam spheres with diameters in the range of 1.5 to 2.0 mm. The mean density of the granular material was 16.8 kgm^{-3}, where one single particle had a mass of 0.2 mg and its terminal falling velocity in air was 0.5 ms^{-1}.

As a result, a dependency of the steady terminal velocity v_e of the avalanche from the number N_p of involved particles was found. (The terminal velocity was also parametrisized by the slope angle of the chute). The measured scaling law $v_e \sim N_p^{\frac{1}{6}}$ for the terminal avalanche velocity agreed well with the theoretical prediction by Kosugi et al. (1994) as depicted in Figure 3.12.

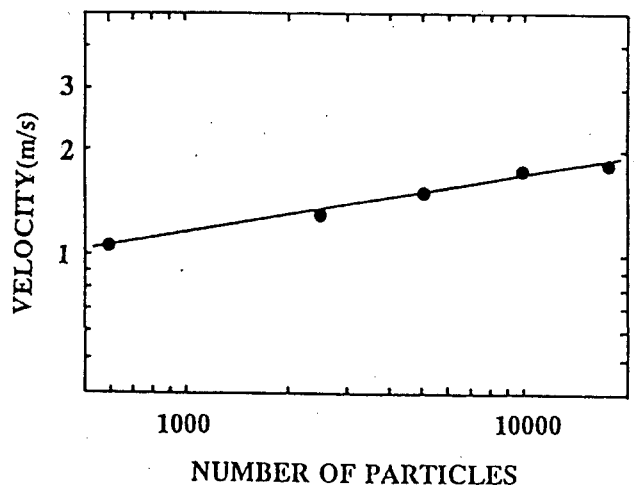

Figure 3.12: *Dependency of terminal avalanche velocity from particle number. The line represents the theoretical prediction with a scaling exponent of* $\frac{1}{6}$. *Figure taken from Nohguchi (1997).*

With increasing particle number N_p, the model avalanches were evolving an increasingly clearly visible head-tail structure. The evolution of the avalanche structure is governed by the dimensionless structure parameter $\Gamma = \frac{v_e^2}{L_c g}$ which has the shape of a Froude number. L_c denotes the chute length and g the gravitational acceleration.

An avalanche with a typical head-tail structure evolved, if the Froude num-

ber Γ was sufficiently small, i.e. if $\Gamma << 1$.

3.2.8 Avalanches of table tennis balls

Chute experiments with table tennis balls performed by Kosugi et al. (1994) were concerned with similar questions as the above described styrene foam avalanche experiments.

For the table tennis ball experiment, an outdoor chute with a 15 m long inclined section with a slope angle of 30° and 12 m long curved section was used. The bottom of the chute with rectangular cross section was smooth and made of wood, where the side walls were made of glass.

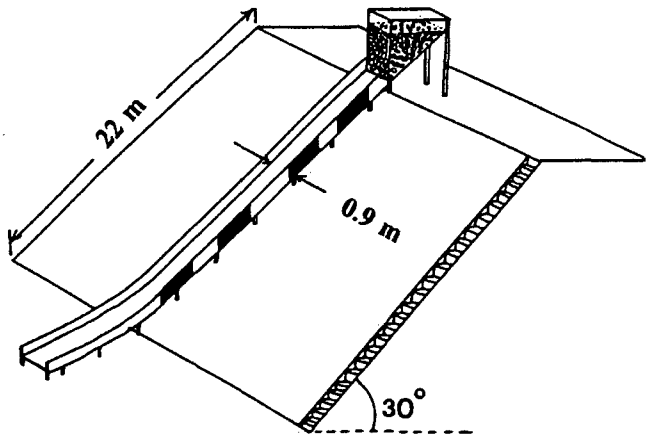

Figure 3.13: *Experimental chute for observation of table tennis ball avalanches. Figure taken from Nohguchi & Nishimura (1996).*

Avalanches were formed by up to 10,000 table tennis balls, which had a diameter of 37.7 mm, a mass of 2.48 g and a terminal velocity $v_{e,s}$ of 4.5 ms^{-1}, when moving down the slope as single particles.

The avalanche was observed by a high-speed video camera in the curved part of the chute. Some coloured balls were used as tracer particles to support visual observation of the granular table tennis ball avalanche.

The evolution of an avalanche with head-tail structure could be observed. The head had a downslope velocity of 8 ms^{-1}, while the tail of the avalanche

reached only a velocity of 4.5 ms^{-1}.

The smooth chute surface caused a higher particle number density and smaller velocity fluctuations in the flow layers adjacent to the bottom than in higher flow layers. Flow height in the head region was much larger than in the tail region, where the flow consisted mainly of one single ball layer.

Investigations of table tennis ball avalanches without lateral constraint were performed in summer of 1995 by Nishimura et al. (1996) on the runout of the Olympic ski jump in Sapporo.

The runout of the ski jump was 150 m long and 30 m wide at a maximum inclination of 30°. The surface of the runout was covered with artificial lawn mats, which can be termed as "rough" within the dimensions of the experiment. Due to the size of the experiment, air transport and -friction played an important role on the avalanche dynamics. As table tennis balls are nearly elastic and spherical, they form the simplest possible granular material for investigation of the formation of a 2-phase flow in air.

The investigated model avalanches consisted of up to 250,000 table tennis balls which were simultaneously released by instantly opening a container with the balls inside.

Global flow behaviour was recorded as well as single particle dynamics by several video cameras. The extension of the ball debris was recorded after standstill of the model avalanche. Furthermore, impact forces of the ball avalanche and velocities of entrained air along the avalanche track were measured by ultrasonic anemometers.

As shown in Figure 3.14, after a flow distance of 65 m, the 40 ball diameters high avalanche front had reached a steady velocity of 15 ms^{-1}, which was decreasing with decreasing slope angle at the end of the runout. As the front velocity was about 1.5 times the free fall velocity of a single ball in air, this can be interpreted as an indication of the strong interaction of the avalanche with air: a two phase flow of fluidized balls had evolved.

The terminal front velocity v_e of the avalanche was found to depend on the number of balls involved in the flow and was scaling as $v_e \sim N_p^{\frac{1}{6}}$ as derived in Nohguchi (1997) or Nohguchi & Nishimura (1996). For example, the

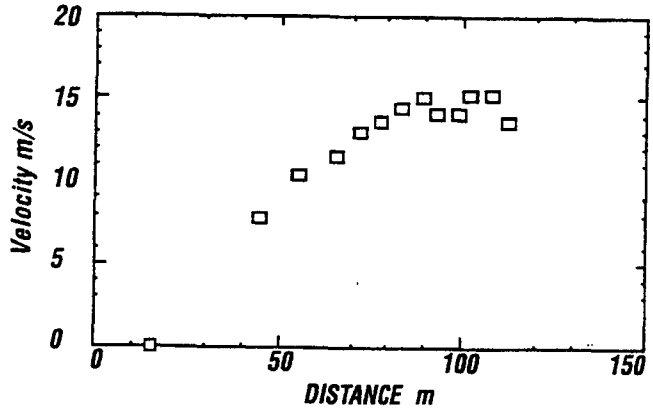

Figure 3.14: Leading edge velocity vs flow distance of a table-tennis-ball avalanche consisting of 250'000 balls. The avalanche reaches its terminal velocity after 65 m flow distance (note that the start position is at x=15m). Figure taken from Nishimura et al. (1996).

terminal velocity of two balls independently rolling and bumping down the runout of the ski jump was just 2.8 ms^{-1}.

3.2.9 Comments

Experiments on granular avalanches listed above were concerned either with validations of predictions on the global flow shape and behaviour made by models based on continuum mechanical description of granular flows or they were investigating special aspects of granular flow as the interaction of a single particle with a rough surface or the evolution of inverse grading in a binary mixture of spheres.

Physical modelling of granular avalanches, as described above, is confined by the limited possibility of systematic variation of all interesting flow or particle parameters, respectively. Experiments are mostly designed to investigate each one aspect of granular flow behaviour and it is difficult to achieve a comprehensive picture including single particle interaction as well as global flow behaviour.

For example, the investigation of single particle interaction with a rough

plane by Dippel et al. (1997) cannot make any statement on how the observed mechanics will affect global flow behaviour if included in a granular avalanche. Or, giving another example, the proof of inverse grading by Savage & Lun (1988) remains rather qualitative, for the model does not include systematic variations of parameters as particle size and densities or particle material properties.

3.3 Conclusion

This chapter was concerned with the observation of granular flows in the field and in laboratory experiments.

Field observations of debris flow or avalanches are mostly limited to an indirect investigation of the granular flow by regarding the steady material deposited by the flow events. Direct observation of granular flow properties is rather expensive in preparing time and required instrumentation. Furthermore, the possibility of direct observation of natural avalanche or debris flow depends on whether the conditions in the field permit the release of an avalanche or debris flow event.

Laboratory model experiments, however, are reproducable and can be designed in a way that allows to focus on the investigation of a distinct interesting flow property.

Model experiments are limited in the sense, that they are designed to investigate specific flow properties with respect to distinct boundary conditions. Instrumentation is expensive and information about internal flow behaviour as velocity profiles apart from the boundaries or distribution of particle fluctuation energy is difficult to access.

This difficulties are circumvented by mathematical or numerical flow models. The latter ones are even much more flexible for they provide an easy possibility to vary material parameters of granular particles. Furthermore, compared to physical modelling, there are not such great constructive efforts neccessary to establish different boundary conditions.

Chapter 4

Mathematical modelling

4.1 Introduction

This chapter is concerned with the mathematical description of avalanches and granular flow by analytical and numerical means. The philosophy underlying this chapter is the attempt to embed the explanation of the inverse segregation effect chosen in the current work into the fields of mathematical avalanche and granular flow modelling. This attempt is made due to the history of the current work, which was initiated by the need to understand the physical reason of the effectiveness of the avalanche airbag. Common avalanche dynamics models are not able to reproduce the effect of inverse grading which is a typical feature of granular flows. Starting from simple center-of mass avalanche flow models, increasingly specific descriptions of avalanche and granular flow are reported. While the avalanche models account for general snow flow avalanche behaviour, analytic and discrete element descriptions of granular flow can also describe the specific effect of inverse grading.

Common center-of mass and continuum avalanche models are reported in Section 4.2. They deal with general avalanche flow behaviour, represented by flow velocities and runout geometries. In some models, aspects of granular flows are used in friction or continuum constitutive laws, but no qualitative new understanding of granular flow behaviour is provided.

Section 4.3 is concerned with a quasi thermodynamical approach to granular flow which is similar to kinetic gas theory. These kinetic theories support continuum balance laws for the granular flow motion but, due to neccessary assumptions, are valid only in very narrow parameter ranges. The theories provide principle insight in the origin of the continuum mechanical aspects of granular flow.

In Section 4.4, discrete particle models, which can describe granular flows over a broad range of parameters, are introduced. Depending on the flow regime, either soft sphere models for dense, macroviscous flows or hard sphere models for rapid, collisional flows are used.

In Section 4.5, finally, two analytical approaches to the effect of inverse grading are referred. One is based on kinetic theory, the other one on a phenomenological picture of the segregational process. These descriptions, however, are of more principle nature, so that a numerical discrete particle model should be preferred for a systematic investigation of the inverse segregation effect in granular flow.

4.2 Common snow avalanche models

This section provides an overview over common snow flow avalanche models. Beginning with simple center-of-mass sliding block models, there has been a *development to continuum mechanical deformable body avalanche models*, which can also account for flow and deposit geometry with respect to the terrain topography.

4.2.1 Rigid body models

Rigid body models (also termed "sliding block" or "lumped mass" models) describe an avalanche as rigid body on a slope moving according to the sum of forces acting on its center of mass. Models of this type do not make any statement about the deformation of the avalanche mass. For the derivation of the equations of motion, either force or energy considerations with respect to the center of mass are employed. In the following, we briefly list some

commonly used rigid body models with respect to their basic assumptions and general features which are relevant for continuum and granular dynamic description of avalanche motion.

Körner energy line block model

A description of the rigid block motion by energy considerations is given by Körner (1976) and Körner (1980). The block velocity v at each point of the path is $v = \sqrt{2gh_v}$, where h_v is the vertical distance of the center of mass of the block and a so-called "energy line". The energy line is a graphical representation of the energy conservation law, which states that the sum of potential and kinetic energy and the loss of energy along the path due to friction is constant. For example, for constant Coulomb basal friction with a Coulomb coefficient μ as the only resistive process, the energy line is a straight line with a downslope inclination $\theta = \tan^{-1}(\mu)$. Similar considerations have almost been employed by Heim (1932) to describe the motion of debris flows (see Sect. 3.1.1).

Dade and Huppert energy line block model

Dade & Huppert (1998) suggested an energy balance approach to rigid block motion, in which the potential energy gained by the avalanche flow is balanced by the frictional work W:

$$m_{bl}gH = W, \tag{4.1}$$

where m_{bl} is the avalanche block mass, g the gravitational acceleration and H the difference of topographic elevation travelled by the avalanche. W can be obtained by different frictional laws as, for example, by a law of reduced basal friction due to to accoustic fluidisation of the flow or by a friction law for the relaxation of stress. In the latter case, taking $W = \tau A_c L$ with $A_c = \lambda_{f,r} L^2$ the total area covered by an event, L the length, over which resistance forces act and τ the resisting basal shear during runout, one can estimate the area covered by avalanche debris as

$$A_c = \sqrt[3]{\lambda_{f,r}\left(\frac{m_{bl}gH}{\tau}\right)^2}. \tag{4.2}$$

A problem of this approach is the appropriate choice of τ, which, for example, is assumed to be equivalent to the yield strength τ_y of unconfined debris in transport.

Voellmy block model

To calculate runout distances of dense snow flow avalanches, Voellmy (1955) considered the sliding mass as unbounded fluid with depth H as depicted in Figure 4.1. The avalanche mass reaches a terminal velocity v_t by balance of gravitational and shear forces on an infinitely long slope of inclination θ_1. Employing hydraulic theory, the resulting shear is computed as the sum of dynamic drags at the free surface and the bed and the Coulomb forces proportional to normal forces on the bed. The balance of gravitational and shear forces then yields

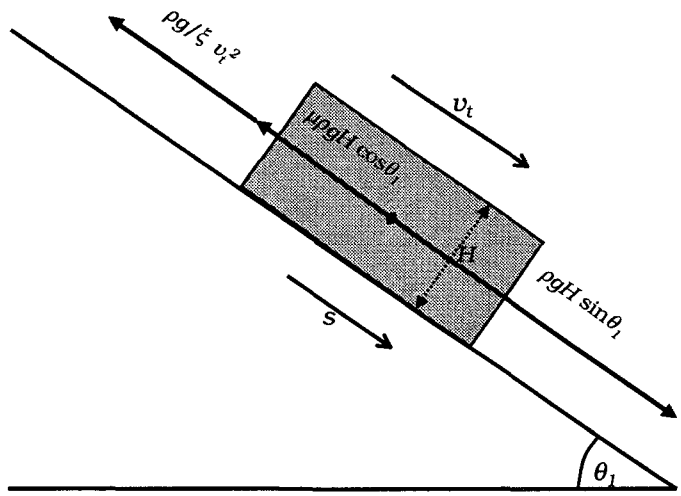

Figure 4.1: *Principle sketch of Voellmy block model. The forces exerted on the avalanche mass are assumed to act on the center of mass of the "fluid block".*

$$v_t = \sqrt{\xi H(\sin\theta_1 - \mu\cos\theta_1)}, \tag{4.3}$$

where ξ is the "coefficient of turbulent friction" and μ is the Coulomb friction coefficient. (The coefficients of dynamic frictional processes proportional to the square of velocity have been lumped together into ξ.) The runout distance s_r is computed from the point where the slope angle equals $\tan^{-1}(\mu)$ by energy considerations of a decelerating block on a slope with constant inclination $\theta_2 < \theta_1$:

$$s_r = \frac{v_t^2}{2g(\mu \cos\theta_2 - \sin\theta_2) + v_t^2 g/\xi H_D}, \tag{4.4}$$

where H_D is the mean depositional depth accounting for energy loss due to pile-up of the debris.

The PCM block model

Voellmy' s model has been extended to a 2 parameter model called PCM (Perla, Cheng, McClung) model by Perla et al. (1980). It describes an avalanche as an 1D block of finite mass moving on a path of varying curvature. The varying curvature is taken into account by a slope angle θ which depends on the downslope position s of the center of mass of the avalanche: $\theta = \theta(s)$. The momentum balance, including a Coulomb frictional term, centrifugal forces due to path curavture, dynamic drag and inertia resistive ploughing, leads to a linear differential equation for the square of the avalanche speed along the track:

$$\frac{1}{2}\frac{dv^2}{ds} = g(\sin\theta - \mu\cos\theta) - \frac{D}{M}v^2, \tag{4.5}$$

where $\theta(s)$ is the local inclination of the track, s the downslope position of the center of mass of the avalanche and g is the acceleration of gravity. $\frac{D}{M}$ is called "mass to drag ratio" and is a collection of all coefficients of resistive forces depending on v^2.

In the limit of constant parameter values and inclination along the avalanche track, the model converges to the simple Voellmy model. The validity of the PCM model depends on the knowledge of parameter values which have to

be determined by applying the model to known avalanche events. Extensive calibration work on the Voellmy and the PCM block model has been performed by Buser & Frutiger (1980).

The VSG refined block model

The VSG (Voellmy, Salm and Gubler) refined block model is the most commonly used model for operational avalanche simulation in Switzerland and Austria. It is based on the work of Voellmy (1955) Salm et al. (1990) Salm (1980) and Gubler (1993).

Given the initial width W_0 and flow height h_0 of an avalanche, the model computes the avalanche motion in a track with defined width using the Voellmy equations for the terminal velocity v_p in the considered section of the avalanche track. The avalanche runout length is determined by time dependent computation of the avalanche front motion assuming a linear decrease of the velocity square according to

$$v^2 = H_D \xi(\mu \cos\theta_s - \sin\theta_s). \tag{4.6}$$

Here, H_D is the mean deposit height and θ_s is the average inclination of the runout zone of the avalanche. The runout length s_r is given by

$$s_r = \frac{H_D}{2g} \ln(1 + \frac{v_p}{v^2}), \tag{4.7}$$

where v_p is the terminal velocity of the avalanche in the track section above the runout zone.

Furhermore, the VSG model takes into acount the transfer of kinetic (avalanche speed) to potential (flow height) energy.

The results of the VSG model are strongly depending on input values of initial witdth W_0 and flow hight h_0 in the avalanche starting zone, friction coefficients μ and ξ, cross section of the avalanche track, and inclinations of track and runout zone. As the model, besides flow velocities and runout distances, also returns the dynamic pressure exerted to obstacles in the

avalanche track, it can be used to define the red zone in avalanche hazard maps (the red zone is the zone, where no building activity is permitted), by computing the location of the 30 kbar line of constant pressure.

Other sliding block models

McClung (1990) employs concepts of granular flow to explain the fact that speeds and runout distances are nearly independent of slope steepness if they are scaled by a suitable length: higher basal shear rates are inreasing dynamic friction which compensates the increasing driving forces on steeper paths. The mathematical form of the model is similar to the Voellmy model, but its application is proceeding into the opposite direction: runout distances and avalanche speeds are employed to determine (speed dependent) granular friction.

Perla et al. (1984) model an avalanche as a collection of approximately 1000 particles moving randomly and independently due to gravity and randomly fluctuating resistive forces. The model uses equations of motion for each particle mass center and includes entrainment by including new particles at the avalanche front. Note that this model is no granular flow but a statistical model, in which the randomly fluctuating resistive forces acting on the particles are determined by Monte-Carlo simulation. Computed particle statistics provided reasonable simulation of observed avalanche speeds and debris distribution.

Irgens et al. (1998) employ a center-of-mass model for the description of avalanche motion along a retaining dam. Similar to the Voellmy model, the model contains Coulomb and dynamic drag resistive forces. As the center-of-mass consideration does not take into account dynamic effects of the avalanche extension, the validity of model results is limited.

Nohguchi (1989) models the motion of an avalanche mass center on an arbirary 3D surface using resistive forces (Coulomb friction and dynamic drag) analoguous to the Voellmy model and, additionally, the confining forces exerted onto the avalanche due to the topography of the slope. For suitable parameter values, the modelled avalanche follows the observed path of the

avalanche in the field: For this reason, the model can be used to calibrate parameter values by simulating real avalanche paths.

Maeno & Nishimura (1987) and Nishimura (1990) model the motion of the center of mass of an avalanche on an 3D topography similar to Nohguchi (1989). Snow entrainment is included in their model approach as well as Coulomb friction, viscous resistance and resistance due to turbulent forces, where the Coulomb coefficient of friction is assumed to decrease exponentially with velocity.

Similar center-of-mass- models have been developed independently in Russia or the USSR, respectively, since the early 1930's. A comprehensive compilation of literature concerning all aspects of avalanche science including center-of-mass-modelling of avalanches is given by Bozhinsky & Losev (1998). Though similar in basic ideas, Russian models are generally of mathematically more restrictive form than parallel or later western work.

Summary

Center-of-mass models can describe avalanche motion in terms of velocity and maximum runout length of the center of mass of the considered avalanche. Though partly employing concepts of granular dynamics to estimate shear forces, they cannot make any statement on the internal flow structure. For this reason, Coulomb and turbulent friction coefficients of the rigid block modelling have to be determined empirically by simulating known real avalanche events.

4.2.2 Continuum dynamic description

There exists a great number of snow flow avalanche models which describe avalanches as deformable bodies employing continuum dynamic balance equations for mass and momentum. A comprehensive overview is given by Harbitz (1998). Most continuum avalanche models interprete avalanches as unsteady fluid flow which can be described according to shallow-water theory. Granular behaviour of the avalanche flow is taken into account by

continuum constitutive equations for granular media entering the momentum balance equations. In the following, basic assumptions, general structure of balance and constitutive laws of continuum avalanche models are explained.

Assumptions

Continuum flow assumption: In these kinds of models, the avalanche flow is assumed to be a fluid continuum with constant mean density (see Bartelt & Gruber (1998)) or, speaking differently, as homogeneous, incompressible one-phase continuum medium by Barbolini & Nettuno (1998). Another common formulation is the one of a "mathematical deformable body" in the frame of the NIS model developped by Norem et al. (1986), Norem et al. (1989) and Norem & Schieldrop (1991). Models incorporating granular mechanical effects like the ones of Hutter & Koch (1991), Sampl (1998) or Lang & Leo (1994) assume flows of "incompressible cohesionless granular material" to be describable in terms of continuum dynamic balance equations.

Unsteady flow assumption: In the case of modelling avalanches as continuum fluids, they are looked upon as unsteady, non uniform flows by Bartelt & Gruber (1998). Shallow water equations similar to those of unsteady flows (flood waves) in rivers or on slopes are used by Eglit (1998), Bozhinsky & Losev (1998), Barbolini & Nettuno (1998) and others.

Hydrostatic assumption: Frequently, hydrostatic vertical pressure distribution in the flow is assumed as for example by Bartelt & Gruber (1997), Bartelt et al. (1997), Barbolini & Nettuno (1998) or Murty & Eswaran (1994b) and Murty & Eswaran (1994a).

Depth averaging: Fluid dynamical modelling of avalanches is commonly performed using depth averaged equations of mass and momentum balance, see Eglit (1998), Hutter & Koch (1991) and others.

Granular assumption: Models by Breitfuss & Scheidegger (1974), Yoshimatsu (1991), Norem & Schieldrop (1991), Kumar (1994), Hutter & Koch (1991) or Sampl (1998) take into account the granular nature of avalanche or debris flows. The granular nature of the flows is incorporated in the continuum dynamical description by regarding dynamic shear and dispersive pressure due to interparticle collisions and friction. The dispersive pressure is assumed to be normal to the shearing direction and balancing pressure due to gravitation.

Other assumptions: Depending on the specific model, there are many other assumptions, as known channel geometry or flow width used, for example, by Bartelt & Gruber (1998) and Irgens et al. (1998). Furthermore, centrifugal forces due to curvature of the avalanche track or forces acting on the free surface are either neglected by Bartelt & Gruber (1998), Hutter & Koch (1991), Barbolini & Nettuno (1998), or taken into account by Norem et al. (1986) Norem et al. (1989) Norem & Schieldrop (1991) and Irgens et al. (1998).

Balance laws

Assuming that avalanche motion is describable in terms of continuum dynamics, one starts with the general mass and momentum balance equations of fluid dynamics for the mass density and velocity fields $\varrho(\mathbf{x}, t)$ and $\mathbf{v}(\mathbf{x}, t)$:

$$\partial_t \varrho = \nabla \cdot (\varrho \mathbf{v}) \tag{4.8}$$

and

$$\varrho(\partial_t + \mathbf{v} \cdot \nabla)\mathbf{v} = -\nabla p + \nabla \cdot \hat{\mathbf{T}} + \mathbf{f}_{ext}, \tag{4.9}$$

where $p(\mathbf{x}, t)$ is the instantaneous pressure field, $\hat{\mathbf{T}}$ the deviatoric stress inside the flowing continuum and $\mathbf{f}_{ext}$ denotes the external volume forces acting on it. The continuum equation (4.8) describes the conservation of mass, where Equation (4.9) is an expression for the balance of momentum.

The left hand side of Equation (4.9) is the convective time derivative of flow velocity accounting for the local rate of change of momentum caused by the gradient of the instantaneous pressure field, stresses due to deformation of the flowing continuum and by external forces acting on the flowing continuum.

The specific shape of the balance law equations depends on the model assumptions made for the avalanche motion. For example, the assumptions of hydrostatic, homogeneous one-dimensional avalanche flow in downslope x direction, which can be described in the frame of shallow-water theory by the depth-averaged downslope velocity $v(x,t)$, results in the following mass and momentum conservation equations given by Eglit (1998):

$$\partial_t h + \partial_x(hv) = 0, \tag{4.10}$$

$$(\partial_t + v\partial_x)v = g\sin\psi - \frac{1}{2h}\partial_x\left[h^2\left(g\cos\psi + \frac{v^2}{R}\right)\right] - (f_1 + f_2), \tag{4.11}$$

where $v(x,t)$ and $h(x,t)$ are the flow velocity and the flow depth, $\psi(x)$ is the slope angle and $R(x)$ the curvature radius of the slope. With μ the coefficient of dry Coulomb friction and k the coefficient of turbulent friction, the expressions f_1 and f_2 account for the decelerating forces caused by dry and hydraulic friction, respectively:

$$f_1 = \mu\ \mathrm{sgn}(v)\left(g\cos\psi + \frac{v^2}{R}\right), \tag{4.12}$$

$$f_2 = k\ \mathrm{sgn}(v)\frac{v^2}{h}. \tag{4.13}$$

The second right hand side term of Equation (4.11) describes the downslope gradient of hydrostatic pressure and pressure caused by centrifugal force due to curvature of the avalanche track and corresponds to the pressure gradient $-\nabla p$ in the general momentum balance (4.9). External forces $\mathbf{f}_{ext}$ in (4.9) are provided by the gravitational acceleration $g\sin\psi$ and the dry and hydraulic friction, respectively.

As another example, consider a one-dimesional hydrostatic shallow water model with known flow width disregarding centrifugal forces. The known flow width allows to perform the averaging not only over the flow depth but also over the cross sectional area of the avalanche flow. The resulting balance laws obtained by Bartelt & Gruber (1998) read :

$$\partial_t A + \partial_x Q = 0 \tag{4.14}$$

and

$$\partial_t Q + \partial_x \left(\alpha \frac{Q^2}{A} \right) = -\lambda g A \cos\psi \partial_x h + g A (S_0 - S_f). \tag{4.15}$$

Here, $Q(x,t)$ is the mass flow, $A(x,t)$ the cross sectional area and $h(x,t)$ the flow depth of the avalanche flow. The slope angle is denoted by $\psi(x)$, λ is the so-called active-passive pressure coefficient and $\alpha(x,t)$ a velocity profile factor. The slopes S_0 and S_f account for accelerating gravitational and frictional forces, respectively, where, depending on the specific avalanche model version, S_f incorporates dry and hydraulic friction or frictional forces induced by the constitutive behaviour of the model continuum. The left hand side of Equation (4.15) corresponds to the convective time derivative of (4.9) and the first rhs term describes the downslope pressure gradient due to variation of flow depth.

Generally, one can state that in a continuum model, all external and internal forces acting on avalanche snow are formally accounted for by a pressure gradient or external force terms. Stresses due to deformation of the continuum are incorporated into frictional force terms as f_2 or S_f. Note that this way of proceeding also allows to include dispersive pressure and shear due to granular collisional and frictional particle interaction, if the granular nature of avalanche flow is taken into account. Formally, the constitutive behaviour of the model continuum (which can also be derived from granular kinetics) enters the balance equations in the form of frictional or driving terms (see, e.g. Hungr (1995)).

To model the lateral avalanche motion as well, the Equations(4.8) and (4.9) have to be formulated for the downslope flow direction x as well as for the

lateral y direction taking into account the specific avalanche flow model assumptions.

Constitutive laws

The deformation of a continuum material reacting to stresses applied on it is described by its constitutive law, which, in its most general form, reads:

$$\mathbf{T} = 2\underline{\mathcal{A}}\mathbf{D}, \tag{4.16}$$

where $\mathbf{T}(\mathbf{x}, t)$ denotes the stress tensor describing flow dependent stresses, $\mathbf{D}(\mathbf{x}, t)$ is the "stretching" tensor and $\underline{\mathcal{A}}(\mathbf{x}, t)$ is a fourth-order viscosity tensor with 36 independent components describing the deformation history. The stretching $\mathbf{D}$ is defined by the velocity gradients in the continuum flow:

$$D_{ij} = \frac{1}{2}(\partial_j v_i + \partial_i v_j), \tag{4.17}$$

where ∂_i is a spatial derivative with respect to the x_i coordinate, and $v_i(\mathbf{x}, t)$ is the i component of the local flow velocity field. The total stress $\mathbf{T}(\mathbf{x}, t)$ in the material is the sum of the isotropic pressure p and the flow dependent extra stresses $\mathbf{T}_{fl}(\mathbf{x}, t)$:

$$\mathbf{T} = -p\mathbf{1} + \mathbf{T}_{fl}, \tag{4.18}$$

where $\mathbf{1} = \delta_{ij}$ is the unit tensor.

Rigid body avalanche flow models (Sect.4.2.1) and continuum models assuming Voellmy flow law behaviour (see Equ.(4.3)) do not take into account the distribution of stresses within the avalanche mass, but regard external dry Coulomb and hydraulic (turbulent) basal friction acting on the flowing snow mass as a whole. (The basal Coulomb friction is caused by the hydrostatic pressure normal to the slope.) The constitutive behaviour for such a "plug flow" can simply be characterized by

$$\mathbf{D} = 0 \Longleftrightarrow \mathbf{T} = 0. \tag{4.19}$$

Dent & Lang (1983), Bartelt & Gruber (1998) and others describe avalanches employing a Bingham flow law. A Bingham fluid has two regions of constitutive behaviour, distinguished by a treshold stress intensity $T_0 = \|\mathbf{T}_0\|$. Below T_0 no deformation occurs, while for higher values the deformation is proportional to the amount of stress intensity $T = \|\mathbf{T}\|$ exceeding T_0:

$$\begin{aligned} \mathbf{T} = \mathbf{D} = 0 \qquad & T < T_0 \\ \mathbf{T} = \eta\mathbf{D} + \mathbf{T}_0 \qquad & T \geq T_0, \end{aligned} \tag{4.20}$$

where η is the dynamic viscosity. Bingham flow is used to describe a non deforming avalanche plug flow which is moving on a layer of fluidized snow (or granular material) which is subject to rapid shearing.

To describe granular as well as visco-elastic and plastic aspects of avalanche flow behaviour, Norem et al. (1986) introduced a plastic and a Criminale-Ericksen-Filby fluid law (Criminale et al. (1958)) into a twodimensional continuum avalanche model. The CEF (Criminale-Ericksen-Filby) fluid law describing stationary shear flow of non Newtonian fluids has the form

$$\mathbf{T} = 2\eta\mathbf{D} + (2\nu_1^* + 4\nu_2^*)\mathbf{D}\cdot\mathbf{D} - \nu_1^*(\dot{\mathbf{D}} - \mathbf{W}\cdot\mathbf{D} + \mathbf{W}\cdot\mathbf{D}), \tag{4.21}$$

where

$$\mathbf{W} = W_{ij} = \frac{1}{2}(\partial_j v_i - \partial_i v_j), \tag{4.22}$$

ν_1^* and ν_2^* are the primary and secondary normal stress coefficients, respectively. Note that the rotation rate and the deformation rate tensors $\mathbf{W}$ and $\mathbf{D}$ are not commutative.

For simple steady shear flow

$$v_x = \dot{\gamma}y, \quad v_y = v_z = 0, \tag{4.23}$$

η, ν_1^* and ν_2^* are defined by the viscometric functions

$$\begin{aligned} \eta &= \frac{T_{xy}}{\dot{\gamma}}, \\ \nu_1^* &= (T_x - T_y)\frac{1}{\dot{\gamma}^2}, \\ \nu_2^* &= (T_y - T_z)\frac{1}{\dot{\gamma}^2}, \end{aligned} \tag{4.24}$$

where T_{xy} is the shear stress and T_x, T_y and T_z the extra normal stresses caused by simple steady shear. The shear rate $\dot{\gamma} = \sqrt{\mathbf{D} : \mathbf{D}}$ reduces to $\dot{\gamma} = \partial_y v_x$ for simple steady shear flow.

Including plastic flow behaviour, Norem et al. (1986) propose the following constitutive behaviour for the granular avalanche flow:

$$\begin{aligned} \mathbf{T} = {} & \frac{2}{\dot{\gamma}}\left(a_c + b_{fr} p_e^{\tilde{k}}\right)\mathbf{D} + \\ & 2\eta\mathbf{D} + (2\nu_1^* + 4\nu_2^*)\mathbf{D}\cdot\mathbf{D} - \nu_1^*(\dot{\mathbf{D}} - \mathbf{W}\cdot\mathbf{D} + \mathbf{W}\cdot\mathbf{D}). \end{aligned} \tag{4.25}$$

This is the constitutive behaviour of the CEF fluid (4.21) supplemented by an additional term (first term on the rhs of Equation 4.25) which accounts for the plasticity response. The viscometric functions η, ν_1^* and ν_2^* are modelled by power laws:

$$\begin{aligned} \eta &= \varrho\tilde{m}\dot{\gamma}^{\tilde{n}-1} \\ \nu_1^* &= \varrho\nu_1\dot{\gamma}^{q-2} \\ \nu_2^* &= -\varrho\nu_2\dot{\gamma}^{\tilde{r}-2}. \end{aligned} \tag{4.26}$$

Here, ϱ, ν_1, ν_2, $\tilde{m}$, $\tilde{n}$, $\tilde{r}$ and q are constant material parameters. For steady simple shear flow (4.23), the constitutive law (4.25) becomes

$$\begin{aligned} T_{xy} &= a_c + b_{fr} p_e^{\tilde{k}} + \varrho\tilde{m}\dot{\gamma}^{\tilde{n}}, \\ T_{xz} &= T_{yz} = 0, \\ T_y &= -p - \varrho\nu_2\dot{\gamma}^{\tilde{r}}, \end{aligned}$$

$$\begin{aligned} T_x &= -p + \varrho\nu_1\dot{\gamma}^q - \varrho\nu_2\dot{\gamma}^{\tilde{r}}, \\ T_z &= -p, \end{aligned} \tag{4.27}$$

where a_c is the cohesion coefficient, $\tilde{m}$ the shear stress viscosity and p is the isotropic pressure acting on the continuum. (For definition of the stress tensor components see Figure 4.2.)

The pressure can be considered to consist of an effective pressure p_e transferred by the particle lattice of the granular material, and the pore pressure p_u of the interstitial fluid, which equals the ambient atmospheric pressure for the case of flowing snow avalanches: $p = p_e + p_u$. The meaning and the values of the remaining parameters are discussed in the following.

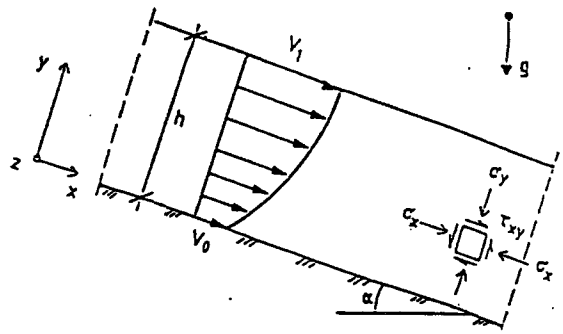

Figure 4.2: *Definition of normal and shear stresses described by Eqs. 4.27 and 4.28. Note that here T_{xy} is denoted by τ_{xy}. σ_x, σ_y and σ_z correspond the normal stresses T_x, T_y and T_z in Equation (4.27). Figure taken from Norem et al. (1989).*

The parameter b_{fr} has the character of a friction parameter and is assumed to be close to the tangent of the static internal friction angle ϕ_{fr} of the considered granular material: $b_{fr} = \tan\phi_{fr}$. Experimental results by Stadler & Buggish (1985) allow to assume that the shear strength in granular media is proportional to the applied normal pressure and therewith to determine $\tilde{k}$ in Equation (4.27) to be $\tilde{k} = 1$.

Bagnold (1954) showed that the flow induced pressure $\varrho\nu_2\dot{\gamma}^{\tilde{r}}$ is proportional to the dynamic shear stress $\varrho\tilde{m}\dot{\gamma}^{\tilde{n}}$ for varying shear rates $\dot{\gamma}$ and volumetric densities ϱ and that $\tilde{n} = \tilde{r} = 2$ in the inertial regime, where the granular motion is dominated by interparticle collisions.

Including these assumptions into (4.27), one ends up with the constitutive equations which are incorporated via momentum balance laws into continuum avalanche models (e.g. by Norem et al. (1989) or Bartelt et al. (1997)).

$$\begin{aligned} T_{xy} &= a + \tan\phi_{fr} p_e + \varrho \tilde{m} \dot{\gamma}^{\tilde{r}}, \\ T_{xz} &= T_{yz} = 0, \\ T_y &= -p_e - p_u - \varrho \nu_2 \dot{\gamma}^{\tilde{r}}, \\ T_x &= -p_e - p_u + \varrho(\nu_1 - \nu_2)\dot{\gamma}^{\tilde{r}}, \\ T_z &= -p. \end{aligned} \tag{4.28}$$

Summary

Modelling avalanches as continuum fluid flow in the frame of shallow water theory allows to analyze the deformation of the flowing avalanche mass and therewith to account for the reaction of the avalanche shape on applied external forces due to topography. Besides the simplest case of Voellmy fluid, where the acting dry and hydraulic frictional forces are acting on the non-deformable avalanche body as a whole, the deformation of the continuum due to external forces is characterized by its constitutive behaviour.

For setting up appropriate constitutive laws for avalanche flows, aspects of granular flow behaviour are incorporated: the existence of a layer of fluidized granular material subject to rapid shear carrying a nearly rigid plug flow layer is represented by the biviscous Bingham flow law. On the other hand, the viscosity and visco-plasticity of granular flow is described by the Criminale-Ericksen-Filby flow law, which also accounts for dynamic shear and dispersive pressure due to collisional and frictional interaction of the moving granular particles.

4.2.3 Discussion

Except of most simple cases where a Voellmy fluid law is employed, descriptions of granular flow behaviour enter mathematical (and therefore numerical) avalanche flow models. In the case of the Dade & Huppert (1998) energy

line block models, for example, this is done by employing the lateral yield stress of unconfined debris as basal friction acting on the flowing avalanche block mass.

Continuum (or deformable body) avalanche models include granular flow behaviour by continuum constitutive laws for granular media, which enter the momentum balance equations.

Note however, that the granular constitutive behaviour is an input of the models, which therefore can explain internal flow structure employing known constitutive behaviour of granular material, but do not provide a further principle understanding of specific granular behaviour.

To obtain deeper insight into granular dynamics, one would have to investigate the evolution of granular constitutive behaviour from the interaction of individual granular particles (see Sect. 4.3.4).

4.3 Continuum dynamic description of granular flows

Granular dynamics can be described in terms of transport theory as used in statistical gas dynamics. Considering the time development of the average $\langle \Psi(\mathbf{x}, t) \rangle$ of a particle property Ψ, continuum dynamic balance laws and constitutive relations can be derived. In dilute gas dynamics, this can either be done by direct analysis or by employing the Boltzmann equation for particle velocity distribution functions, as outlined by Reif (1987). Following the general spirit of the work of Lun et al. (1984), Jenkins & Richman (1985), Lun et al. (1986) Farrell et al. (1986), Jenkins & Mancini (1987), Jenkins & Mancini (1989), Jenkins (1998) or Sela & Goldhirsh (1998), the basic features of the derivation of continuum dynamical balance equations and constitutive laws of granular media from the binary kinetics of granular particles will be reported in the following.

4.3.1 Assumptions

Kinetic theories of granular flows have a formal shape similar to the one of the statistical gas dynamics description. However, a substantial difference is the fact that the energy dissipation occuring during interparticle collisions has to be included into the kinetic granular flow description.

For reasons of simplicity, the granular material is assumed to consist of smooth, spherical particles, which are, depending on the degree of sophistication of the theories, (slightly) inelastic, different sized or have "rough" surfaces supporting the transfer of spin between colliding particles.

The collisions are assumed to be of binary, instantaneous nature. That means that the flow is dominated by interactions of each two particles, which are considered to happen in one distinct time point: the particles are hard in the sense that the contact time is negligible in comparison to the mean collisional period. For a more detailed discussion of the instantaneous binary collision assumption, see Section 5.2.4.

In the following, the general shape of kinetic theory of granular flows is sketched for the simplest case of granular flow consisting of equal sized, smooth, slightly inelastic spherical particles.

4.3.2 Basic equations

Consider a function $\Psi(\mathbf{x}, \mathbf{c}, t)$, which describes a property of a particle with velocity $\mathbf{c}$ situated at $\mathbf{x}$ at time t. The average of Ψ is given by

$$\langle \Psi \rangle = \frac{1}{n(\mathbf{x}, t)} \int d\mathbf{c} f(\mathbf{x}, \mathbf{c}, t) \Psi(\mathbf{x}, \mathbf{c}, t), \tag{4.29}$$

where $n(\mathbf{x}, t)$ is the mean particle number density and $f(\mathbf{x}, \mathbf{c}, t)$ is the single particle velocity distribution function so that $f(\mathbf{x}, \mathbf{c}, t)d\mathbf{c}$ gives the differential number of particles with a velocity in the range of $[\mathbf{c}, \mathbf{c} + d\mathbf{c}]$ per unit volume. The pair distribution function $f^{(2)}(\mathbf{x}_1, \mathbf{c}_1, \mathbf{x}_2, \mathbf{c}_2, t)$ is defined analoguously to the single particle velocity distribution function in the way that $f^{(2)}(\mathbf{x}_1, \mathbf{c}_1, \mathbf{x}_2, \mathbf{c}_2, t)d\mathbf{x}_1 d\mathbf{x}_2 d\mathbf{c}_1 d\mathbf{c}_2$ is the number of pairs of particles which

have velocities in the ranges $[\mathbf{c}_1, \mathbf{c}_1 + d\mathbf{c}_1]$ and $[\mathbf{c}_2, \mathbf{c}_2 + d\mathbf{c}_2]$, respectively, in the volume elements $d\mathbf{x}_1$ and $d\mathbf{x}_2$ centered at $\mathbf{x}_1$ and $\mathbf{x}_2$.

The time development of the average of Ψ can be described by the Maxwell transport equation (for derivation see Reif (1987)):

$$\partial_t \langle n\Psi \rangle = n\langle D\Psi \rangle - \nabla \cdot \langle n\mathbf{c}\Psi \rangle + \phi_c, \tag{4.30}$$

where

$$D\Psi = \frac{d\mathbf{c}}{dt} \cdot \frac{\partial \Psi}{\partial \mathbf{c}} = \frac{\mathbf{F}}{m} \cdot \frac{\partial \Psi}{\partial \mathbf{c}}. \tag{4.31}$$

Here, $\mathbf{F}$ denotes the external force acting on a particle with mass m and ϕ_c is the collision induced change of Ψ per unit volume.

The explicit form of ϕ_c is obtained by considering a binary collision of two smooth, hard, inelastic spherical particles 1 and 2 with uniform particle diameter σ. In the instance of collision, the center $\mathcal{O}_2$ of particle 2 is situated at $\mathbf{x}$, the center $\mathcal{O}_1$ of particle 1 at $\mathbf{x} - \sigma\mathbf{k}$, where $\mathbf{k}$ is the unit vector pointing from the center of particle 1 to the one of particle 2. In the time interval dt before collision, particle 1 moves relative to particle 2 over a distance $\mathbf{c}_{12}dt$, where $\mathbf{c}_{12} = \mathbf{c}_1 - \mathbf{c}_2$ is the relative velocity of particle 1 with respect to particle 2. For a collision of particles 1 and 2 to occur within the time interval dt, the center of particle 1 has to lie within the volume

$$\sigma^2 \delta\mathbf{k}(\mathbf{c}_{12} \cdot \mathbf{k})dt. \tag{4.32}$$

So the probable number of collisions, where the center of particle 2 lies in the volume element $d\mathbf{x}$ and the particles have velocities $\mathbf{c}_1$, $\mathbf{c}_2$ and a collisional vector $\mathbf{k}$ lying in the ranges $\delta\mathbf{c}_1$, $\delta\mathbf{c}_2$ and $\delta\mathbf{k}$, respectively, is

$$\sigma^2(\mathbf{c}_{12} \cdot \mathbf{k}) f^{(2)}(\mathbf{x} - \sigma\mathbf{k}, \mathbf{c}_1; \mathbf{x}, \mathbf{c}_2; t) d\mathbf{k} d\mathbf{c}_1 d\mathbf{c}_2 dt. \tag{4.33}$$

The values of Ψ carried by particle 2 before and after collision are Ψ_2 and Ψ_2', respectively, so that the gain of Ψ for particle 2 due to a collision is $\Psi_2' - \Psi_2$. The total collisional rate of change ϕ_c of Ψ is obtained by considering

only particle pairs with $(\mathbf{c}_{12} \cdot \mathbf{k}) > 0$ corresponding to the particles being about to collide:

$$\phi_c = \sigma^2 \int\limits_{\mathbf{c}_{12}\cdot\mathbf{k}>0} d\mathbf{k}d\mathbf{c}_1 d\mathbf{c}_2 (\boldsymbol{\Psi}_2' - \boldsymbol{\Psi}_2)(\mathbf{c}_{12} \cdot \mathbf{k}) f^{(2)}(\mathbf{x} - \sigma\mathbf{k}, \mathbf{c}_1; \mathbf{x}, \mathbf{c}_2; t). \quad (4.34)$$

Expanding $f^{(2)}(\mathbf{x} - \sigma\mathbf{k}, \mathbf{c}_1; \mathbf{x}, \mathbf{c}_2; t)$ into a Taylor series and

substituting of the expanded pair distribution function into (4.34), after some manipulation, results in a splitting of ϕ_c into a collisional transfer contribution $\boldsymbol{\Phi}$ and a source-like term $\boldsymbol{\Theta}$:

$$\phi_c = -\nabla \cdot \boldsymbol{\Phi} + \boldsymbol{\Theta}, \quad (4.35)$$

where

$$\begin{aligned} \boldsymbol{\Phi} &= \frac{\sigma^3}{2} \int\limits_{\mathbf{c}_{12}\cdot\mathbf{k}>0} d\mathbf{k}d\mathbf{c}_1 d\mathbf{c}_2 (\boldsymbol{\Psi}_1' - \boldsymbol{\Psi}_1)(\mathbf{c}_{12} \cdot \mathbf{k})\mathbf{k} \\ &\times \left[\sigma 1 - \frac{1}{2!}\sigma\mathbf{k} \cdot \nabla + \frac{1}{3!}(\sigma\mathbf{k} \cdot \nabla)^2 + \ldots\right] \\ &\times f^{(2)}(\mathbf{x}, \mathbf{c}_1; \mathbf{x} + \sigma\mathbf{k}, \mathbf{c_2}, t) \end{aligned} \quad (4.36)$$

and

$$\boldsymbol{\Theta} = \frac{\sigma^2}{2} \int\limits_{\mathbf{c}_{12}\cdot\mathbf{k}>0} d\mathbf{k}d\mathbf{c}_1 d\mathbf{c}_2 (\boldsymbol{\Psi}_2' + \boldsymbol{\Psi}_1' - \boldsymbol{\Psi}_2 - \boldsymbol{\Psi}_1)(\mathbf{c}_{12} \cdot \mathbf{k}) f^{(2)}(\mathbf{x} - \sigma\mathbf{k}, \mathbf{c}_1; \mathbf{x}, \mathbf{c}_2; t). \quad (4.37)$$

Note that, if $\boldsymbol{\Psi}$ is a summational invariant such as the momentum of two colliding elastic particles before and after collision, the source term $\boldsymbol{\Theta}$ vanishes.

The inelasticity of the spherical granular particles is accounted for by the longitudinal restitution coefficient e which describes the change of the component of the velocity difference of two particles parallel to $\mathbf{k}$ due to collision of these particles:

$$\mathbf{k} \cdot \mathbf{c}'_{12} = -e(\mathbf{k} \cdot \mathbf{c}_{12}), \tag{4.38}$$

where $\mathbf{c}'_{12}$ denotes the particles' velocity difference after collision.

4.3.3 Balance laws

Taking mass m, momentum $m\mathbf{c}$ and kinetic energy mv^2 as particle properties Ψ of individual particles, the Maxwell transport equation (4.30) with respect to Eqs (4.35), (4.36) and (4.37) results in the common hydrodynamic equations:

$$\begin{aligned} \partial_t \varrho &= -\nabla \cdot (\varrho \mathbf{u}), \\ \varrho(\partial_t + \mathbf{u} \cdot \nabla)\mathbf{u} &= -\nabla \mathbf{t} + \mathbf{f}_{ext}, \\ \frac{3}{2}\varrho(\partial_t + \mathbf{u} \cdot \nabla)T &= -\mathbf{t} : \nabla \mathbf{u} - \nabla \cdot \mathbf{q} - \gamma. \end{aligned} \tag{4.39}$$

In these equations, $\mathbf{u} = \langle \mathbf{c} \rangle$ is the bulk velocity, $\varrho = nm = \nu \varrho_p$ is the (continuous) mass density, where ν is the bulk solids fraction, ϱ_p the single particle mass density. The collisional rate of energy dissipation per unit volume is defined as $\gamma = \Theta(\frac{1}{2}m\mathbf{c}^2)$, $\mathbf{t}$ is the total stress tensor, $\mathbf{q}$ the fluctuation energy flux and $\mathbf{f}_{ext}$ is the external body force per unit mass.

With $\mathbf{C} = \mathbf{c} - \mathbf{u}$, the specific energy of the velocity fluctuations $\mathbf{C}$ is defined by $\frac{3}{2}T = \frac{1}{2}\langle C^2 \rangle$. The quantity T is also known as "granular Temperature". Due to the structure of the transport equation (4.30), the stress $\mathbf{t}$ and the energy flux $\mathbf{q}$ consist of a kinetic and a collisional part, denoted by the indices k and c, respectively:

$$\mathbf{t} = \mathbf{t}_k + \mathbf{t}_c = \varrho \langle \mathbf{CC} \rangle + \Phi(m\mathbf{C}) \tag{4.40}$$

and

$$\mathbf{q} = \mathbf{q}_k + \mathbf{q}_c = \frac{1}{2}\varrho \langle C^2 \mathbf{C} \rangle + \Phi(\frac{1}{2}mC^2). \tag{4.41}$$

4.3.4 Constitutive laws

The derivation of constitutive equations for granular media is (explicitly or implicitly) based on the assumption that gradients of mean flow properties such as velocity or bulk density are in some sense small. This requirement implies that the energy dissipation by one particle collision is small compared to the mean particle kinetic energy. For this reason, the more simple descriptions of the constitutive granular behaviour assume a nearly elastic collisional behaviour of uniform spherical granular particles (i.e. the restitution coefficient e is close to unity). As outlined by Savage (1993), constitutive laws for granular flows of slightly inelastic spherical particles can be derived either by making use of the Boltzmann equation or by moment methods using the Maxwell transport equation (4.30) which has been described by Reif (1987) and others for the case of dilute gas dynamics. Following the general course of this approach, one starts with the assumption that the single particle velocity distribution function $f^{(1)}$ can be written as

$$f^{(1)} = f^{(0)}(1 + f'), \tag{4.42}$$

where f' is a small perturbation of the local equilibrium Maxwell single velocity distribution function

$$f^{(0)}(\mathbf{x}, \mathbf{c}, t) = \frac{n}{(2\pi T)^{\frac{2}{3}}} \exp\left(-\frac{(\mathbf{c} - \mathbf{u})^2}{2T}\right). \tag{4.43}$$

Furthermore, the so-called Enskog assumption is employed, which states that the correlation between velocities of colliding particles just before collision can be ignored and the pair velocity distribution function $f^{(2)}$ can be written als product of single velocity distribution functions (see Jenkins (1998)):

$$f^{(2)}(\mathbf{x}_1, \mathbf{c}_1; \mathbf{x}_2, \mathbf{c}_2, t) = g_0(\nu) f^{(1)}(\mathbf{x} - \sigma\mathbf{k}, \mathbf{c}_1, t) f^{(1)}(\mathbf{x}, \mathbf{c}_2, t), \tag{4.44}$$

where $g_0(\nu)$ is a simple form of the radial distribution function, which incorporates the influence of the volume occupied by the spherical particles on

their collision frequency and is given as a function of solid volume fraction $\nu = \frac{1}{6}\pi\sigma^3$:

$$g_0(\nu) = \frac{2-\nu}{2(1-\nu)^3}. \tag{4.45}$$

Assuming a specific form of the perturbation f' of the Maxwell single particle velocity distribution function (4.43), the following expressions for the total stress tensor $\mathbf{t}$ and the translational fluctuating energy flux $\mathbf{q}$ are obtained:

$$\mathbf{t} = \mathbf{t}_k + \mathbf{t}_c = [\varrho T(1+4\nu g_0) - \mu_b \nabla\cdot\mathbf{u}]\mathbf{1} - \left[\left(\frac{2\mu_s}{g_0} + \frac{16\mu_s\nu}{5}\right)\left(1+\frac{8}{5}\nu g_0\right)^2 + \frac{6}{5}\mu_b\right]\hat{\mathbf{D}}, \tag{4.46}$$

where

$$\mu_b = \frac{256\mu_s\nu^2 g_0}{5\pi}, \quad \mu_s = \frac{5m\sqrt{T/\pi}}{16\sigma^2}. \tag{4.47}$$

$\hat{\mathbf{D}}$ is the deviator of the shear rate tensor:

$$\hat{D}_{\alpha\beta} = \frac{1}{2}(\partial_\beta u_\alpha + \partial_\alpha u_\beta) - \frac{1}{3}\delta_{\alpha\beta}\partial_\kappa u_\kappa, \tag{4.48}$$

where the greek indices represent the cartesian spatial coordinate directions. Figure 4.3 shows the theoretically obtained dependency of the normal stress from the solids concentration ν in the case of simple shear obtained by a similar analysis.

The energy flux vector finally is

$$\mathbf{q} = \mathbf{q}_k + \mathbf{q}_c = -\frac{\lambda_e}{g_0}\left[\left(1+\frac{12}{5}\nu g_0\right)^2 + \frac{512}{25\pi}(\nu g_0)^2\right]\nabla T, \tag{4.49}$$

where

$$\lambda_e = \frac{75m\sqrt{T/\pi}}{64\sigma^2} \tag{4.50}$$

is the thermal conductivity of the granular flow. The collisional rate of energy dissipation in the zeroth order approximation of the perturbated Velocity distribution function reads

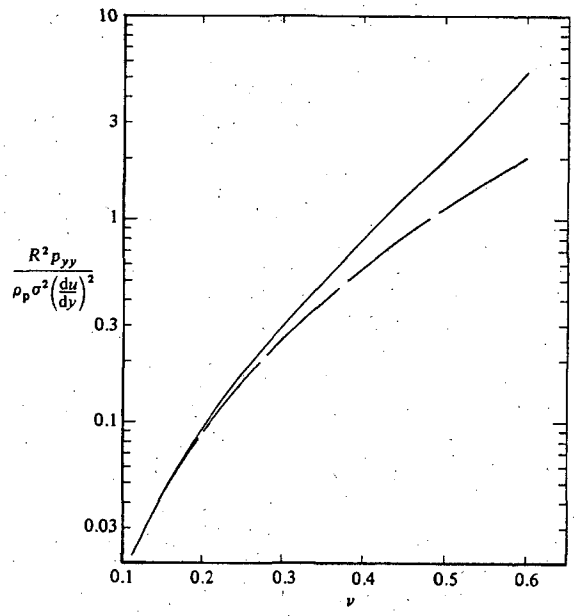

Figure 4.3: *Dependency of nondimensional normal stress from solids concentration as obtained from kinetic theory. The so-called R-parameter is defined as* $R = \sigma \frac{du}{dy} \sqrt{\langle C^2 \rangle}$. *The density of the particles with diameter* σ *is denoted by* ρ_p *and* p_{yy} *corresponds to the normal stress* t_{yy} *in simple shear flow. The two lines are referring to the use of different expressions for the radial distribution function* $g_0(\nu)$. *Figure taken from Lun et al. (1984).*

$$\gamma = \frac{24}{\sqrt{\pi}}(1-e)\frac{\varrho_p \nu^2}{\sigma} g_0 \sqrt{T}^3 \tag{4.51}$$

and vanishes in flows of elastic spheres with e=1.

4.3.5 Discussion

For the simple case of elastic (or slightly inelastic), uniform, smooth, spherical particles, the derivation of continuum balance and constitutive laws was demonstrated. The derivation follows the course of derivation of fluid dynamical balance and constitutive equations. The main difference to gas dynamics, however, is the need to incorporate energy dissipation during particle collisions, which causes considerable computational effort to gain approximate solutions of the transport equations. Though sophisticated theories, e.g. of Lun et al. (1986), Jenkins & Richman (1985) or Sela & Goldhirsh (1998) can almost account for longitudinal and tangential restitution as well as for friction during particle collisions, they provide a more principle physical insight than approaches to real problems, for the accessible ranges of parameter space are strongly limited by the assumptions entering the theoretical considerations. Therefore, practical problems related to granular flows are commonly treated by numerical modelling.

4.4 Discrete particle models of granular flows

Granular flows can be modelled by so-called discrete particle or discrete element models (DEM), in which the motion of individual particles and interactions between them are considered. One can assemble the granular flow by two-dimensional discs or cylinders, or, in a more realistic way, by three dimensional spherical particles. Although there exist flow models of polygonal shaped granular material, most models use circular or spherical particle geometries, because they are easier to handle computationally.

Depending on the used interaction model, one distinguishes between *hard sphere models* and *soft sphere models*. The main advantage of numerical modelling of granular flows is that the accessible range in the parameter

space of particle properties is not as limited as in the case of continuous kinetic models which have to make confining assumptions on particle properties. In the following, the main features and ranges of applicability of hard and soft sphere granular flow models are discussed.

4.4.1 Soft sphere models

Soft sphere models are used to model granular flows with high particle number densities in the continuous, quasistatic regime where particle contacts are extended in time and the flow is dominated by multiple particle contacts. They explicitly integrate the equations of motion of the individual particles with respect to the contact forces mutually exerted by the interacting particles.

According to Savage (1993), there is no analytical description of dense granular flow, which can account for long term and multiple particle contacts. For this reason, the direct deterministic modelling by soft sphere models is needed to provide principle insight into parameter ranges not accessible by kinetic theory, and, on the other hand, to investigate real problems involving long-term rubbing contacts.

Basic ideas and assumptions

Soft sphere models belong to the class of discrete element models (DEM): they set up granular flows or assemblies by distinct particles which can displace independently from each other (Cundall & Strack (1979)). For the models comprise particle contacts extended in time, the equations of motion of the individual particles have to be explicitly integrated in time with respect to the contact forces which the particles are mutually exerting on each other. According to Herrmann & Luding (1998), the total transfer of momentum $\delta\mathbf{p}$ during an interaction over a contact time period t_c, where a time dependent contact force $\mathbf{f}(t)$ is exerted to a particle, is given by

$$\delta\mathbf{p} = \int_{t_0}^{t_0+t_c} dt'\mathbf{f}(t'), \tag{4.52}$$

which is an integral form of Newton's 2nd law of motion.

The following forces are considered in common soft sphere models.

- Elastic repulsive forces are commonly represented by spring potentials, where the elastic repulsive force $\mathbf{f}_{el}$ depends linearly on the deformation or overlap $\mathbf{a}$ of the particles: $\mathbf{f}_{el} = k_{spr}\mathbf{a}$, where k_{spr} is the stiffness of the repulsive model spring. The normal and tangential components $f_{el,n}$ and $f_{el,t}$ of the elastic repulsive force are considered by spring constants k_n and k_s for normal and tangential direction, respectively. As an alternative to the spring model, a repulsive Lenard-Jones Potential has been used by Hirshfeld & Rapaport (1996), whereas Schwarz et al. (1998) employed a power law to model the non-linear elastic repulsive contact force.

- The inelasticity of particle contacts is accounted for by viscous damping in dashpot potentials, so that the viscous damping force $\mathbf{f}_{visc}$ is given by $\mathbf{f}_{visc} = c_{visc}\mathbf{v}$, where $\mathbf{v}$ is the deformation or overlap velocity and c_{visc} is a viscous damping coefficient, as explained, for example, by Cundall & Strack (1979) and Ting et al. (1993). As Savage (1993) reports, another approach to account for the inelasticity of particle interaction is to use springs with different rigidities k_1 and k_2, where $k_2 < k_1$, to model the normal contact forces during approach and rebound of the interacting particles. The longitudinal restitution coefficient e is defined as the ratio of longitudinal component of the velocity difference δv before and $\delta v'$ after the inelastic interaction of the particles: $e = \frac{\delta v'}{\delta v}$. It can be written as $e = \sqrt{k_2/k_1}$ in terms of different spring constants k_1 and k_2 for normal approach and rebound. This approach was introduced by Walton & Braun (1986) and has also been used by Dent (1986), Walton (1992) and Dent (1993). Figure 4.4 shows a sketch of the spring model for the repulsive and viscous normal and tangential contact forces.

- Coulomb frictional forces $f_{slip} = \mu f_n$ for tangential slip of the interacting particles are considered in all current soft sphere models, if the computed tangential contact forces f_t are exceeding the value

$f_{t,max} = \mu f_n$.

- Modelling the packing and compaction processes of powder assemblies consisting of very small particles with diameters in the range of $[0.1; 100] \times 10^{-6}$ m, Lian & Shima (1994) also take into account cohesive and electrostatic attractive forces.

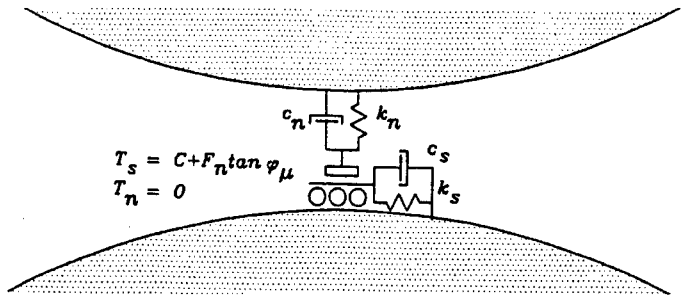

Figure 4.4: *Spring model for normal and tangential contact forces. T_s and T_n denote the maximum values for tangential shear strength and normal tensile strength of the contact. F_n is the normal contact force. Here, C is the cohesion and φ_μ is the angle of dry Coulomb friction. Spring rigidities and viscous damping coefficients in normal and tangential direction are denoted by k_n, k_s, c_n and c_s, respectively. Figure taken from Ting et al. (1993).*

As the actual deformation of interacting soft particles is hard to determine, the deformation of the particles is modelled by their overlap. Particles are allowed to penetrate each other and the repulsive forces depend on the degree of deformation or overlap, repectively, via spring or other repulsive potentials.

The contact forces are assumed to act on the so-called contact point: the contact points of two interacting particles are defined in such a way that the line connecting them forms the common normal of the two particles. Other definitions determine the contact points as the mid point of the line or plane connecting the intersecting points or lines of two penetrating particles. For spherical particles, the contact points can be found straightforwardly, but for particles with elliptic or ellipsoidal shape, the determination of the contact points as performed by Lin & Ng (1995) requires some computational effort. As Ting et al. (1993) point out, assemblies of elliptical or ellipsoidal particles

circumvent the difficulty that internal friction angles displayed by discrete particle modelling with spherical particles are too low in comparison with friction angles of real materials. The elliptical particle shape reduces the decrease of the internal friction due to rolling particle motion.

Limitations of soft sphere models

Soft sphere models are well suited for the modelling of dense granular flows in the viscous, quasistatic regime which is characterized by long term interactions in which multiple particles can be involved. In principle, also rapid flows dominated by binary, instantaneous interactions could be modelled by the soft sphere approach. As the interaction durations in the so-called inertia regime are very short, the interactions would have to be resolved into time steps which are very short compared to the mean free flight time of the particles and so would make the computations extremely ineffective.

To give an idea of particle solids concentrations, where the usage of soft sphere models is reasonable, a soft sphere and a hard sphere simulation of stresses developped in granular flow are compared. The maximum solid fraction according to a 2D close packing of discs is $\nu = 0.887$. Schwarz et al. (1998) performed 2D soft sphere simulations of stress fluctuations in a solids concentration range from $\nu = 0.75$ to $\nu = 0.87$, whereas, on the other hand, hard sphere simulations of Couette flow by Lun (1996) were performed at solid concentrations of $\nu \in [0.54; 0.75]$. Note that for reasons of comparison, 2D solid concentrations ν_{2D} were related to 3D solid concentrations ν_{3D} by $\nu_{3D} = 4/3\pi^{-1/2}\nu_{2D}^{3/2}$. (Of course, the solid concentration depends on the (fluctuational) velocity and the shear rate of the flow - the higher the velocity, the lower the density will be.)

Examples of application of soft sphere models

Some examples of practical application may elucidate the above statements on basic features and limitations of soft sphere models.

Cundall & Strack (1979) used the soft sphere model developed by them to reproduce the experimentally obtained contact force network of a static

assembly of photoelastic discs with different radii under horizontal and vertical load. The numerical modelling of loading of the assembly employing the known material properties of the experimentally used discs resulted in a satisfactory qualitative agreement of experimentally and numerically obtained contact force vector plots, as can be seen from Figure 4.5.

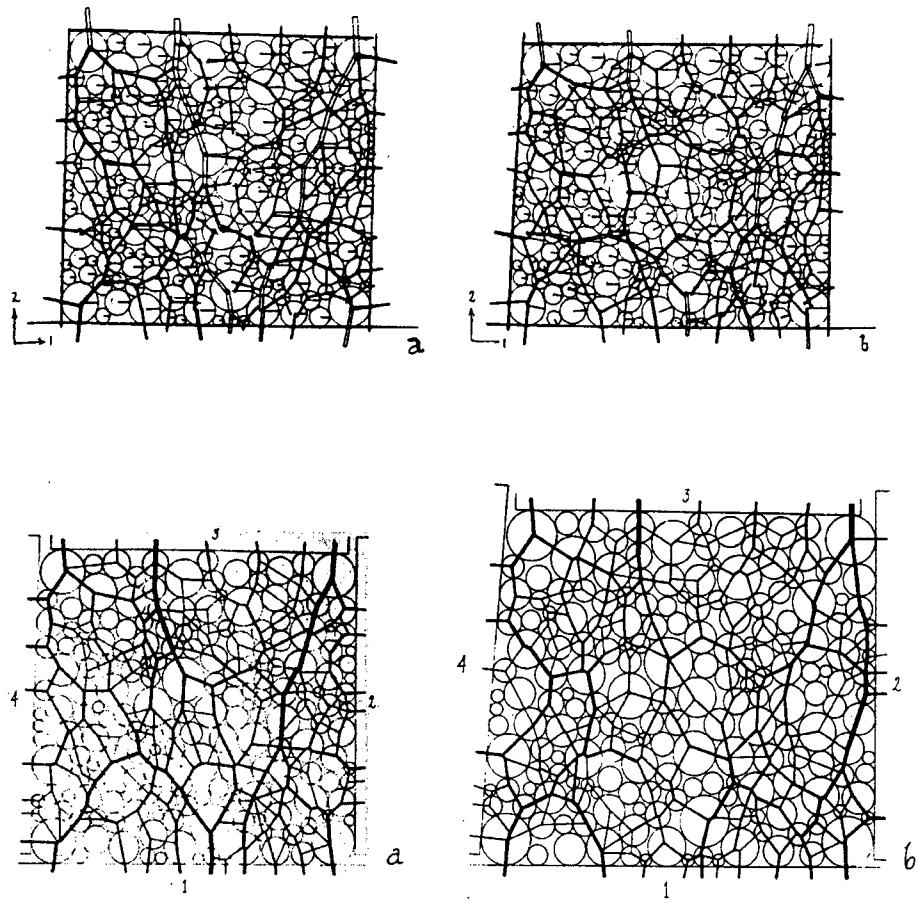

Figure 4.5: *Numerical reproduction (upper graphs) of experimentally obtained surface force vector plots (lower graphs). Figures taken from Cundall & Strack (1979).*

Simulations of flow of monodisperse, inelastic and frictional spheres with 1mm diameter on an 17° inclined chute performed by Walton (1992), resulted in mean downslope velocity profiles depending on the particle material parameters e and μ, where e is the longitudinal restitution coefficient of the particles as explained before and μ is the Coulomb surface friction co-

efficient of the particles. The obtained velocity profiles are shown in Figure 4.6. Note that the flow height axis is given in units of particles per unit area when counting the number of all particles projected on an unit area from the corresponding flow height. Deeper flows with same material parameter values tend to move faster than corresponding shallow flows. This may give a hint for the explanation of long runout distances of large avalanches or landslides.

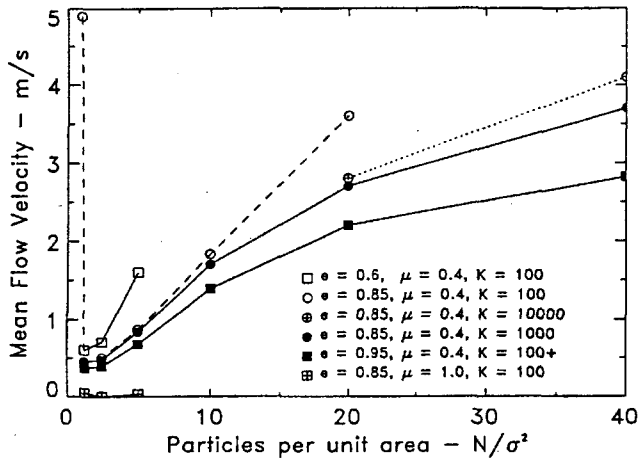

Figure 4.6: *Mean downslope flow velocity profiles for simulated monodisperse flow of spheres with 1 mm diameter on a 17° inclined plane for different particle material parameters. Figure taken from Walton (1992).*

Lian & Shima (1994) observed the formation of piles of powder and its packing behaviour under applied vertical load for small particles with diameters ranging from 80 to 200 μm taking into account repulsive inelastic forces, dry surface friction and cohesion. The influence of cohesion on the angle of repose of the forming pile was investigated (see Fig. 4.7).

The dependence of stress behaviour of a gravity free Couette flow of frictional inelastic discs from the solids concentration was investigated by Schwarz et al. (1998). They observed that the flow was undergoing a transition in the stress behaviour at a critical (2D) solids concentration $\nu_{2D} = 0.82$, where the stresses exerted by the granular material at given strain rates

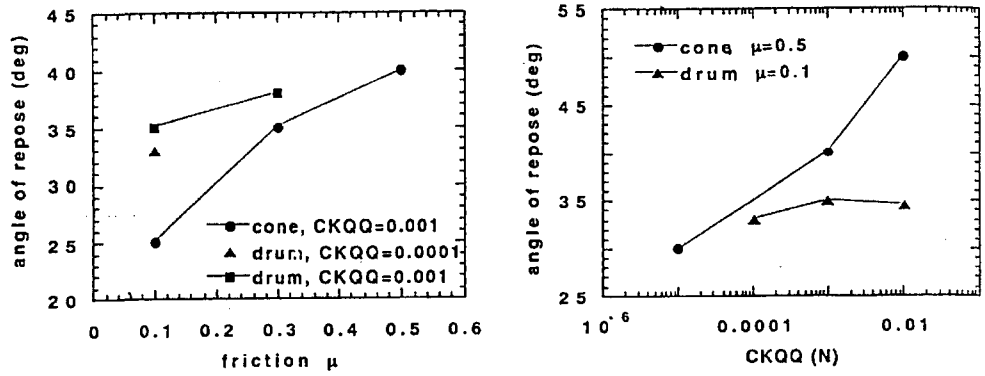

Figure 4.7: *Dependency of the angle of repose of a forming powder pile from Coulomb friction coefficient μ and cohesion of the powder particles. Figure taken from Lian & Shima (1994).*

were significantly increasing (see fig. 4.8). This behaviour was related to the evolution of stress "chains" over the entire flow depth, which are assumed to be characteristic for the transition from rapid collisional to macroviscous flow behaviour.

A 2D flow on an inclined chute consisting of 2000 disc shaped particles together with 20 "large" particles with same density but double diameter as the smaller ones was used by Hirshfeld & Rapaport (1996) to investigate the dependency of the segregational velocity of the larger particles from average flow velocity (which is depending again on the slope angle). The particles were interacting via a repulsive Lenard Jones potential used in molecular gas dynamics or nuclear physics and by dry Coulomb friction. Depending on the slope angle, a steady downslope flow velocity evolved. The effect of inverse grading was developing increasingly fast and significantly with increasing mean downslope flow velocity, as shown in Figure 4.9.

Tai & Sadd (1997) numerically studied the propagation of planar waves through fabrics represented by 2D assemblies of discs which are packed with different degrees of anisotropy. The wave motion is introduced by dynamic loading to boundary particles. The particles interact by a non-linear hysteretic contact law. The wave propagation characteristics were obtained in

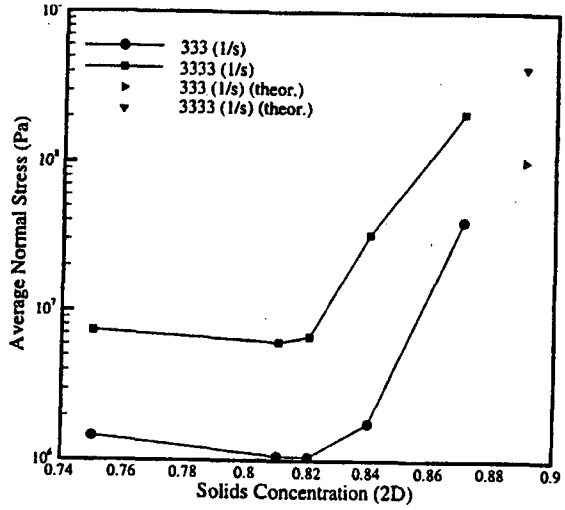

Figure 4.8: *Dependency of normal stress developed by gravity free 2D Couette flow from solids concentration at given strain rates. Figure taken from Schwarz et al. (1998).*

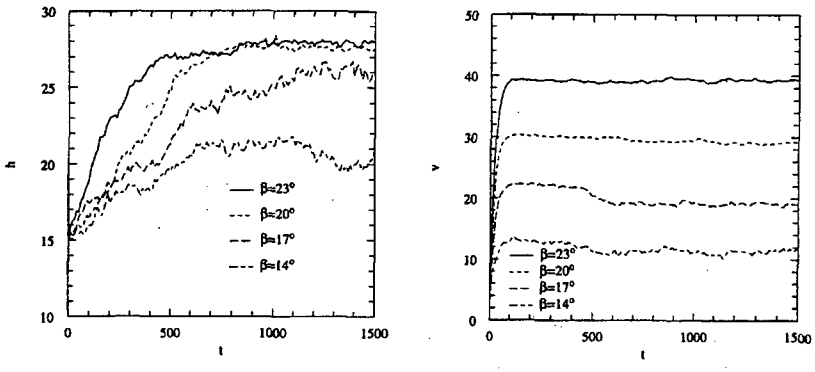

Figure 4.9: *Time series of mean height of large particles and time evolution of mean downslope velocity for different chute inclination angles. Figure taken from Hirshfeld & Rapaport (1996).*

dependence of the granular microstructure of the fabric, which could be described in terms of branch vector structures, void characteristics and path microstructures.

A reproduction of experimental results concerning 2D granular flow is reported by Drake & Walton (1995). A glass walled chute flow of cellulose acetate spheres with a diameter of 6 mm in a chute with the dimensions 3.5m×0.5m×0.0067m was studied. Due to the dimensions of the chute, the flow could be considered to be two-dimensional. The bottom was roughened by fixed spheres with random distance. The soft sphere simulations considered particle contact forces as well as the fluid drag, which affects fast moving particles in glass wall chutes. The simulation was performed employing experimentally obtained material parameters of the spheres and resulted in a good agreement of experimental and numerical velocity and particle spin profiles. The quantitative predictions of the simulations were found to be insensitive against details of the particle interaction model as particle stiffness but well sensitive against parameter variations concerning the chute geometry or external forces such as fluid drag.

The above examples show, that soft sphere models can account for a variety of quasistatic and dynamic granular flow problems as long as the condition of dominating long-term multiple particle contacts is satisfied.

4.4.2 Hard sphere models

In hard sphere models as well as in soft sphere models, the granular flow is assembled of individual interacting particles. The main difference to soft sphere models lies in the description of the interaction of the particles. Hard sphere models assume the interaction to be of binary, instantaneous nature: the contact time t_c in Equation (4.52) tends to zero and the shape of time dependent contact forces tends towards a Dirac δ-function. This means that only two-particle interactions can be considered which are not extended in time. A particle can only interact with one single other particle by instantaneous exchange of momentum and spin. In the following, basic ideas of hard sphere models and some examples of application are provided.

Basic ideas and assumptions

Hard sphere models are commonly used to model rapid granular flows which are dominated by binary particle interactions of short duration. As explained before, this means that the contact time t_c in Equation 4.52 tends to zero which, according to Hoomans et al. (1996), corresponds to contact forces of totally impulsive character. Therefore, the particle interaction can be described in terms of exchanged linear and angular momentum. Speaking differently, this means that the whole particle interaction for hard spheres is assumed to occur at one discrete time. The theoretical and experimental background of the assumption of instantaneous particle interaction is outlined in Section 5.2.4, page 142.

As a consequence of the assumption of instantaneous particle interaction, the entire interaction happens at the contact point of the indeformable particles. As the particles are rigid and do not deform during interaction, the contact point of spherical particles can be determined quite straightforwardly. The motion of the interacting rigid particles can be described in a 2D plane, in which the centers of mass of the particles are moving.

The particle material properties are represented by their longitudinal and tangential coefficients of restitution e and b as well as by the Coulomb coefficient μ of dry surface friction. The restitution coefficients describe the inelasticity of the particle collision in longitudinal and tangential direction by relating the longitudinal and tangential difference velocities of colliding particles at the contact point before and after collision. If $\delta\mathbf{v}$ and $\delta\mathbf{v}'$ denote the difference of velocities of two particles with restitution coefficients e and b before and after collision and $\mathbf{k}$ is the normal vector pointing from one colliding particle center to the other, the relation of velocity differences before and after collision reads:

$$\begin{aligned} \mathbf{k} \cdot \delta\mathbf{v}' &= -e\, \mathbf{k} \cdot \delta\mathbf{v}, \\ \mathbf{k} \times \delta\mathbf{v}' &= -b\, \mathbf{k} \times \delta\mathbf{v}. \end{aligned} \tag{4.53}$$

The maximum tangential force, or, in the instantaneous interaction picture, the exchanged tangential momentum, is limited by the dry Coulomb friction

of the particle surfaces. If the tangential momentum exchange δp_t exceeds $\mu \delta p_n$, where δp_n is the normal momentum exchange, a sliding motion is assumed and the tangential momentum exchange during the interaction is $\delta p_t = \mu \delta_n$. For details of the collisional mechanics of hard sphere particles, see Section 5.2.4.

The individual hard sphere particles perform an undisturbed motion in the gravity field until they are involved in an "event", which is defined either as a particle-particle collision or a particle impact on the bottom. As the trajectories of the freely moving particles as well as the changes of the particle motion after an instantaneous impact are analytically known, the modelling of a hard sphere granular flow is straightforward: For each particle, the time until the next event is determined. The trajectories of all particles are computed until any of the particles is involved in an event. The new velocities and spins of the particles involved in an event after their collision are computed and the procedure starts again with the determination of the next event time point. Details of this so-called "event-driven" algorithm are outlined in Section 5.2.3.

The above mentioned basic assumptions have been introduced and used in two-dimensional flows of rigid spheres in the work of Campbell (1993) and Nakagawa & Imaizumi (1992). Three-dimensional modelling of hard sphere granular flow based on the same assumptions was performed by Louge (1994), Lun & Bent (1994), Lun (1996) and Hoomans et al. (1996). For an overview and positioning of the hard sphere approach among other model and theoretical concepts refer to Savage (1993) or Herrmann & Luding (1998).

Some of the above mentioned works are reported in the following as examples for the use of hard sphere models.

In the current work, a hard sphere model with a multidisperse size distribution is used to investigate the parametrical dependencies of the time evolution of profiles of the mean particle radius as an indicator of inverse grading occuring in the considered model flow. The question to be answered is whether and if, in which particle material parameter ranges of a 3D hard sphere model, inverse grading can be observed.

Examples of application of hard sphere models

Campbell (1993) modelled a two-dimensional Couette flow of inelastic frictional discs to investigate the influence of boundary conditions on the overall flow behaviour. The flow was vertically bounded by two horizontal walls which were vertically separated by a distance H, where the lower, "bottom" wall was static and the upper one was moving with a constant velocity U. Periodic boundary conditions in lateral direction allowed studies of horizontally unbounded flow. Two hypothetical principle mechanisms of force transfer from the boundaries to the flow particles were investigated (see Fig. 4.10):

- In the first case (type A wall interaction), indefinite friction between the wall and particles colliding with the walls was assumed to ensure maximum torque transfer.
- The wall interaction type B did not apply any torque on the interacting particles, for the forces exerted by the boundaries were assumed to act directly on the centers of the colliding particles.

As a result of the simulations, it was stated that the way, in which the boundaries transmit torque to the particles has a great influence on overall flow. Figure 4.10 shows an example for the dependency of flow profiles on the boundary force transfer mechanism.

More realistic boundary conditions were obtained by glueing particles on the boundary walls. Small spacings between these particles resulted in an effectively nearly flat boundary, where larger spacings supported higher effective roughness; there existsts a spacing which yields maximum effective roughness. Also for the more realistic boundary conditions, their strong influence on flow properties could be observed.

A similar, but three-dimensional numerical Couette flow model was used by Lun & Bent (1994) and Lun (1996) to investigate the influence of solids concentration and particle properties e and μ on the mean stresses and velocity profiles developed by steady simple shear flow within the Couette flow assembly. 64 to 720 spherical particles were moving in a control volume with

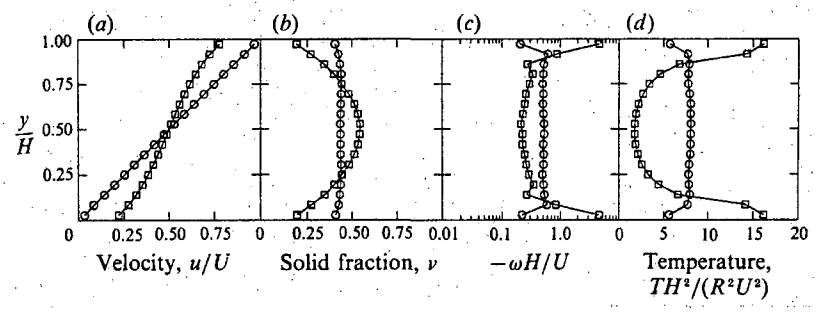

Figure 4.10: *Flow profiles of horizontal velocity, solid fraction, rotational velocities, and granular temperature for type A (squares) and type B (circles) boundary conditions in 2D Couette flow. Figure taken from Campbell (1993).*

lateral periodic boundary conditions. The flow was vertically confined by parallel, bumpy plates moving in opposite directions with velocity respective velocities $\pm U\hat{e}_x$. The plates were roughened by fixed half spheres.

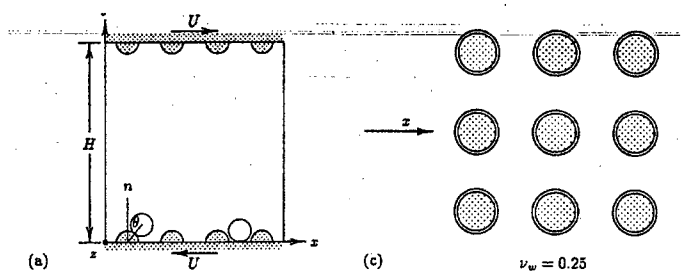

Figure 4.11: *Sketch of Couette flow model for simple shear flow of inelastic frictional spheres. (a) side view of the Couette flow cell, (c) Top view of bottom and top plates. Figure taken from Lun (1996).*

Figure 4.11 shows a sketch of the Couette flow model and Figure 4.12 gives an example of the dependency of the mean normal and shear stresses in the bounded Couette flow from the solids concentration. The stresses were decreasing with decreasing longitudinal restitution coefficient e and increasing Coulomb friction coefficient μ of the spherical particles.

At high solid concentrations, a critical value for the concentration was found to exist, above which abrupt changes in flow properties are caused by layering effects, formation of high density micro-structures and an increase in

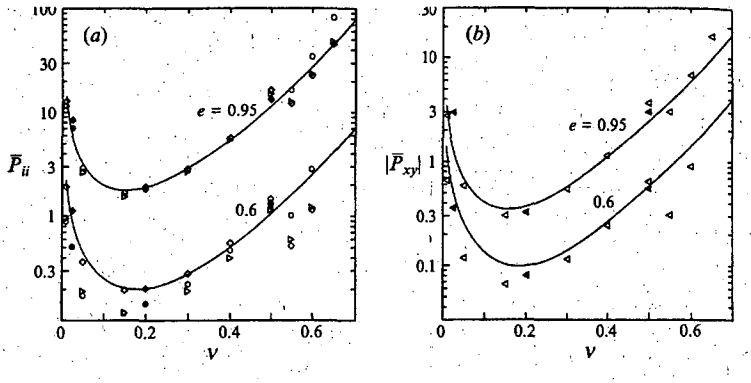

Figure 4.12: *Influence of longitudinal restitution coefficient and solids fraction on the mean normal (a) and mean shear stress (b) in simple shear flow. Figure taken from Lun & Bent (1994).*

correlation in particle velocities.

Furthermore, the model flow was found to be relatively insensitive against varying initial conditions. This behaviour also could be observed in the frame of the current work, see Section 5.4.2.

Louge (1994) used a similar Couette flow model to check theoretical predictions of Jenkins (1992) concerning the interaction of a rapid granular flow of spheres with a flat, frictional wall and could confirm the theoretical predictions for the boundary behaviour at low friction as well as the statement that the ratio of the normal and shear stresses produced by the granular flow is lower than the Coulomb friction coefficient of single particles.

Hard sphere models are used to obtain principle new information concerning for example the nature of boundary interactions in rapid Couette shear flows. Mean normal and shear stresses in steady simple shear flow can be determined for vertically bounded Couette flows. As hard sphere models are valid in the flow ranges of rapid flows of nearly elastic spheres, they can also be used to check theoretical predictions on the flow behaviour.

Limitations of hard sphere models

The hard-sphere approach is valid for rapid flows of rigid particles in the grain inertia regime, in which binary, instantaneous collisions are predominant. Therefore, hard sphere models are appropriate to check predictions of analytic theories of granular flow in this flow regime as done by Lun (1996). The numerical procedure of the event-driven algorithm used by hard sphere models is very effective, as the free particle motion, the particle interaction and the times until the next event can be computed analytically. This effectiveness has its price in the fact that the entire collisional interaction is concentrated in one single time point, and the hard sphere model therefore can only account for binary interactions. As Savage (1993) states, hard sphere models are absolutely inappropriate for modelling granular flows in the multiple-contact, quasi static regime.

As mentioned before, there exist different ranges of particle number densities, in which either soft or hard particle models are approriate descriptions. For example, Lun & Bent (1994) determine a solids concentration of $\nu = 0.65$ as the maximum possible solids concentration that can be modelled as hard sphere flow with a particle longitudinal restitution coefficient of $e = 0.95$. In the frame of the current work, the modelling of segregational granular flows were mainly performed with a longitudinal restitution coefficient of e=0.8 where the solid concentrations were lying in the range $\nu = [0.35, 0.67]$.

The occurence of multiple particle contacts in hard sphere models can be circumvented somehow, if they do not occur too often. However, if the model flow tends towards the quasistatic regime, the hard-sphere simulation breaks down, because, instead of real longterm multiple particle contacts, increasingly numerous particle interactions separated by increasingly short time intervals occur in the hard sphere representation of the flow. This effect is termed "inelastic collapse" by Luding & Mcnamara (1998) and Herrmann & Luding (1998) and has also been observed in the course of this work, as mentioned in Section 5.3.2. The idea standing behind the "inelastic collapse" is also reflected in Sokrates' paradoxon of Achilles and the turtle.

In this work, the modelling of inverse segregational flows was performed in

the parameter range leading to rapid flows, which were governed by binary particle interactions. Breakdown of the simulations due to inelastic collapse was only observed in parameter ranges, which did not lead to flows exhibiting inverse grading.

4.4.3 Discussion

Discrete particle models can describe the entire range of granular flow behaviour. Macroviscous flow behaviour and quasistatic motion of granular assemblies with long term multiparticle contacts are described by soft sphere models, in which the particle interaction is described by contact forces extended over a contact time period $t_c > 0$. The free motion of particles as well as the particle interaction by mutual deformation is computed by explicitly integrating the contact force laws determining the particle interactions. On the other hand, rapid, collision dominated flows, which are characterized by binary, instantaneous particle collisions, can be described more effectively in the frame of hard sphere models. In such models, the entire interaction between rigid particles is assumed to happen at one instance at one defined contact point of the colliding particles.

The choice of the model depends on the range of granular flow behaviour which is intended to be investigated by the model. For example, 2D Couette flows have been investigated using soft sphere models as well as hard sphere models, depending on the solid concentration of the considered flow – there exists a maximum solid concentration, above which a reasonable description of the model flow is possible only by soft sphere models.

The effect of inverse grading has been investigated modelling a 2D chute flow of equal sized inelastic discs with some larger discs in the frame of a soft sphere model. The question underlying the current work is immediately arising from there: Does the effect of inverse grading also occur in rapid collisional flows, which are described in the frame of hard sphere models ?

4.5 Analytical Approaches to inverse grading

Granular dynamics and inverse grading as one of its typical features is taking place on the mesoscopic scale, i.e.

- The number of involved individual particles is too low for describing granular dynamics, like in gas or continuum dynamics, by performing a thermodynamical limit. Aspects of complex behaviour as, for example, inverse grading, would not be taken into account because they would be "averaged away" in the thermodynamical limit dealing with typically 10^{23} molecules.
- On the other hand, the granular dynamics are evolving from global interaction of a number of individual particles which is too large to explain the dynamics solely from single particle behaviour. Typical behaviour enters by complex interaction of a great number of individuals, which cannot be resolved down to single processes.

Attempts of explaining inverse grading have been made by employing balance laws as in continuum mechanics description of granular flow (see Sect. 4.3) or, on the other hand, by simple geometrical and phenomenological considerations. Each approach can reproduce some basic aspects of inverse grading of a granular material, but none of them provides a satisfactorily comprehensive description of the effect.

Here we will report characteristic features of the continuum dynamics and the phenomenological approach to inverse grading.

4.5.1 Inverse grading and continuum dynamics

Following Lun et al. (1984), Farrell et al. (1986) and Jenkins (1998), inverse grading can, in principle, be described in the frame of a kinetic continuum mechanical theory. Regard a mixture of spherical particles of two species a and b, which have the masses m_a and m_b and radii r_a and r_b, respectively. The particles are assumed to interact by collisions which are prametrized by the longitudinal restitution coefficient e as defined in Equation (4.38)

and to be nearly elastic (i.e. $1 - e << 1$). The continuum mechanical momentum equations for each a and b particles are derived in a similar way as sketched in Section 4.3. Note however, that for a description of the bidisperse particle mixture, the collisional supply $\mathbf{\Phi}$ and collisional flux $\mathbf{\Theta}$ of particle properties as defined in Equations (4.36) and (4.37) have to account for collisions between particles of different species.

Substraction of the momentum balance equations for a and b particles leads to an equation for the diffusive velocities $\mathbf{v}_a$ and $\mathbf{v}_b$ of a and b particles. This equation can be regarded as a description of segregation:

$$\begin{aligned} \overset{\cdot}{\overline{\mathbf{v}_a - \mathbf{v}_b}} + \mathbf{v}_a \cdot \nabla \mathbf{v}_a - \mathbf{v}_b \cdot \nabla \mathbf{v} &= \frac{1}{\varrho_a} \nabla \cdot \mathbf{t}_a - \frac{1}{\varrho_b} \nabla \cdot \mathbf{t}_b + \frac{1}{\varrho_a} \phi_a - \frac{1}{\varrho_b} \phi_b \\ &\quad + \frac{1}{m_a} \mathbf{F}_a - \frac{1}{m_b} \mathbf{F}_b. \end{aligned} \tag{4.54}$$

Here, $\mathbf{t}_a$ and $\mathbf{t}_b$ are the so-called species stresses of a and b particles, ϕ_a and ϕ_b are the momenta produced by collisions of a and b particles and, finally, $\mathbf{F}_a$ and $\mathbf{F}_b$ are the external body forces acting on a and b particles.

Further assumptions made by the analytical kinetic model are made on the structure of the pair velocity distribution functions:

- any correlation of velocities of colliding particles is ignored
- the correlation of the positions of the colliding particles is described by assembling the pair distribution function $f_{ij}^{(2)}$ of colliding particle pairs of i and j particles $(i, j = a, b)$ by the single particle distribution functions $f_i^{(1)}$ of each colliding spheres and an equilibrium radial distribution function g_{ij}, which accounts for the influence of the solid volume fraction on the collision frequency of particles.
- in the lowest order of approximation, the single particle velocity distribution functions are assumed to be Maxwell distributions of the form (4.43), what is strictly true only for perfectly elastic particles in thermal equilibrium.

These assumption finally allow to solve Equation (4.54) for the difference of species diffusion velocities $\mathbf{v}_a - \mathbf{v}_b$ and lead to the simplest possible description of segregation of a and b particles in the frame of a kinetic continuum dynamic model:

$$\mathbf{v}_a - \mathbf{v}_b = \frac{n^2}{n_a n_b} D_{ab} \mathbf{d}_a, \tag{4.55}$$

D_{ab} is the diffusion coefficient and $\mathbf{d}_a$ is the diffusive force of a particles.

$$D_{ab} = \frac{n_a n_b}{n} \frac{r_{ab}}{K_{ab}} \sqrt{\frac{\pi}{32} \frac{m_{ab}}{m_a m_b} T}, \tag{4.56}$$

where K_{ab} accounts for the volume occupied by the colliding particle pair a, b. Note that the diffusion coefficient depends like $\sqrt{T}$ on the fluctuating energy T of the granular flow, i.e. without fluctuating motion of the flow there will no segregation take place.

The resulting diffusive force $\mathbf{d}_a$, finally, is due to the gradients of partial pressures , external forces, and concentration and fluctuating energy gradients within the dense flowing granular material:

$$\begin{aligned} \mathbf{d}_a \;=\; & -\frac{\varrho_a}{\varrho} \frac{1}{nT} \left[\nabla P + \varrho_b \left(\frac{\mathbf{F}_a}{m_a} - \frac{\mathbf{F}_b}{m_b} \right) \right] \\ & + \frac{1}{n} \left(\frac{1}{T} \frac{\partial p_a}{n_a} - \frac{1}{n_a} K_{ab} \right) \nabla n_a + \frac{1}{n} \left(\frac{1}{T} \frac{\partial p_a}{n_b} + \frac{1}{n_b} K_{ab} \right) \nabla n_b \\ & + \frac{1}{nT} \left(n_a + K_{aa} + 2 \frac{m_a}{m_{ab} K_{ab}} \right) \nabla T, \end{aligned} \tag{4.57}$$

where $P = p_a + p_b$ is the sum of the partial particle pressures of a and b particles, $\rho = \rho_a + \rho_b = n_a m_a + n_b m_b$ is the sum of the mass densities of a and b particles ($n = n_a + n_b$ is the sum of particle number densities) . Segregation in a dense, bidisperse mixture of different sized elastic spheres is mainly due to size differences of the two particle species and may be described by Equations (4.55),(4.56) and (4.57). Segregation only takes place, if $\mathbf{v}_a - \mathbf{v}_b$ is different from zero, otherwise there is a steady balance between the gradients of fluctuating energy and gradients of number densities.

Discussion

For inverse grading, gravity provides the preferential direction of diffusion velocities. Note however, that in the frame of the above description of segregation, gravity is vanishing in the external force terms and is entering the formal description (4.57) only through the pressure gradient of the hydrostatic condition induced by gravity.

However, in granular media, this assumption will hold only in very special cases. Thus the validity of this description is at least somehow questionable. Furthermore, mechanisms contributing to inverse grading like falling of particles through voids generated by the fluctuating network of flowing granular particles (see sect. 4.5.2) cannot be taken into account.

These problems arise, because the same conceptual background as in the derivation of macroscopic gas or fluid dynamics from dynamics at molecular scale is used. In principle, the above description was obtained the same way as the equations of state of gases: by performing a thermodynamical limit upon the molecular dynamic description of particle (molecular) interaction. Proceeding this way presumes a sufficiently large number of particles (molecules) for performing the thermodynamical limit. (Note that introducing the concept of local field fluctuations into the derivation, which were a neccessary presumption to obtain a description of segregation, implicitly assumes continuous conditions with particle number densities large enough to perform local averaging). As the particle number densities in granular media are far away from typical orders of magnitude of 10^{23} in gases or fluids, the usage of concepts used to obtain macroscopic continuum or gas dynamics laws is omitting the fact that granular flows are qualitatively different as they are taking place at the mesoscopic scale.

Conclusion

Kinetic theory of a mixture of spherical elastic particles can describe segregation of different sized particles due to fluctuating motion of the granular material. Inverse grading with accumulation of larger particles near the top and smaller particles being more likely to be found in lower regions of

the moving granular material has a preferential direction defined by gravity. Describing inverse grading in the frame of kinetic theories at the thermodynamical limit is questionable, for the influence of gravity enters the theory only by pressure gradients, which can not in any case be assumed to be hydrostatic for granular media. This problem arises, because the theoretical approach does not take into account the mesoscopic nature of granular flow.

4.5.2 Inverse grading and statistics: a phenomenological model

The mechanics of the size segregation process during flow of dry particles of equal mass density down a rough inclined chute were investigated by Savage & Lun (1988) in the frame of a simple phenomenological statistical model as well as by an experiment, which has been mentioned before in section 3.2.2.

Here we closely follow Savage & Lun (1988) and report the basic ideas and statistical formulation developed in the frame of their work.

Some of the essential segregational mechanisms were isolated and studied by considering a simplified, steady, two-dimesional model flow of a binary mixture of small and large spheres of equal mass density down a rough inclined chute. The flow of the spherical particles was assumed to take place in layers being in motion relative to each other due to the mean shear caused by the rough chute surface.

The overriding of flow layers and the continuous rearrangement of particles within a flow layer during flow motion causes the network of contact forces and the distribution of voids between the flowing particles to continuously undergo random changes.

Based upon visual observations of model flows of binary mixtures of spheres, there were two main mechanisms proposed to be responsible for the effect of inverse size segregation. Both mechanisms could qualitatively be demonstrated in the frame of the current numerical work (see p. 179, sect. 5.18):

- At any instant, there exists a distribution of randomly evolving voids in a flow layer. If a void between flowing particles in a layer is large enough, a particle from an overriding flow layer can fall into this void.

Assuming a given constant overall solid concentration, the probability of finding a void, into which a small particle can fall, is larger than the probability of finding a void which is wide enough for a large particle. This size dependent mechanism preferring small particles' percolation to lower flow layers is termed "random fluctuating sieve mechanism".

- To satisfy the condition of no overall mass flux perpendicular to the downslope flow direction, there was an additional mechanism suggested, which has neither an inherent preferential direction nor is size dependent: if the contact forces instantaneously exerted on one particle by the ones around are sufficiently imbalanced, a particle can be squeezed out of one layer into another. One can imagine this mechanism as similar to a piece of soap which is sliding out of one's fist when squeezing it. Due to this analogy the mechanism is termed "squeeze expulsion" effect.

Random sieve effect

Regarding the random sieve effect from a more quantitative point of view, it is neccesary to decide whether a particle is likely to fall into a void in a lower flow layer. This decision requires knowledge about the distribution of void sizes in this flow layer.

Considering a binary mixture of large and small spheres with diameters D_a and D_b, respectively, in a region U_l in a flow layer, on defines a "void sphere" with diameter D_v as largest sphere, which can fit into a void formed by the "random continuous network" of the spherical granular particles. For definition of D_v see also Figure 4.13.

Furthermore, a "void diameter ratio" E is defined as

$$E := \frac{D_v}{\bar{D}} \quad \text{where} \quad \bar{D} = \frac{n_a D_a + n_b D_b}{n_a + n_b} \tag{4.58}$$

Statistical analysis with respect to the so-called "maximum entropy approach" yields the following probability distribution for the void sphere ratio:

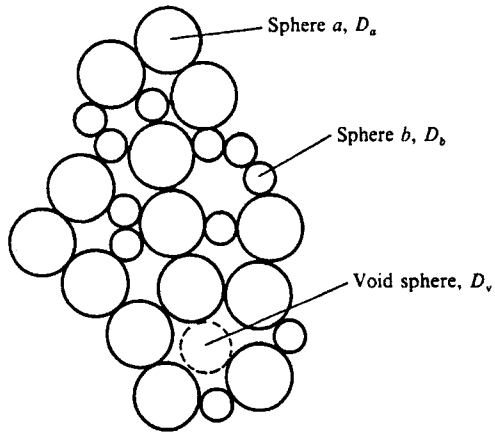

Figure 4.13: *Definition of void sphere diameter D_v. Figure taken from Savage & Lun (1988).*

$$p(E) = \frac{1}{\bar{E} - E_m} \exp\left(-\frac{E - E_m}{\bar{E} - E_m}\right). \tag{4.59}$$

Here, E_m denotes the minimum possible void diameter ratio, which, for example, is $E_m = 0.1547$ for the closest packing of equal sized spheres.

Capture of a particle

Now the capture of a particle from layer A by a void space in the underlying flow layer B as shown in Figure 4.14 is considered. The particle from the upper flow layer A will fall into the void in layer B, if its centre lies in the capture region which is defined by the capture diameter D_c. The capture diameter D_c consists of the void sphere diameter D_v and the radii of particles adjacent to the void sphere, so that the capture diameter is approximately given by

$$D_c \approx D_v + \bar{D} = \bar{D}(E + 1). \tag{4.60}$$

Regarding a lateral projection of a flow layer, n_p denotes the number of particles per unit area and n_V is the number of voids per unit area.

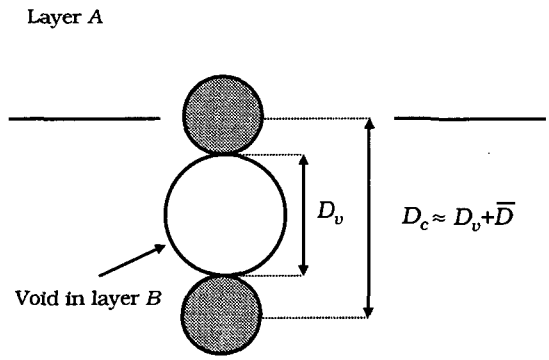

Figure 4.14: *Capture of a particle by a void in an underlying flow layer*

As a consequence, the number of particles captured by a void per unit time is $u_r D_c n_p$, where u_r is the velocity of the upper flow layer relative to the underlying flow layer containing the void. So the number of small b particles captured by a void per unit time interval is

$$\frac{n_b}{n_a + n_b} u_r D_c n_p, \tag{4.61}$$

and the number of spheres captured by a void with a diameter in the range between D_v and $D_v + dD_v$ is

$$n_V \frac{n_b}{n_a + n_b} u_r D_c n_p p dE, \tag{4.62}$$

Small b particles will fall into an underlying void, if the void is large enough, i.e, if $E = \frac{D_V}{\bar{D}} > \frac{D_b}{\bar{D}} = E_b$.

So, finally, the number N_b of b particles falling in an underlying void per unit time and area is

$$N_b = \int_{E_b}^{\infty} n_V \frac{n_b}{n_a + n_b} u_r D_c n_p p dE, \tag{4.63}$$

which, employing (4.59), can be rewritten to

$$N_b = n_V \frac{n_b}{n_a + n_b} u_r n_p \bar{D} [E_b + \bar{E} - E_m + 1] \exp\left(-\frac{E_b - E_m}{\bar{E} - E_m}\right). \tag{4.64}$$

Analoguously, the number N_a of large a particles falling into an underlying void per unit time and area is

$$N_a = n_V \frac{n_a}{n_a + n_b} u_r n_p \bar{D}[E_a + \bar{E} - E_m + 1] \exp\left(-\frac{E_a - E_m}{\bar{E} - E_m}\right), \qquad (4.65)$$

where $E_a = \frac{D_a}{\bar{D}}$.

Effective percolation velocity and squeeze expulsion

The mean percolation velocities q_a and q_b in y direction perpendicular to the flow direction (x direction) of both large and small spheres are generated by particles falling into voids in the underlying layer. Accordingly, they are directed towards to negative y direction. This, however, is a contradiction to the assumption that there is no mean mass flux in y direction in the steady flow, which is homogeneous in flow direction (i.e flow height h, the velocity profile $u(y)$ and the mean bulk density ϱ_s do not depend on the downslope position x).

To balance the mass flux by the downward percolation of large and small particles, there must exist another mechanism generating an upward counterflow with a mean "squeeze expulsion velocity" q_{SE}. It is assumed that the fluctuating contact forces between the particles can produce imbalances, which can "squeeze" out a particle from its layer to an adjacent one, if there is space available for the particle or if the force imbalance is large enough. This postulated additional mechanism is supposed to be neither gravity driven nor size preferential.

Setting the mass flux j_y in y direction to zero yields

$$j_y = \varrho_a q_a + \varrho_b q_b + \varrho q_{SE} = 0, \qquad (4.66)$$

with $\varrho = \varrho_a + \varrho_b$ being the sum of the masses of a and b particles per unit volume. The balance condition can be rewritten as

$$\varrho_a q_{a,net} = -\varrho_b q_{b,net}, \qquad (4.67)$$

where

$$q_{a,net} = q_a + q_{SE} \quad \text{and} \quad q_{b,net} = q_b + q_{SE}. \tag{4.68}$$

The net volume averaged percolation velocities of a and b particles are denoted by $q_{a,net}$ and $q_{b,net}$.

The mass fluxes related to a- and b- particles in y- direction read.

$$\varrho_a q_{a,net} = \frac{\varrho_a \varrho_b}{\varrho}(q_a - q_b) = -\frac{\varrho_b}{\varrho} m_a N_a + \frac{\varrho_a}{\varrho} m_b N_b, \tag{4.69}$$

and

$$\varrho_b q_{b,net} = \frac{\varrho_a \varrho_b}{\varrho}(q_b - q_a) = \frac{\varrho_b}{\varrho} m_a N_a - \frac{\varrho_a}{\varrho} m_b N_b. \tag{4.70}$$

Besides the motion in y direction, particles are transported in x direction with a mean, flow height dependent downstream velocity $u(y)$ as shown in Figure 4.15. With $\hat{\mathbf{i}}$ and $\hat{\mathbf{j}}$ the unit vectors in x- or y direction, respectively, one can write down the volume averaged velocities of a and b particles :

$$\mathbf{v}_a = u(y)\hat{\mathbf{i}} + q_{a,net}\hat{\mathbf{j}}, \tag{4.71}$$

and

$$\mathbf{v}_b = u(y)\hat{\mathbf{i}} + q_{b,net}\hat{\mathbf{j}}, \tag{4.72}$$

which can be combined to the global volume averaged "bulk velocity"

$$\mathbf{v} = \frac{\varrho_a}{\varrho}\mathbf{v}_a + \frac{\varrho_b}{\varrho}\mathbf{v}_b. \tag{4.73}$$

Solution of mass conservation equation

Since there is no mass transfer between particles of species a and b, the mass conservation is valid for each components of the flow:

$$\nabla \cdot (\varrho_a \mathbf{v}_a) = 0, \quad \nabla \cdot (\varrho_b \mathbf{v}_b) = 0. \tag{4.74}$$

Assuming a linear velocity profile

$$u(y) \sim y, \tag{4.75}$$

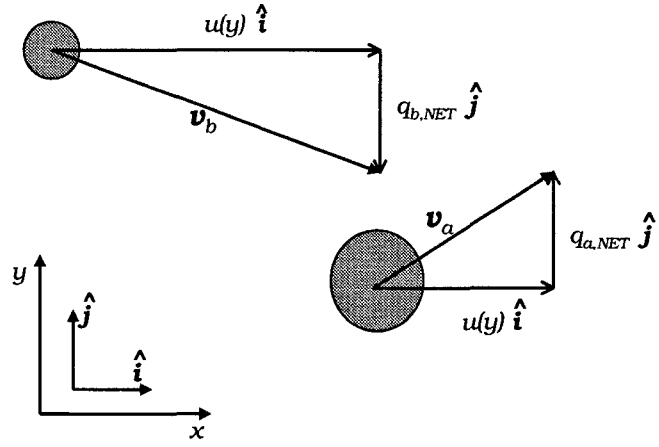

Figure 4.15: *Effective mean particle velocities for a and b particles*

finally leads to the following solution for the for the particle number ratio $\eta_p = \frac{n_b}{n_a}$ in the dilute case $\eta_p \to 0$:

$$\eta_p = \frac{n_b}{n_a} = f(x + \frac{y^2}{2D_a\tilde{q}_{b,net}}), \tag{4.76}$$

which is equivalent to the statement that η is constant on surfaces

$$y = \sqrt{y_0^2 - 2D_a\tilde{q}_{b,net}x}, \tag{4.77}$$

where y_0 is a constant corresponding to the vertical position of a line of constant concentration at the start position $x = 0$ of the flow and $\tilde{q}_{b,net} = \frac{q_{b,net}}{D_a(du/dy)}$. Given the initial depth profile $\eta_{p,0} = \eta_p(x = 0, y)$, it is possible to compute depth profiles of η_p at each downstream position x of the flow.

Using the mass conservation of b particles over the entire flow height, this allows to determine the flow depths $\delta_{0\%}$ and $\delta_{100\%}$, where the concentration of smaller b particles is 0% (only large particles) or 100% (only small particles), respectively:

$$\delta_{0\%} = \sqrt{h^2 - 2D_a\tilde{q}_{b,net}} \tag{4.78}$$

and

$$\delta_{100\%} = \sqrt{2D_a\tilde{q}_{b,net}\eta_{p,0}\sigma^3 x}. \tag{4.79}$$

Total unmixing or segregation, respectively, is achieved, when the lines 0% and 100% concentration join at $x = x_s$. By equating (4.78) and (4.79), x_s is determined to be

$$x_s = \frac{h^2}{2D_a\tilde{q}_{b,net}(1+\eta_{p,0}\sigma^3)}. \tag{4.80}$$

The downstream development of the particle concentration is shown in Figure 4.16 .

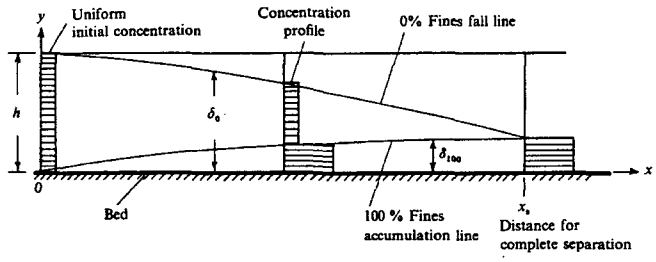

Figure 4.16: *Development of concentration of fine b particles in downstream direction. Figure taken from Savage & Lun (1988).*

The predictions of the described statistical segregation model have been tested with the experimental setup reported in section 3.2.2 (p. 58). Though providing reasonable qualitative agreement, severe problems were arising when trying to experimentally support the conditions of steady flow at constant flow depth: in the experiment, the degree of segregation was determined by placing splitter plates into the flow, which obviously violated the theoretically assumed flow conditions.

Discussion

The reported model is able to describe the development of inverse size segregation of a binary mixture of spherical particles of uniform density under steady flow conditions along an inclined chute. The model is based on the

assumptions of steady flow conditions at constant flow height and solid volume concentration. The mass conservation equation is the only physical law entering the model which otherwise is employing solely geometrical and statistical considerations. As it does not include a physical description of particle interaction, the model cannot make any statement about the influence of particle material properties and their mode of interaction. However, it provides a reasonable qualitative attempt of explaining the effect of inverse segregation, which also is not in contradiction to visual observations made in the frame of the current work (see Sect. 5.18).

4.6 Conclusion

Mathematical and numerical descriptions of avalanche and granular flows at different stages of generality were discussed to embed the investigations of inverse grading in the current work into the frame of existing avalanche and granular dynamics descriptions. This should also have enlightened the train of thought leading to the use of a hard sphere model for the investigation of inverse grading.

Snow avalanches can be described by simple center-of-mass models which interpret the flowing avalanche as a rigid sliding block or, at a more evolved stage, by continuum mechanical deformable body models. Some snow flow avalanche models include aspects of granular flow behaviour into friction laws or continuum constitutive laws, respectively. This inclusion of known granular flow properties, however, does not provide an insight into the granular nature of avalanche flows.

Regarding the derivation of continuum mechanical flow laws for granular media analoguous to kinetic gas theory provides some principle insight into granular flow by considering the joint properties and differences to gas dynamics. Compared to gas dynamics, the quasi-thermodynamical description of granular flows uses heavy, inelastic "molecules". This results in the need to handle systems apart from thermodynamical equilibrium, where the theoretical formulation by means of velocity distribution functions is difficult and only possible by using numerous assumptions. These assumptions are

narrowing the ranges of particle (in)elasticity, in which the continuum models of granular flow are valid.

Discrete particle models circumvent these principle problems by directly assembling the granular flow from the individual motions of all involved particles. Depending on flow density and -speed, either soft sphere models describing macroviscous or quasistatic granular motion or hard sphere models for collision-dominated rapid flow regimes are used. The macroviscous or quasistatic granular motion is charcterized by long term multiple particle contacts, while the rapid, so-called inertia flow regime is dominated by binary, instantaneous particle interactions. Flow properties as velocity profiles and stresses developped by specific cases of granular flow can be investigated in both flow regimes using the appropriate models. Even inverse grading could be observed in the frame of a 2D soft sphere modelling of the flow of inelastic discs.

In a rather general sense, kinetic models of granular flows can account for particle segregation, but for reasons of their restricted ranges of applicability, they are not appropriate for systematic investigations of parametrical dependencies of the effect. The same statement is also valid for a phenomenological statistic description which, however, provides an intuitive insight into the effect of inverse grading.

The question arising now is, how far inverse grading can be observed in the rapid collisional flow regime represented by hard sphere models of granular flows. This question will be considered in detail in the following chapters. Anyway, it has to be stated that, with the use of a hard sphere model, one has moved far apart from classical snow avalanche dynamics before finding an appropriate tool for a parametrical investigation of the inverse segregation effect displayed by the avalanche airbag.

Chapter 5

Inverse grading in a hard sphere model

5.1 Introduction

This chapter is concerned with the simulation of granular flows by a kinetic hard sphere model as described before in section 4.4.2. The granular material is assumed to consist of different sized spherical particles, which are interacting by instantaneous binary collisions. The main goal of the numerical simulations is an understanding of the influence of individual particle properties on global flow behaviour, especially on the formation of inverse grading. Speaking differently, it is tried to observe the formation of a flow out of a great number of particle interactions. As the goal of modelling in the frame of this work is a principle insight into the mechanism of inverse segregation and not an accurate mapping of reality, the model can be kept very simple.

It is an astonishing fact that complex segregational behaviour shows up in a model flow based on very few simple assumptions. Though the used hard sphere model does not require extraordinarily large computer resources, it allows parametrical investigation of the flow behaviour depending on particle material properties over a wide range of parameter values or global flow velocities, respectively.

Physical foundations of the model as interaction mechanism, physical meaning of the material parameters of the particles and boundary conditions are explained in section 5.2. Section 5.3 is concerned with the numerical implementation of the model and of the tools for visualisation and statistical evaluation.

Section 5.4 supports the results of the numerical simulations from different points of view: Qualitative visual observations, quantitative investigations of parametrical dependencies of flow behaviour are discussed with special respect to inverse grading. An attempt is made to interprete the granular model flow in the frame of continuum mechanics. Finally, the method of stochastic analysis is introduced to extract deterministic segregational dynamics of individual particles from the model data.

5.2 Components of the used hard sphere model

This section provides a description of the hard sphere model used in the current work. After a brief overview in Section 5.2.1, the components of the model are explained in detail.

5.2.1 The basic ideas of the model

For the modelling of inverse segregation in granular flow one can confine to a homogeneous granular flow on an infinite, inclined plane, assuming that boundary effects do not principally influence the formation of segregational behaviour in the flow. In the present model, granular material is homogeneously distributed over a rough, inclined, laterally infinite plane. The granular material consists of a mixture of different sized spheres which are initially at rest and then released. To observe the time dependent behaviour and, especially, the formation of inverse grading, it is sufficient to record the flow in a cut of the infinite plane : As the flow is laterally infinite and homogeneous, one can replace this situation by a box filled with granular material, which is moving inside the box. The walls are permeable and are representing boundary conditions in the sense that particles leaving the box

through a wall are entering it again through the opposite wall.

Granular flow is assembled from spherical particles which are moving freely subject only to gravity until any two particles collide. The collision between two particles is assumed to happen instantly at one distinct time point.

In the case of collision, the velocities and spins of the two colliding particles after collision are computed from spins and velocities before the collision, employing the conservation of momenta. The collisional mechanics are parametrized by the longitudinal and tangential restitution coefficients describing the inelastic behaviour of the particles in longitudinal and tangential direction and by the Coulomb friction coefficient of the particle surfaces.

This approach implies that the whole interaction physics occuring during the collision of two particles is assumed to take place at one distinct time point. The collision normally is extended over a interval of contact time, where (in)elastic deformation and rebound are taking place, shock waves passing through the particles and so on. The description of the collisional physics as an instantaneous event has the advantage that the particle interaction has not to be resolved into time steps, which saves a large amount of computing time. Moreover, the solutions of the particles' equations of motion are analytically known. So it is straightforward to assemble the granular flow from individual particle motions: all particle trajectories are traced until a collision between any two particles occurs. The new spins and velocities of the colliding particles after collision are computed. Employing these new start conditions, all particle trajectories are traced again until the next collision.

5.2.2 Boundary conditions

We want to investigate time-dependent behaviour of a laterally homogeneous granular flow on an inclined, infinite plane with periodic boundary conditions. The flow is observed by regarding it over a rectangular cut of the plane. One can imagine a box with permeable walls, through which the flow passes and in which it can be analysed. The granular material is represented by an assembly of spherical particles with a random radius distribution $r_i \in [r_{min}, r_{max}]$. The flow finally is formed by the whole of the

particles, which can move freely subject only to gravity until they collide with another particle or with the bottom of the box.

The box has a length l_x, width l_y and is infinitely high (see Fig. 5.1). The permeable walls are equivalent to periodic boundary conditions in the sense that granular particles leaving the box through a wall enter the box through the opposite wall again. For the lateral coordinates x_i and y_i of a particle i this means that

$$\begin{aligned} x_i \geq l_x &\implies x_i = x_i - l_x, \\ x_i < 0 &\implies x_i = x_i + l_x, \\ y_i \geq l_y &\implies y_i = y_i - l_y, \\ y_i < 0 &\implies y_i = y_i + l_y. \end{aligned} \tag{5.1}$$

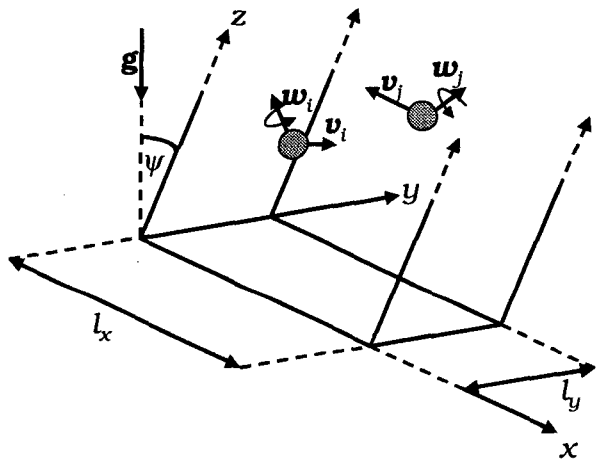

Figure 5.1: *Box with periodic boundary conditions.*

The box is inclined by an angle ψ and its bottom is "roughened" by a periodic function

$$f(x,y) = |a_r \sin(b_x x)\sin(b_y y)| + c_r, \tag{5.2}$$

where

$$b_{x,y} = \frac{n_{x,y}\pi}{l_{x,y}}.$$

The number of "bumps" on the bottom in x- or y-direction is denoted by n_x or n_y, respectively, with $n_x, n_y \in \mathbf{N}$.

5.2.3 Time to next event

As stated before in Section 5.2.1, the model makes use of the "time to the next event" algorithm. This means that all particles are moving freely subject only to gravity until the next "event" occurs. An event occurs, if

- any two particles are colliding
- a particle collides with the bottom of the box
- a particle passes one of the permeable side walls of the box.

After an event, the particles move freely again until the next event happens. For each particle participating in the flow, the time to the next event, in which this particle is involved, has to be computed. The minimum of the times to the next event of all particles is the time to the next event of the whole flow. We now explicitly write down the relations governing the time to the next event for any particle. For this purpose, we regard the fact that in the box coordinate system depicted in Figure 5.1, any particle i is moving according to

$$\ddot{\mathbf{x}}_i = \mathbf{g} \qquad \text{with} \quad \mathbf{g} = \begin{pmatrix} g\sin\psi \\ 0 \\ -g\cos\psi \end{pmatrix}, \tag{5.3}$$

where ψ denotes the angle of incination of the box and g is the vertical gravitational acceleration.

Collision of two particles

Collision between two particles can occur either between two freely moving particles or between a flying particle and a particle lying on the ground. Let us first consider the collision of two flying particles i and j with radii r_i and r_j, respectively. At a time point t_0 their centers of masses have the coordinates $\mathbf{x}_i$ and $\mathbf{x}_j$ and the particles are moving with the velocities $\mathbf{v}_i$ and

$\mathbf{v}_j$. We now define the distance vector $\delta\mathbf{x} := \mathbf{x}_i - \mathbf{x}_j$, the velocity difference $\delta\mathbf{v_c} := \mathbf{v}_i - \mathbf{v}_j$ and the sum of the particle radii $d := r_i + r_j$. The unit vector $\mathbf{k} := \frac{\delta\mathbf{x}}{|\delta\mathbf{x}|}$ points from the center of particle j to the center of particle i. Figure 5.2 depicts the situation for two particles at the time of collision.

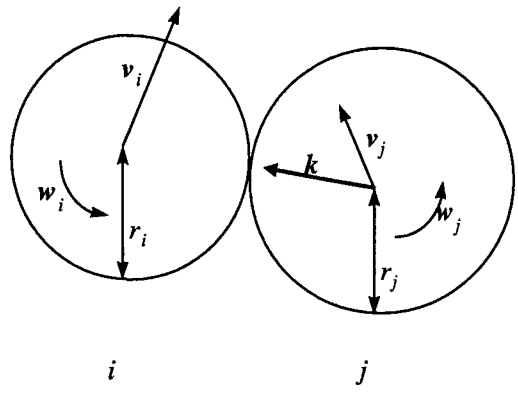

Figure 5.2: *Two colliding spherical particles i and j at the time point of contact.*

We now can set $t_0 = 0$ and state that a collision between particles i and j occurs after a time t_{ij}, if

$$\delta\mathbf{x} + \delta\mathbf{v_c} t_{ij} = \mathbf{k}d, \tag{5.4}$$

which is equivalent to

$$(\delta\mathbf{x})^2 - d^2 + (2\delta\mathbf{x} \cdot \delta\mathbf{v_c})\ t_{ij} + (\delta\mathbf{v_c})^2 t_{ij}^2 = 0. \tag{5.5}$$

If there exists a positive real root t_{ij} of this quadratic equation, the particles will collide. In the case of two positive real roots we will choose the smaller one as the collision time t_{ij}. The larger root corresponds to the particles mutually penetrating each other and then touch each other "from inside".

If one of the colliding particles is lying on the ground, no longer both particles are accelerated by gravity. By this way, a gravitational term enters Equation (5.4):

$$\delta\mathbf{x} + \delta\mathbf{v_c} t_{ij} + \frac{1}{2}\mathbf{g}t_{ij}^2 = \mathbf{k}d, \tag{5.6}$$

The scalar form of (5.6) then reads:

$$(\delta\mathbf{x})^2 - d^2 + (2\delta\mathbf{x}\cdot\delta\mathbf{v_c})\, t_{ij} + ((\delta\mathbf{v_c})^2 + \delta\mathbf{x}\cdot\mathbf{g})t_{ij}^2 + \delta\mathbf{v_c}\cdot\mathbf{g}t_{ij}^3 + \frac{1}{4}\mathbf{g}^2 t_{ij}^4 = 0. \quad (5.7)$$

The flying and the lying particle collide, if there exists a positive real root t_{ij} of the fourth order equation (5.7). In the case of more positive real roots we again choose the smallest one as collision time t_{ij}.

The time t_{ij} until collision is computed for any pair i, j of particles. To reduce the number of computations, only collision times of particles (j) lying in the vicinity

$$U_\epsilon(\mathbf{x}_i) = \{\mathbf{x} \in \mathbf{R}, |\mathbf{x} - \mathbf{x}_i| < \epsilon\}, \qquad \epsilon > 0 \quad (5.8)$$

of particle i are computed. For rapid flows, ϵ typically is chosen as two particle diameters.

As we employ periodic boundary conditions, particles in the vicinity of a wall must also be able to interact with particles in the vicinity of the opposite wall, or, speaking differently, also U_ϵ is subject to periodic boundary conditions. Regard two particles i and j with radii r_i and r_j at different places $\mathbf{x}_i$ and $\mathbf{x}_j$, each in the vicinity of one of the opposite walls of the box with (periodicity) lengths l_x and l_y in $x-$ and $y-$ direction. The distance vector between the particles is

$$\delta\mathbf{x} = \mathbf{x}_i - \mathbf{x}_j = \begin{pmatrix} \delta x \\ \delta y \\ \delta z \end{pmatrix} \quad (5.9)$$

If particle i and j are near opposite walls, the computation of the time to their collision has to be based on a distance vector $\delta\mathbf{x}^*$ modified according to the periodic boundary conditions. With $d = r_i + r_j$, this can be formulated as follows:

$$\delta x \geq l_x - 2d \implies \delta x^* = \delta x - l_x \mathrm{sgn}(\delta x) \quad (5.10)$$

$$\delta y \geq l_y - 2d \implies \delta y^* = \delta y - l_y \mathrm{sgn}(\delta y). \quad (5.11)$$

Note that only the distance vector $\delta\mathbf{x}$ is changed for the computation of the time until collision of particles i and j, which keep their positions near opposite walls.

Collision of a particle with the bottom

Particles colliding with the bottom of the box are reflected with new velocities and spins. The collision of a particle with the bottom of the box therefore is an "event" in the sense that the movement of all particles can be assumed as free until this event, where the movement of a particle changes, requiring new computation of the time until the next event. As stated before in 5.2.2, the bottom of the box is "roughened" by the periodic function (5.21).

In order to simplify the computation of the time until a particle touches the bottom, the bottom is assumed to be flat. The roughness is introduced by periodically changing the direction of the (unit) collision vector $\mathbf{k}_b$, which is pointing from the center of an imaginary bump at the bottom to the center of the particle colliding with the bottom:

$$\mathbf{k}_b = \frac{\delta\mathbf{x}_b}{|\delta\mathbf{x}_b|}, \tag{5.12}$$

where

$$\delta\mathbf{x}_b = \begin{pmatrix} -a_r \cos(\mathrm{mod}(b_x x_i, \pi)) \\ -a_r \cos(\mathrm{mod}(b_y y_i, \pi)) \\ a_r |\sin a x_i| \; |\sin a y_i| + c_r \end{pmatrix}. \tag{5.13}$$

This simple trick allows a straightforward determination of the time $t_{i,b}$, when particle i (with radius r_i) hits the ground by taking the smaller positive root of

$$z_i - r_i + v_z t_{i,b} + g_z t_{i,b}^2 = 0, \tag{5.14}$$

where z_i is the vertical position of the center of particle i, v_z is its vertical velocity and g_z is the vertical component of gravitational acceleration in the box coordinate system.

Time until a particle passes a side wall of the box

According to Equation (5.1), a particle leaving the box through a wall enters the box through the opposite wall again. To prevent these particles from leaving the box too far before the next collision event occurs, it is reasonable to handle also the passing of a particle center through a wall or its entering at the opposite wall, repectively, as an event. In the following, the times t_{ii} until passing of a particle through a side wall and through the front- and rear wall, respectively, are given in Equations (5.15). Similar to the computation of collision times between two particles, we compute the "wall-time" t_{ii} only if a wall is situated in the surrounding $U_\epsilon(\mathbf{x}_i)$ of particle i.

The time t^*_{ii} until particle i with position $\mathbf{x}_i = \begin{pmatrix} x_i \\ y_i \\ z_i \end{pmatrix}$ and velocity $\mathbf{v}_i = \begin{pmatrix} v_{x,i} \\ v_{y,i} \\ v_{z,i} \end{pmatrix}$ passes a side wall is (see fig. 5.3)

$$\begin{aligned} t^*_{ii} &= \frac{l_y - y_i}{v_{y,i}} \qquad \text{for} \qquad v_{y,i} > 0 \\ t^*_{ii} &= -\frac{y_i}{v_{y,i}} \qquad \text{for} \qquad v_{y,i} < 0 \\ t^*_{ii} &= \infty \qquad \text{for} \qquad v_{y,i} = 0. \end{aligned} \tag{5.15}$$

Time until a particle passes a front- or rear wall

Computing the "wall time" for particle i until it passes the front or rear wall of the box, we also have to take into account the downslope gravitational acceleration g_x. This means, that for particles moving in upslope direction, one has to check, whether they reach and pass the upslope (the rear) wall

or whether they turn back and finally pass the downslope (front) wall of the box. In x - direction, t_{ii} is computed as the root of

$$\frac{1}{2}g_x t_{ii}^2 + v_{x,i}t_{ii} + \Delta\xi = 0, \tag{5.16}$$

where $\Delta\xi$ is the distance of the particle center to the "nearest" wall. If the particle moves in downslope direction, i.e. $v_{x,i} \geq 0$, $\Delta\xi = l_x - x_i$ and we obtain

$$t_{ii} = \frac{1}{g_x}\left(-v_{x,i} + \sqrt{v_{x,i}^2 + 2g_x(l_x - x_i)}\right). \tag{5.17}$$

In the case of upslope movement $\Delta\xi = x_i$ and

$$t_{ii} = \frac{1}{g_x}\left(-v_{x,i} + \sqrt{v_{x,i}^2 - 2g_x x_i}\right). \tag{5.18}$$

If the discriminant $\sqrt{v_{x,i}^2 - 2g_x x_i}$ has no real solution, this means that the particle does not reach the upslope wall but is turning back in downslope direction. In this case, we have to set $\Delta\xi = l_x - x_i$, which leads again to

$$t_{ii} = \frac{1}{g_x}\left(-v_{x,i} + \sqrt{v_{x,i}^2 + 2g_x(l_x - x_i)}\right). \tag{5.19}$$

Finally, the only thing left to do is to set

$$t_{ii} = \min(t_{ii}, t_{ii}^*) \tag{5.20}$$

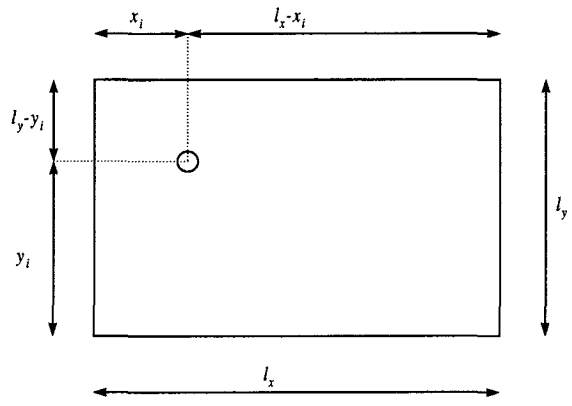

Figure 5.3: *Distances of a particle center from the walls.*

according to either the passing of a side wall or the passing of the front- or rear wall, respectively, being the next wall event of particle i.

5.2.4 Collision mechanism

Formal description of binary, instantaneous collisions

The interaction between particles happens by instantaneous, binary collisions. This means, that the interaction of two particles by exchange of momentum and spin is supposed to take place at one distinct time point. For the formal description of this kind of collisional mechanics between spherical particles, we generalize a 2D description of collisions of discs as reported by Nakagawa & Imaizumi (1992), Lun (1996) or Herrmann & Luding (1998).

The translational velocities $\mathbf{v}'$ and angular velocities $\mathbf{w}'$ after a collision are related to velocities $\mathbf{v}$ and rotational velocities $\mathbf{w}$ before the collision:

$$(\mathbf{v}', \mathbf{w}') = f_{[e,b,\mu]}(\mathbf{v}, \mathbf{w}), \tag{5.21}$$

where the expression $f_{[e,b,\mu]}$ contains the physics of the instantaneous binary particle interaction.

The mechanical properties of the individual particles are described by the longitudinal and transversal restitution coefficients e and b representing the inelastic behaviour of two particles encountering a collision and by the transversal Coulomb friction coefficient μ. The coefficients e of longitudinal and b of tangential restitution are defined as the ratio of longitudinal or tangential relative velocity after and before the collision of two particles.

In case of slip occuring between the colliding particles, the Coulomb coefficient μ of friction relates the mutually exerted tangential forces between the colliding particles to the longitudinal contact forces, or, in the picture of instantaneous collision employed here, to the transfer of longitudinal momentum. Some physical interpretation of the material parameters will be provided after the following derivation of the relations between particle motion before and after a collision.

Regard two particles i and j with radii r_i and r_j at the time of contact (see Fig. 5.2). The velocities and (angular) rotational velocities of the particles

are $\mathbf{v}_i$ and $\mathbf{w}_i$ or $\mathbf{v}_j$ and $\mathbf{w}_j$, respectively. The particles' masses and momenta of inertia are m_i, Θ_i or m_j and Θ_j. The vector $\mathbf{k}$ denotes the unit vector between the centers of the particles:

$$\mathbf{k} = \frac{\mathbf{x}_i - \mathbf{x}_j}{|\mathbf{x}_i - \mathbf{x}_j|}, \tag{5.22}$$

where $\mathbf{x}_i$ and $\mathbf{x}_j$ denote the positions of the particle centers.

The velocity difference $\delta\mathbf{v}$ at the point of contact can be expressed as

$$\begin{aligned} \delta\mathbf{v} &= \mathbf{v}_i - \mathbf{v}_j - (r_i\mathbf{w}_i + r_j\mathbf{w}_j) \times \mathbf{k} \\ &= \delta\mathbf{v}_c - (r_i\mathbf{w}_i + r_j\mathbf{w}_j) \times \mathbf{k}. \end{aligned} \tag{5.23}$$

Regarding the inelastic interaction parametrisized by the longitudinal and tangential restitution coefficients e and b, the velocity difference $\delta\mathbf{v}'$ at the contact point after the momentum and spin exchange satisfies the following relations:

$$\begin{aligned} \mathbf{k} \cdot \delta\mathbf{v}' &= -e\ (\mathbf{k} \cdot \delta\mathbf{v}) \\ \mathbf{k} \times \delta\mathbf{v}' &= -b\ (\mathbf{k} \times \delta\mathbf{v}). \end{aligned} \tag{5.24}$$

The conservation of momentum can be written as:

$$\begin{aligned} m_i\mathbf{v}_i' &= m_i\mathbf{v}_i + \delta\mathbf{p} \\ m_j\mathbf{v}_j' &= m_j\mathbf{v}_j - \delta\mathbf{p} \end{aligned} \tag{5.25}$$

and, similarly, the conservation of spin:

$$\begin{aligned} \Theta_i\mathbf{w}_i' &= \Theta_i\mathbf{w}_i - \mathbf{k} \times \delta\mathbf{p} \\ \Theta_j\mathbf{w}_j' &= \Theta_j\mathbf{w}_j + \mathbf{k} \times \delta\mathbf{p} \end{aligned} \tag{5.26}$$

In these balance equations, $\delta\mathbf{p}$ denotes the momentum exchange between the particles. Using Equations (5.23), (5.24), (5.25) and (5.26), $\delta\mathbf{p}$ can be expressed by the velocity difference $\delta\mathbf{v}$ before the collision of the two particles:

$$\delta\mathbf{p} = \mathcal{C}\delta\mathbf{v} + \tilde{\mathcal{C}}\mathbf{k}(\mathbf{k} \cdot \delta\mathbf{v}), \tag{5.27}$$

where

$$\mathcal{C} = \frac{1+b}{\tilde{m}+\tilde{\kappa}}, \qquad \tilde{\mathcal{C}} = \frac{1+e}{\tilde{m}} - \mathcal{C} \tag{5.28}$$

and

$$\frac{1}{\tilde{m}} = \frac{1}{m_i} + \frac{1}{m_j}, \qquad \tilde{\kappa} = \frac{r_i^2}{\Theta_i} + \frac{r_j^2}{\Theta_j}. \tag{5.29}$$

Slip between particles occurs, if

$$|\mathbf{k} \times \delta\mathbf{p}| > \mu\ \mathbf{k} \cdot \delta\mathbf{p}, \tag{5.30}$$

where μ is the Coulomb friction coefficient. If slip occurs, the maximum possible tangential momentum exchange is $\mu\ \mathbf{k} \cdot \delta\mathbf{p}$. Using Equation (5.27), this results in a new tangential restitution coefficient b_{slip}, which also takes slip into account:

$$b_{slip} = \mu(1+e)(1+\frac{\tilde{\kappa}}{\tilde{m}})|\cot\gamma| - 1, \tag{5.31}$$

where $\gamma :=$ angle $(\mathbf{k}, \delta\mathbf{v})$. In the case of slip between the particles, the momentum transfer $\delta\mathbf{p}$ in Equation (5.27) has to be recalculated with the new, "actual" tangential restitution coefficient b_{slip}, otherwise the calculation with the previously given restitution coefficient b is valid.

Now, with Equations (5.25), (5.26) and (5.27), the velocities $\mathbf{v}'$ and spins $\mathbf{w}'$ of the particles after collision read:

$$\begin{aligned}
\mathbf{v}_i' &= \mathbf{v}_i - \frac{1}{m_i}(\mathcal{C}\delta\mathbf{v} + \tilde{\mathcal{C}}\mathbf{k} \cdot (\mathbf{k} \cdot \delta\mathbf{v})) \\
\mathbf{v}_j' &= \mathbf{v}_j + \frac{1}{m_j}(\mathcal{C}\delta\mathbf{v} + \tilde{\mathcal{C}}\mathbf{k} \cdot (\mathbf{k} \cdot \delta\mathbf{v})) \\
\mathbf{w}_i' &= \mathbf{w}_i - \frac{r_i}{\Theta_i}\mathcal{C}\mathbf{k} \times \delta\mathbf{v} \\
\mathbf{w}_j' &= \mathbf{w}_j - \frac{r_j}{\Theta_j}\mathcal{C}\mathbf{k} \times \delta\mathbf{v}.
\end{aligned} \tag{5.32}$$

In principle, the model allows to associate individual parameters e_i, b_i and μ_i to each particle i. Collision of two particles i and j with different parameter sets $\{e, b, \mu\}_i$ and $\{e, b, \mu\}_j$ and different masses m_i and m_j can be accounted for in the frame of the above formalism by mass weighted mean values such as

$$\langle e \rangle_m = \frac{m_i e_i + m_j e_j}{m_i + m_j} \tag{5.33}$$

and similarly for the other parameters b and μ. However, this approximation is only valid if the parameters of the i and j particles differ not too much.

Imagine, for example the collision of a heavy, perfectly elastic particle i with a light, perfectly plastic particle j. With $e_i = 1$, $e_j = 0$ and $m_i \gg m_j$ the collision has to be computed with $\langle e \rangle_m \approx 1$, which is an absolutely inappropriate description for the collision dynamics of the small particle.

For this reason, in the numerical investigations the granular material was assumed to consists of particles with uniform parameter sets.

Collisional parameters and their physical meaning

To enlighten the role of the material parameters in the frame of the above description, it is useful to have a look at the physical processes occuring during the collision - this will also provide an idea of the simplifications and assumptions implied in the used hard-sphere approach.

When a binary particle collision happens, two particles approach each other, encounter each other, stay in contact for a short time, separate afterwards and finally are moving apart with new velocities and spins.

As stated by Hwang & Hutter (1995), the binary impact can generally be divided into two phases, the *flying phase* and the *contact phase*. In the flying phase, the two particles have a total kinetic energy T (besides the potential energy, which can be omitted here without loss of generality).

During collision in the contact phase, the kinetic energy is completely changed into vibrational or "elastic" energy, respectively. The generated mechanical waves are propagating through the particles, are refracted and reflected and return to the contact point again. There, kinetic energy T is recreated, but less than T of both particles before encounter. The difference between kinetic energy before and after contact has been dissipated in plastic deformation and damping of eigenoscillations of the particles during the collision.

Ideally, the elastic wave is supposed to be dissipated into heat, before the next collision of the particle occurs, so that consecutive collisions of a particle do not affect each other.

This picture makes no statement about the forces mutually exerted between the particles during collision. The longitudinal coefficient e of restitution is

defined by an artificial kinematic relationship as ratio of velocities along the common unit normal vector of the particles after and before contact (see eqs. 5.22 and 5.24):

$$e := \frac{\delta \mathbf{v}' \cdot \mathbf{k}}{\delta \mathbf{v} \cdot \mathbf{k}}. \tag{5.34}$$

This approach is termed "Newton's law" by Wang & Mason (1992).

Following another path of physical interpretation, one firstly regards the normal contact force $F_c(t)$ acting along the common unit normal vector $\mathbf{k}$ of the particles during the contact. The contact starts at the time point t_- and ends at t_+ as depicted in Figure 5.4. Employing the definitions (5.23) and (5.25), the normal component of the relative particle velocity $\delta \mathbf{v} \cdot \mathbf{k}$ changes sign at the time point t_c of maximum normal contact force.

The normal momentum $\delta p_n = \delta \mathbf{p} \cdot \mathbf{k}$ exchanged during the particle contact can be expressed as

$$\delta p_n = \int_{-\infty}^{+\infty} dt\ F_c(t) = \int_{t_-}^{t_c} dt\ F_c(t) + \int_{t_c}^{t_+} dt\ F_c(t) = \delta p_{n,-} + \delta p_{n,+}, \tag{5.35}$$

where $\delta p_{n,-}$ and $\delta p_{n,+}$ are the normal components of momentum exchanged before and after the paroxysm t_c of the collision, as defined by Zimmermann et al. (1989).

Figure 5.4 shows the relation between normal contact force and exchanged momentum. $\delta p_{n,-}$ can be regarded as responsible for the change of kinetic into elastic energy and, vice versa, $\delta p_{n,+}$ for the recreation of kinetic from elastic energy. Except in the case of ideal elastic collision, $\delta p_{n,+} < \delta p_{n,-}$ due to dissipation of energy during the contact. From this point of view, the coefficient e of normal or longitudinal restitution can be defined as

$$e = -\frac{\delta p_{n,+}}{\delta p_{n,-}}, \tag{5.36}$$

which is also termed the "Poisson's hypothesis". Assuming that also in tangential direction elastic strain energy can be stored and is recoverable

into kinetic energy, one ends up at a definition for the tangential coefficient b of restitution, which is analogous to the definition of e :

$$b = -\frac{\delta p_{t,+}}{\delta p_{t,-}}, \tag{5.37}$$

where

$$\delta p_n = \delta \mathbf{p} \times \mathbf{k} = (\delta \mathbf{p} \times \mathbf{k})_- + (\delta \mathbf{p} \times \mathbf{k})_+ = \delta p_{t,-} + \delta p_{t,+}. \tag{5.38}$$

This relation only holds in the case of no tangential slip between the particles at the contact point during the collision. Otherwise, the tangential momentum that can be exchanged between the particles is limited by the Coulomb law of friction :

$$\delta p_{t,+} = -\mu \delta p_{n,-}, \tag{5.39}$$

or

$$(\delta \mathbf{p} \times \mathbf{k})_+ = -\mu (\delta \mathbf{p} \cdot \mathbf{k})_-, \tag{5.40}$$

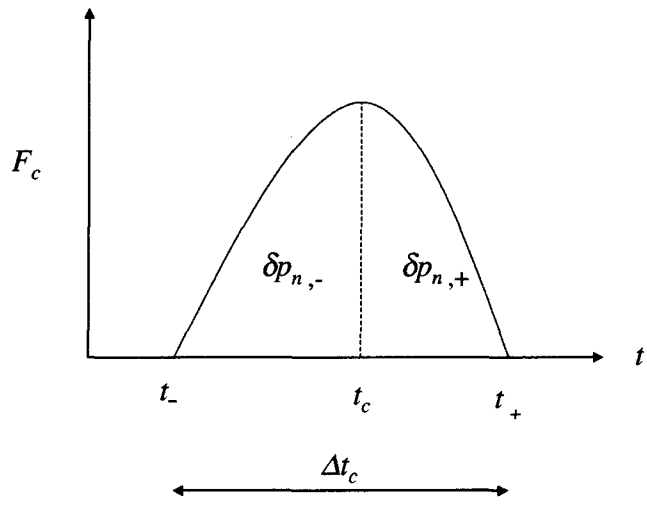

Figure 5.4: *Time dependent normal contact force F_c during the collision of particles, which lasts from time point t_- to t_+. The time point of reversal or maximum contact force, respectively, is denoted by t_c. Momenta exchanged before and after t_c are termed $\delta p_{n,+}$ and $\delta p_{n,-}$.*

respectively. Note that, via Equation (5.35), the definitions (5.37) and (5.39) allow coexistence of (or, speaking differently, change between) slip and no slip during the duration Δt_c of one particle collision event, as stated by Wang & Mason (1992). This possibility is omitted in the simple collision model presented above which assumes the whole of the particle interaction being concentrated in one time point.

As also mentioned by Wang & Mason (1992), in the frame of the Poissons hypothesis one can, by employing Routh's impact process diagram method, distinguish between 5 types of binary collisions depending on the order of sliding and sticking during the collisional process.

This order is governed by the parameters e and μ as well as by the collision geometry. In comparison to Newton's law approach, the Poissons hypothesis has the advantage of avoiding a violation of energy conservation, which may occur in some cases of describing collisions by Newton's law.

Assuming the particle interactions to be of instantaneous nature ($\Delta t_c \to 0$), the description of the collision by Equations (5.35)-(5.39) looses its dynamical character.
$F_c(t) \to \delta p_n \delta(t_c)$ no longer resolves the dynamical behaviour during collision. For $\Delta t_c \to 0$, F_c causes a discontinuity in the momenta of the colliding particles, a phenomenon, for which the Newton's law picture is a well suited description. An evaluation of stroboscopic photographs of collisions of small spheres with diameters of 3 mm and 6 mm performed by Foerster et al. (1994) also indicates the Newton's law picture being an appropriate description of particle collision.

5.3 Numerical implementation

The granular flow model outlined in the previous sections has been implemented by a C-Code, which has mostly been running under HP UX on a HP 9000/780 workstation with 256 MB RAM. In this section, the numerical realisation of the granular flow model and its interaction with the associated evaluation tools will be described. At any event time point, the model

provides a $9N$ dimensional state vector

$$\Psi_i(t) = (\mathbf{x}_i(t), \mathbf{v}_i(t), \mathbf{w}_i(t)) \tag{5.41}$$

of the flow, which contains position, spin and velocity of each of the N particles participating in the flow. The numerical routines for the simulation of the granular flow are described in 5.3.2, where also problems and numerical limitations are reported. Section 5.3.3 provides details of the evaluation routines, which compute flow profiles of e.g. velocities, particle size distribution as well as the global time behaviour of the flow (mean velocities, densities and so on) from $\Psi_i(t)$. Furthermore, the flow can qualitatively be observed by a visualisation routine, which is shortly demonstrated in 5.3.3. To give a general idea of how granular flow data are generated and statistically evaluated, the following section 5.3.1 provides an overview over the used program packages and their interactions.

5.3.1 Programs and their interconnections

Before describing the programs in detail, a brief overview over their general features will be be provided. The way in which they interact by exchange of input or output data, respectively, is of special interest here and will be explained in the following. Figure 5.5 is a simplified flow chart of the course of simulation and evaluation of a granular flow with some explanations on the function of the involved routines or programs. The data exchange between the involved programs is sketched in Figure 5.6.

The routines of the abs program

The name **abs** stems from the practical use of inverse grading as function principle of avalanche balloons, which are also called ABS-Balloons.

The **abs** program is consisting of routines generating a hard sphere granular flow based on the "time to the next event" algorithm, which is described in Sections 5.2 and 5.2.4. It requires start- and boundary conditions of the granular flow and material properties of the granular material as input, which is provided by the **def.dat** file. The output of **abs** is called

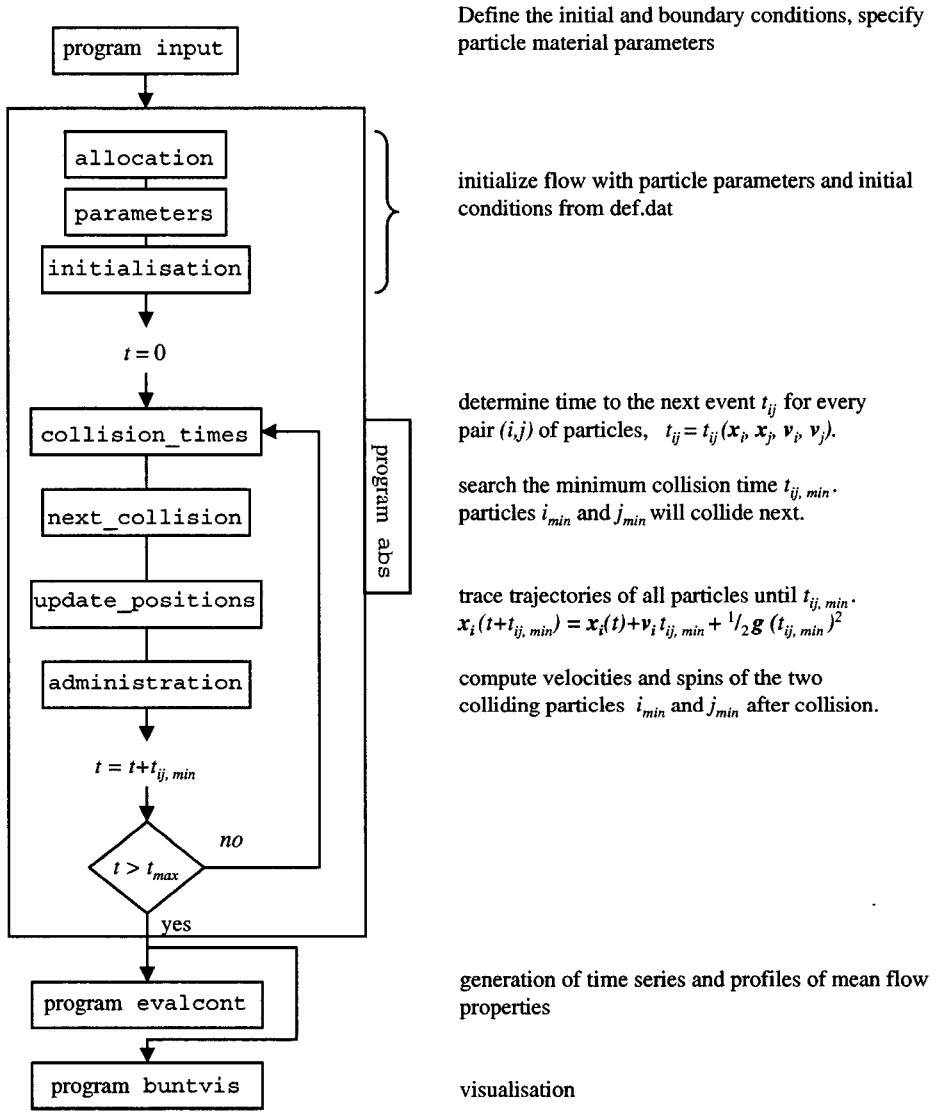

Figure 5.5: *Flow chart of programs and routines involved in simulation and evaluation of a hard sphere granular model flow*

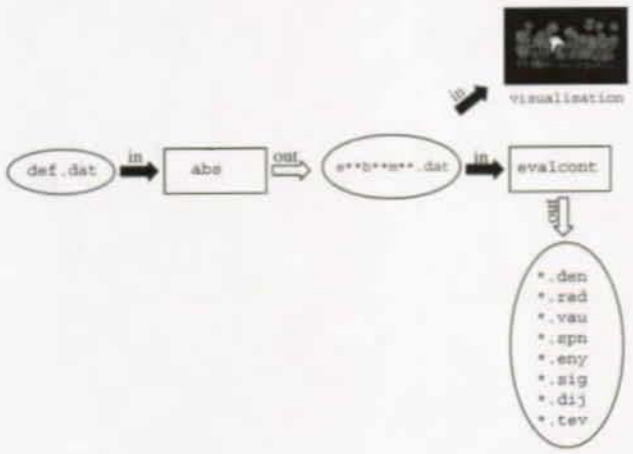

Figure 5.6: *Programs and data exchange*

`e**b**m**.dat`, where `e**`, `b**` and `m**` are indicating the values of the parameters e, b and μ. For example, `e07b08m02.dat` contains the output related to a flow with single particles' material parameters $e = 0.7$, $b = 0.8$, and $\mu = 0.2$. In principle, the `e**b**m**.dat` file contains the state vector $\Psi_i(t)$ of the flow and some additional information about momentum exchange between interacting particles for any event time point t. The exact structure of `def.dat` and `e**b**m**.dat` will be explained later on.

The `evalcont` program

The evaluation of the `abs` output is done by the `evalcont` program which processes the data provided in the `e**b**m**.dat` files. By time and spatial averaging over distinct time windows and flow layers, respectively, flow profiles of the following quantities are computed. These flow profiles are stored in files, which are labelled with file name extensions related to the averaged quantities :

- mean particle number density, extension `.den`
- mean particle size, extension `.rad`
- mean velocity, extension `.vau`

- mean spin, extension `.spn`
- mean particle energy, extension `.eny`
- mean stress tensor, extension `.sig`
- mean deformation tensor, extension `.dij`
- Additionally, the time development of mean quantities averaged over the whole flow height are computed and saved in a file with the extension `.tev`.

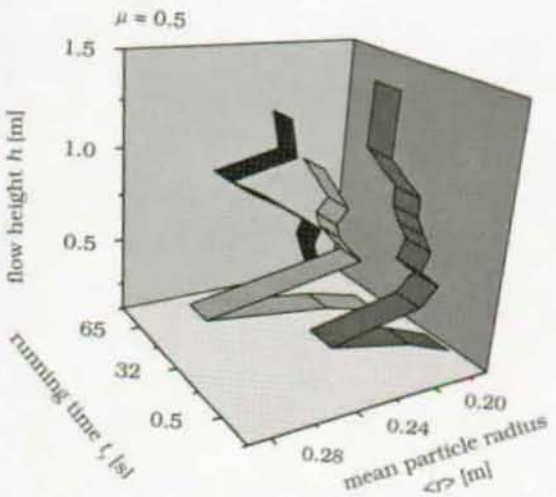

Figure 5.7: *Example for mean particle size profiles at 3 equidistant time points. Averaging interval $t_{av} = 0.5s$ for every profile.*

Summarizing, the `evalcont` program does the following: for equidistant time points, height-dependent profiles of mean quantities and their standard deviation are computed. The computation of the mean values of a certain quantity in a profile height h is based upon averaging this quantity over all particles i contained in a layer of the flow with $z_i \in [h, h + \delta h]$ and over a time interval $[t_n, t_n + t_{av}]$. Figure 5.7 shows an example for mean velocity profiles at 3 different time points of the flow.

The output files of `evalcont` are named "`e**b**m** **t**.***`", where `e`, `b` and `m`, like in the `e**b**m**.dat` file, denote the material parameter

values of the flow, and `**t**` stands for the start and end times t_n and $t_n + t_{av}$ of the averaging, respectively. Finally, the extension `.***` indicates the quantity, for which the mean profiles were computed, as explained at begin of this section.

For example, a file named `e08b06m0515t20.vau` contains the mean velocity profile of a flow with parameters e=0.8, b=0.6, μ=0.5 averaged over the time interval [1.5 s, 2.0 s]. The `.tev` files have a special role, for here the averaging is performed over the whole flow height and not over distinct layers of the flow, whereas the time averaging is done over a time window t_{win} which is moved over the entire time extent of the flow in small steps Δt, such that a proper picture of the mean time development of the flow is obtained. Figure 5.8 shows an example of the time evolution of the mean flow velocity.

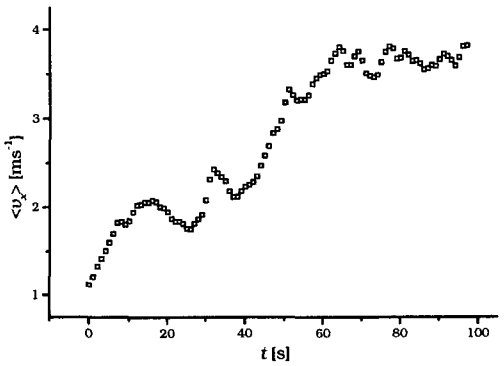

Figure 5.8: *Example for time evolution of mean flow velocity* $< v_x(t) >$ *generated by the* `evalcont` *routines with* $\Delta t = \delta t_{win} = 1s$. *Particle material parameters* $e = 0.8$, $b = 0.4$, $\mu = 0.4$.

Visualisation

In the frame of the "AVS" software (Advanced Visual Systems Inc. (1992)), a so-called "network" was constructed, which is able to read the `.dat` files containing the state vectors $\Psi_i(t) = (\mathbf{x}_i(t), \mathbf{v}_i(t), \mathbf{w}_i(t))$ of the flow at any event time point. It converts them into a 3D picture of the flow. Figure 5.9

shows an example for such a visualisation.

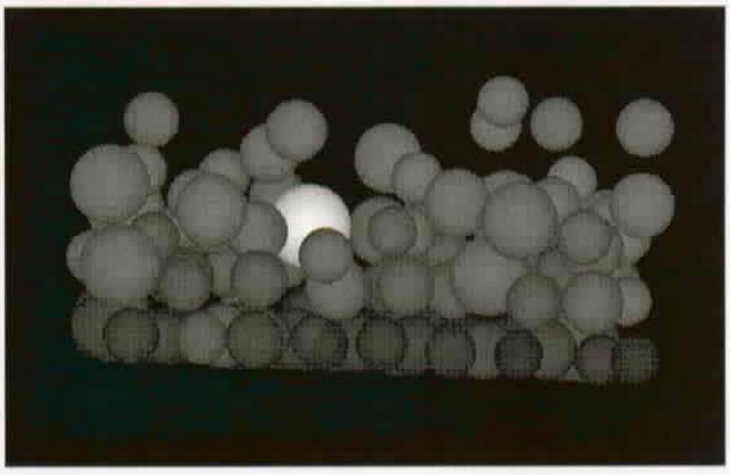

Figure 5.9: *Example of flow visualisation. The state vector $\Psi_i(t)$ is shown as a 3D plot of the particle assembly at a given event time point t_{ij}.*

5.3.2 The abs simulation routines

When looking upon the involved programs in some more detail, we firstly turn to the `abs` program, which is a collection of routines for initialisation and computation of a hard sphere granular flow. It is useful to explain the exact structure of input and output data before turning to the internal structure of the `abs` program.

Input - the `def.dat` - files

The `abs` program needs some flow parameters and numerical values as input. They are supported by the `def.dat` file, which can be edited by a little routine called `input`. The `def.dat` file consists of the following parameters:

- t_{max} is the maximum runtime of the modelling. If the granular model flow does not come to rest before, the `abs` program will terminate at t_{max};
- e is the longitudinal restitution coefficient of the spherical particles of which the flow consists;

- μ is the Coulomb coefficient of friction is supported here;
- b denotes the tangential restitution coefficient as defined in Equation (5.37);
- ϱ_{min} is the minimum density of a particle in kgm^{-3};
- ϱ_{max} is the maximum particle density. The particles i of the flow will have a random density distribution $\varrho_i \in [\varrho_{min}, \varrho_{max}]$;
- r_{min} is the minimum particle radius in m;
- r_{max} is the maximum particle radius in m . Particle radii r_i are randomly chosen from the interval $[r_{min}, r_{max}]$;
- v_{mean} denotes the initial mean velocity of the flow in x-, i.e. in downslope direction. The individual particle velocities are distributed in the interval

$$\begin{aligned}[0.9v_{mean}, 1.1v_{mean}] \times [-0.1v_{mean}, 0.1v_{mean}] \times \\ \times [-0.1v_{mean}, 0.1v_{mean}] \in \mathbf{R}^3,\end{aligned} \tag{5.42}$$

  so that in y and z- direction, there are some local velocity fluctuations but no mean motion;
- f_{factor} determines the time resolution of the stored flow data. The state vector $\Psi_i(t)$ is stored only after f_{factor} collisional events. Each event corresponds to a time step as explained in 6.31. If there is not a very fine time resolution of flow data required, this helps to save disc space;
- *box* is a structure containing information on the boundary conditions, which are represented by the inclined box with permeable walls and roughened bottom mentioned in 5.2.2.
  - box$\rightarrow l_x$ is the periodicity length in x-direction;
  - $box \rightarrow aspect\ ratio$ denotes the ratio $\frac{\text{periodicity length in } x- \text{ direction}}{\text{periodicity length in } y- \text{ direction}}$.
  - $box \rightarrow \psi$ is the slope angle, at which the box is inclined.

  - $box \rightarrow rough_1$, $box \rightarrow rough_2$ and $box \rightarrow rough_3$ correspond to the parameters b_x, b_y and c, which parametrisize the periodic function (equ. 5.21) for the modelling of bottom roughness.

- *name* is the file name in `e**b**m**.dat` format, under which the output of `abs` will be stored.

- ϵ_{ekin} is a lower bound of particle kinetic energy, below which a particle is regarded to be at rest. This parameter is needed to avoid inelastic collapse of the flow described by Luding & Mcnamara (1998).

- $\epsilon_{distance}$ and $\epsilon_{collision}$ are some lower bounds of computational accuracies needed for the numerical solution of 4th order Equation (5.7) governing flying-lying particle impact times.

- r_{ABS}: One single distinct particle normally is used as tracer in the model flow. It is normally used to follow the segregation-induced lifting of a larger particle in the granular model flow. For this purpose it is initially positioned at the bottom of the box before the flow starts.

- ϱ_{ABS} is the density of the tracer particle.

Output - the `e**b**m**.dat` - files

The data produced by the `abs` program related to a flow with a certain parameter set $\{e, b, \mu\}$ is stored in a `e**b**m**.dat` file, which consists of the state vectors $\Psi_i(t_{ev})$, $i = 0, \ldots, N$ of all N particles at distinct times

$t_{ev} \in [t_0; t_{max}]$ of the flow. The stored data has the following structure :

$$\begin{array}{c} \Psi_0(t_0 = 0) \\ \vdots \\ \Psi_N(t_0 = 0) \\ \vdots \\ \Psi_i(t_{ev}) \\ \vdots \\ \Psi_0(t_{max}) \\ \vdots \\ \Psi_N(t_{max}), \end{array} \tag{5.43}$$

where the state vector $\Psi_i(t_{ev})$ of one particle i at any event time point t_{ev} has the following components:

$$\Psi_i(t_{ev}) = (\mathbf{x}_i, \mathbf{v}_i, \mathbf{w}_i, r_i, \varrho_i, T_i, t_{ev}, \wp_i, \delta\mathbf{x}_i, \delta\mathbf{p}_i)\,, \tag{5.44}$$

The components of $\Psi_i(t)$ have the following meanings:

$\mathbf{x}_i$ is the position of particle i in the box coordinate system;

$\mathbf{v}_i$ is the velocity of particle i;

$\mathbf{w}_i$ denotes the rotational momentum of particle i;

r_i: radius of particle i;

ϱ_i: density of particle i;

T_i is the total kinetic energy of particle i:

$$T_i = \frac{1}{2}\left(\frac{4\pi}{3}\varrho_i r_i^3\left(\mathbf{v}_i^2 + \frac{2}{5}r_i^2\mathbf{w}_i^2\right)\right); \tag{5.45}$$

t_{ev} is the event time after f_{factor} events, where the state vector Ψ_i is saved;

$\wp_i$ is a boolean variable, which indicates whether particle i is involved in a collision with another particle or with the bottom at time point t_{ev}

$$\wp_i = \begin{cases} 0 & \text{particle } i \text{ is not involved in a collision} \\ 1 & \text{particle } i \text{ is involved in a collision.} \end{cases} \tag{5.46}$$

$\delta\mathbf{x}_i$: If $\wp_i = 1$, $\delta\mathbf{x}_i$ denotes the distance of the centers of particle i and the other particle involved in the collision. If $\wp_i = 0$, $\delta\mathbf{x}_i$ is not defined.

$\delta\mathbf{p_i}$ denotes the total momentum exchange at the contact point in case of a collision, i.e. in case of $\wp_i = 1$. If $\wp_i = 0$, $\delta\mathbf{p}_i$ is not defined.

The real data structure in the `e**b**m**.dat` files is slightly adjusted to the requirements of the evaluation and visualisation routines:

$$\Psi_i(t_{ev}) = (x_i, y_i, z_i, r_i, T_i, \wp_i, t_{ev}, v_{x,i}, v_{y,i}, v_{z,i}, \cdots \\ \cdots, w_{x,i}, w_{y,i}, w_{z,i}, \delta p_{x,i}, \delta p_{y,i}, \delta p_{z,i}, \delta x_{x,i}, \delta x_{y,i}, \delta x_{z,i}), \quad (5.47)$$

where x_i, y_i, z_i and $v_{x,i}, v_{y,i}, v_{z,i}$ denote the components of position and translational velocity vectors of particle i. The same index convention as for the translation velocity is valid for angular velocity as well as for momentum exchange and displacement to the colliding particle in case of collision.

A typical simulation of a monodisperse flow consisting of $N = 200$ equal sized spheres ($r_i = 0.18$ m for all particles) with parameters $\{e = 0.8$, $b = 0.7$ and $\mu = 0.4$ over a time interval $[0, 30$ s$]$ results in 980 stored time steps t_{ev}, where each f_{factor}=500 events occured before saving $\Psi_i(t_{ev})$. The total size of `e08b07m04.dat` is approximately 55 MB. This means, the total amount of data produced for this flow is 500×55 MB$\approx$ 27.5 GB. Anyway, the storage of data with f_{factor}=500 allows reasonable averaging in the evaluation routines at a moderate amount of disc memory. Evaluation of stress and strain tensors require a higher time resolution or lower value of f_{factor}, respectively.

Algorithms

The `abs` program is a collection of routines for preparing and carrying out the computation of a granular model flow. The routines are worked through in the following order, which shows the general course of `abs` :

```
{
        allocation();
        parameters();
        initialisation();
        t=0;
        while(t<=tmax){
                collision_times();
                tmin=next_collision();
                update_positions(tmin);
                administration();
                t+=tmin;
        }
}
```

The routine `allocation` prepares memory for the particle representation and for collisional time tables, `parameters` takes over the parameters for flow description from the `def.dat` input file. The initial particle assembly and the initial conditions of the flow are generated by the `initialisation` routine.

The flow itself is generated by a series of loops, each of them describing one single event and the collective particle motion in the time interval from the last until the current event: `collision_times` computes the time t_{ij} passing from the current time point t until collision for any particle pair ij, $i \neq j$, and the times t_{ii} until a wall event or bottom impact of each particle i and lies them down into a collisional time matrix $\mathtt{t_{ij}}$.

The routine `next_collision` determines the minimum t_{min} of $\mathtt{t_{ij}}$, which is the time until the next event in the flow occurs. `update_positions` integrates all particle trajectories from the current time t until the time point $t + t_{min}$ of the next event.

Finally, `administration` decides, whether the next event is a collision between two flying particles, between a flying and a lying particle, a wall event or a bottom impact of one particle. According to what kind of event has been detected, new linear and angular momenta of the involved particles after the event are computed then. After setting the current time to $t = t + t_{min}$, the

procedure starts again with searching and performing the next event.

In the following, closer look at the inner structure of the routines is provided:

allocation: In this routine, the memory for the representation of N particles is allocated where each particle is described by a `PARTICLE` data structure:

```
typedef struct{
    int i;          /* particle number i                          */
    int boxnumber;
    double r[3];    /* space coordinate                           */
    double v[3];    /* velocity                                   */
    double om[3];   /* spin                                       */
    double rho;     /* density of particle                        */
    double radius;  /* radius of particle                         */
    double mu;      /* Coulomb friction coefficient               */
    double e;       /* longitudinal restitution coefficient       */
    double b;       /* tangential restitution coefficient         */
    double ekin;    /* kinetic energy                             */
    double dp[3];   /* momentum transfer in case of collision     */
    double dr[3];   /* distance vector to other colliding particle */
    int state;      /* particle flying or lying ?                 */
} PARTICLE;
```

The `PARTICLE` data structure allows to assign individual material parameters to each particle.

Furthermore, the routine allocates memory for the collision time table t_{ij}, which contains the time until particles i and j , $i, j = 0, \ldots, N$ will collide. (The diagonal elements t_{ii} represent the time until particle i undergoes a wall event.) Times $t_{i,b}$ until impact of a particle i at the bottom are seperately saved in a bottom impact time list, for which also memory is allocated.

parameters reads in flow parameters provided by the `def.dat` file. The structure of `def.dat` is explained above. Furthermore, the routine opens an `e**b**m**.dat` file for writing of the flow state vector $\Psi_i(t)$.

initialisation: generates the initial particle assembly and the initial condi-

tions of the entire flow. The initial particle assembly is built by subsequently placing particles i, $i = 0, \ldots, N_{max}$ with radii $r_i \in [r_{min}, r_{max}]$ distributed at randomly chosen positions inside a region U_{start} inside the periodic box. If particle i does not fit inbetween the previously placed particles j, i.e. if

$$|\mathbf{x}_i - \mathbf{x}_j| > r_i \quad \forall\, i,j : j < i, \quad \mathbf{x}_i, \mathbf{x}_j \in U_{start} \tag{5.48}$$

is not satisfied, it is tried to fit it in by stepwise decreasing its radius, maximally down to $r_i = r_{min}$. If this does not succed in finally placing the particle, the procedure starts again with the same particle at another position $\mathbf{x}_i \in U_{start}$. Setting up the initial assembly is stopped if either the maximum number N_{max} of particles is placed or if more than n_{trial} successless attempts have been made to place one particle. Figures 5.10 and 5.11 show a particle size distributions and the related cumulative size distributions for two different sized start regions U_{start}. In one case, U_{start} is double as large as in the other case. For a starting region volume $V(U_{start}) = V_s$, the placing procedure is terminated after $n_{trial} = 10^4$ placing attempts and the related (cumulative) particle size distribution is dominated by the smaller particles.

The assymetry in the size distribution is due to the preference of smaller particles in the case of limited space $V(U_{start}) = V_s$. In the case of infinite assembly space $U_{start} \to [-\infty, \infty]^3$, a homogeneous particle size distribution would result. Increasing the volume of the start region to $V(U_{start}) = 2V_s$, the assembling ends with reaching the maximum particle number N_{max}, which, in this example, is $N_{max} = 200$. The assymetry of the distribution is a little bit flatter and the distribution shows a plateau of medium sized particles, which "survived" their placing without being downsized.

To ensure that there initially is at least one "large" particle in the near of the bottom, the assembling starts with the tracer particle $i = 0$, which has a radius $r_0 = r_{max}$ and is placed at the centerline of the box near the upslope wall. Condition (5.48) avoids particles to be in contact with each other at start of the flow, which would let the "event-driven" algorithm break down. The whole assembly is initially at rest or it is been given a mean initial

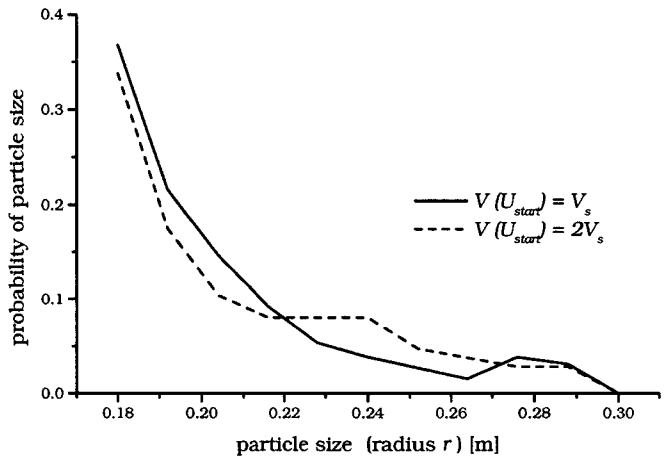

Figure 5.10: *Size distribution emerging from placing within different sized start regions U_{start} with volumes $V(U_{start}) = V_s$ and $V(U_{start}) = 2V_s$.*

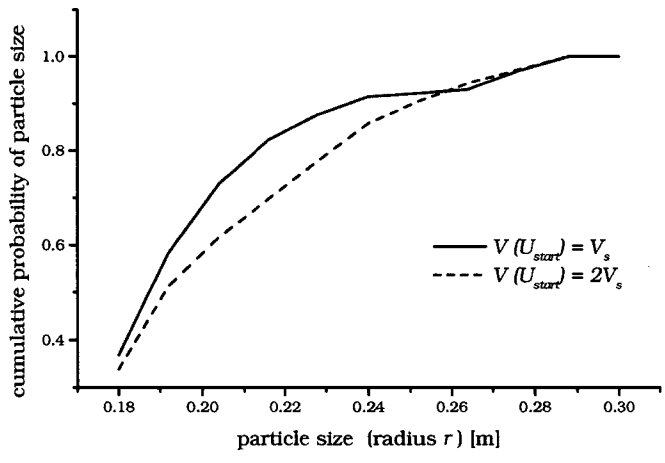

Figure 5.11: *Cumulative size distribution emerging from placing within different sized start regions U_{start} with volumes $V(U_{start}) = V_s$ and $V(U_{start}) = 2V_s$.*

velocity $\mathbf{v}_{mean}$ according to (5.42).

collision_times: This routine computes the times to the next event as described in section 6.31. Depending on the "state" s_i and s_j of the involved particles i and j, for any combination of i and j, $i, j = 0, \ldots, N$ the time to the next event is computed and stored in the collision time matrix t_{ij} or in the bottom impact time list $t_{i,b}$, respectively. The state s_i of particle i can either be 0 indicating that the particle is freely moving or 1 for a particle lying on the ground. As outlined in section 6.31, one distinguishes between different kinds of events:

$$i \neq j \quad \left\{ \begin{array}{lll} (s_i = 0) & \vee & (s_j = 0) \\ /((s_i = 0) & \vee & (s_j = 0)) \end{array} \right\} \text{ collision at } t_{ij} \tag{5.49}$$

$$i = j \quad (s_i = 0) \left\{ \begin{array}{l} \text{wall event at } t_{ii} \\ \text{bottom impact at } t_{i,b} \end{array} \right. \tag{5.50}$$

Collision between different particles $i \neq j$ can happen between two flying particles ($s_i = s_j = 0$), or between a flying and a lying particle, where one of the particles has state 1 and one has state 0. In the first case, the time t_{ij} until collision is the smaller positive root of the 2nd order equation (5.5), whereas t_{ij} for collision of a flying with a lying particle is determined as root of the 4th order equation (5.7).

If $i = j$, the next event is a single particle passing through a wall at time point t_{ii}. This time point is determined according to Equations (5.3)-(5.20) and stored in the event time table t_{ij}. Furthermore, the time $t_{i,b}$ until impact on the box bottom is computed (see Equ.5.14).

next_collision determines the minimum entry $t_{ij,min}$ of t_{ij}. The particles i_{next} and j_{next} corresponding to $t_{ij,min}$ are the next ones which collide. If $i_{next} = j_{next}$, the next event is a wall event or bottom impact. In this case, particle i passes a wall at time point $t_{ij,min} = t_{ii}$ or hits the ground at $t_{ij,min} = t_{i,b} < t_{ii}$. The minimum entry of the event time table is determined according to the simple rule :

$$\begin{aligned} &1.: \quad t_{ij,min} = \infty \\ &2.: \quad \forall i,j = 0,\ldots,N: \quad t_{ij} \leq t_{ij,min} \Longrightarrow t_{ij,min} = t_{ij}. \end{aligned} \tag{5.51}$$

update_positions traces all particle trajectories $\mathbf{x}_i(t)$ from the current time t until the time $t + t_{min}$ of the next event:

$$\mathbf{x}_i(t + t_{min}) = \mathbf{x}_i(t) + \mathbf{v}_i t_{min} + \frac{1}{2}\mathbf{g}t_{min}^2. \tag{5.52}$$

Before performing this update of particle positions, periodic boundary conditions (5.1) are applied to particles leaving the box through a wall. If f_{factor} time steps or events, respectively, have been performed before, the flow state vector $\Psi_i(t)$ (see Equ. 5.44) is saved to the `e**b**m**.dat` file in the shape described in Equation (5.47).

administration: Employing the states of the two particles i_{next} and j_{next} determined by `next_collision`, this routine decides, what kind of event is actually happening and carries it out:

- $i_{next} \neq j_{next}$, $s_{i_{next}} = s_{j_{next}} = 0$: A collision between two flying particles happens and the linear and angular momenta of the two colliding particles are computed according to Equation (5.32).

- $i_{next} \neq j_{next}$, $s_{i_{next}} \neq s_{j_{next}}$ describes a collision between a flying and a lying particle. Momenta after collision are computed the same way as for two flying particles. If the lying particle gains enough kinetic energy by the impact (more than ϵ_{ekin}), it can change into a freely moving one (with respect to geometrical constraints by the bottom and surrounding particles). On the other hand, if the particle, which collides with the lying one, has less than ϵ_{ekin} kinetic and potential energy, it changes its state into "lying" (i.e. $s = 1$). Introducing the energy constraint ϵ_{ekin} is neccessary to avoid the occurence of particles getting infinitely slow by subsequent collisions. In this case, collisional velocities would converge to zero by an infinite number of impacts with infinitely short time steps between them.

- $i_{next} = j_{next}$ is synonymous to a wall event, which has no influence on the momenta of particle i_{next}. In this case, just the periodic boundary

conditions are applied. The other meaning of $i_{next} = j_{next}$ is a bottom impact of particle i_{next}, which is treated as described in Equations (5.12), (5.13) and (5.32).

Limitations of the abs routines

Some principle and numerical constraints of the instantaneous binary collision mechanism in the **abs** program have to be taken into account.

Inelastic collapse: Slow particles come to rest due to an infinite number of subsequent inelastic bottom impacts with decreasing velocity and time steps. In this case, the algorithm needs an infinite number of computational time steps for an infinitely small real time intervall, where hardly any actual particle movement happens. This pathological behaviour can be avoided by introducing an energy bound ϵ_{ekin}, below which a particle is regarded to be at rest.

Mutual penetration of particles may occur in the course of simulation due to limited computational accuracy. If the collision time $t_{ij,min}$ of particles i and j is slightly overestimated due to computational inaccuracies, the particles will penetrate a little bit, before they get their new momenta after collision according to Equation (5.32). In this case, collision is treated as if the particles would not have been penetrating.

Once two spherical particles have penetrated each other, all collision time solutions of (5.5) and (5.7) lead to collisions of inner surfaces or of an inner and an outer surface of the particles – they are "linked" together. This link can be broken again, if at the next collision time of the concerned particles, they keep their momenta without being reflected "inside" and so can separate again.

Three-body-problem: the treatment of collisions in **abs** is based on the assumption of instantaneous binary particle interactions. This model mechanism can only handle the interaction of two particles. To deal with instantaneous interactions of more than two particles, contact forces between all the involved particles have to be numerically modelled, which can be done by soft sphere models as described in Section 4.4.1. This means, that the

process is considered as extended in time and has to be resolved into time steps. This, however, does not fit into the hard sphere model approach employed here. Fortunatedly, the constraint to binary interactions does not affect the behaviour of the regarded rapid collision dominated flows. Within computational accuracy, the used hard sphere model does not produce exactly instantaneous collisions between three or more particles.

The (extremely unlikely) case of an instantaneous 3-body interaction would result in penetration of the two particles, whose interaction is ignored by the binary collision mechanism. The penetration would then be treated as described above.

Problems arise on the treatment of particle collisions with a particle lying on the ground. This situation is an 3-body-problem, which can not properly be treated by the binary collision mechanism. In practice, this complication is circumvented by fixing lying particles i_{lying} in a vertical distance of $10^{-6} r_{i,lying}$ above the bottom. An impact of a flying particle then immediately is followed by a bottom event of the hit particle, if the latter has gained enough (i.e. more than ϵ_{ekin}) kinetic energy by the impact.

Of course, this description is only a very raw picture of what actually happens physically. Also deposition and erosion of granular material cannot satisfactorily be modelled, because one always has to avoid instantaneous contact of more than two particles, which, on the other hand, is a generic property of erosional and depositional processes.

5.3.3 The evaluation routines

The flow data produced and stored in `e**b**m**.dat` files by the `abs` routines must be visualised or statistically processed to provide qualitative and quantitative information about global flow and segregational behaviour. The `evalcont` program routines perform statistical evaluations of time dependent flow state vectors $\Psi_i(t_{ev})$. After explaining the structure of `evalcont` input and output, the internal program structure will be described in detail. Finally, this subsection provides an insight into the mechanism of flow data visualisation.

Averaging - the `evalcont` routines

The `evalcont` program reads the `e**b**m**.dat` files, which have been generated by the `abs` program and performs spatial and time averaging of measures connected with particle motion:

For n_{av} equidistant time points, `evalcont` computes height dependent profiles of mean quantities and their standard deviations. This is done by averaging the concerning quantities over all particles i contained in a flow layer l with thickness δh during the averaging time interval. This means, that the averaging is performed over all particles i which have vertical positions

$$z_i \in [h_l, h_l + \delta h] \tag{5.53}$$

during the averaging time interval

$$[t_n, t_n + t_{av}]. \tag{5.54}$$

For determination of global flow behaviour, single particle motions are averaged over the entire flow height and over a time window t_{win}, which is subsequently moved over the whole flow duration with a step width Δt_{fl}.

Input

The `evalcont` routines need the following input parameters, which are promted for by the program itself:

- t_0: event time point, where the statistical evaluation starts.
- t_{end}: event time point, where statistical evaluation ends.
- n_{av}: number of evaluations in the time interval $[t_0, t_{end}]$.
- t_{av}: width of time window for the computation of profiles of mean quantities.
- Δt_{fl}: time step for the computation of the mean time dependent flow behaviour.

- t_{win}: time window for computation of mean flow behaviour over the time window $[t_k, t_k + t_{win}[$ beginning at any time step t_k with $t_{k+1} = t_k + \Delta t_{fl}$.

Output

The averaged flow measures are stored in result files "`e**b**m** ***t***.***`", which are labelled by the file name extensions `.***` in the way lined out in Section 5.3.1. The obtained averaged measures ζ are of scalar, vectorial or tensorial structure :

scalar : particle energy (extension `.eny`), particle radius (extension `.rad`) and particle number density (extension `.den`).

vectorial : velocity (extension `.vau`) and angular velocity (extension `.spn`).

tensorial : stress (extension `.sig`) and strain rate (extension `.dij`).

The common structure of the output files is the one of height-dependent profiles of each averaged measure ζ :

$$n_l \quad h_l \quad <\zeta>_l \quad S_l^2(\zeta), \tag{5.55}$$

where the flow height is accounted for by the index l as depicted in Figure 5.12.

Averaging is performed over all particles with their centers in a flow layer with thicknes δh. Flow layers are labeled by the index l as shown in figure 5.12. In flow layer l, the averaging is performed over a time interval t_{av} including n_l particles i having vertical positions $z_i \in [h_l, h_l + \delta h[$, where $h_l = l\delta h$. The average of measure ζ in flow layer l is denoted by $<\zeta>_l$ and $S_l^2(\zeta)$ is the 2nd order structure function or, respectively, the square of the standard deviation of ζ:

$$\langle\zeta\rangle_l := \frac{1}{n_l}\sum_{i=0}^{n_l}\zeta_i, \tag{5.56}$$

$$S_l^2(\zeta) := \langle(\zeta - \langle\zeta\rangle)_l^2\rangle \tag{5.57}$$

$$= 2(\langle\zeta^2\rangle_l - \langle\zeta\rangle_l^2). \tag{5.58}$$

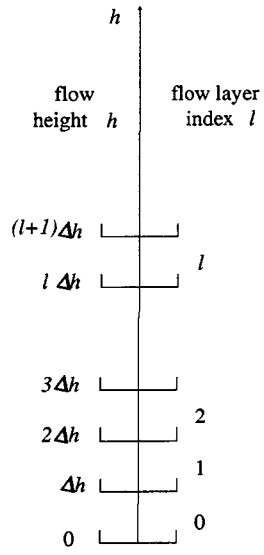

Figure 5.12: *Indexing of flow layers*

Within the frame sketched above, the structures of the output files vary, depending on the currently treated measure. In the following, an overview over output file structures is provided. All averagings $\langle\zeta\rangle_l$ are performed over the current flow layer l:

.vau files: they contain the mean flow velocity profiles $\langle\mathbf{v}\rangle_l$ in the form (5.55). A line of the velocity profile file corresponding to the flow layer l (see fig 5.12) then looks like this:

$$n_l \quad h_l \quad \langle v_x\rangle_l \quad S_l^2(v_x) \quad \langle v_y\rangle_l \quad S_l^2(v_y) \quad \langle v_z\rangle_l \quad S_l^2(v_z). \tag{5.59}$$

.eny files: the mean particle energy profiles are written as

$$\begin{aligned} n_l \quad h_l \quad \langle T\rangle_l \quad S_l^2(T) \quad \langle T_{trans}\rangle_l \quad S_l^2(T_{trans}) \quad \langle T_{rot}\rangle_l \ldots \\ \ldots \quad S_l^2(T_{rot}) \quad \langle V_{pot}\rangle_l \quad S_l^2(V_{pot}) \quad \langle E\rangle_l \quad S_l^2(E). \end{aligned} \tag{5.60}$$

The mean translational and rotational kinetic particle energies are denoted by $\langle T_{trans}\rangle_l$ and $\langle T_{rot}\rangle_l$, respectively, $\langle T\rangle_l$ is the total mean particle kinetic, $\langle V_{pot}\rangle_l$ the mean particle potential energy and, finally, $\langle E\rangle_l$ is the mean total particle energy.

.spn files: mean particle angular rotational velocities **w** are averaged and stored in the same form as the linear velocities:

$$n_l \quad h_l \quad \langle w_x \rangle_l \quad S_l^2(w_x) \quad \langle w_y \rangle_l \quad S_l^2(w_y) \quad \langle w_z \rangle_l \quad S_l^2(w_z). \tag{5.61}$$

.den files: mean particle solid densities $\langle \varrho_p \rangle_l$ and particle number densities $\nu_l = \frac{n_l}{l_x l_y \delta h}$ are grouped in this order:

$$n_l \quad h_l \quad \nu_l \quad \langle \varrho_p \rangle_l \quad S_l^2(\varrho_p). \tag{5.62}$$

.rad files: besides the mean radius $\langle r \rangle_l$ and the 2nd order Structure function $S_l^2(r)$ in each flow layer l, the **.rad** file contains additional information about the size distribution in the granular flow. Particle radii $r \in [r_{min}, r_{max}]$ are divided into ten classes $r_q = \{r : r \in [r_q, r_{q+1}[\}$ with $q = 0, \ldots, 10$ and $r_{q+1} = r_q + \Delta r$, where $\Delta r = \frac{r_{max} - r_{min}}{10}$, $r_0 = r_{min}$ and $r_{10} = r_{max}$.

The number of particles in the entire flow belonging to class q is n_r^q, the number of particles of class q in flow layer l is $n_{r,l}^q$. With n_l the total number of particles in flow layer l, one line of the radius profile data file represents flow layer l in the following form :

$$n_l \quad h_l \quad \frac{n_{r,l}^0}{n_r^0} \quad \frac{n_{r,l}^0}{n_l} \quad \ldots \quad \frac{n_{r,l}^{10}}{n_r^{10}} \quad \frac{n_{r,l}^{10}}{n_l} \quad \langle r \rangle_l \quad S_l^2(r). \tag{5.63}$$

.sig files contain the averaged stress tensors $\sigma_{ij} := k_i \delta p_j D_l$, where **k** denotes the unit vector in the direction of the connecting line of two colliding particles, δ**p** is the total momentum exchanged between the colliding particles (see equ. 5.27). D_l is the part of the line connecting colliding particles, which is lying in layer l.

The 2nd invariant σ_{II} of σ_{ij} is defined as $\sigma_{II} := \frac{1}{2}\sigma_{ij}^2$. The averaging here is performed only over particles, which are involved in a collision, with their centers lying in layer l. To get a sufficient number of colliding particles for averaging, the amount of data provided by saving the flow state vectors each f_{factor} events may not be sufficient for high values of f_{factor}. This parameter should be decreased then to ensure proper averaging. Finally, the data structure of the **.sig** file looks like

$$n_{l,col} \quad h_l \quad \langle \sigma_{II} \rangle_{l,col} \quad \langle \sigma_{ij} \rangle_{l,col}, \quad i,j = 1,2,3. \tag{5.64}$$

`dij` files: in continuum dynamics, the strain rate tensor D_{ij} usually is defined as $D_{ij} := \frac{1}{2}(\partial_i v_j + \partial_j v_i)$. For averaging this measure over a flow layer l, we compute the ratio of velocity difference components and displacement vector components of any particle pair (m, n) in the flow layer: $\partial_i v_j \approx \langle \frac{v_{i,m} - v_{i,n}}{x_{j,m} - x_{j,n}} \rangle_l$, where the suffix $_{i,m}$ is related to the ith component of the velocity or spatial vector of particle m. The data structure of `.dij` files is similar to the one of `.sig` files :

$$n_{l,col} \quad h_l \quad \langle D_{II} \rangle_l \quad \langle D_{ij} \rangle_l \quad i,j = 1,2,3. \tag{5.65}$$

Time dependent global flow measures are saved in `.tev` files, which have a special structure. Instead of height dependent flow profiles at distinct time, the global flow behaviour averaged over the whole flow height is traced over the entire duration of the flow. Averaging $\langle \cdot \rangle_{flow}$ is performed over a time window t_{win}, which is moved over the time axis of the flow with steps Δt_{fl}. Speaking differently, particle properties are averaged for all particle state vectors $\Psi_i(t)$ with $t \in [t_k, t_k + t_{win}[$ where $t_{k+1} = t_k + \Delta t_{fl}$. The structure of a `.tev-` file data line corresponding to a time step t_k is as follows :

$$\begin{aligned} t_k \quad \langle v_x \rangle_{flow} \quad S^2_{flow}(v_x) \quad \langle v_{x,max} \rangle_{flow} \quad \langle T_{trans} \rangle_{flow} \quad \langle T_{rot} \rangle_{flow} \cdots \\ \cdots \langle T \rangle_{flow} \quad \langle E \rangle_{flow} \quad \langle \nu \rangle_{flow} \quad \langle \varrho_p \rangle_{flow} \quad h_{max}, h_{ABS}, \end{aligned} \tag{5.66}$$

where t_k is the time point, at which the averaging time window starts, $\langle v_x \rangle_{flow}$ is the mean downslope flow velocity averaged over the whole flow height, $S^2_{flow}(v_x)$ is the 2nd order structure function (i.e. the square of standard deviation) of v_x and $v_{x,max}$ is the maximum downslope particle velocity occuring in the flow during the averaging interval $[t_k, t_k + t_{win}]$. The mean translational and rotational kinetic particle energies are denoted by $\langle T_{trans} \rangle_{flow}$ and $\langle T_{rot} \rangle_{flow}$, respectively. $\langle T \rangle_{flow}$ is the total mean particle kinetic energy and, finally, $\langle E \rangle_{flow}$ is the mean total particle energy. Furthermore, $\langle \nu \rangle_{flow}$ and $\langle \varrho_p \rangle_{flow}$ are the mean particle number density of the flow and the mean particle density. The maximum flow height is saved as h_{max}, h_{ABS} is the vertical position of the tracer particle.

Algorithms

To gain an idea of the course of the statistical data evaluation, we consider the order in which the evaluation routines are worked through and what kind of operations are performed inside each of them:

```
{
input();
start=tstart;
end=tstart+tavr;
deltat=(tend-tstart)/avrtms;
if ((fdatpointer=fopen(datname,"r"))==NULL) {
        printf("cannot open file %s \n", datname);
        exit(1);}
while (end<=tend)
{
        offs=data_location();
        hmaxval=hmax(offs,length);
        maxindex=mindex(hmaxval,deltah);
        if (!allocation(maxindex))
                printf("\n allocation failure \n");
        evaluate(offs);
        write_data();
        start+=deltat;
        end+=deltat;
}
timevol();
}
```

In the first seven lines of the `evalcont` program code, after prompting for the input parameters by the the `input()` routine, start and end time points `tstart` and `tend` for mean flow profile computations are fixed. The spacing between the computation time points for the mean profiles is called `deltat` where `avrtms` is the number of profiles computed within this time interval. Furthermore, the `.dat` file, which provides the flow data to be evaluated, is opened.

The following `while` loop is passed through for each computation time in-

terval [start, end], with end =start + tavr; tavr corresponds to the averaging time interval t_{av}, start is the program code equivalent to t_n (see fig. 5.13).

Firstly, the routine data_location searches the first state vector $\Psi_0(t_n)$, which has the time component t=start in the flow data file.

As next step, the routine hmax subsequently reads the vertical components of the position vectors of all particles. That means, that the vertical position z_i is extracted from all state vectors $\Psi_i(t)$ with $i = 0, \cdots, N$ and $t \in [t_n, t_n + t_{av}]$ or $t \in$ [start, end], respectively. The maximum particle flight height h_{max} during the averaging time interval is simply determined by

$$z_i \geq h_{max} \quad \Longrightarrow h_{max} = z_i, \tag{5.67}$$

where the start value of h_{max} is $h_{max} = 0$. The standard flow layer thickness is $\delta h = \frac{h_{max}}{20}$ or deltah = hmaxval/20.0, respectively, in programming code notation.

The indexing of flow layers is done by the mindex routine. The program code line

```
maxindex=mindex(hmaxval,deltah);
```

associates a flow layer with thickness δh or deltah respectively, to the "highest" particle determined before according to the labelling rules depicted in Figure 5.12. The uppermost flow layer determined this way gets the index l_{max} or maxindex, respectively.

In the allocation routine , memory space is allocated for a (maxindex+1)-dimensional data structure of type "SUITCASE", which is called "bag":

```
bag=(SUITCASE*)malloc(sizeof(SUITCASE)*(maxindex+1));
```

Each dimension of "bag" corresponds to a flow layer indexed by the flow layer index l or hindex, respectively. The bag variable contains the mean values of all flow measures ζ. For example,

```
bag[hindex].vxmean[1]=bag[hindex].vxmean[0]/bag[hindex].memberno
```

is the mean value of downslope velocity in flow layer hindex, where

`bag[hindex].memberno` is the current number of particles in flow layer `hindex`.

The `evaluate` routine subsequently reads in all particle state vectors $\Psi_i(t)$ with $t \in [t_n, t_n + t_{av}]$ or, in code notation, $t \in$ `[start, end]`. Figure 5.13 depicts the definition of averaging times. Each particle represented by a Ψ_i state vector gets a flow layer index l (`hindex`) according to its vertical position z_i and the indexing convention defined in Figure 5.12. When a

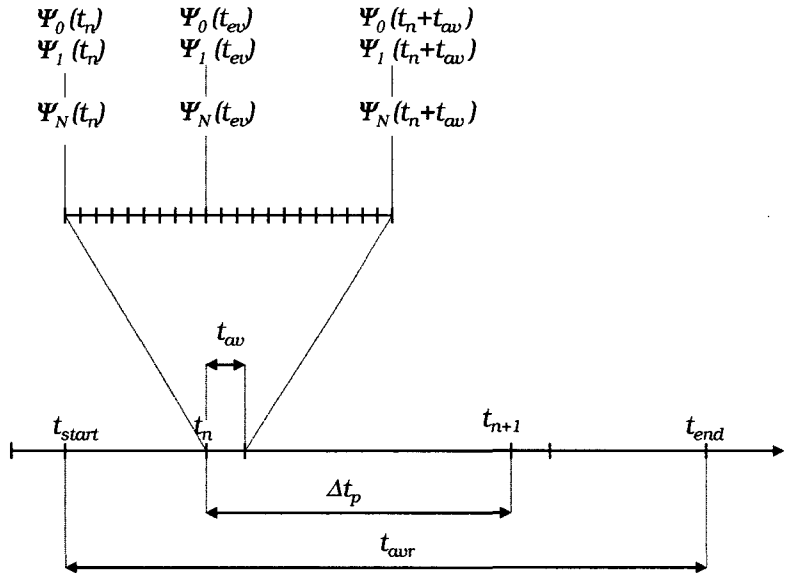

Figure 5.13: *Averaging times for flow layer averaging.*

particle is joining flow layer l, the particle number n_l in layer l is increased by one :

`bag[hindex].memberno++.`

The averaging in layer l or `hindex` now is done by adding the interesting particle measure to the sum of this measure from all particles, that joined the flow layer before and dividing this sum by the current (just actualized) particle number `bag[hindex].memberno`. The following example shows this averaging procedure for the downslope velocity component v_x:

```
bag[hindex].vxmean[0]+=vau[0];
```

```
bag[hindex].vxmean[1]=bag[hindex].vxmean[0]/bag[hindex].memberno;
bag[hindex].vxmean[2]+=vau[0]*vau[0];
bag[hindex].vxmean[3]=bag[hindex].vxmean[2]/bag[hindex].memberno-
        -bag[hindex].vxmean[1]*bag[hindex].vxmean[1];
```

The `[0]` component of `bag[hindex].vxmean` is the sum of downslope velocities of all particles having been associated to layer `hindex` before including the velocity of the "new" particle. The averaging is done by division by the current number `bag[hindex].memberno` of particles in the flow layer. So `bag[hindex].vxmean[1]` is the current average downslope velocity $\langle v_x \rangle_l$ in flow layer l. The `[2]` component is the sum of downslope velocity squares, and, finally, the `[3]` component represents the 2nd order structure function of velocity fluctuations or, respectively, the square of standard deviation of mean downslope velocities according to Equation (5.56).

After passing through all particle state vectors $\Psi_i(t)$ with $t \in [t_n, t_n + t_{av}]$, the `bag` structure finally contains the mean values and squares of standard deviations of all particle measures, averaged over all flow layers during the time interval $[t_n, t_n + t_{av}]$.

After finishing averaging, the results contained in `bag` are written into the result files in the form explained before. Then the `bag` structure is reset and the evaluation loop starts again at the beginning $t_{n+1} = t_n + \Delta t$ of the next time window: `start+=deltat; end+=deltat`.

Time-dependent evaluation of global flow behaviour follows, in principle, the same course as the computation of flow layer averages. The only difference lies in the interpretation of the entire flow as one flow layer, which has the special index `maxindex+1`. Averaging is, as shown in Figure 5.14, performed over time intervals $[t_k, t_k + t_{win}]$, where $t_{k+1} = t_k + \Delta t_{fl}$, with $k \in \mathbf{N} : t_k \in [t_{start}, t_{end}]$. For each t_k an entry in the shape of (5.66) is written into the `.tev` file.

Visualisation

The visualisation of the flow data in the `e**b**m**.dat` files is done by an AVS^{TM}network supplemented by a "handwritten" routine, which converts

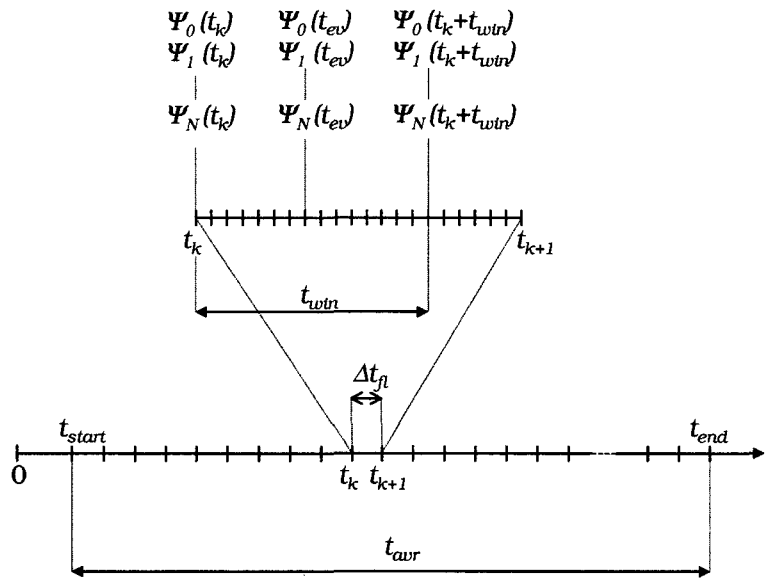

Figure 5.14: *Averaging times for tracing of mean global flow behaviour*

particle positions $\mathbf{x}_i$, particle radii r_i and particle kinetic energies $T_{kin,i}$ into the internal AVS data format. This permits the AVS network called `buntvis` to build a 3D picture of particles i with radii r_i at positions $\mathbf{x}_i$. An example for such a flow picture is given in Figure 5.9.

The particle kinetic energies are encoded by the appearing particle colours. The red, green and blue values for particle colours range from 0 to 1. In the display of the flow particles, the green value is fixed to 0, the blue value to 1. The red value of particle i is a mapping of its kinetic energy $T_{kin,i} \in [0, \infty[$ to the interval $[0, 1[$:

$$\xi_{red} = \frac{2}{\pi} \arctan\left(\frac{T_{kin,i}}{\varsigma_{colour}\xi_{red}}\right), \tag{5.68}$$

where $\xi_{red} \in [0, 1[$ is the red colour factor and ς_{colour} is a scaling factor for the kinetic particle energy. According to (5.68), particles with low kinetic energy appear blue, high energetic particles are displayed violet. The nonlinear mapping by the arctan function emphasizes the transition from slower to faster particles in energy ranges according to the selection of the scaling factor ς_{colour}. Colliding particles, i.e. particles i with $\wp_i = 1$ are displayed

white, i.e. red, green and blue colour values are each set to 1. The tracer particle "0" is an exception of this colouring convention, for it is always displayed as a white one.

A current flow picture at an event time point t_{ev} is built by reading the positions $\mathbf{x}_i$ of all particles $i, i = 0, \ldots, N$ and radii r_i from the according particle state vectors $\Psi_i(t_{ev})$ and converting them into a picture. By subsequently producing such pictures for all event time points stored in the `.dat` file, an animation of the particle flow is obtained. Additionally, at each event time point the visualisation routine allows to extract and save the current flow picture to a postscript file.

5.4 Numerical results

In this section, results of the numerical hard sphere model are presented and discussed. After shortly describing qualitative observations of the global and segregational flow behaviour, parametrical dependencies of flow measures and segregational flow behaviour are reported. Finally, two attempts to describe aspects of the model in terms of hydrodynamical and stochastic concepts are demonstrated.

5.4.1 Qualitative views

As explained in Section 5.3.3, the granular model flow data can be converted into a 3D graph displaying positions and size of each spherical particle at each time of the flow. Plotting all particle positions at subsequent times allows direct visual observation of the time evolution of the flow. Qualitative behaviour of the flow as accelerating or decelerating is observable as well as the formation of a kind of gas state or the flow coming to rest.

Furthermore, graphical flow display provides a tool for flow model development, helping to detect violations of boundary conditions and giving a sensual impression of principle limitations of the used hard sphere model. Savage & Lun (1988) have suggested two principle mechanisms governing segregational behaviour in gravity currents of granular media.

On one hand, "random sieving" is responsible for the diffusion of smaller particles through randomly forming voids between the flowing (and fluctuating) granular particles to lower flow layers.

On the other hand, larger particles are squeezed out of lower flow layers due to imbalance of powers exerted by other, smaller particles colliding with the larger ones. These effects were directly visible by graphically displaying the time evolution of the positions of the particles participating in the flow. In the following, some examples of visual observations are given.

Accelerating - decelerating

Depending on restitution and friction coefficients e, b and μ of the involved particles and on the slope angle ψ, the model granular flow shows global accelerating and decelerating behaviour. If the energy dissipation provided by particle inelasticity (described by the restitution coefficients e and b) and friction is too low to balance the downslope acceleration, a dilute gas state evolves in which the vertical collisional momentum transport is balanced by gravity.

Otherwise, a high dissipation rate corresponding to low particle restitution coefficients and high Coulomb friction causes deceleration of the flow and increasing particle density until standstill. Figures 5.15, 5.16 and 5.17 show the evolution of decelerating and accelerating flows from the same initial configuration.

Detection of problems

During development of the program code of the granular model, problems caused by not properly implemented boundary conditions could be easily detected by visualisation: particles "escaped" from the periodic boundary box. Also problems with the inelastic collapse and mutal penetration, mentioned in 5.3.2, were identified by direct visual observation. In the case of inelastic collapse, there was no visible change in the particle positions even after a large number of time steps. Mutual penetration is directly visible in the graphical flow representation.

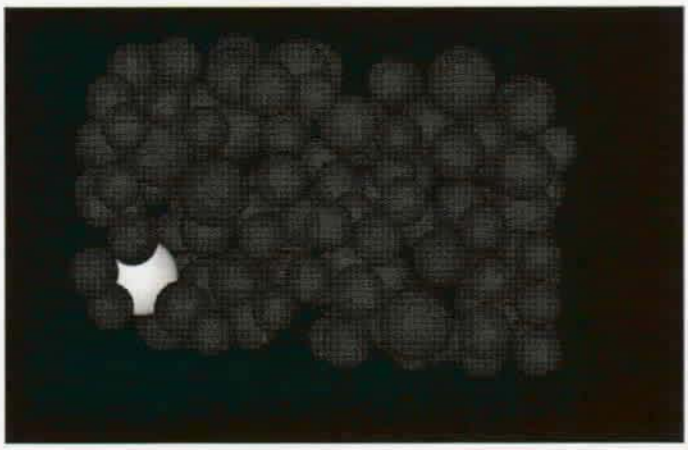

Figure 5.15: *Initial state of granular model flow.*

Figure 5.16: *Decelerating flow after 2.675 s running time. Particle material parameters are e=0.7, b=0.4, μ=0.6.*

Figure 5.17: *An accelerating flow reaches a dilute gas-like state. Picture of model flow after 79 s of running time. Particle material parameters are e=0.8, b=0.8, μ=0.4.*

Random sieving

Comparing the graphical representation of the initial particle configuration of a 130 particle granular sphere flow with parameters $e = 0.8$, $b = 0.6$ and $\mu = 0.5$ with the flow state after some (real) flow time, one can observe indications of inverse grading: the initial state is a homogeneous mixture of different sized particles with a defined size distribution. Note, that the initial state does not represent the closest packing, but there is some space left between the particles. Releasing this configuration down the inclined plane, the particles settle, and, by gain of potential energy while settling, accelerate in downslope direction. Fluctuations of relative particle positions form random voids, which are necessary for the sieve effect. Indeed, the picture displayed in Figure 5.18, which was taken after 10 s running time, shows an accumulation of smaller particles near the base of the model flow.

Squeeze expulsion

The squeeze expulsion process is contemplementary to random sieving; it is responsible for the movement of larger particles to higher flow layers. For observation of squeeze expulsion, we start with a developped flow state of equal-sized (r=0.18 m) particles, between which a large particle (r=0.3 m) is placed at the bottom. After 10 s of running time, the large particle can be seen riding on the next higher flow layer: it must have been squeezed out of the bottom layer. Indeed, regarding the corresponding elevation time series of the large particles, the particle has changed its flow height nearly instantly, where the amount of of this flow height change is corresponding to one (small) particle diameter.

Summarizing, the direct visual observation allows to watch generic qualitative flow behaviour and is also a helpful tool for detection of principle and numerical problems within the numerical hard-sphere granular model.

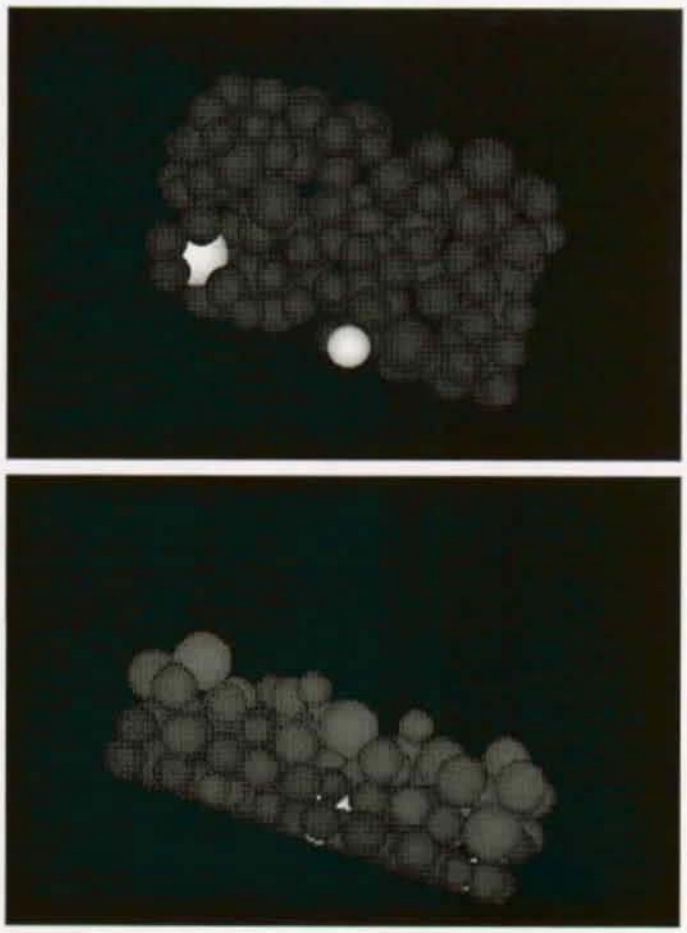

Figure 5.18: *Initial particle configuration (upper picture) and flow shape after 10s of (real) flowing time (lower picture) with accumulation of smaller particles near the bottom of the periodic boundary box.*

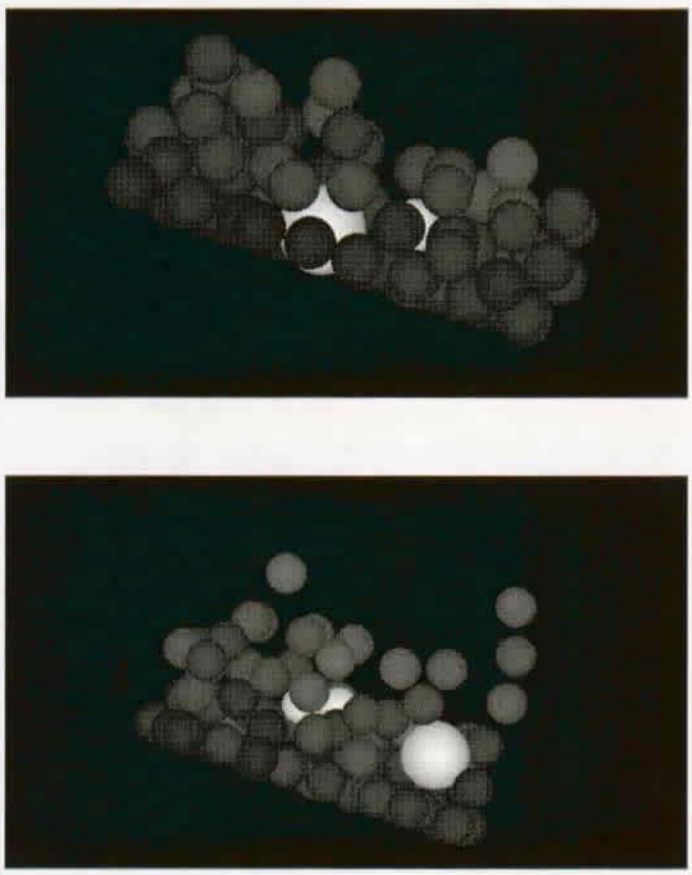

Figure 5.19: *Initial particle configuration (upper picture) and flow shape after 10s of (real) flowing time (lower picture) with large particle squeezed out of the lowest flow layer.*

5.4.2 Quantitative investigations

In order to characterize global flow and segregational behaviour of the used model and its dependencies from single particle material parameters, the model output was statistically evaluated as described in 5.3.3. The current section gives a comprehensive overview over the results of this model flow analysis. The measures used to characterize the flow were

- mean downslope flow velocity $\langle v_x \rangle$
- particle number density ν as defined in Equation (5.62)
- flow height of the tracer particle: h_{ABS}
- mean particle size profiles $\langle r(h) \rangle$
- mean particle velocity profiles $\langle \mathbf{v}(h) \rangle$
- mean deformation rate
- mean stress

It was investigated, how these characteristic flow measures are influenced by variation of the following flow parameters:

- single particle material parameters e, b and μ
- slope angle ψ
- density of the tracer particle: ρ_{ABS}
- boundary conditions: box dimensions, impermeable rear box wall
- initial conditions: initial particle number density and mean downslope velocity $\langle v_{x,0} \rangle$

Of course, not all measure's dependencies from each flow parameter are shown in the following. We will confine to those measures, which are most appropriate to display the reaction of the flow to variation of the currently investigated parameter.

If not explicitly mentioned to be different, the following parameters have been used as input for the modelling (their meanings are explained in section 5.3.2):

- t_{max}=100 s
- e : varied parameter
- μ : varied parameter
- b : varied parameter
- $\varrho_{min} = \varrho_{max} = 400\frac{\text{kg}}{\text{m}^3}$: all particles have the same density.
- r_{min}=0.18m
- r_{max}=0.3m
- v_{mean}=0 : Start of particle flow from rest
- f_{factor}=500
- $box \rightarrow l_x$=4m
- $box \rightarrow aspect\ ratio$=0.5
- $box \rightarrow \psi$=0.5
- $box \rightarrow rough_1$=10
- $box \rightarrow rough_2$=1
- $box \rightarrow rough_3$=1
- *name* variable file name in `e**b**m**.dat` format.
- ϵ_{ekin}=0.1
- $\epsilon_{distance}$= 0.1
- $\epsilon_{collision}$ = 0.01
- r_{ABS}=0.3
- ϱ_{ABS}= $400\frac{\text{kg}}{\text{m}^3}$

Dependency of flow behaviour from the longitudinal restitution coefficient e

(a) mean downslope flow velocity $\langle v_x \rangle$

The global accelerating or decelerating behaviour of the granular model flow can be traced by its mean downslope velocity $\langle v_x(t) \rangle$, where the averaging is performed over all particles participating in the flow according to (5.66).

Low values of of the longitudinal restitution coefficient e cause high translational kinetic energy dissipation $\Delta T_{diss} \sim (1-e)^2$ at each particle collision. For this reason, flows with low e come to rest after some running time, which is increasing with e (see fig. 5.20). On the other hand, high e values correspond to low translational kinetic energy loss by dissipation and, accordingly, result in an accelerating flow.

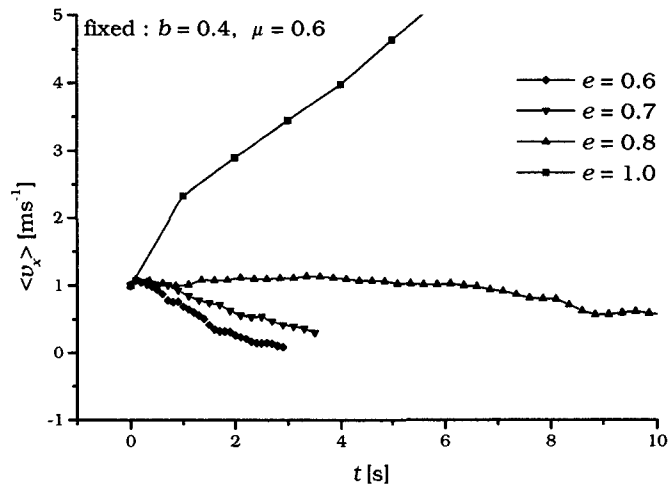

Figure 5.20: *Variation of time development of mean downslope velocity by change of longitudinal restitution coefficient e with fixed parameter values for b and μ. Example shown for fixed values $b = 0.4$ and $\mu = 0.6$.*

(b) Downslope velocity profiles $v_x(h)$

The influence of variation of e can also be observed regarding depth profiles $v_x(h)$ of downslope velocity taken after $\frac{2}{3}$ of total running time, as shown in Figure 5.21.

For $e = 0.7$, the flow will come to rest. After $\frac{2}{3}$ of total running time, the flow is very compact and the lower flow layers show an uniform velocity close to zero as depicted in Figure 5.21 a). Only the upper flow layers have preserved a linear increase of velocity with height.

Figure 5.21 b) shows a more dilute, steady flow state corresponding to $e = 0.8$, which displays a nearly linear velocity profile with a mean value of approximately $5ms^{-1}$. Also this flow finally comes to rest after 15s running time by slight deceleration.

Finally, a value of $e = 1.0$ provides no dissipation of longitudinal translational kinetic energy and so produces a continuously accelerating flow with decreasing particle number density (see Figure 5.21 c)). While the lower flow layers are influenced by bottom roughness and show some shear effect, the upper, more gas-like flow layer has a more uniform structure.

(c) Mean particle number density

Starting in each case from an identical initial particle configuration at rest with a normalized particle number density $\nu = 1$, the influence of the longitudinal restitution coefficient e on global flow behaviour also is reflected in the time development of mean particle number density of the flow as shown in Figure 5.22.

For $e = 0.7$ and $e = 0.8$ the particle number density ν increases with time.

Note that there does not exist a general final particle number density for the flow coming to rest in the frame of the present model. This is due to the fact that the used hard sphere model in principle cannot describe a close packing of particles being equivalent to instantaneous interaction of (much) more than two particles. In the current model simulation, the flow computation stops, if more than 10 instaneous interactions have occured.

For $e = 1.0$, which is equivalent to a continuously acelerating flow, the mean particle number density is decreasing with time corresponding to increasing flow height with a growing gas-like, dilute layer.

(d) Change of mean particle size profiles by variation of e: Onset of inverse grading

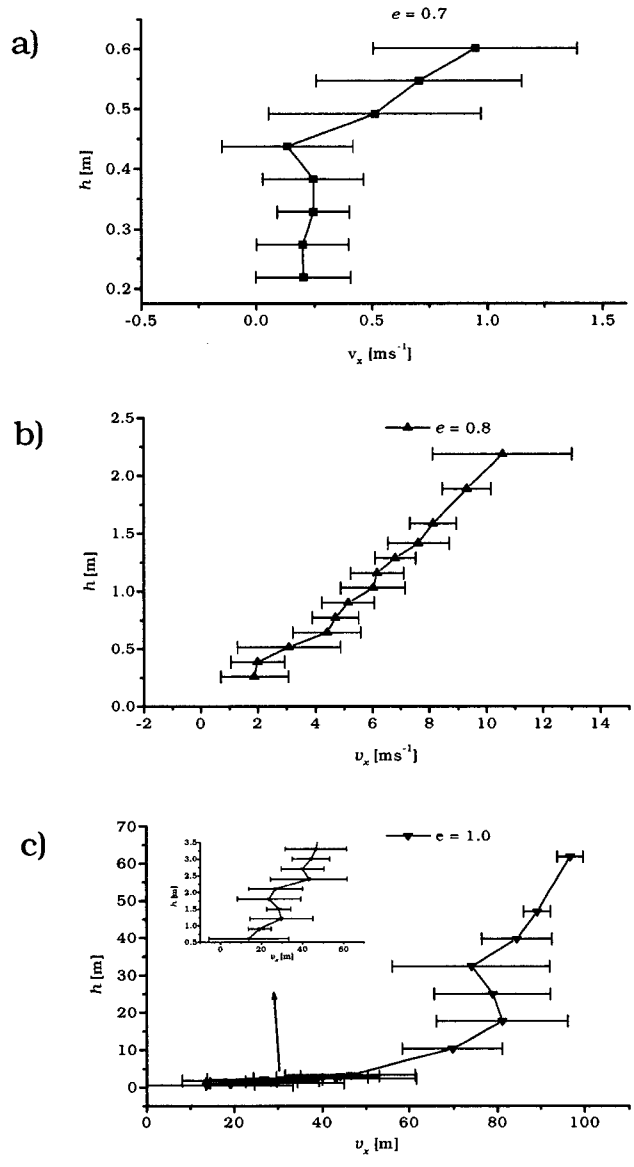

Figure 5.21: *Variation of e causes change of downslope velocity profile shape $v_x(h)$. Decelerating flow ($e = 0.7$, plot a)) has a uniform velocity near the bottom, accelerating flow ($e = 1.0$, plot c)) is uniform in upper, gas-like flow regions. The nearly steady flow for $e = 0.8$ has a nearly linear flow profile, as shown in plot b).*

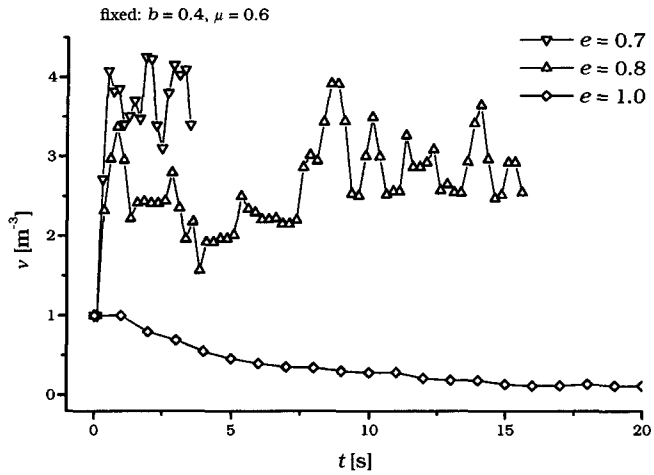

Figure 5.22: *Time evolution of mean particle number density ν parametrisized by longitudinal particle restitution coefficient e with fixed parameters b and μ. Example shown: $b = 0.4$ and $\mu = 0.6$.*

Comparing the mean particle size profiles of model flows with $e = 0.7$ and $e = 0.8$, and fixed values of the other particle material parameters b and μ, after $\frac{2}{3}$ of total running time one can observe a qualitative difference (see fig. 5.23).

While for $e = 0.7$, larger particles have accumulated near the bottom in a compact flow, the profile for $e = 0.8$ shows the maximum mean particle size in a higher flow layer. The uppermost flow layers in this case are too dilute to provide enough vertical forces acting on the large particles by collisions of other particles, so that the maximum of particle size does develop more in the mid than in the top layers of the segregating flow.

The qualitative difference between segregating and not segregating flow can also be observed in the time development of the mean particle size profiles (fig. 5.24). While for $e = 0.7$, the flow height is decreasing with time and the peak indicating maximum mean particle size is remaining near the bottom of the flow, the flow of particles with $e = 0.8$ evolves to a more dilute state with slightly increasing flow height. The peak of maximum mean particle size is moving to a higher flow layer with time in the latter case.

Generally speaking, the longitudinal restitution coefficient e is the most

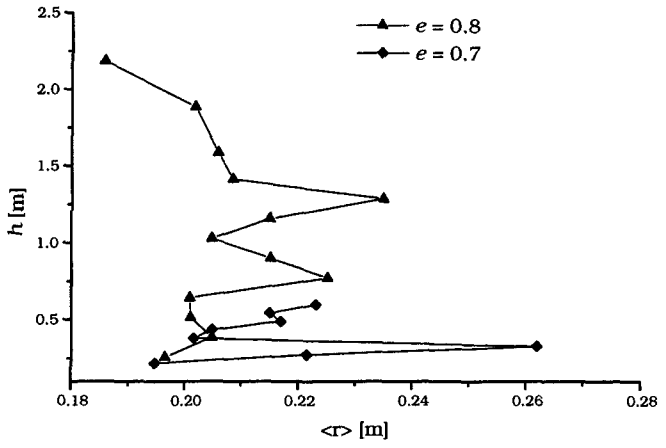

Figure 5.23: *Mean particle size profiles after $\frac{2}{3}$ of total flow time for $e = 0.7$ and $e = 0.8$. Parameters b and μ have been fixed at $b = 0.6$ and $\mu = 0.4$ for this example.*

dominant parameter influencing the global flow behaviour, which can be traced best by the time development of mean downslope flow velocity $\langle v_x(t) \rangle$ (see fig. 5.20). For the commonly used slope angle ψ=0.5, only for values of $e = 0.8 \pm 0.03$ model flows could be produced, which neither stopped before inverse grading could develop nor were accelerating to a kind of gas state too dilute for development of inverse grading.

With respect to this fact, all further investigations on the influence of variation of the other particle material parameters b and μ have been performed with fixed values of $e = 0.8$ and $\psi = 0.5$

Dependency of flow behaviour on the tangential restitution coefficient b

The influence of variation of the tangential restitution coefficient b was investigated for model flows with fixed values of e and μ. The longitudinal restitution coefficient e was fixed at $e = 0.8$, as mentioned above.

As the tangential restitution coefficient b and the Coulomb friction coefficient μ are both acting on the tangential collisional processes, we will parallely also regard the effect of change of μ in some examples to enlighten the

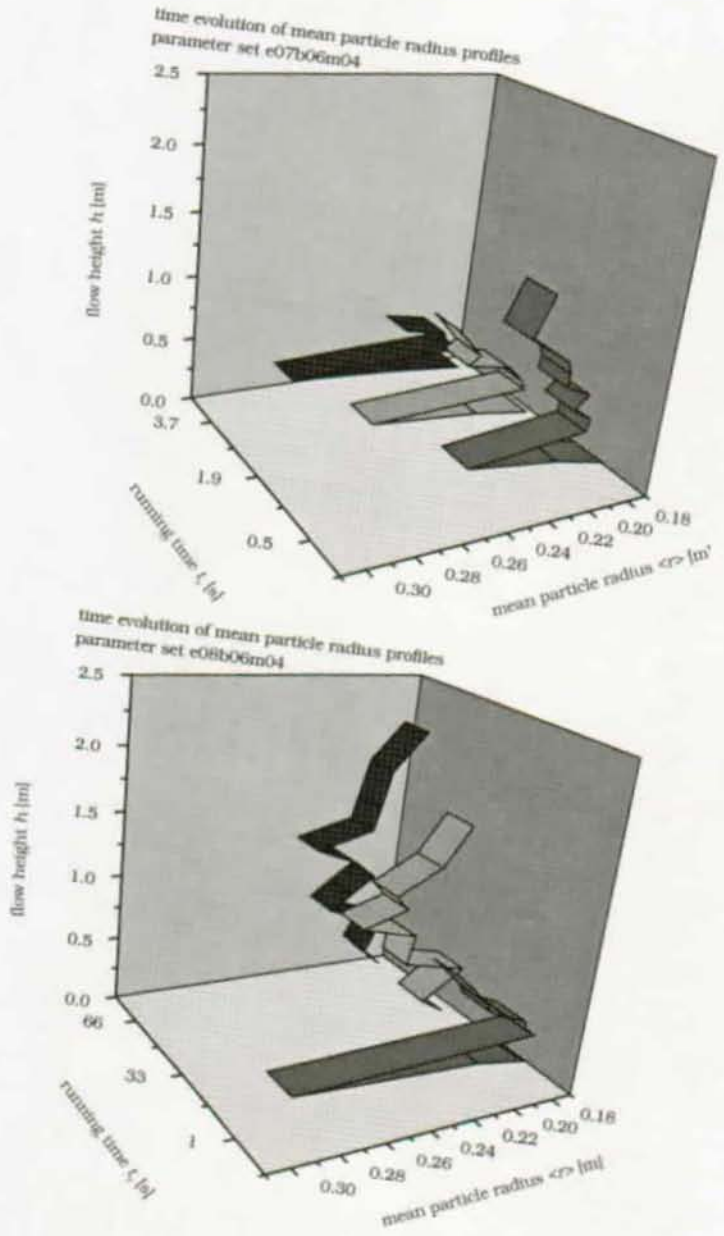

Figure 5.24: *Mean particle size time evolution for e=0.7 and e=0.8 at fixed values of* $b = 0.6$ *and* $\mu = 0.4$

interfering influence of b and μ on granular model flow behaviour.

(a) Mean downslope velocity $\langle v_x(t) \rangle$

For fixed particle material parameters e and μ, an increase of tangential restitution coefficients of the particles causes an increasingly accelerating behaviour for $\mu = 0.4$ (see fig. 5.25) and a transition from decelerating and finally stopping to a stable flow for $\mu = 0.6$ as shown in Figure 5.26. The increase of the Coulomb friction coefficient μ from 0.4 to 0.6 changes the general flow behaviour and therewith its reaction to variation of b.

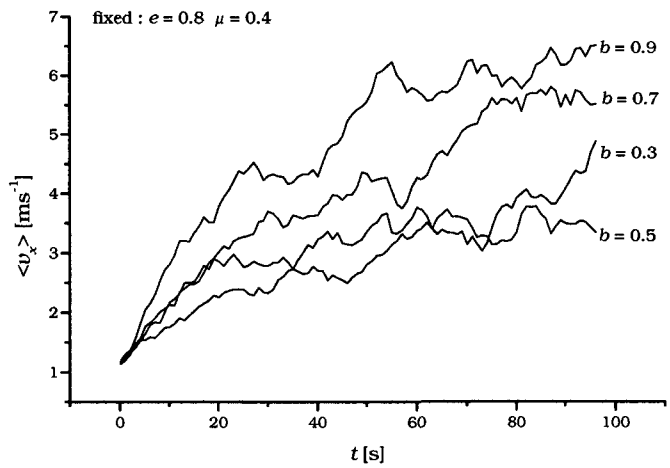

Figure 5.25: *Increasing b from 0.3 to 0.9 causes increasingly accelerating flow behaviour for fixed parameter values of* $e = 0.8$ *and* $\mu = 0.4$

(b) Segregational behaviour: Mean particle size profiles and single particle elevation time series

The influence of a change of the tangential restitution coefficient b on segregational flow behaviour, like on mean downslope velocity, is depending on the common Coulomb friction coefficient μ of the particles. While for flows with fixed particle material parameters of $e = 0.8$ and $\mu = 0.4$, an increase of b from 0.5 to 0.9 causes the peak of maximum mean particle size in the mean particle size profile $\langle r(h) \rangle$ to move to higher flow layers (see Fig. 5.27), for particles with a higher friction coefficient $\mu = 0.6$, an increase of b has no effect on the qualitative particle size profile shape, as shown in Figure 5.28.

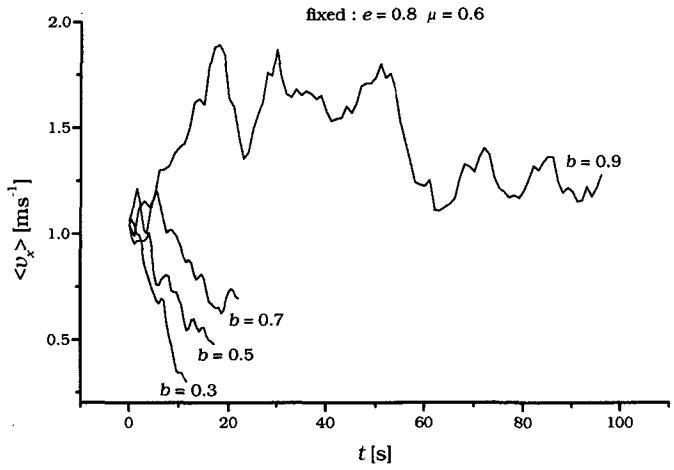

Figure 5.26: *Transition from decelerating and stopping to stable flow by increase of tangential particle restitution coefficient b. Other parameters fixed at* $e = 0.8$ *and* $\mu = 0.6$ *for all particles.*

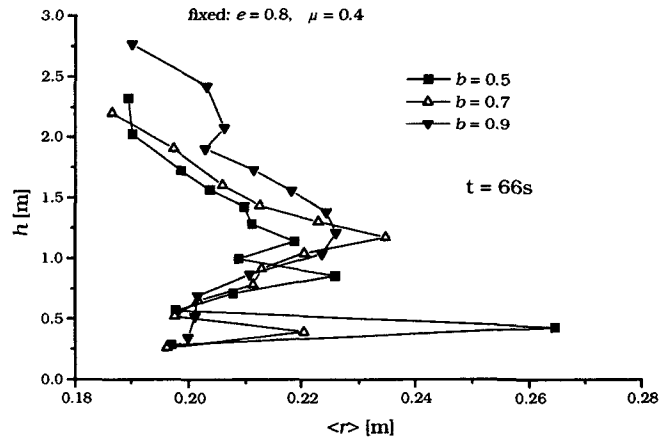

Figure 5.27: *Mean particle size profiles for fixed particle parameter values* $e = 0.8$ *and* $\mu = 0.4$ *after* $\frac{2}{3}$ *of total running time. Increase of b from 0.5 to 0.9 causes onset of inverse grading: The peak in the profile representing an accumulation of larger particles is shifting to higher flow layers.*

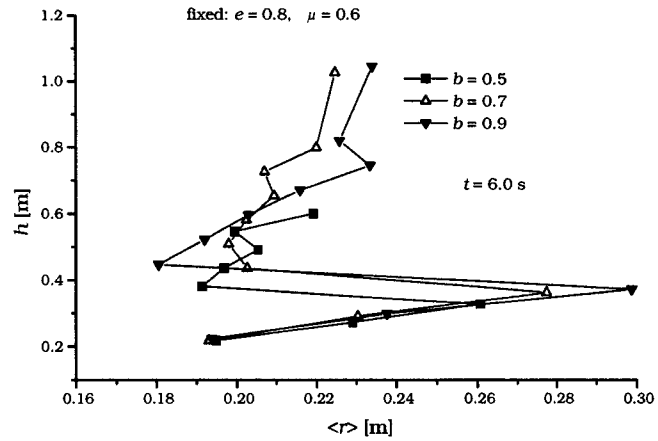

Figure 5.28: *Mean particle size profiles for fixed particle parameter values* $e = 0.8$ *and* $\mu = 0.6$*: Increase of* b *from 0.5 to 0.9 does not result in any qualitative change of profile shape: The flow consisting of particles with* $\mu = 0.6$ *does not develop segregational behaviour as it does for* $\mu = 0.4$.

Observing the segregational behaviour of the flow by the elevation time series of a single large particle leads to the same conclusion as the analysis of mean particle size profiles: For $e = 0.8$ and $\mu = 0.4$, an increase of b from b=0.5 to 0.9 leads to a transition to segregational behaviour: While for $b = 0.5$, the particle stays in the lowest flow layer over the whole model flow time, it is squeezed out of the lowest flow layer for $b = 0.7$ and $b = 0.9$.

The higher the value of b, the earlier the squeezing happens (see fig. 5.29). For a flow of particles with a higher Coulomb coefficient $\mu = 0.6$, the large particle does not move out of the lowest flow layer. The flow even stops after 15 or 21 s of running time, respectively. This is shown in Figure 5.30.

These findings support the hypothesis that the squeeze expulsion behaviour of large particles is strongly influenced by their surface roughness represented by the Coulomb friction coefficient μ in the model flow. (Regarding the practical use of inverse grading by the avalanche balloon system, this fact may influence the selection of the materials of balloons and ski suits.) A more detailed analysis of the influence of the particle Coulomb friction coefficient μ on flow and segregational behaviour will be given later on.

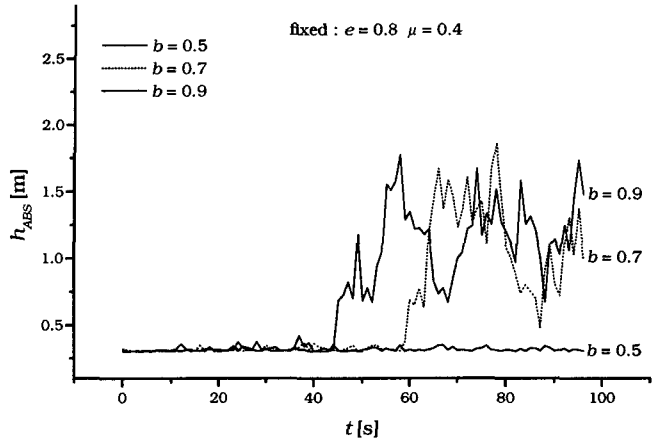

Figure 5.29: *Elevation time series of a single large particle with* $r = 0.3$ *m. Increase of* b *causes onset of inverse grading for* $b = 0.7$ *and* $b = 0.9$. *The particle material parameters* e *and* μ *are fixed at* $e = 0.8$ *and* $\mu = 0.4$ *for this example.*

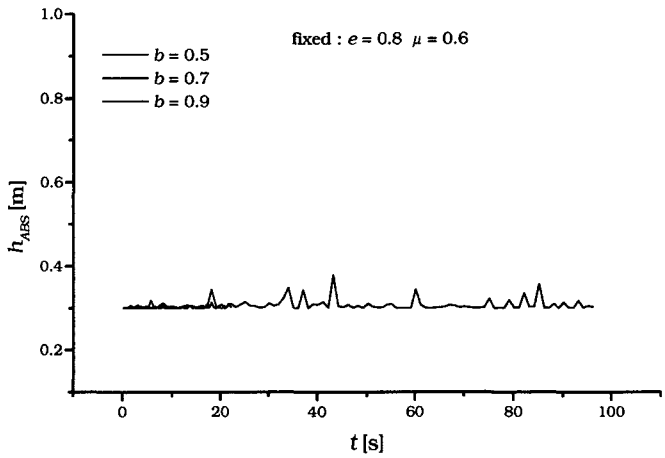

Figure 5.30: *Elevation time series for same particle as in 5.29, but particles involved in the flow now have a friction coefficient of* $\mu = 0.6$. *In this case, the large particle is not subject to squeeze expulsion.*

(e) Mean particle number density

The flow behaviour dependencies on b explained by the examples of mean velocity and elevation time series and velocity and mean particle size profiles also show up in the reaction of the particle number density time series on change of b.

For fixed particle material parameters $e = 0.8$ and $\mu = 0.4$, a change of the tangential particle restitution coefficient b does not much affect the mean particle number density ν of the resulting flows, as shown in Figure 5.31: after a short initial increase, the flow stabilizes at a value corresponding to a flow 2-3 times as dilute as the initial particle configuration at rest.

This picture, however, changes completely for flows of more frictional particles with $\mu = 0.6$. In this case, only for $b = 0.9$ the flow can persist for longer time at a particle number density approximately 1.5 times lower than the one of the start configuration (see Fig. 5.32).

For $b = 0.7$ and $b = 0.5$, the flow stops after a short running time at a more dense than the initial state, as shown in Figure 5.32.

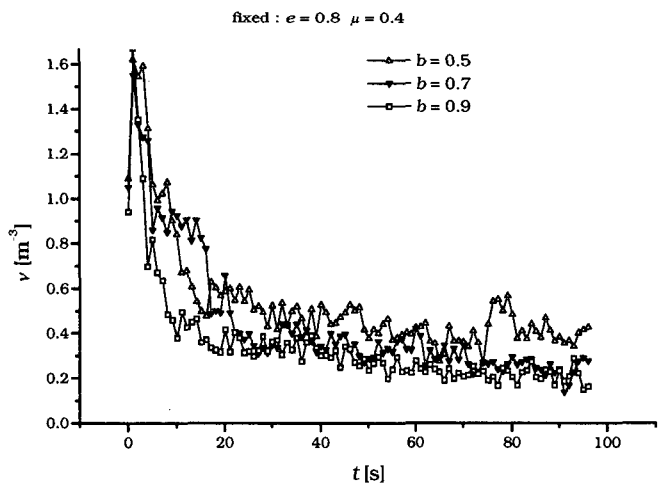

Figure 5.31: *Time evolution of mean particle number density ν of flows with varying tangential restitution coefficients b of the involved particles at fixed parameters $e = 0.8$ and $\mu = 0.4$. Variation of b has no significant qualitative influence on the flow density.*

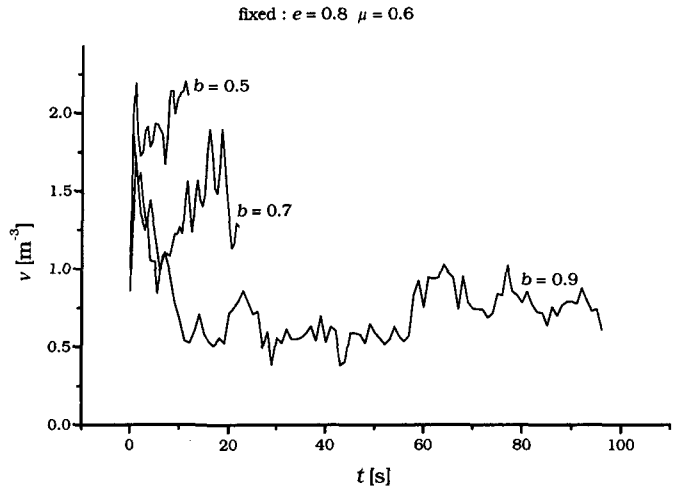

Figure 5.32: *Time evolution of mean particle number density ν of flows with varying tangential restitution coefficients b of the involved particles and fixed parameters $e = 0.8$ and $\mu = 0.6$. Decrease of b causes compaction and standstill of the flow.*

Summarizing, we can state that the influence of the tangential particle restitution coefficient b is strongly depending from the Coulomb friction coefficient μ, which together with b is governing the tangential energy and momentum transfer mechanism of colliding particles.

Dependency of flow behaviour on Coulomb friction coefficient μ

Though already considered in connection with the effect of tangential restitution coefficient b, the influence of particle Coulomb friction coefficient μ on the granular model flow will be described here.

(a) Time evolution of mean downslope velocity $\langle v_x(t) \rangle$

With fixed restitution coefficients e and b, a slight change of the Coulomb friction coefficient μ of the particles can cause a transition from accelerating to decelerating global flow behaviour, as depicted in Figure 5.33.

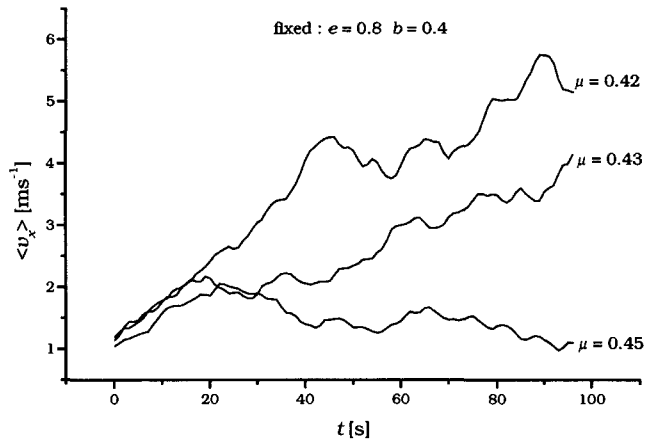

Figure 5.33: *Increase of Coulomb friction coefficient μ from 0.42 to 0.45 causes a transition from accelerating to decelerating flow behaviour. Restitution coefficients are fixed at $e = 0.8$ and $b = 0.4$ in this example.*

(b) Downslope flow velocity profiles $v_x(h)$

Considering the dependency of downslope velocity profiles $\langle v_x(h) \rangle$ provides similar findings as the observation of the influence of μ on global downslope flow velocity: the downslope movement of the granular model flow is sensible to variation of the Coulomb friction coefficient μ of particles, when the restitution coefficients e and b of the particles are fixed.

The downslope velocity profiles in Figure 5.34 are taken after $\frac{2}{3}$ of total flow time. They show a shift to higher velocities with decreasing μ and an increasing flow height corresponding to decreasing density of increasingly

rapid flows. This effect is observable for values of the tangential restitution coefficient of $b = 0.4$ as well as for $b = 0.6$. In the latter case, μ values need to be slightly higher to compensate higher tangential restitution.

This suggests that the influence of the Coulomb friction μ on flow behaviour is more dominant than the one of the tangential restitution b, where a reaction to changes of the flow could only be observed for a sufficiently low friction coefficient μ.

(c) Onset of inverse grading: Particle size profiles $r(h)$

As stated before, a low value of particle Coulomb friction μ is supporting the onset of the squeeze expulsion effect for large particles in the granular flow. Another requirement for inverse grading is that the flow is sufficiently rapid to provide enough lifting forces by particle impacts on the large particles and to produce enough random voids between the flowing and fluctuating particles for the random sieving effect. The lower the particle Coulomb friction μ is, the stronger is the tendency of the flow to evolve into a rapid, dilute state.

From this point of view, it is not surprising that with decreasing values of μ at fixed restitution coefficients e and b, the model flow tends to exhibit segregational behaviour: in the particle size profile, the peak of maximum particle size next to the bottom is vanishing with decreasing μ and the larger particles tend to accumulate in higher flow layers. Figure 5.35 shows an example for the evolution of invrese grading with decreasing particle Coulomb friction.

The strong influence of μ on flow particle size profiles is also observable in the time development of particle size profiles as shown in Figures 5.36 and 5.37. The particle material parameter set $e = 0.8$, $b = 0.6$ and $\mu = 0.51$ leads to a flow in which the peak indicating predominance of large particles stays near the bottom of the flow. A slight decrease of Coulomb friction to $\mu = 0.5$, however, causes the larger particles to accumulate in higher flow layers after $\frac{2}{3}$ of the total running time of 100 s. Figures 5.36 and 5.37 show the time evolution of particle size profiles for $\mu = 0.51$ and $\mu = 0.50$, respectively.

a)

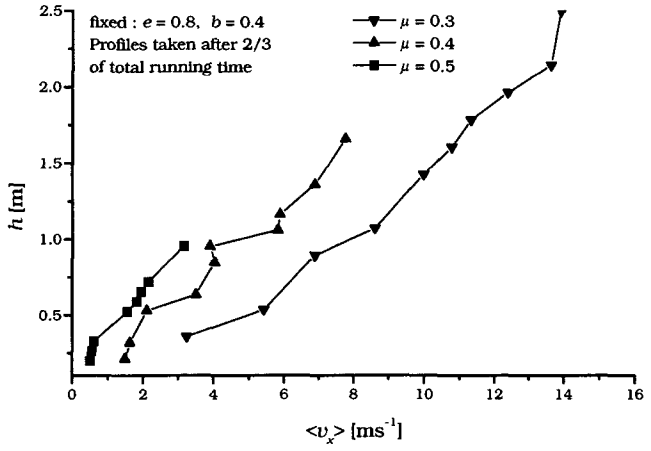

b)

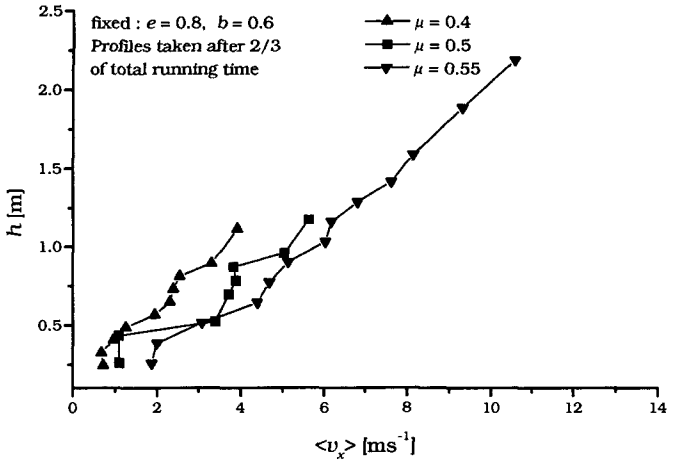

Figure 5.34: *For fixed values of particle restitution coefficients* $e = 0.8$ *and* $b = 0.4$ *(plot* a *) or* $b = 0.6$ *(plot* b *), respectively, decreasing Coulomb friction causes a shift of the profiles to higher downslope velocities and an increase of flow height indicating more rapid, dilute flow behaviour.*

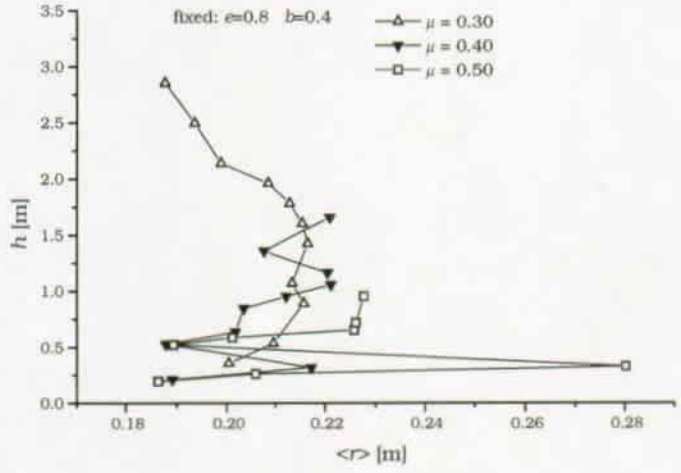

Figure 5.35: *Mean particle size profiles after $\frac{2}{3}$ of total running time for flows with fixed parameters $e = 0.8$ and $b = 0.4$. Decrease of Coulomb friction μ causes large particles to accumulate in higher flow layers. In the case of $\mu = 0.3$, the small particle sizes at $h \geq 2.0$ m correspond to a dilute, gas-like cloud of small particles bouncing on the more compact lower flow layers.*

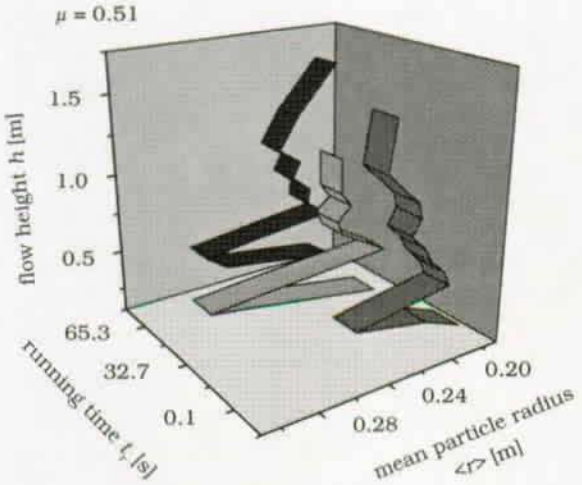

Figure 5.36: *Time evolution of mean particle size profiles of a granular model flow with parameter values $e = 0.8$, $b = 0.6$ and $\mu = 0.51$. There is no inverse grading observable.*

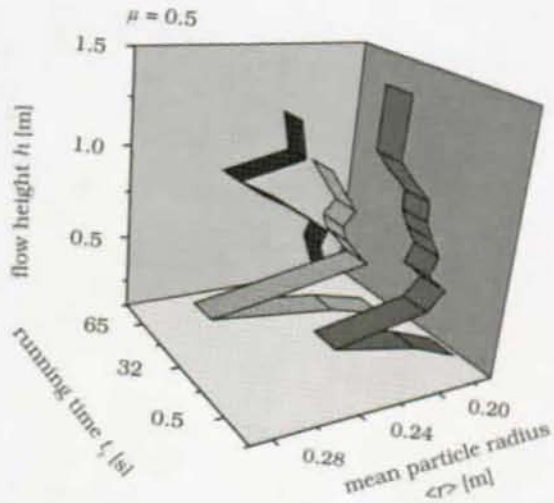

Figure 5.37: *Time evolution of mean particle size profiles of a granular model flow with the same boundary and initial conditions as the flow shown in Figure 5.36, but with particle Coulomb friction $\mu = 0.50$. The profile taken at $t = 65.3$ s indicates a developped segregated state.*

(d) Single particle elevation time series $h_{ABS}(t)$

Increasing the particle Coulomb friction μ in the model flow with fixed particle restitution coefficients $b = 0.8$ and $\mu = 0.4$, elevation time series of a single large particle which is initially placed at the bottom within the start configuration of particles at rest, show three types of qualitative behaviour:

- For $\mu = 0.2$, the model flow is accelerating to a dilute, gas-like state, in which the considered large particle is mainly moving freely.
- A Coulomb friction of $\mu = 0.3$ leads to a denser flow, which, nevertheless, is rapid enough to cause squeeze expulsion of the large particle which is rising to a higher flow layer without falling back into the lowest flow layer.
- Finally, $\mu = 0.4$ prevents the large particle from being squeezed out of the lowest flow layer over the entire flow period.

(e) Mean particle number density

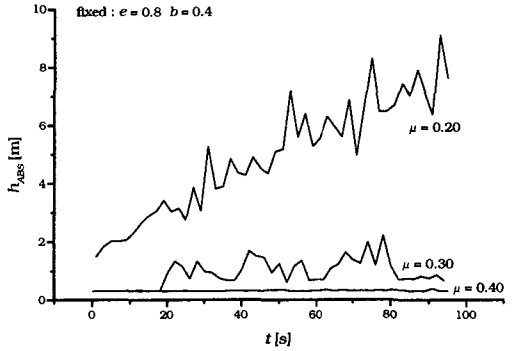

Figure 5.38: *Elevation time series of a large particle within a model flow with fixed particle restitution coefficients* $e = 0.8$ *and* $b = 0.4$.

The higher the particle Coulomb friction μ, the lower is the mean downslope flow velocity and diluteness of the granular model flow. While for lower values of μ, the model flow is stabilizing at a dilute state after some time, it stops after short running time in a compact state for high values of μ. In case of stable running flows, the mean particle number density is decreasing with increasing μ. An example for the reaction of the particle number density of the flow on variation of μ is given in Figure 5.39.

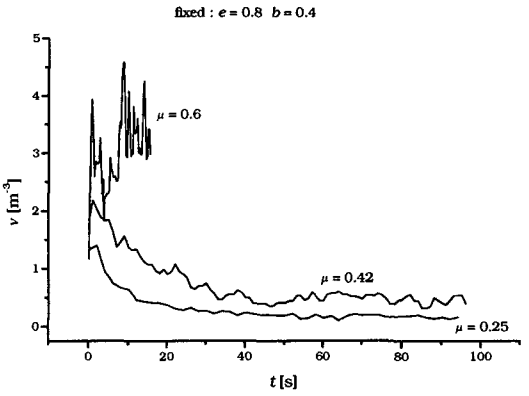

Figure 5.39: *Mean particle number densities of flows with fixed restitution coefficients* $e = 0.8$ *and* $b = 0.4$ *and different Coulomb friction* μ.

Particle material parameter range exhibiting inverse grading

As already mentioned, in the regarded parameter set $\{e, b, \mu\}$, the longitudinal particle restitution coefficient e most dominantly governs the behaviour of the model flows. For a slope angle of $\psi = 0.5$, inverse grading could only be observed for flows of particles with longitudinal restitution coefficients e in the vicinity of $e = 0.8$. More generally, the influences of particle tangential restitution coefficient b and Coulomb friction coefficient μ is displayed by Figure 5.40, which shows, at a fixed value of the restitution coefficient $e = 0.8$, all parameter combinations of b and μ, for which the corresponding flows show segregational behaviour.

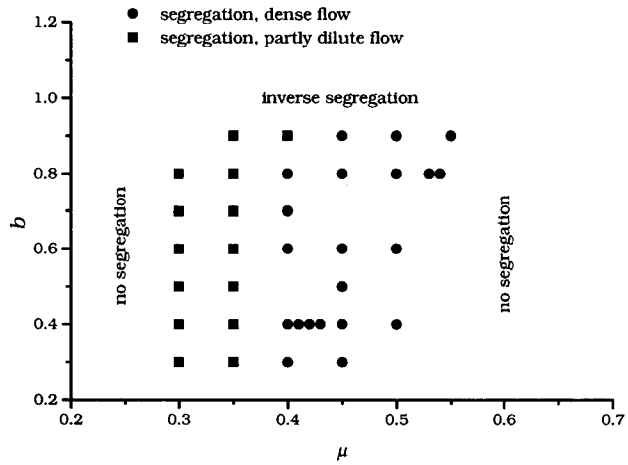

Figure 5.40: *Cut through the 3D parameter space $\{e, b, \mu\}$ for e=0.8. The regions in the $b - \mu$ plane leading to flows exhibiting inverse grading are indicated by dots. Parameter values marked by squares lead to flows with accelerating tendency, but still exhibit inverse grading.*

Low values of b and high values of μ cause the flow to stop before evolution of inverse grading, where high b and low μ values result in rapid flows, which are too dilute to exhibit segregational behaviour.

Squeeze expulsion of heavy particles

The squeeze expulsion effect is supposed to be responsible for the lifting of larger particles to higher flow layers in a granular flow. In order to enlighten the role of particle density on the development of the squeeze expulsion effect, one larger particle with a radius of $r = 0.3$ m was placed at the bottom of the inclined slope. All other particles of the model flow were equal sized and had a common radius of $r = 0.18$ m and a particle density of $\varrho_{p,s} = 400\text{kgm}^{-3}$.

In the initial state at rest, the large particle was completely covered by the smaller ones. Always starting from the same initial configuration, the density ϱ_{ABS} of the large particle was varied in the range of $\varrho_{ABS} = 200...4000$ kgm^{-3}. For each value of $\varrho_{p,s}$, a model run was performed with the particle material parameters $e = 0.8$, $b = 0.7$ and $\mu = 0.4$.

The elevation time series in Figure 5.41 show the lifting of the large particle after some flow time. The higher the density of the large particle, the longer the duration until the lifting forces provided by collisions with small particles were sufficient to squeeze out the large one out of the lowest flow layer.

For $\varrho_{ABS} = 200\text{kgm}^{-3}$ the large particle is lifted very fast to an average height of 1 m, which is corresponding to the vertical position of the center of the large particle, which is lying on two vertically stacked small particles. For higher densities, i.e. for $\varrho_{ABS} = 700\text{kgm}^{-3}$ or $\varrho_{ABS} = 1200\text{kgm}^{-3}$, respectively (note: this corresponds to 2-3 times the density of the small particles !), the large particle is squeezed out of its position near the bottom to a flow height corresponding to a large particle radius and a small particle diameter.

The squeezing out of the large particle from the bottom is working up to a large particle density $\varrho_{ABS} = 1600\text{kgm}^{-3}$, which is four times as high as the density of the surrounding small particles. For higher densities, after having been squeezed out, the large particle is "squeezing back" down to the bottom again. An example for this is given for $\varrho_{ABS} = 2000\text{kgm}^{-3}$ in Figure 5.42. If the large particle is denser than $\varrho_{ABS} = 2200\text{kgm}^{-3}$, it is no longer squeezed out of its position near the bottom, but causes the flow to

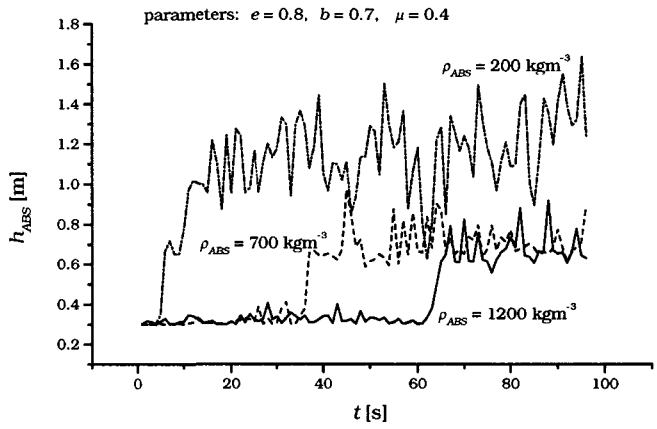

Figure 5.41: *Elevation time series $h_{ABS}(t)$ of a large particle with $r = 0.3$m in a monodisperse flow of small particles with radius $r = 0.18$m and a density of $\varrho_{p,s} = 400\text{kgm}^{-3}$ and material parameters of $e = 0.8$, $b = 0.7$ and $\mu = 0.4$. Squeeze expulsion of the large particle happens for all values of large particle density ϱ_{ABS}. For a density $\varrho_{ABS} = 200\text{kgm}^{-3}$ of the large particle, the particle is squeezed out into a flow height corresponding to two small particle diameters*

stop after some time. Once a large particle with a density not exceeding the density of the surrounding particles too much, has been sqeezed out from the bottom flow layer, it normally persists in a higher flow layer. Although it can in principle go back to a position near the bottom, this is relatively unlikely, and, if this happens, the large particle is soon lifted up again as shown in Figure 5.58.

Influence of initial conditions on flow behaviour

Initial conditions of the granular model flow are supported by the particle number density ν_0 of the initial particle configuration and the model flow's initial mean downslope velocity $v_{x,0}$. As the mean downslope flow velocity is a good measure for the global flow behaviour, we consider the effect of varying initial conditions on the time series of mean downslope flow velocity. In order to do this, flows of 212 multidisperse particles with the material parameters $e = 0.8$, $b = 0.6$ and $\mu = 0.5$ were simulated with varying $v_{x,0}$ and ν_0, where each one of these two initial conditions was fixed.

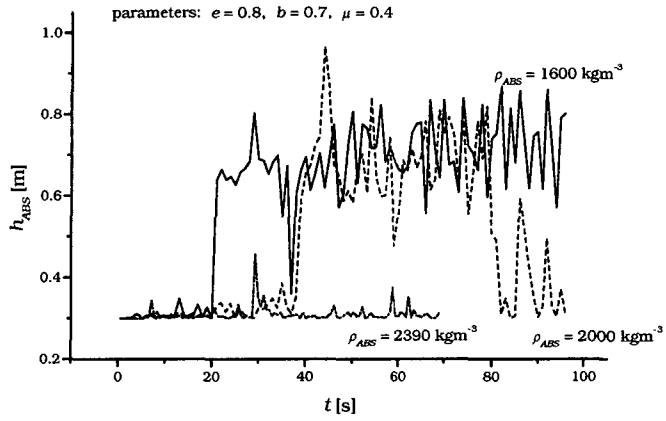

Figure 5.42: *Elevation time series $h_{ABS}(t)$ of a large particle with $r = 0.3$m in a monodisperse flow of small particles with radius $r = 0.18$m and a density of $\varrho_{p,s} = 400\text{kgm}^{-3}$ and material parameters of $e = 0.8$, $b = 0.7$ and $\mu = 0.4$. Squeeze expulsion of the large particle is persisting for densities of the large particle up to $\varrho_{ABS} = 1600\ kgm^{-3}$.*

(a) Effect of initial downslope velocity $\langle v_{x,0} \rangle$

Several simulations were performed with fixed particle material parameters and fixed initial particle number density $\nu_0 = 6.8\ \text{m}^{-3}$ which corresponds to a solid volume fraction of $\nu_{sol} = 0.28$. Regarding the time series of the mean downslope flow velocity $\langle v_x \rangle$ shown in Figure 5.43, for model flows started with different initial mean downslope flow velocities $v_{x,0}$, one does not observe a significant qualitative difference between the time series, if the initial velocities are $v_{x,0} = 0$, $v_{x,0} = 1.0\ \text{ms}^{-1}$ and $v_{x,0} = 2.0\ \text{ms}^{-1}$, respectively. (Of course, the different initial velocities are clearly visible). If however the initial downslope velocity is higher than the maximum mean downslope velocity of the flows started from rest or from moderate initial velocities, the flow velocity does not converge towards the mean velocities of those flows. This behaviour is shown for the example of a starting velocity of $\langle v_{0,x} \rangle = 5\ \text{ms}^{-1}$ in Figure 5.43.

(b) Influence of initial particle number density

The model flow mentioned above (212 multidisperse particles with material parameters $e = 0.8$, $b = 0.6$, $\mu = 0.5$) also was started from rest with

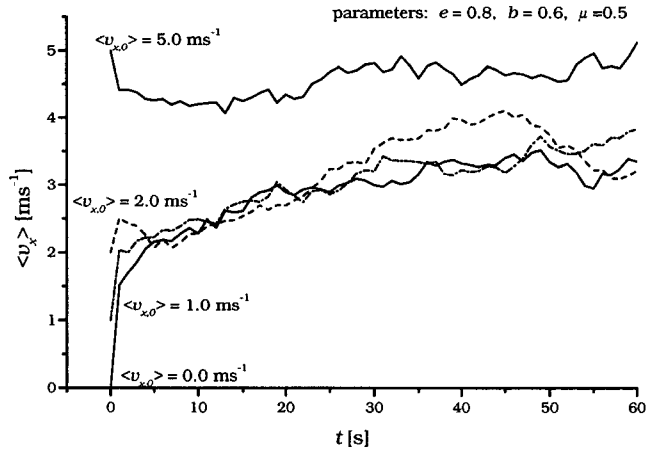

Figure 5.43: *Mean downslope velocity time series for model flow started with different initial mean velocities* $\langle v_{0,x} \rangle$. *Parameters of flow particles were* $e = 0.8$, $b = 0.6$, $\mu = 0.5$.

different initial particle number densities.

Note, that due to the initialisation algorithm, the initial particle number density also influences the particle size distribution. Speaking differently, the more space is available for the initial particle assembly, the more large particles it contains, as shown in Figures 5.10 and 5.11. The influence of initial particle number density on particle size distribution is shown in Figures 5.44 and 5.45.

A value of $\nu_0 = 6.8$ corresponds to the maximum possible initial particle number density of the multidisperse sphere mixture. Decreasing ν_0 at fixed initial downslope velocity $\langle v_{x,0} \rangle = 0$ leads to higher mean downslope velocities immediately after release of the model flow due to gain of kinetic energy when the initial dilute particle configuration settles down in the initial flow phase (see fig. 5.46). There appears to be no persisting monotone dependency of $\langle v_{x,0} \rangle$ from ν_0.

Dependency of flow behaviour from slope angle ψ

(a) Mean downslope velocity $\langle v_x(t) \rangle$.

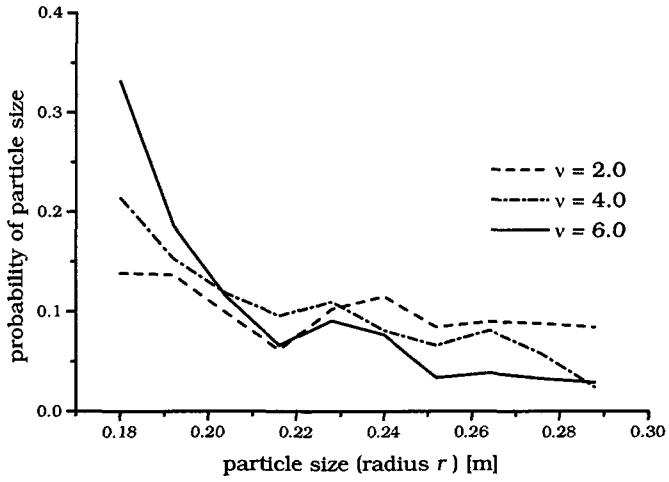

Figure 5.44: *Dependency of grain size distribution from initial particle number density.*

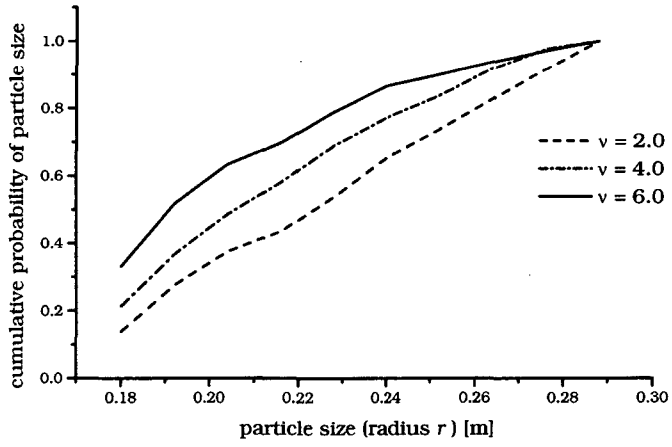

Figure 5.45: *Dependency of cumulative grain size distribution from initial particle number density.*

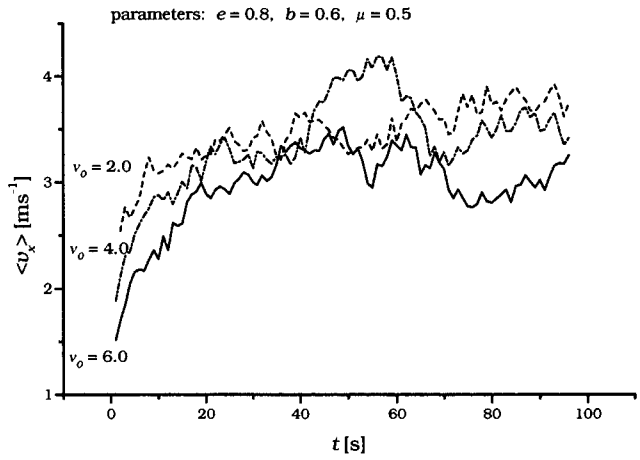

Figure 5.46: *Mean downslope velocity time series of flows started from rest with different initial particle number densities ν_0. Particle material parameters for this example: $e = 0.8$, $b = 0.6$, $\mu = 0.5$.*

The behaviour of the granular model flow is sensible to changes of the slope angle of the infinite inclined plane on which the flow runs. Figures 5.47 show the dependency of mean downslope velocity $\langle v_x(t) \rangle$ from the slope angle ψ. A change of only 0.01 rad $\approx 0.57°$ causes a significant change in the mean downslope velocity time series. In the transition regime at $\psi \approx 0.48$, flow behaviour changes from accelerating to decelerating with decreasing slope angle.

From Figure 5.47, one might assume, that the friction coefficient μ of the individual particles is approximately the macro friction $\bar{\mu}$ of the entire model flow. For a slope angle $\psi = 0.48$rad$= 25.64°$ of transition from accelerating to decelerating global flow behaviour and for the special case of the particle parameter set e=0.8, b=0.6 and $\mu = 0.48$ at a flow slope angle of $\psi = 0.5$, this assumption seems to be reasonable. Note however, that the global frictional behaviour of the flow is not just determined by the individual particle friction, but in major parts is also determined by interparticle collisions which are governed by the particle restitution cefficients e and b. Regard, for example Figure 5.33 where the transition from accelerating to decelerating flow behaviour happens at a particle friction angle of arctan(0.44)=23.75°

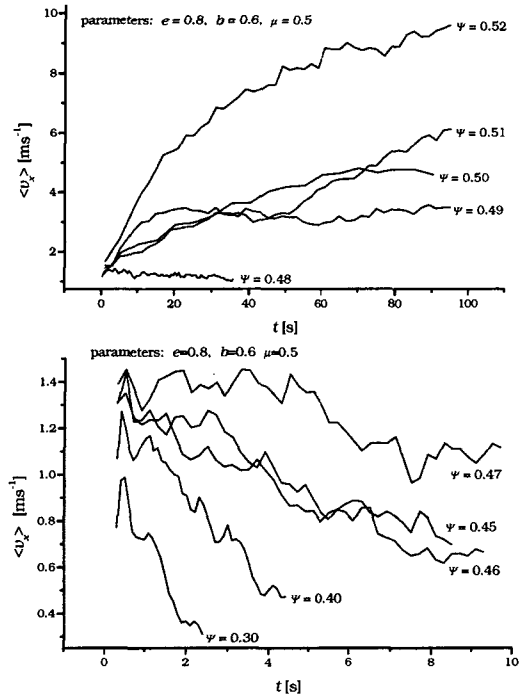

Figure 5.47: *Mean downslope velocity time series of flows with particle material parameters* $e = 0.8$, $b = 0.6$, $\mu = 0.5$ *started from rest on planes inclined at different slope angles* ψ. *The flow undergoes a transition from accelerating to decelerating at* $\psi \approx 0.48$.

at a flow slope angle of $\psi = 0.5$ or $\psi = 28.64°$, respectively. In this case, the particle restitution coefficients were e=0.8 and b=0.4 leading to a transitional particle friction angle deviating from the flow slope angle: the internal friction of the flow here is also governed by inelastic tangential restitution behaviour.

(b) Particle size profiles

As already stated before, inverse grading can only occur in sufficiently rapid granular flows which support enough collisional lateral forces for squeeze expulsion and voids for the random sieving effect. As the slope angle strongly influences flow velocity and therewith internal fluctuation, it also influences the onset of inverse grading, as shown in Figure 5.48. The maximum of mean particle size in the mean particle radius profile moves upwards into higher flow layers by an increase of slope angle ψ.

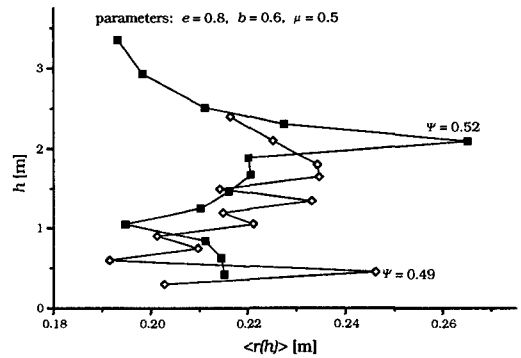

Figure 5.48: *Mean particle radius profiles for flows with* $e = 0.8$, $b = 0.6$ *and* $\mu = 0.5$ *at different slope angles* ψ *after* $\frac{2}{3}$ *of total running time. An increase from* $\psi = 0.49$ *to* $\psi = 0.52$ *amplifies the accumulation of larger particles in higher flow layers.*

5.4.3 Influence of air friction

In snow avalanches, inverse grading is occuring only in the dense flow part of the avalanche, where air friction by surrounding air can be neglected. For powder avalanches, or underwater gravity currents, the velocity-dependent friction caused by air or surrounding water plays an important role. In the

current work, air friction has not been taken into account. We assume that this approximation is valid but check it by introducing a velocity-dependent frictional force $\mathbf{F}_{fr}$ into the equations of free motion of the spherical particles between their respective collisions:

$$\mathbf{F}_{fr} = \frac{1}{2}\varrho_{fl} A_p c_w v^2 \frac{\mathbf{v}}{v}, \tag{5.69}$$

where ϱ_{fl} is the density of the ambient fluid, A_p the frontal area of the particle with respect to the direction of the relative velocity $\mathbf{v}$ of the particle against the fluid and $v = |\mathbf{v}|$ is the amount of the relative velocity. The so-called c_w value of a spherical particle is 1.

For a particle moving in a surrounding fluid, the ratio of forces F_{fr} and F_g due to fluid friction and gravity is

$$\frac{F_r}{F_g} = \frac{3}{2}\frac{\varrho_{fl}}{\varrho_{p,s}}\frac{c_w v^2}{gr}. \tag{5.70}$$

Here, ϱ_p is the particle solid density, g the acceleration of gravity and r denotes the particle radius. The equilibrium sink velocity v_s of a particle in the ambient fluid can be computed by setting $F_{fr} = F_g$ as

$$v_s = \sqrt{\frac{2}{3}\frac{\varrho_{p,s} gr}{\varrho_{fl} c_w}}. \tag{5.71}$$

Velocity-dependent frictional forces acting on particles moving in fluids are also termed "Newton friction".

The difference velocity $\mathbf{v}$ between granular material and surrounding air or fluid, which determines the magnitude of Newton friction, is reduced by entrainment of fluid or air by the flow. The interaction between granular particles and ambient fluid leading to entrainment depends on the solids concentration and is rather complicated.

For the raw estimation of the role of Newton friction intended here, we assume that $\mathbf{v}$ vanishes for particles situated in the dense bottom layers of the model flow and increases linearly with the elevation h of the particles. If the elevation h_i of particle i exceeds a certain limit h^* which corresponds to

upper, dilute flow layers, the particle is assumed to move in the surrounding fluid which is at rest. So the difference velocity causing air friction of a particle i is determined by the particle elevation h_i and the particle velocity $\mathbf{v}$:

$$\begin{aligned} \mathbf{v} &= \frac{h_i}{h^*}\mathbf{v}_i \quad \text{for} \quad 0 \leq h_i \leq h^* \\ \mathbf{v} &= \mathbf{v}_i \quad \text{for} \quad h > h^* \end{aligned} \tag{5.72}$$

As the time steps produced by the time-to-the-next-event algorithm of the used hard sphere DEM are rather small (in the order of 10^{-3}s), the Newton frictional force can be numerically implemented by simply adding a term which includes Equations (5.69) and (5.72) to Equation (5.3), which describes the particle motion between collisions.

Including air friction into the modelling of a multidisperse flow of spherical particles with radii r in the range of $r \in [0.18 \text{ m}, 0.3 \text{ m}]$ and a density of $\varrho = 400 \text{ kgm}^{-3}$, which corresponds to the density ofdense snow lumps occuring in snow flow avalanches, the influence of air friction can be observed in the time evolution of the mean flow velocity: Figure 5.49 shows the time evolution of a multidisperse flow for the two cases of included and non included air friction. As for a representative particle with the mean particle radius $\langle r \rangle$=0.22691 m and a density of $\varrho = 400 \text{ kgm}^{-3}$ and the observed mean downslope velocity $\langle v_x \rangle \leq 6 \text{ ms}^{-1}$ the ratio of air friction and gravity acceleration is small, the inclusion of air friction causes only a slight decrease of the mean downslope velocity. Note that according to Equation (5.70), $\frac{F_{fr}}{F_g} \approx 0.08$. Also the fact that the corresponding sink velocity $v_s = 20.97 \text{ ms}^{-1}$ of a representative particle is high against the mean downslope flow velocity, indicates that the air friction is of minor importance for the global flow motion.

Regarding a multidisperse flow of particles whose density corresponds to the one of rock and which are moving under water, the Newton friction causes the flow to stop after a short time. The short acceleration showing up in the plot of the mean downslope velocity in Figure 5.50 is due to settling of the dilute initial particle configuration.

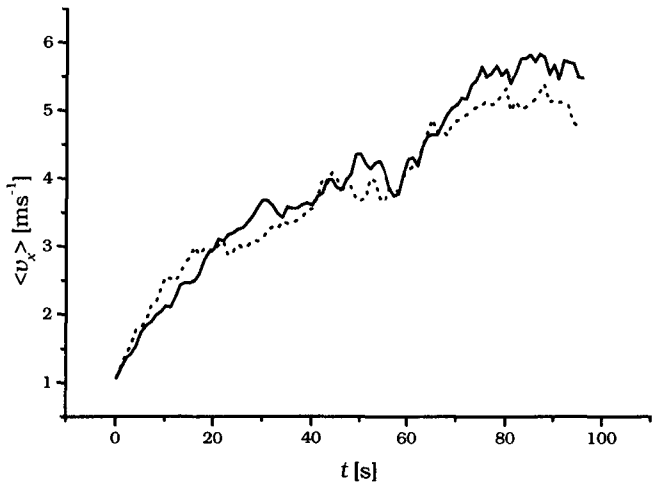

Figure 5.49: *Influence of air friction on the time evolution of the mean downslope flow velocity of a multidisperse granular model flow. Solid line: flow without air friction, dotted line: flow subject to air friction. Density of ambient air:* $\varrho_{fl} = 1.29$ kgm^{-3}, *particle density* $\varrho_p = 400$ kgm^{-3}. *Particle radii* $r \in [0.18\text{ m}; 0.3\text{ m}]$, *mean particle radius* $\langle r \rangle = 0.21691$ m, *particle material parameters* $e = 0.8$, $b = 0.7$ *and* $\mu = 0.4$. *The incorporation of air friction causes only a slight decrease of mean downslope velocity of the multidisperse model flow.*

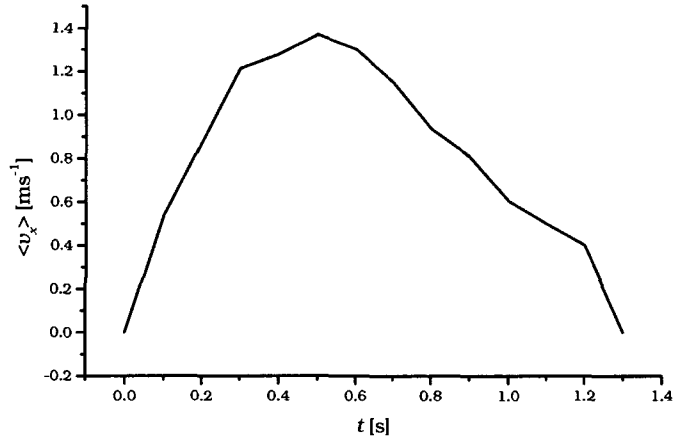

Figure 5.50: *Same parameters as in Figure 5.49 but with fluid density* $\varrho_{fl} = 1000$ kgm^{-3}, *particle density* $\varrho_p = 3000$ kgm^{-3}. *After a short acceleration due to settling, the flow stops within a short time after release.*

Concluding we can state, that for granular flows with particle sizes and densities in the range used in the current investigations, the neglection of air friction does not change the model flow behaviour significantly, if a similarity of the model flows to snow flow avalanches is intended. Note that the considered relative velocity profile is rather a worst-case scenario: in reality, the relative fluid velocity would be decreased much stronger by entrainment than assumed by Equation (5.72).

5.4.4 Continuum mechanical interpretation of the model flow

Motivation

The modelling of the granular flow by a hard sphere approach is based on assembling the flow from single particles and their interactions. The global flow behaviour emerges from the synthesis of all individual particle interactions. From a conceptually opposite point of view, one describes the granular flow as a flowing continuum, which contains particle interactions only in the thermodynamical limit. This interpretation is valid only in a limited sense for granular flows, due to their mesoscopic character: Speaking off-handly, they contain too few particles to perform a thermodynamical limit. Due to this constraint, continuum mechanical descriptions always have to make assumptions about the constitutive behaviour (i.e. about the relation of stress and strain) of the flowing granular material. These principle problems have been mentioned in Chapter 4.

Basic idea

In principle, the statistical evaluation of the flow model data allows direct determination of the measures stress and strain in the model flow. So the constitutive behaviour of the granular flow can be determined as relation between stress and strain, which is finally depending on the material properties of single granular particles. This is important, because it makes the granular approach conceptually compatible to the classical continuum mechanical avalanche description.

Formal shape of analysis

In the following, spatial coordinates are denoted by greek letters. Referring to the subdivision of the model flow in layers l as explained in 5.3.3, we compute the stress tensor $\sigma_{\alpha\beta}$ in this layer as average of all momenta $\delta\mathbf{p}$ transferred between colliding particles in this layer:

$$\sigma_{\alpha\beta} = \langle s_{\alpha\beta} \rangle_{c,l}, \qquad \alpha, \beta = 1, \ldots, 3. \tag{5.73}$$

where $\langle \cdot \rangle_{c,l}$ denotes the average over all collisions occuring in flow layer l within a defined time intervall and

$$s_{\alpha\beta} := k_\alpha \delta p_\beta D_l \tag{5.74}$$

are the stresses produced by one single particle collision. The unit collision vector is denoted as $\mathbf{k}$ and D_l $(0 \leq D_l \leq 1)$ is the part of the connecting line between the colliding particles which is lying in layer l.

In terms of continuum dynamics, the deformation rate tensor $D_{\alpha\beta}$ usually is defined as

$$D_{\alpha\beta} := \frac{1}{2}(\partial_\alpha v_\beta + \partial_\beta v_\alpha). \tag{5.75}$$

We approximately compute the spatial derivatives as ratio of velocity difference and spatial displacement, averaging over all particle pairs (m, n) in flow layer l.

$$\partial_\beta v_\alpha \approx \left\langle \frac{v_{\alpha,m} - v_{\alpha,n}}{x_{\beta,m} - x_{\beta,n}} \right\rangle_l, \tag{5.76}$$

where $\langle \cdot \rangle_l$ denotes an averaging over all particle pairs (m, n) in flow layer l and the indices (α, m) stand for the α component of the position or velocity vector of particle m.

According to Vulliet & Hutter (1988), one possible expression of a constitutive law for a nonlinear viscous compressible medium is

$$\sigma_{\alpha\beta} = \tilde{\sigma}(\nu_p, D_{\alpha\beta}), \tag{5.77}$$

where

$$\nu_p = 1 - \nu \frac{4\pi}{3} \langle r \rangle^3$$

is the porosity defined using the mean particle radius $\langle r \rangle$ and particle number density ν. For incompressible flow or in the special case of steady-state flow with constant porosity, this relationship reduces to

$$\sigma^d_{\alpha\beta} = \tilde{\sigma}(D^d_{\alpha\beta}), \tag{5.78}$$

where $\sigma^d_{\alpha\beta}$ is the deviatoric part of $\sigma_{\alpha\beta}$,

$$\sigma^d_{\alpha\beta} = \sigma_{\alpha\beta} - \frac{1}{3}\delta_{\alpha\beta}\sigma_{\gamma\gamma} \tag{5.79}$$

and $D^d_{\alpha\beta}$ is the deviatoric part of $D_{\alpha\beta}$,

$$D^d_{\alpha\beta} = D_{\alpha\beta} - \frac{1}{3}\delta_{\alpha\beta}D_{\gamma\gamma}. \tag{5.80}$$

Squaring Equation (5.78) yields the invariant form

$$\sigma^d_{II} = \tilde{\sigma}(D^d_{II}) \tag{5.81}$$

with the second deviatoric invariants

$$\sigma^d_{II} = \sqrt{\frac{1}{2}\sigma^d_{\alpha\beta}\sigma^d_{\alpha\beta}} \quad \text{and} \quad D^d_{II} = \sqrt{\frac{1}{2}D^d_{\alpha\beta}D^d_{\alpha\beta}}. \tag{5.82}$$

The shape of the function $\tilde{\sigma}$ can be determined by simply plotting σ^d_{II} as a function of D^d_{II}.

Result

In each layer l of the model flow, effective stress and strain rates were computed by the `evalcont` routine at distinct times of the granular model flow. A flow exhibiting reasonably steady flow conditions and being of approximately homogeneous porosity as shown in Figures 5.51 and 5.52 was achieved by the particle material parameters e=0.8, b=0.7 and μ=0.4. Particles had an uniform size of r=0.18 m.

Plotting effective stresses and strain rates obtained for the different flow layers against each other, one obtains a constitutive relation between σ^d_{II}

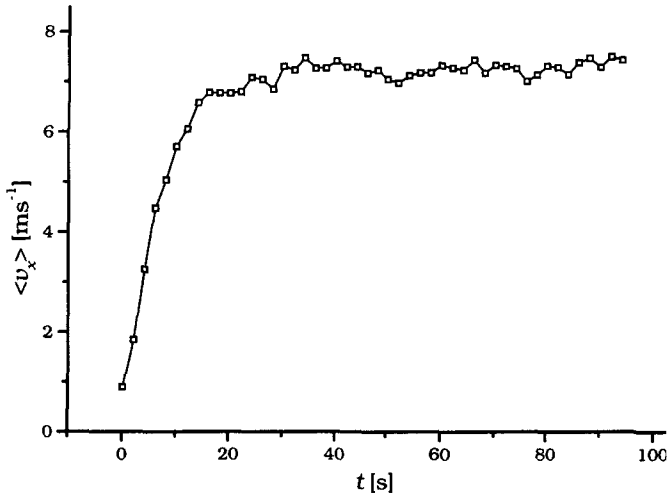

Figure 5.51: *Mean downslope velocity $\langle v_x \rangle$ of model flow with parameters: e=0.8, b=0.7 and μ=0.4 indicates approximately steady flow behaviour.*

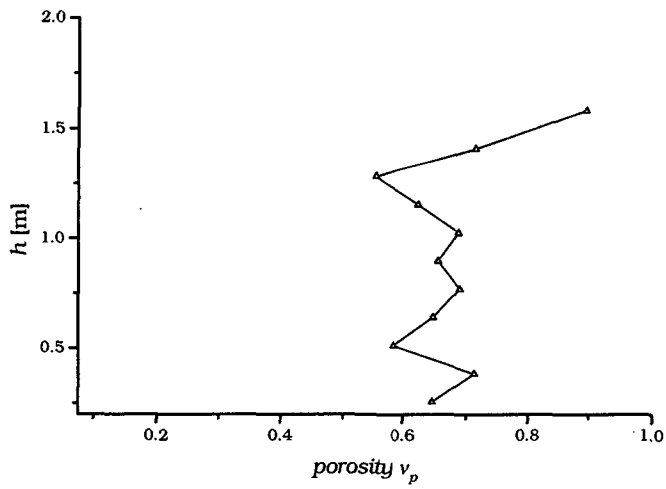

Figure 5.52: *Profile of mean porosity at time t=60s of same model flow as in Figure 5.51. The high porosity for $h > 1.3$ corresponds to a dilute layer of bouncing particles. The constitutive relation of the flow was regarded for $h < 1.15$, where the flow is assumed to be of sufficiently uniform porosity.*

and D^d_{II} of the model granular flow. Figure 5.53 shows a plot of the second invariant of the deformation rate tensor against the second invariant of the stress tensor. The data can be fitted linearly or a by a power law, which corresonds to Newton or Norton flow behaviour, respectively.

In the case of Newton flow behaviour, the constitutive relation (5.78) explicitly reads

$$\sigma^d_{II} = \eta(D^d_{II}) \tag{5.83}$$

where η is the Newtonian viscosity. From the linear fit in Figure 5.53, η can be determined as $\eta = 0.29$ Pas which lies approximately three orders of magnitude above the value of $\eta_{w,100} = 0.000288$ Pas of boiling water. On the other hand, glycerine ($\eta_{glyc} = 1.59$ Pas) is more viscous than the regarded granular model flow.

The fit of the data to a Norton power law

$$\sigma^d_{II} = a(D^d_{II})^b \tag{5.84}$$

results in $a = 2.12$ (Pa)$^{1.67}$s and $b = 1.67$.

Unfortunately, in the various calculations, an unique functional dependency of stress and deformation rate could not be found. The obtained relations were varying strongly depending on the times, at which the averagings were performed, so that no generic constitutive behaviour could be observed. This may be due to the fact that the model flow is not steady enough and because compressibility as well as nonuniform porosity profiles enter into the picture. Though being in a certain mean velocity range over longer times, the used model flow exhibits fluctuations in its velocity and particle number density field. As the averaging in Equation (5.73) can only be performed over colliding particles, the time duration for averaging has to be in an order (of approximately one second), which inevitably also contains fluctuations, which may be responsible for the non-uniqueness of the obtained constitutive relations.

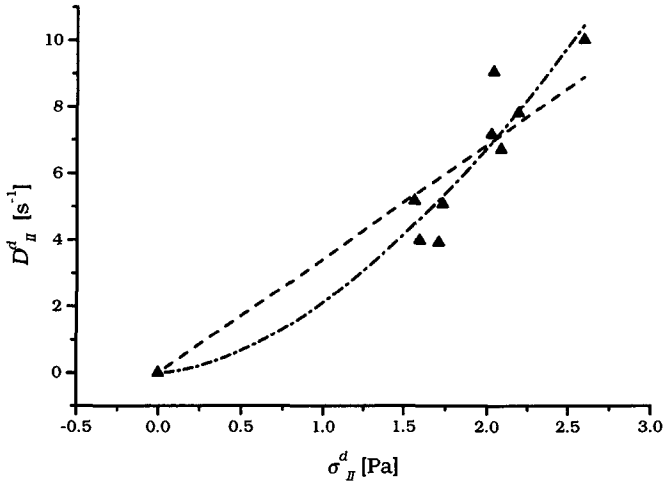

Figure 5.53: *Example for a constitutive relation between effective stress and strain rate within the granular model flow. Parameters: e=0.8, b=0.7, μ=0.4. The dashed and dotted lines are fits to Newton and Norton flow laws as explained in the text.*

The mentioned flow fluctuations also collide with the requirements of a rigid geometrical analysis of the problem of derivation of deformation rate tensors in granular media byHe & Huet (1999): The motions of single particles are demanded to be sufficiently smooth in time within a closed domain, the so-called representative assembly element (RAE). Furthermore, a minimum number of particles is neccessary for the averaging over a RAE to allow the transition to fluid mechanical description, or speaking differently, the size ratio of the RAE and the granular particles have to satisfy the condition

$$d^{(i)}(\mathbf{n}) << d(\mathbf{n}) \quad \forall i \in \mathbf{N} \quad \text{and} \quad \forall \mathbf{n} \in \mathbf{R}^3, \tag{5.85}$$

where $d^{(i)}(\mathbf{n})$ is the Feret diameter of particle i with respect to the unit vector $\mathbf{n}$ and $d(\mathbf{n})$ is the Feret diameter of the RAE with respect to $\mathbf{n}$. Using one flow layer l with a thickness of the order of one particle diameter, this condition is clearly violated in vertical direction, when evaluating the flow as explained in 5.3.3.

To fulfil the condition (5.85), the particle layer thickness must be increased at least by one order of magnitude. As horizontal particle velocities (and therewith the deformation rate) are strongly varying within a few particle

layers, one would average over a vertically strongly inhomogeneous RAE, which again is a contradiction to the requirement of smooth particle movement.

We leave the problem umsolved at this state and note that there is need for further conceptual investigations as well as for numerical analysis with particle numbers an order of magnitude higher than in the current work.

5.4.5 Stochastic analysis of single particle segregational dynamics

General considerations and definitions

Tracing the vertical position h of a single particle in the granular model flow, one observes a noisy, "stochastic" time series, which is produced by the up- and down movement of the particle due to particle collisions, similar to the Brownian motion of gas molecules. For an example of single particle elevation time series, see Figure 5.29. It is possible to extract deterministic laws characterizing the segregational behaviour from the noisy elevation time series of single particles:

A recently developed method allows derivation of differential equations out of noisy data sets of complex systems with Markov properties. Motivation and application of the method to turbulence and chaotic data can be found in Siegert et al. (1998), Naert et al. (1997) and Friedrich & Peinke (1997). Basic introduction is provided by van Kampen (1981) and Risken (1989).

A dynamical system is said to be Markovian, if the current dynamics of the system depends only on its present state and not on its history (see Honerkamp (1990)). At first sight, the dynamics of the granular model flow, wich is described in Section 5.2.4, is totally deterministic. The state of the granular flow is connected to all previous flow states by deterministic collisional laws and equations of motion governing the motion of all particles.

This situation changes completely, however, if only the time evolution of the vertical elevation h of one single particle in the flow is regarded. The present elevation h of a single particle cannot be related to the elevation of

the particle before its last collision: the value of the 1D measure h before collision cannot be back-calculated from the present h value, because the deterministic collision laws demand 9D state vectors $\psi = (\mathbf{x}, \mathbf{v}, \mathbf{w})$ for the two colliding particles as well as particle sizes and material parameters for a complete deterministic description of collisional dynamics.

Confining to the particle elevation h, the current value of this measure does not depend on its history before the last collision. This means, that the dynamics of $h(t)$ has Markov properties. This statement can be expressed in terms of conditional probability density distributions as

$$p(h_n, t_n | h_{n-1}, t_{n-1}; \ldots; h_1, t_1) = p(h_n, t_n | h_{n-1}, t_{n-1}), \tag{5.86}$$

where

$$p(h_n, t_n | h_{n-1}, t_{n-1}; \ldots; h_1, t_1) = \frac{w(h_n, t_n; h_{n-1}, t_{n-1}; \ldots; h_1, t_1)}{w(h_{n-1}, t_{n-1}; \ldots; h_1, t_1)} \tag{5.87}$$

and $w(h_n, t_n; \ldots; h_1, t_1)$ is the probability of the particle having been elevated at heights h_i at times t_i $\forall i \in 1, \ldots, n$, $n \in \mathbf{N}$.

Following Siegert et al. (1998), we apply a general method on the $h(t)$ time series of a single particle in the granular model flow. This method allows the determination of drift and diffusion coefficients of Fokker-Planck equations for continuous systems with Markov properties from noisy time series generated by these systems.

Regarding the 1D Markovian measure $h(t)$ of one particle in the granular model flow, the time evolution of the probability density function $w(h, t)$ of the stochastic variable h can be described by a Fokker-Planck equation.

$$\partial_t w(h,t) = -\partial_h \left(D^{(1)}(h,t) w(h,t) \right) + \partial_h^2 \left(D^{(2)}(h,t) w(h,t) \right). \tag{5.88}$$

$D^{(1)}$ and $D^{(2)}$ are the drift- and diffusion coefficients, respectively. They are defined as

$$\begin{aligned} D^{(1)}(z,t) &= \lim_{\tau \to 0} \frac{1}{\tau} \langle \tilde{h}(t+\tau) - h \rangle |_{\tilde{h}(t)=h} \\ &= \lim_{\tau \to 0} \frac{1}{\tau} \int_{-\infty}^{+\infty} d\tilde{h} \;\; p(\tilde{h}, t+\tau | h, t)(\tilde{h}(t+\tau) - h) \end{aligned} \tag{5.89}$$

and

$$D^{(2)}(z,t) = \lim_{\tau\to 0}\frac{1}{\tau}\langle(\tilde{h}(t+\tau)-h)^2\rangle|_{\tilde{h}(t)=h} \tag{5.90}$$
$$= \lim_{\tau\to 0}\frac{1}{\tau}\int_{-\infty}^{+\infty} d\tilde{h}\;\; p(\tilde{h},t+\tau|h,t)(\tilde{h}(t+\tau)-h)^2.$$

Equation (5.88) can be used for the description of the time development of statistical properties of turbulent cascades, see Naert et al. (1997) or Friedrich & Peinke (1997). For the analysis of elevation dynamics in the granular flow, we use the fact that the Fokker-Planck equation (5.88) is mathematically equivalent to a Langevin equation governing the dynamics of a stochastic measure. For the single particle elevation h, the Langevin equation reads:

$$\dot{h} = d_1(h,t) + d_2(h,t)\Gamma(t), \tag{5.91}$$

where $\Gamma(t)$ is a δ-correlated noise term with vanishing mean:

$$\langle\Gamma(t)\rangle = 0 \tag{5.92}$$
$$\langle\Gamma(t)\Gamma t'\rangle = \delta(t-t'). \tag{5.93}$$

The Langevin equation (5.91) is related to the Fokker-Planck equation by

$$d_1(h,t) = D^{(1)}(h,t) \tag{5.94}$$
$$d_2(h,t) = \sqrt{D^{(2)}(h,t)}, \tag{5.95}$$

so that according to Risken (1989) we finally can write:

$$\dot{h} = D^{(1)}(h,t) + \sqrt{D^{(2)}(h,t)}\Gamma(t). \tag{5.96}$$

So, by Equations (5.89) and (5.90), we can extract drift- and diffusion coefficients $D^{(1)}$ and $D^{(2)}$ directly from the noisy $h(t)$ time series of the particle

and relate them to a deterministic description of the time evolution of the single particle elevation h. The formal shape of Equation (5.91) allows to separate the deterministic part of the h- dynamics described by the SDE $\dot{h} = D^{(1)}(h,t)$ from the stochastic, noisy part $\sqrt{D^{(2)}(h,t)}\Gamma(t)$.

We now have gained a method to characterize the segregational dynamics of individual particles within the granular model flow. It is expected that $D^{(1)}(h,t)$ depends on the particle size and material parameters reflecting whether a specific particle tends to rise or sink down within the moving granular material.

Single large particle elevation dynamics in the granular model flow

Evaluation

Time series of the vertical position of single particles in the granular model flow were evaluated according to Equations (5.89) and (5.90) employing a numerical algorithm recently developed by Siefert (1999). To achieve reasonable averaging in (5.89) and (5.90), the evaluated time series need to consist of at least 10^4 data points. In the granular model flow, particle heights at times before and after a collision of the traced particle form a dynamic system with Markov properties described by (5.86). This is a necessary condition for the Fokker-Planck formalism to be applicable for the evaluation of the height time series.

As the mean interaction frequency of a single particle in the used granular model flow with particle material parameters $e = 0.8$, $b = 0.7$ and $\mu = 0.4$ is approximately 56 Hz, the model running time of 100 s normally used in the current work does not provide enough single particle elevation data points before and after a collisional event for reasonable evaluation of (5.89) and (5.90). For this reason a 1000 s elevation time series of a large particle with radius r=0.3 in a flow with granular material parameters $e = 0.8$, $b = 0.8$ and $\mu = 0.4$ was generated. The particle height h was only recorded for times when the particle was involved in a collision, so that the time series had Markov properties according to (5.86).

Figures 5.54, 5.55 and 5.56 show the components of the Langevin equation

(5.91) for the elevation time series of the large particle.

For reasons of comparison. from now the particle elevation $h^* = \frac{h}{h_{max}}$, which is normalized by the maximum flow height h_{max} of the regarded particle is considered. As the investigated flow was nearly stationary, the time dependencies in the drift- and diffusion coefficients $d_1(h^*,t)$ and $d_2(h^*,t)$ have not been taken into account. The coefficient d_1 governs the deterministic behaviour of the particle elevation, the diffusion coefficient d_2 denotes the strength of the noise $\Gamma(t)$.

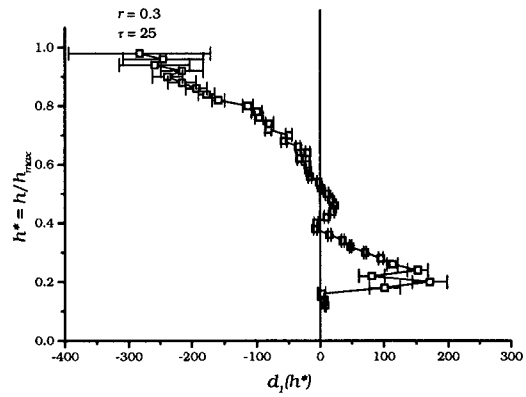

Figure 5.54: *Drift Term $D^{(1)}(h^*,t)$ of the Fokker Planck equation (5.88) or deterministic term $d_1(h^*,t)$ of the Langevin equation (5.91) for the elevation time series of a single large particle in the model flow. Plot against $h^* = \frac{h}{h_{max}}$: the particle elevation h is normalized by maximum elevation h_{max}. Time dependencies are not regarded in steady flow.*

As required by Equation (5.92), the noise term $\Gamma(t)$ depicted in Figure 5.56 has a (nearly) vanishing mean. Regarding the correlation function of $\Gamma(t)$ (fig. 5.57), the requirement of δ- correlation of $\Gamma(t)$ in equ. (5.92) can be assumed to be reasonably satisfied.

Interpretation

Omitting the noise term $d_2(h^*,t)\Gamma(t) = \sqrt{D^{(2)}(h^*,t)}\ \Gamma(t)$ in the Langevin equation (5.91), $d_1(h^*,t)$ can be interpreted as a deterministic description of the time evolution of the vertical position of the particle in the flow. Assuming the flow to be nearly steady, we can leave out the explicit time

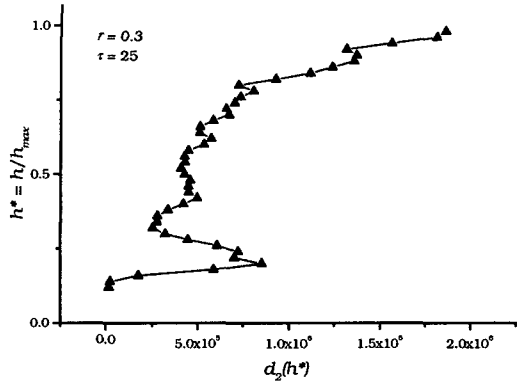

Figure 5.55: *Diffusion Term $D^{(2)}(h^*,t)$ of the Fokker Planck equation (5.88) or noise strength term $d_2(h^*,t)$ of the Langevin equation (5.91) for the elevation time series of a single large particle in the model flow. Plot against $h^* = \frac{h}{h_{max}}$: the particle elevation h is normalized by the maximum elevation h_{max}. Time dependencies are not regarded in steady flow.*

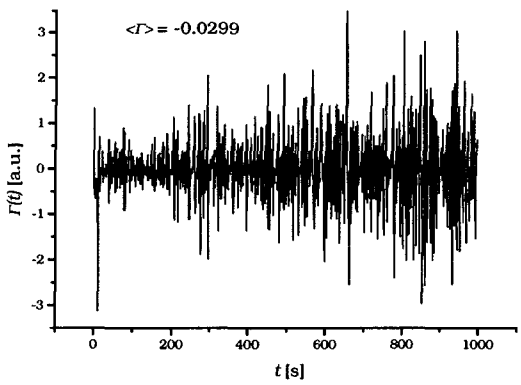

Figure 5.56: *Noise $\Gamma(t)$ of the Langevin equation (5.91) for for the elevation time series of a single large particle in the model flow.*

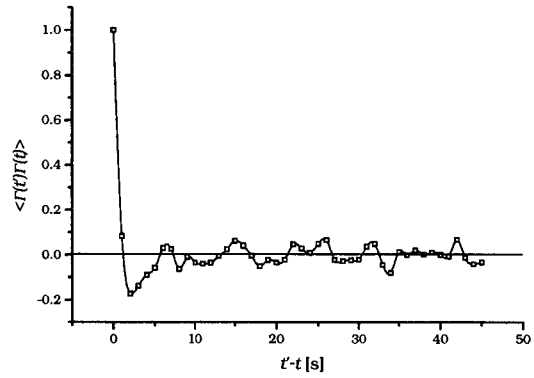

Figure 5.57: *Correlation function $\langle \Gamma(t')\Gamma(t) \rangle$ of the noise extracted from the elevation time series of a single large particle in the model flow.*

dependency of d_1 and write:

$$\dot{h}^* = d_1(h^*). \tag{5.97}$$

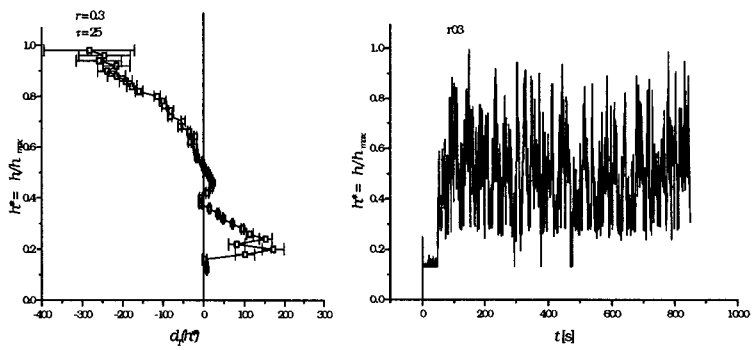

Figure 5.58: *Normalized height profile of $d_1(h^*)$ and normalized time series of particle elevation $h^* = \frac{h}{h_{max}}$ for single large particle.*

Regarding the plot 5.58 of d_1 against the normalized vertical position $h^* = \frac{h}{h_{max}}$ of the particle, one has to distinguish between ranges of $d_1(h^*) > 0$ and $d_1(h^*) < 0$. If $d_1(h^*) = 0$, the vertical particle position h does not change with time, $d_1(h^*) < 0$ means that the particle is sinking down in the flow, whereas $d_1(h^*) > 0$ describes an upward movement of the particle in the flow.

For normal flow heights $h^* < 0.4$, $d_1(h^*)$ is positive. This means that the particle will move to higher flow layers, if it sinks down into layers with $h^* < 0.4$. At $h^* = 0.4$, d_1 is null and the particle is kept constantly at $h^* = 0.4$ if it is not subject to fluctuations rising it into the range $h^* \in]0.4, 0.5]$. There $d_1 > 0$ causes the particle to rise out of this layer to $h^* = 0.5$, where $d_1 = 0$ again.

If the particle rises over $h^* = 0.5$, $d_1 < 0$, which is equivalent to the particle sinking down to $h^* = 0.5$ again. As the particle number density ν is decreasing for $h^* > 0.5$, this behaviour can be interpreted as the large particle moving on the top of the dense flow layer, to which it sinks back, if it is bouncing into higher layers, where there are not enough particle collisions to maintain the segregational effect. Figure 5.59 shows a normalized particle number density profile of the regarded granular model flow.

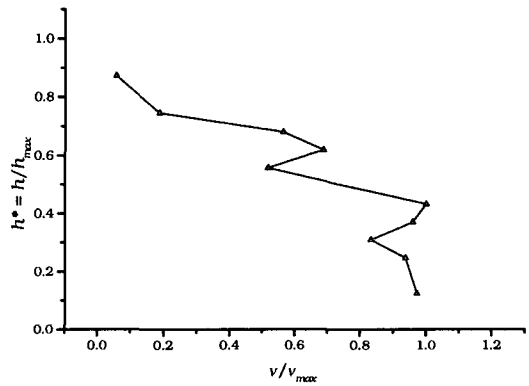

Figure 5.59: *Normalized particle number density profile of the granular model flow with e=0.8, b=0.7 and $\mu = 0.4$ at t=65s.*

The interpretation of $d_1(h)$ given above can also be directly intuitively compared with the normalized particle elevation time series. The particle often is situated at heights $h^* \approx 0.5$, which it reaches from above and below. The large positive values of d_1 at flow heights of $h^* \approx 0.3$ indicate that the particle is strongly driven upwards when sinking down to these lower flow region. Finally, the small d_1 values for $h^* < 0.2$ correspond to the initial flow state, where the large particle is dragged at the bottom of the flow with a small rising tendency, before it is squeezed out into a higher flow layer for the first

time.

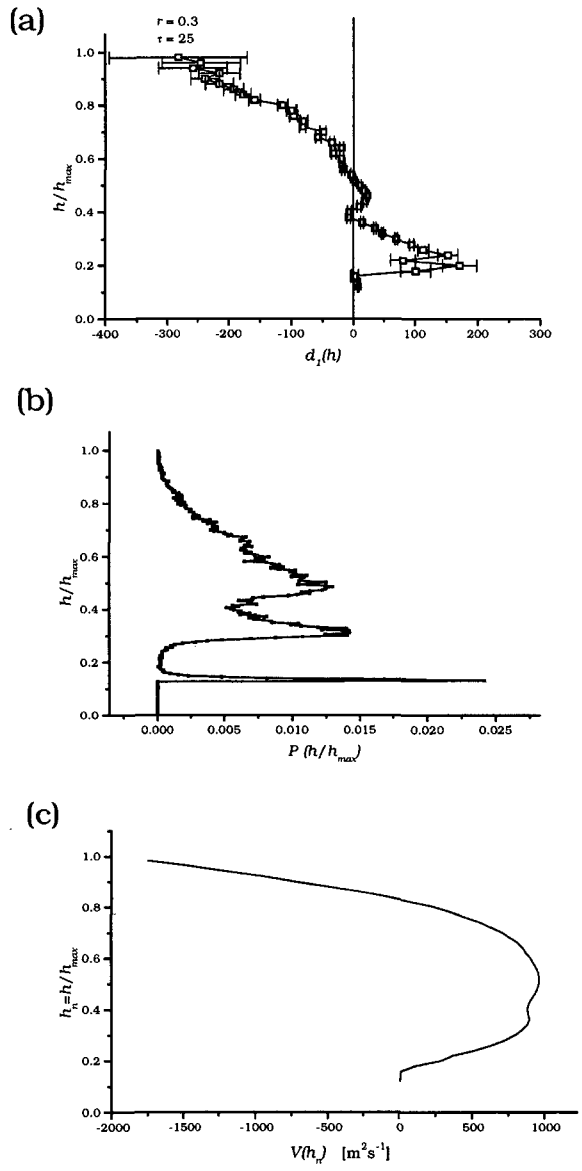

Figure 5.60: *(a) Drift coefficient $d_1(h^*)$, (b) probability of elevation $p(h^*)$ and (c) potential $-V(h^*)$ derived from the large particle elevation time series $h^*(t)$ within a flow of multidisperse particles with parameters $e = 0.8$ $b = 0.7$ $\mu = 0.4$. Potential minima and maxima of elevation probability correspond to stable fixed points h_0^* given by $d_1(h_0^*) = 0$ and $\partial_{h^*} d_1(h_0^*) < 0$.*

The motion of the large particle can also be regarded by the probability

ditstribution $p(h^*)$ of its elevation h^* (see fig. 5.60(b)): The marked lowest maximum corresponds to the particle bouncing downslope on the bottom with only very small elevations. The two maxima at higher elevations h^* correspond to the large particle riding on flow layers of other particles, from which it had been squeezed out before. Note that these two maxima are situated at the same elevations h_0^*, where the drift coefficient curve cuts the zero with a negative slope. Regarding the deterministic part $\dot{h}^*(t) = d_1(h^*)$ of the Langevin equation 5.91, this corresponds to stable fixed points of the elevation dynamics at $h^* = h_0^*$:

$$d_1(h_0^*) = 0, \qquad \partial_{h^*} d_1(h_0^*) < 0. \tag{5.98}$$

These fixed points are reflecting in the increased probabilities of the large particle to be found at elevations h_0^*. So equation (5.98) can be looked upon as the formal expression of particle elevation behaviour phenomenologically explained before.

Another point of view is provided by making use of general potential theory and interpreting $d_1(h^*)$ as gradient of a potential $V(h^*)$ governing the elevation dynamics of the large particle. Starting again from the deterministic part of Equation (5.91), we can write:

$$\dot{h}^* = d_1(h^*) = -\nabla_{h^*} V(h^*) \tag{5.99}$$

or

$$V(h^*) = -\int_0^{h^*} d\tilde{h}\ \ d_1(\tilde{h}). \tag{5.100}$$

The plots of $V(h^*)$ show two local minima at the elevations h_0^* of the stable fixed points of the large particle elevation dynamics. The particle is shifting between the two potential minima corresponding to different flow layers. The transition from one to another potential minimum or stable fixed point or flow layer, respectively, is induced by noise (i.e. fluctuations in the flow) lifting the particle over the barrier separarting the potential minima.

"Small" particle elevation dynamics

To demonstrate the influence of particle size on the single particle segregational dynamics, we now consider the normalized elevation time series $h^*(t)$ of one single "small" particle. Here, "small" means, that the particle had a radius of $r = 0.18$ m within a multidisperse mixture of spheres with a radius distribution $r \in [0.18, 0.3]$ m. Initially, the small particle was placed at the bottom, within the same flow as the large particle investigated before.

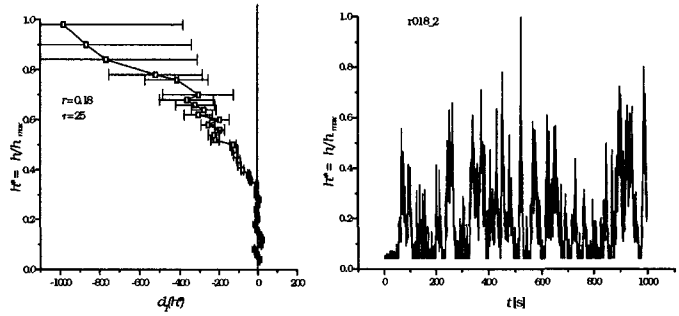

Figure 5.61: *Drift term $d_1(h^*)$ derived from small particle normalized elevation time series $h^*(t)$.*

Comparing the drift coefficient $d_1(h^*)$ of the small particle in Figure 5.61 to the one of the large particle (see fig. 5.58), a significant difference can be stated. For the small particle, $d_1(h^*)$ is hardly exceeding the zero line except some marginal fluctuations but is getting smaller than zero for $h^* > 0.4$. The large errors of d_1 for $h^* > 0.5$ are due to poor statistics: As the small particle elevation extremely seldom is exceeding $h^* = 0.5$, the accuracy in the computation of the conditional probabilities in Equations (5.89) and (5.90) decreases.

The noise strength term $d_2(h^*)$ for the small particle is shown in Figure 5.62. For $h^* < 0.5$, $d_2(h^*)$ is close to zero, which means that the small particle's dynamics $\dot{h}^*(t) = d_1(h^*) + d_2(h^*)\Gamma(t)$ is not strongly driven by noise for lower particle elevations h^*.

Comparing the drift term $d_1(h^*)$ (Fig. 5.63 (a)) with the probability $p(h^*)$ of elevation of the small particle (Fig. 5.63 (b)), the fixed points at h_0^*

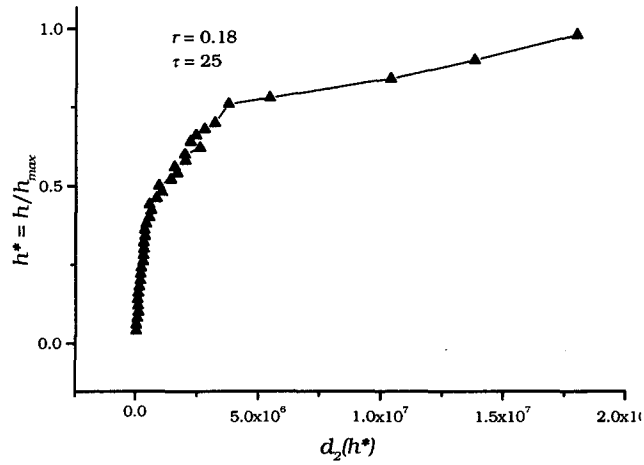

Figure 5.62: *Diffusion term $d_2(h^*)$ derived from small particle normalized elevation time series $h^*(t)$.*

with $d_1(h_0^* = 0,\ \partial_{h^*} d_1(h_0^*) < 0$ again correspond to maximum probabilities of elevation. Note that the $p(h^*)$ axis in Figure 5.63 (b) is logarithmic to amplify the maxima, which are only weakly evolved due to the very low positive values of $d_1(h^*)$. Finally, comparing the plots of $d_1(h^*)$ and $p(h^*)$ with the potential $V(h^*) = \int_0^{h^*} d\tilde{h} d_1(\tilde{h})$ of the small particle plotted in Figure 5.63 (c), a very slight minimum of V corresponds to the maximum in the elevation probability.

Furthermore, the small particle will fall back very fast down from elevations higher than $h^* > 0.4$, as $\dot{h}^* = -\nabla_{h^*} V(h^*)$. Regarding the very weakly evolved minimum of $V(h^*)$ at $h^* = 0.3$, which is separated from another weak minimum at $h^* = 0.15$ by a low barrier, one can conclude that weak noise (or flow fluctuations, respectively) can cause the small particle to fall down again into the lowest flow layer.

Conclusion

The stochastic analysis of particle elevation time series provides a deterministic description of single particle elevation dynamics, which is evidently dependent from particle size. Interpreting the zeros of the diffusion coeffi-

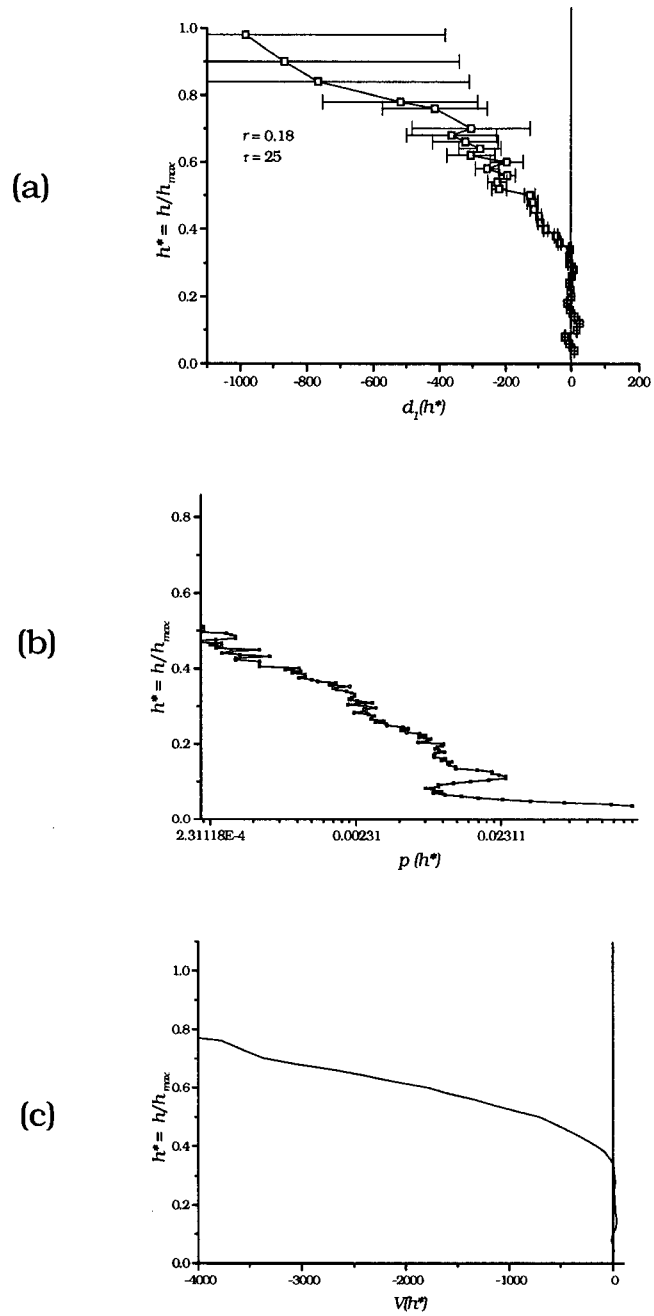

Figure 5.63: *(a) Drift coefficient $d_1(h^*)$, (b) probability of elevation $p(h^*)$ and (c) potential $-V(h^*)$ derived from the small particle elevation time series $h^*(t)$ within a flow of multidisperse particles with parameters $e = 0.8$ $b = 0.7$ $\mu = 0.4$.*

cients $d_1(h^*)$ with negative slopes as stable fixed points of particle elevation dynamics, one can determine the particle elevation, to which single particles of distinct size are driven by the deterministic laws of motion underlying the apparently noisy stochastic particle motion in vertical direction.

Once knowing the deterministic segregational dynamics of different sized particles one can, in principle, determine the segregational behaviour of a multidisperse granular flow without being forced to trace all individual particle trajectories. In the elevation dynamics of particles of distinct size, one has gained a deterministic description of the segregational behaviour of the flow.

The presented method of stochastic analysis of particle elevation time series appears to be a well suited tool for the description of the mesoscopic phenomenon of inverse grading of multidisperse granular flows.

5.5 Summary

This summary consists of some general remarks on the global essence of the present chapter and a more specific survey of the main results.

5.5.1 General Summary

A hard sphere model of multisisperse granular flow of inelastic frictional spheres was developed, which is able to reproduce the effect of inverse grading in granular flows.

Parametrical dependencies of global flow and segregational behaviour were investigated in the frame of the model. The range in the 3D particle material parameter space, for wich the model flow exhibits segregational behaviour, could be fixed.

A general continuum mechanical interpretation of the model flow failed. Nevertheless, in a special case, the constitutive relation between the second invariants of stress and deformation rate tensors could be found.

Stochastic analysis turned out to be a powerful tool for the extraction of deterministic single particle segregational dynamics from the apparently stochastic particle elevation time series.

Generally speaking, the effect of inverse grading could be reproduced by a simple hard sphere model. Analysis of the resulting model flows by various methods led to a deeper principle insight in the nature of the effect of inverse grading.

5.5.2 Main results

This summary gives a retrospective overview over the main results of each section of the chapter.

Section 5.1

Section 5.1 is a short introducing outline of the philosophy underlying the presented numerical work and gives a condensed synopsis of the sections of Chapter 5.

Section 5.2

The hard sphere model of multidisperse flows of inelastic frictional particles which was used for the numerical work is introduced in section 5.2.1. After a short general explanation, the general ideas of the model are outlined in detail:

- Using periodic boundary conditions, a laterally and longitudinally infinite granular flow can be obtained by computationally tracing a moderate number of $10^{2...3}$ particles.
- The model is based on the time-to-the-next-event algorithm. This means that all particles are moving freely subject only to gravity until any of the particles of the flow is involved in an event. An event is either a collision of two particles or the impact of a particle on the ground. So the computational effort needed in the model reduces to

the tracing of the ballistic particle trajectories and the determination of the event times. Both can fairly be done by simple analytical or standard numerical methods.

- The particles are assumed to interact by binary instantaneous collisions. This means that each two particles are interacting and that the whole interaction is assumed to happen in one distinct time point according to the hard sphere assumption. The interaction is parametrized by the longitudinal and tangential restitution coefficients e and b and the Coulomb friction coefficient μ of the colliding particles. According to reported theoretical and experimental investigations, this so-called Newton approach to particle interaction is well suited for binary particle collisions occuring in rapid granular flows which are described by hard sphere granular flow models.

Section 5.3

Section 5.3 is concerned with the numerical implementation of the hard sphere granular flow model and the evaluation of the model results. Flow modelling, evaluation and visualisation are done by the following components of a program package:

- The `abs` program performs the simulation of the hard sphere model flow. It is based on the time-to-the-next-event algorithm. Its discrete element structure is reflected in the simulation routines in which individual particles are represented by multidimensional data vectors consisting of spatial and velocity vectors, size and material properties of each particle.

- The global flow and segregational behaviour of the modelled single particle motions is analyzed by statistical means in the frame of the `evalcont` routines, which compute profiles of mean values and 2nd order moments of scalar, vectorial and tensorial flow properties as particle size, velocities and stress and strain rates.

- A graphic tool named `buntvis` was programmed using the AVS visualisation software. This tool allows direct visual observation of the model flow: the assembly of all particles participating in the flow can be displayed at any given time of the modelling time interval $[t_{start}, t_{end}]$ as defined in Figures 5.14 and 5.13.

In the course of the development of simulation and evaluation routines, the limitations of the used hard sphere model were apparent. Multiple particle interactions cannot be handled by the binary collision mechanism. Direct visual observation and statistical evaluation indicated the occurene of inelastic collapse for dense slow flows of strongly inelastic frictional particles. In the parameter range exhibiting inverse segregation, the simulations did not lead to such critical flow behaviour.

A systematic analysis of hard sphere model flows with various parameter combinations is provided in Section 5.4. The main results can be formulated as follows:

Qualitative views at the level of graphical display of the model flow are reported in 5.4.1. They provide principle insight in generic global flow and segregational behaviour. Depending on parameter values, the evolution of rapid, dilute flows or of dense flows finally coming to rest could be observed. Finally, flow behaviour corresponding to the random sieving and squeeze expulsion mechanisms, suggested by Savage & Lun (1988), could be observed visually.

The statistical tools provided in Section 5.3.3 are used for a more quantitative analysis of the parametrical dependencies of flow and segregational behaviour, which is outlined in Section 5.4.2. The flow behaviour is analysed varying the longitudinal and tangential particle restitution coefficients e and b and the Coulomb friction coefficient μ of the particles at different slope angles, initial flow velocities and particle number densities. The main results concerning the parametrical flow dependencies can be formulated as follows:

- The longitudinal restitution coefficient e is the most dominant parameter governing the behaviour of the model flow: At fixed a slope angle

of $\psi = 0.5\hat{=}28°$, stable flows exhibiting inverse grading only evolved for granular flows consisting of particles with a longitudinal restitution coefficient e in the range $0.75 \leq e \leq 0.85$. For granular flows with e lower than 0.75 the flow stops due to inelastic collapse, before inverse grading can develop for any other combination of the other particle parameters b and μ . The effect of inelastic collapse is related to the multiparticle interaction which is characteristic for slow dense granular flows for which the used hard sphere model cannot account. Values of e higher than 0.85, on the other hand, lead to a rapid flow, which is too dilute to exhibit segregational effects.

- An increase of the slope angle ψ at fixed material parameters e, b and μ causes a transition from decelerating to accelerating flow behaviour.

- Generally, inverse grading could only be observed in steady or slightly accelerating flows.

- An unique relation between the Coulomb particle friction coefficient μ and the flow friction angle (i.e. the bifurcation slope angle ψ at the transition from accelerating to decelerating flow behaviour) could not be found. The flow friction angle is not only determined by the particle friction but also by the particle inelasticity represented by the restitution coefficients e and b.

- The above points suggest that there exists a distinct parameter region in the 3D parameter space $\{e, b, \mu\}$, in which the granular model flows exhibit inverse grading. This parameter range was determined by numerous simulations with varying parameter sets.

- Variation of initial velocity and particle number density at fixed particle material parameters does not significantly affect the model flow and segregational behaviour.

- Lifting of larger particles by surrounding smaller particles ("squeeze expulsion") also works for large particles with densities 2-3 times as high as the densities of the smaller surrounding particles.

- As outlined in Section 5.4.4, a general continuum mechanical interpretation of the numerical results could not be given. The model flow did not satisfy the theoretical requirements of steadyness and homogenity which are necessary for a correct derivation of deformation rate tensors. In some special cases, a relation between the second invariants of stress and deformation rate tensors could be found and be interpreted either as Newtonian (linear) or Norton (power law) constitutive behaviour.

- Deterministic segregational dynamics of single particles could be extracted from the noisy stochastic time series of single particle elevation by the method of stochastic analysis, which is introduced in Section 5.4.5. The derived single particle elevation dynamics were found to depend on the particle size: the fixed points of elevation dynamics of larger particles are situated in higher flow layers than the ones of smaller particles. Stochastic analysis can be considered as a well-suited tool for the investigation of single particle segregational behaviour.

Chapter 6

Experimental work

This chapter contains the experimental and field work done in the frame of the current thesis and within the ABS-project. Section 6.1.1 describes observational and experimental field work, Section 6.2 deals with a laboratory experiment on the longitudinal restitution coefficient of snow balls. Section 6.3, finally, is concerned with the interpretation of the experimental results against the background of the numerical investigations performed in this work.

6.1 Field studies

The following section is concerned with field work on inverse grading in snow flow avalanches. Observations in avalanche debris indicating the occurence of inverse grading in flowing avalanches are reported as well as an experiment on the shape dependency of burial depth of equal sized bodies in an avalanche.

6.1.1 Observation of inverse grading in snow avalanche debris

The footprints of inverse grading in flowing avalanches can be found in the debris of snow flow avalanches. In describing the field obervations, we follow

a chronological path: From first qualitative impressions to the recording of debris profiles of particle size and, finally, a quantitative analysis of granular size distribution by digital processing of photographs of vertical profiles in avalanche debris.

Qualitative observation : The Brämabüel avalanches, April 1, 1997

Noon of March 31, 1997, four snowboarders had subsequently released two avalanches in the northeast exposed Brämabüel slope off the Jacobshorn ski resort near Davos. Fortunatedly, they survived the incident, though two of them had been caught by the avalanche. The slope had an inclination of about 36-40° or $\psi = 0.63 - 0.70$. The debris heights of the two avalanches were 80 and 200 cm, respectively.

Figure 6.1 shows the situation of the two avalanches and the points of observation, where the layering of the avalanche deposits was investigated. A corresponding terrain profile of the avalanches is provided in Figure 6.2.

The first point of observation was situated about 3.5 m upslope a slight terrain wall causing a slight terrain depression, in which the deposits of the first avalanche were situated. At this point of observation, the layer of snow, which had been deposited by the first avalanche, had a depth of about 45 cm. The upper 40 cm of the debris were formed by cube shaped snow lumps of approximately 10 cm diameter with an aspect ratio of about 1, the lowest 5 cm of the debris consisted of nearly spherical snow "granules" with a typical size of 1 cm. Below this layer, an old snow layer was situated, which had not been affected by the avalanche.

The second point of observation in this avalanche was situated 15 m upslope of the first one. There the deposit depth was 60 cm. The uppermost 30 cm were formed by large snow blocks with sharp edges which had been formed by fracture of the initial avalanche snow slab. The blocks had typical sizes of 20-50 cm and an aspect ratio of approximately 2. The next layer with a thickness of 20 cm consisted of smaller snow blocks with sizes of 10-20 cm and aspect ratios of about 2. Their axes of maximum extension were oriented horizontally. The lowest layer had a depth of 10 cm layer and

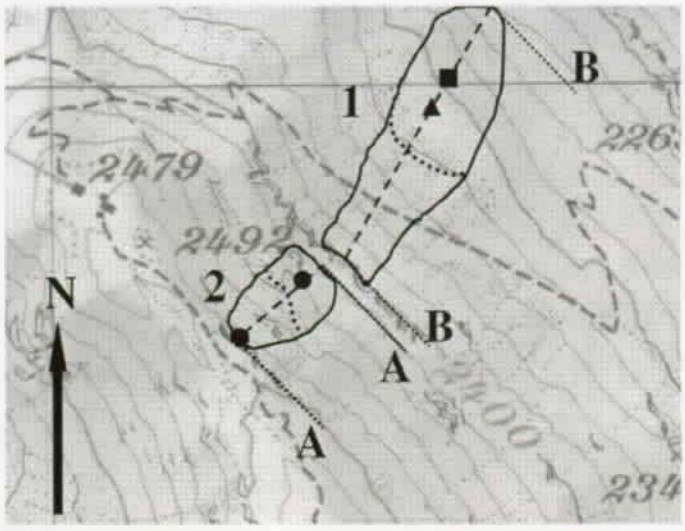

Figure 6.1: *Situation map of Brämabüel avalanches 1 and 2. The square denotes the first, the triangle the second point of observation in avalanche 1. The circle is the point of observation in avalanche 2, which had, according to the snowboard traces, been triggered at the point denoted by a cross. The upslope boundaries of the depositional areas of the avalanches are denoted by dotted lines. Terrain profiles along lines A-A and B-B are shown in Figure 6.2.*

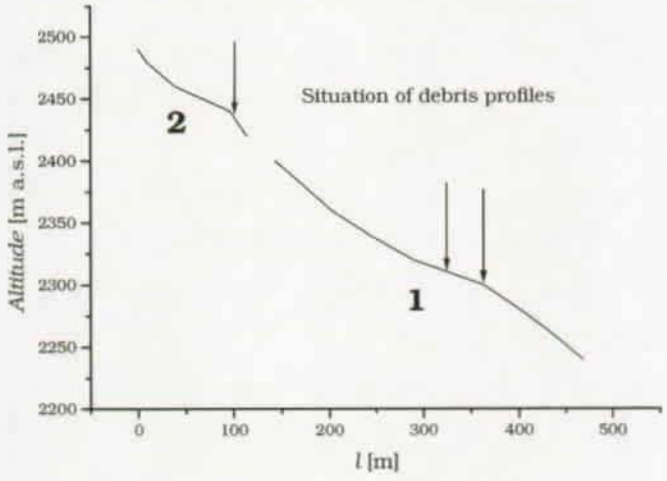

Figure 6.2: *Profile of the avalanche paths of the Bräemabuel avalanches 1 and 2 along lines A-A and B-B in Figure 6.1. Positions of observation are indicated by arrows.*

consisted of small snow lumps with typical diameters of about 2-3 cm.

This debris formation can be interpreted as a result of a plug flow with low internal velocity fluctuations, where the "plug" consisted of of snow blocks formed by fracture of the initial snow slab. The plug had been sliding on a fluidized layer of small snow particles subject to large shear and velocity fluctuations. The accumulation of the smaller spherical particles at the base of the flow may have been due to a random sieving process as well as to continuous fracture to smaller particles at the flow base.

The deposit of the second avalanche was situated above the fracture line of the first avalanche (see fig. 6.1). It was investigated in a terrain depression, where an accumulation region of the avalanche had developped, so that the deposit depth with an amount of approximately 2 m was larger than in the flat regions of the avalanche track. The uppermost 50 cm of the debris were again formed by raw snow blocks with typical sizes of 30-50 cm and an aspect ratio of nearly 1, the next 60 cm deep layer was formed by compressed snow blocks of 20-30 cm size and an aspect ratio of about 2. Their axes of maximum extent were partly oriented in downslope flow direction.

Below this layer, a 40 cm deep layer of small snow "granules" with 1.5-3 cm diameter, mixed with some erratic larger snow blocks was found. The last 40 cm of debris above the unaffected old snow layers were again formed by large, compressed snow blocks with sizes about 10-20 cm and an aspect ratio of about 2-3, which again were oriented in downslope flow direction. The voids between the blocks were filled with small snow particles. This lowest layer might have been the front of the avalanche with a characteristic debris profile similar to the one of the first avalanche, which had been stopped by the terrain depression and subsequently been buried by the following parts of the avalanche.

Concluding, these raw qualitative observations were indicating that snow flow avalanches are also subject to the effect of inverse grading in flowing granular material. Out of this observations, the idea emerged that it should be possible and reasonable to record detailed debris profiles of snow flow avalanches to investigate the segregational behaviour, which is, in some sense, conserved in the deposits of flow snow avalanches.

Debris profiles: Meierhoftälli avalanche, April 7, 1997.

Similar to the Brämabüel avalanche, the Meierhoftälli avalanche was released near the Parsenn ski resort in Davos by an off-piste snowboarder. The avalanche was released in the late morning of April 7 in a 38° inclined (i.e. $\psi = 0.66$), north exposed slope in an elevation of 2580 m a.s.l. The fracture height of the avalanche was 1 m, the avalanche track had a length of approximately 350 m, the width of the depositional zone was 200 m. The snowboarder survived the accident. In the afternoon, a snow profile was recorded in the fracture zone of the avalanche. Furthermore, profiles of particle size, density and snow characteristics in the depositional zone were recorded.

Figure 6.3: *Situation of profiles in the Meierhoftälli avalanche. Cross: situation of fracture profile (see Figure 6.6). Circle: profile in flat region of runout zone. Square: profile in accumulation zone near morraine wall. The upslope boundary of the depositional area is indicated by a dotted line. Line A-A is the profile line of the terrain profile in Figure 6.4.*

In the depositional zone, one profile was recorded in the flat runout zone of the avalanche, the other one was situated in a characteristic accumulation zone behind a moraine wall, as shown in Figure 6.3. A terrain profile of the Meierhofertälli avalanche is provided in Figure 6.4

Comparing the snow profile in the fracture zone (Fig. 6.5) with the debris profile in the flat runout zone (Fig. 6.6), one observes that the subsequence

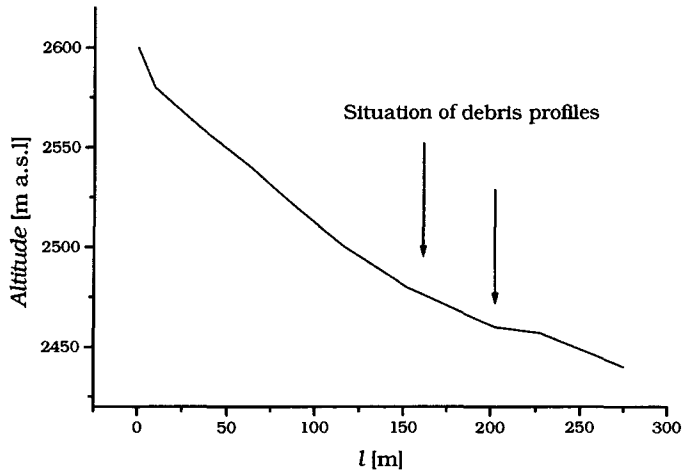

Figure 6.4: *Profile of the avalanche path of the Meierhofertälli avalanche along line A-A in Figure 6.3.*

of dominating snow crystal form is somehow preserved:

The upper layer of the debris is mainly consisting of snow lumps of new and fragmentated snow, which is also forming the upper layers of the snow slab in the fracture zone of the avalanche. Also the crystal form of the next slab layer is dominating the lower debris layers. Nevertheless, there is no one-to-one correlation between the slab layers and the debris layers. Small snow lumps consisting of snow with the same crystal form as the uppermost snow slab layer were also found in the lower debris layers.

This fact can, regarding the height dependence of particle size recorded in the debris profile shown in Figure 6.6, be interpreted as an indicator of inverse grading in the flowing avalanche. Note that the main portion of the uppermost snow slab layer seems to have stayed on the surface of the flowing avalanche, while it had been breaking into large lumps. Only small fracture parts of the upper layer could reach lower flow layers due to random sieving.

In the accumulation zone behind the moraine wall, a total snow depth of 7 m including snow cover and debris was determined by sounding. Regarding the mean depth of the undisturbed snow cover around, the total debris depth was estimated to be 5 m. A debris profile was recorded into a depth of 3.5 m in the accumulation zone. This profile is shown in Figure 6.7.

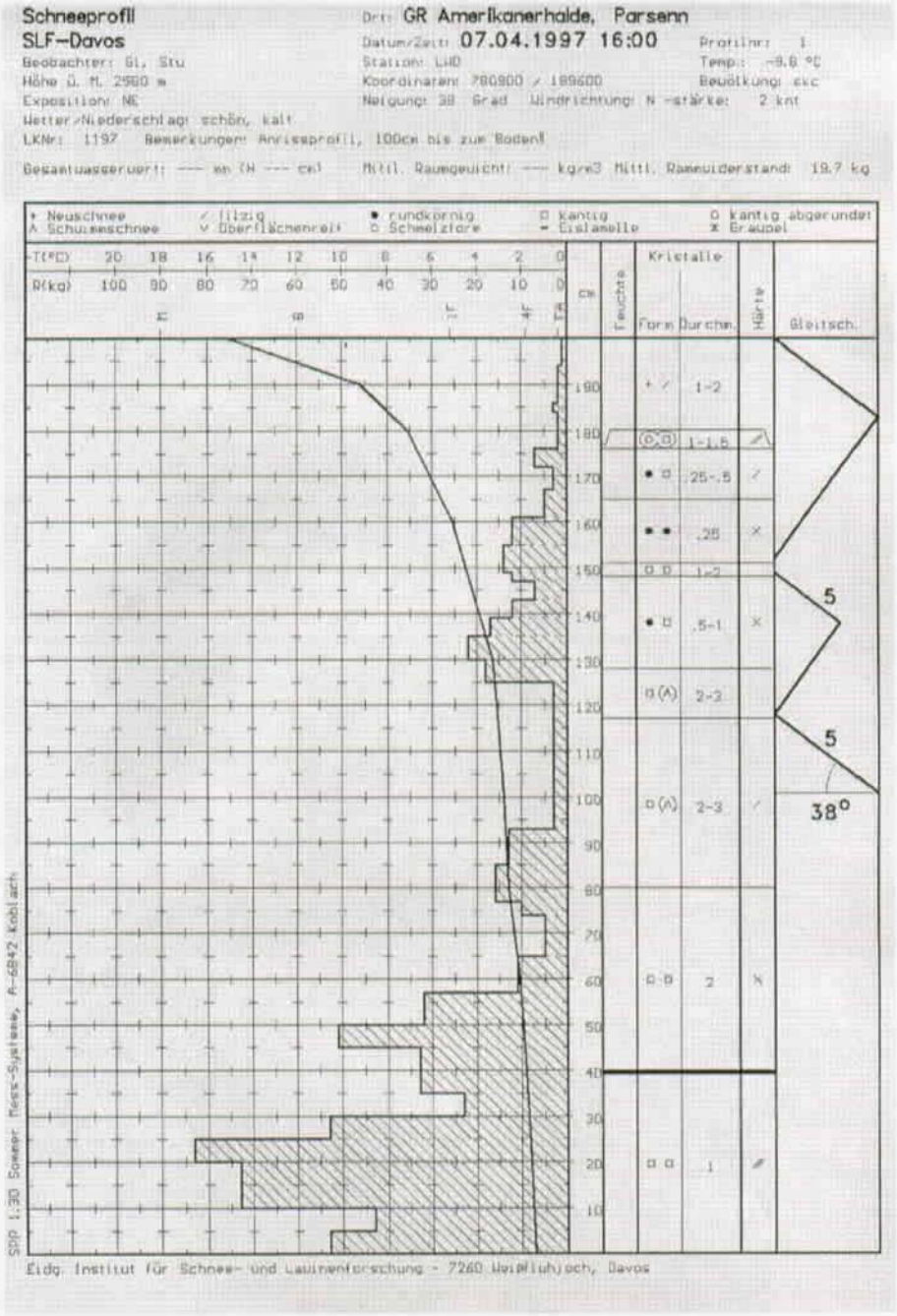

Figure 6.5: *Fracture profile of Meierhoftälli avalanche.*

Similarly to the upslope debris profile in Figure 6.6, the snow crystal type of the upper debris layer is the same as the one in the upper layer of the

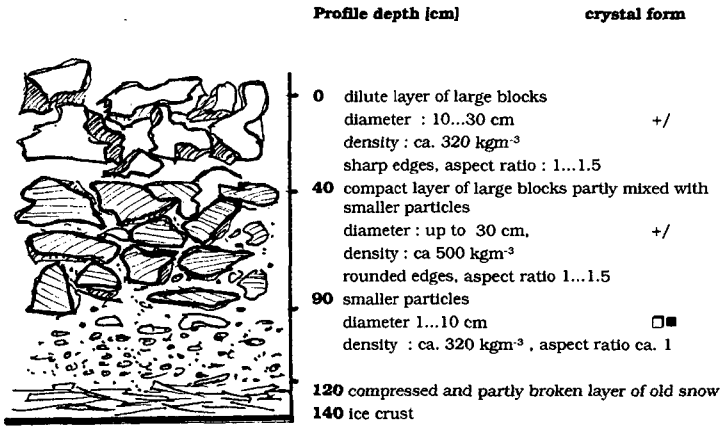

Figure 6.6: *Debris profile in the flat runout zone of Meierhoftälli avalanche.*

snow slab in the fracture zone. The snow crystal types in the lower debris layers seem to be a mixture of the snow crystal types in the lower snow slab layers.

The accumulation zone profile (Fig. 6.7) shows alternating layers of larger and smaller particles. This observation could be explained by the fact that the avalanche head had been stopped by the moraine and then been overtaken by the subsequent, almost segregated avalanche flow. However, comparison of snow crystal subsequence in the fracture zone profile with the one in the debris profile shows good correlation and makes this interpretation less likely.

Assuming that the avalanche flow had been a plug flow with low relative particle velocities in the main part of the flowing layer except a thin shearing layer (the so-called fluidized layer with high relative particle velocities) would leave the original slab layers relatively undisturbed. As no overall mixing of the flowing snow happened, no segregation over the entire debris depth was observable. Segregational behaviour only developped within the separate layers.

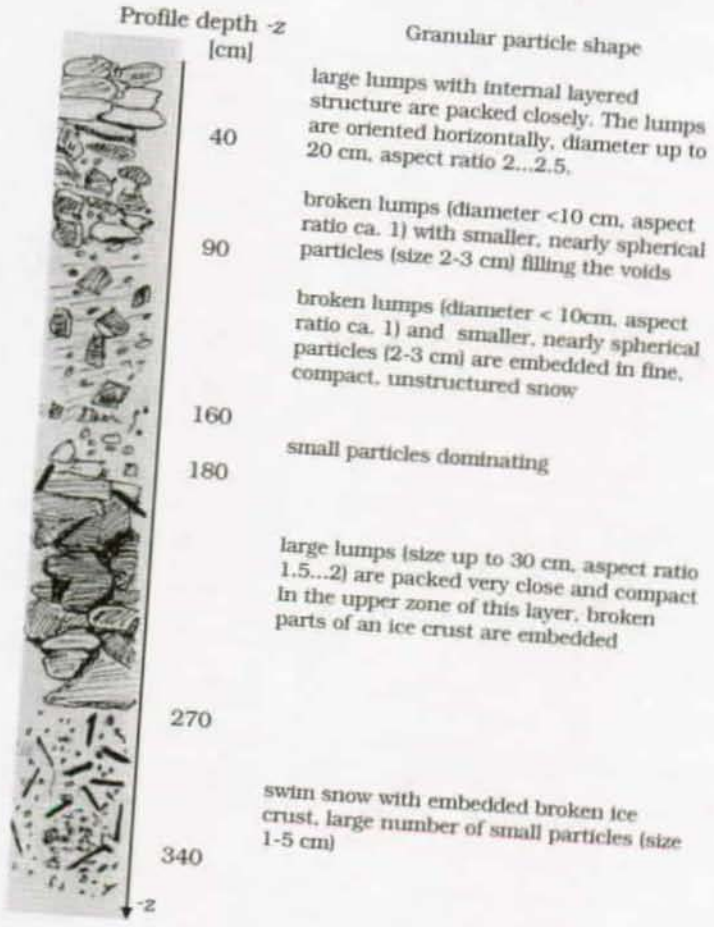

Figure 6.7: *Debris profile of Meierhoftälli avalanche in accumulation zone behind moraine wall.*

The profile in Figure 6.6 then has to be interpreted as "upper part" of the profile shown in Figure 6.7. It had been forming the tail of the avalanche and been deposited upslope the moraine wall in the avalanche track.

Subsuming, the Meierhoftälli avalanche profiles provide evidence for segregational behaviour within separate flow layers, which are conserved as the avalanche shows plug flow behaviour due to a smooth avalanche track.

Dry slab avalanche: Gaudergrat avalanche 09.12.98

During field work at the SFISAR Gaudergrat experimental site near the Parsenn ski resort in Davos, a large snow slab extending over the whole width of the south-exposed slope was released. Snowfalls with northern winds had built up an unstable layer of new snow the days before. The deposit of the avalanche was consisting of the new snow of the recent precipitation period over the entire profile depth. The new snow crystals had been fragmentated by wind and had a size of approximately 0.25 mm. A debris profile was recorded in a flat region of the runout zone of the avalanche; the depth of debris was 1.4 m.

The debris surface was formed by large snow lumps with an average size of 20 cm and a density of 116 kgm^{-3}. The lower layers showed no distinct structure. They consisted of unstructured snow with some embedded small snow particles with 2-5 cm diameter. The most interesting finding is that the mean density of the snow lumps forming the debris surface was appoximately 7% higher than the density of the lower layers of the debris. As the heavier large particles had obviously been transported by the less dense layers of small particles and unstructured snow, the profile may be interpreted as a indicator of inverse grading in the Gaudergrat avalanche.

Wet flow avalanche: Vallée de la Sionne, 15.12.98

In the SFISAR experimental site in Vallée de la Sionne near Sion, VS, a wet flow avalanche was spontaneously released at December 13, 1998. The total length of the avalanche track was about 1500 m, where the slope angle in the south-east exposed fracture zone was about 40-45° ($\psi = 0.70 - 0.79$) and decreased down to 15-20° ($\psi = 0.26 - 0.35$) in the depositional area. The elevation of the fracture zone at "Crêta Besse" was 2490 m a.s.l, the depositional area was divided into two parts which were situated from 2150 m a.s.l. down to 2050 m a.s.l. and from 1800 m a.s.l. down to "Les Evouettes" at 1550 m a.s.l. The avalanche track is shown in Figure 6.8; the terrain profile along the centerline of the avalanche track is provided in Figure 6.9.

Due to its humidity, the flowing snow had formed snow lumps of different

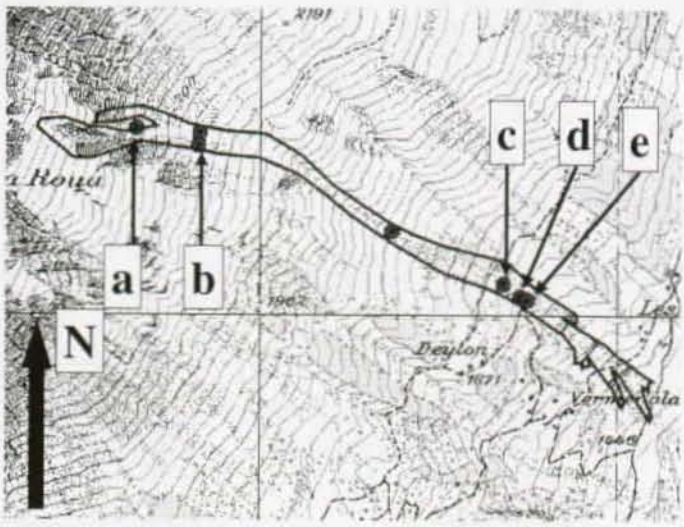

Figure 6.8: *Avalanche track of the Vallée de la Sionne avalanche. The points a-e are the observational points where debris profiles were examined which are referred in the text*

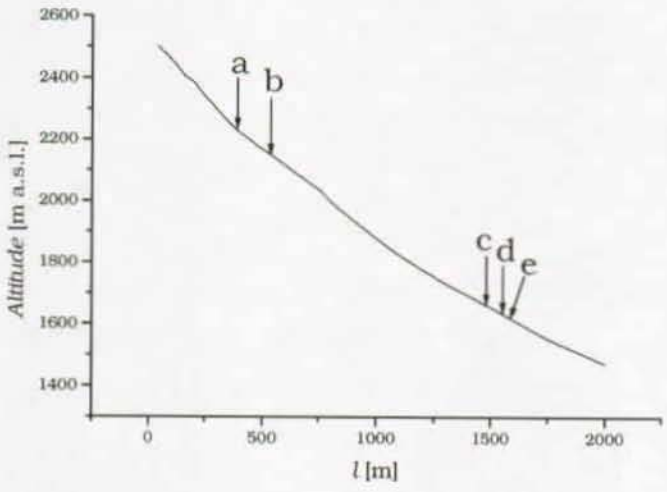

Figure 6.9: *Terrain profile along the centerline of the Vallée de la Sionne avalanche track with observational points as indicated in Figure 6.8.*

sizes with rounded, even nearly spherical shape, as shown in Figure 6.10.

Erosion and deposition profiles were recorded along lines perpendicular to the flow direction at different elevation levels to get a picture of the mass balance of the avalanche. This recordings gave opportunity to also record

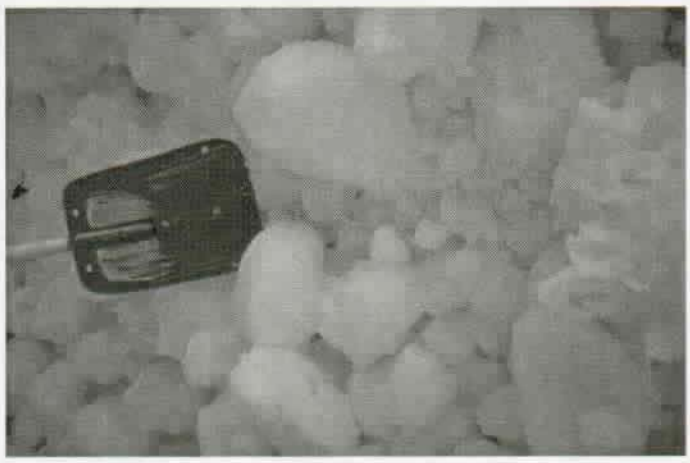

Figure 6.10: *Rounded snow lumps in the debris of a wet flow avalanche in Vallée de la Sionne, VS. Photograph by Peter Gauer, SFISAR.*

the snow particle size distribution in the avalanche deposit at various downslope positions of the deposition area. At any profile position, the deposit consisted of agglomerated, nearly spherical wet snow lumps over the entire profile depth. All particle size profiles indicated that inverse grading had occurred over the entire flow height. The profiles recorded at the positions indicated in Figure 6.8 are described in the following:

(a) The fracture profile and a view over the whole of the fracture line indicated, that the initial snow slab had a thickness of only 20 cm. The main part of avalanche mass had been accumulated by entrainment of the (wet) snowcover in the avalanche track.

(b) The first profile including deposition was taken at an elevation of 2145 m a.s.l., where the depth of debris was 50 cm. Particles with a typical diameter of 20 cm formed the upper 30 cm of debris, particle sizes in the layer below ranged from 5 to 10 cm. At another position at the same elevation, the upper layer of 60 cm debris consisted of lumps with diameters of 30-50 cm, where particle sizes in the lower 20 cm layer were 10-15 cm.

(c) At an elevation of 1660 m a.s.l. the debris was ca. 35 cm deep. The upper 25 cm consisted of snow lumps with sizes of 10-15 cm, some

single lumps were exceeding a size of 30 cm. In the lower 10 cm, particles were smaller than 5 cm, most of them had a size of 1-2 cm.

(d) The profile at 1635 m elevation showed 70 cm deposition depth and could be divided into three characteristic layers: The uppermost 20 cm of the layer consisted of 15-20 cm large lumps. Some single lumps on the deposit surface even had a size of up to 50 cm. In the next 20 cm layer of the debris, typical particle sizes were smaller than 15 cm, some of the particles were smaller than 3 cm. The lowest 20 cm layer consisted of particles smaller than 10 cm.

(e) Somewhat downslope at 1620 m a.s.l., the debris was 50 cm deep and particle sizes were nearly continuously decreasing from 20-30 cm at the surface to 2 cm near the bottom, which was, similarly to all other profile locations, formed by compressed old snow.

In the regions of profiles (d) and (e), vertical cuts of the debris were photographed. The profiles shown in Figure 6.11 were obtained by means of digital image processing: after enhancing the contours of the photographs, the mean projected particle areas in subsequent layers of the photographed profile were determined. The mean effective particle radius shown in the profile graphs was computed as normalized square root of the mean projected particle area.

Inverse grading can clearly be seen in the profiles of mean particle sizes of the avalanche debris.

Large lumps on surfaces of large avalanches

During the extreme precipitation periods in January and February 1999, many large and hazardous avalanches went down in the Alps. In February 26, an excursion was made into the Reuss Valley, UR. Avalanches were photographed from a distance and, if possible, directly from the runout zone. In case of wet snow avalanches, snow lumps had formed, as shown in Figure 6.12. By agglomeration, they had reached sizes of more than 1 meter, even snow "particles" with 3 m diameter could be observed on the surface

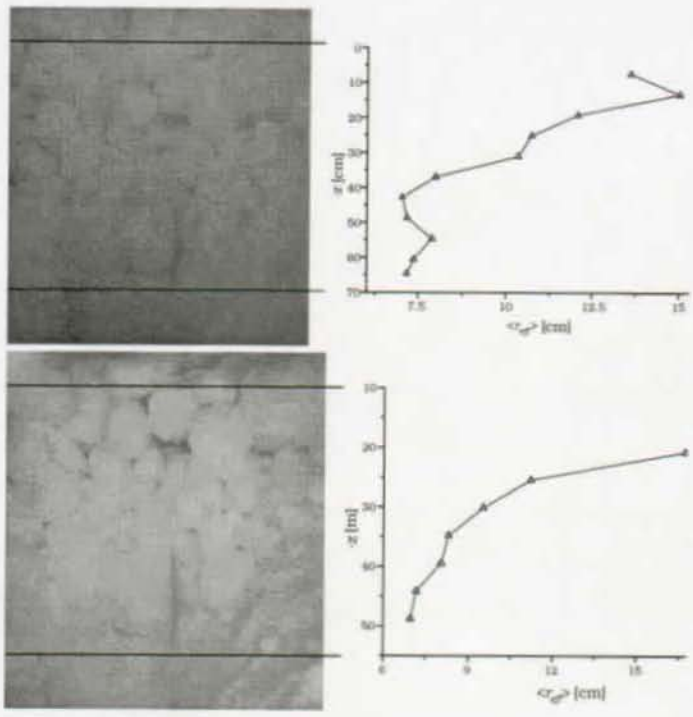

Figure 6.11: *Particle size profiles extracted from photographs of the wet flow avalanche in Vallée de la Sionne.*

of the debris of the large avalanches. Debris heights of the large avalanches had reached more than 10 m. Furthermore, the debris had been frozen after deposition. These conditions did not allow the recording of debris profiles.

Regarding the debris at the sides of the flow channels, however, gave rise to the assumption, that also the snow lumps in the extreme avalanches had been subject to inverse grading.

Figure 6.12: *Wet snow lumps formed by agglomeration on the surface of the debris of Whylerlaui, UR. Photograph by Urs Gruber, SFISAR.*

6.1.2 Field test of shape dependency of inverse grading

The numerical hard sphere model used for the investigation of inverse grading in the frame of the current work can only handle spherical particles. The inclusion of other particle shapes would have increased the computational effort dramatically. In order to get a qualitative idea of shape effects on the segregational behaviour of large particles, a field experiment was performed. In this experiment, the segregational behaviour of large bodies with equal volumes and densities was examined with respect to any dependencies from body shapes. As avalanche field experiments usually consume lots of time and equipment, an important boundary condition of this experiment was to keep the effort as low as possible. Test bodies with equal volume and densities were placed in an avalanche slope. After some time they were embedded by new fallen and wind driven snow. Then an avalanche was artificially released in the test slope and flow- and segregational behaviour of the bodies within the avalanche was studied. An extensive description of the experiment with special respect to practical aspects of avalanche experiments is given by Kern (1998).

Experimental setup

Test bodies

In the experiment, 12 test bodies were used, which each had a volume of 150 l, similar to the volume of an inflated avalanche balloon. Each three of the test bodies had cube, sphere, tetraedrical or cylindrical shape. The test bodies consisted of a wrap made of the same orange coloured nylon material as the avalanche balloons. This material is characterized by its good visibility and sliding properties on snow. The body wraps were equipped with a zip so that they could be filled with snow. The filling of the bodies with packed snow resulted in an overall density of approximately 450 kgm^{-3}, which is slightly higher than the one of the surrounding snow in a flowing avalanche and is also a good approximation to the overall density of a skier with inflated avalanche balloon. As all the test bodies had the same volume and density, their flow- and segregational behavior in an avalanche

Table 6.1: Geometrical characteristics of the test bodies

shape	$\mathcal{A}$	$\mathcal{V}$	$\Omega[\mathcal{V}^{-\frac{1}{3}}]$ or m^{-1}	r_{body} or a_{body}
sphere	$4\pi r_{sph}^2$	$\frac{4}{3}\pi r_{sph}^3$	$\sqrt[3]{\frac{36}{\pi}} \approx 2.25$	$r_{sph} \approx 0.33$ m
cylinder	$2\pi r_{cyl}^2(1+\alpha)$	$\alpha\pi r_{cyl}^3$	$2\frac{1+\alpha}{\alpha}\sqrt[3]{\alpha\pi} \approx 5.81$	$\alpha = 4 \quad r_{cyl} \approx 0.23$ m
cube	$6a_{cub}^2$	a_{cub}^3	6	$a_{cub} \approx 0.53$ m
tetraeder	$a_{tet}^2\sqrt{3}$	$\frac{a_{tet}^3}{6\sqrt{2}}$	$6\sqrt[6]{3} \approx 7.21$	$a_{tet} \approx 1.08$ m

was expected to depend only from their shape. The shape of the test bodies can be parametrisized by the surface-volume ratio Ω:

$$\Omega = \frac{\mathcal{A}}{\mathcal{V}}, \tag{6.1}$$

where $\mathcal{A}$ is the body surface and $\mathcal{V}$ its volume. Table 6.1 lists volume $\mathcal{V}$, surface $\mathcal{A}$ and surface-volume ratio of the used bodies, where r_{body} and a_{body} denote radii and edge lengths of the bodies. The ratio of height h_{cyl} and radius r_{cyl} of a cylinder is α, i.e. $h_{cyl} = \alpha r_{cyl}$. For any body shape, the surface-volume ratio Ω is inversely proportional to the cubic root of the volume. Accordingly, Ω is written in units of $\mathcal{V}^{-\frac{1}{3}}$.

As can be seen in the above table, the surface volume ratio Ω is increasing from sphere to tetraeder via cylinder and cube. The surface volume ratio of tetraedrical bodies is approximately three times as high as the one of a spherical body.

Test site

The following requirements have to be posed to a slope which is intended to be used for avalanche experiments:

- Exposition of slope in the north direction sector. This ensures that the slope lies in the shade which is supporting the evolution of good conditions for avalanche release.
- Sufficient slope inclination angle ($\geq 28°$ or $\psi \geq 0.49$, respectively).
- Good accessibility and vicinity to cable railways are neccesary to allow material transport without use of helicopters.
- No endangering of persons at adjacent ski runs and off-piste ski routes.

These requirements were optimally joined by a nothwest- exposed slope with an inclination of aproximately 37° in the vicinity of the upper exit of the Flüelamäder ski lift in the Pischa ski area near Davos. The slope could be accessed relatively safely by a ridge forming the slope boundary in western direction. From there one could carefully enter the slope in eastern direction.

First test February/March 1998

Preparation and positioning of test bodies

The bodies had to be placed in the slope before an expected period of snowfall. After a long dry period, end of February 1998, a transition of the weather situation towards to a northern situation with precipitations was emerging. Thus in 27th of February, the test bodies were prepared and positioned into the test slope, as indicated in Figures 6.13 and 6.14.

Figure 6.13: *Track of the test avalanche in the test slope near Pischa ski area, Davos. The initial position of the test bodies is denoted by a triangle, the square indicates the final positon of the test bodies after the avalanche event. The avalanche was released at the position ⋆ by an explosive charge. The boundary of the depositional area of the avalanche is marked by a dotted line. Line A-A refers to the terrain profile of the avalanche in Figure 6.14.*

At the scheduled initial position in the slope, the body wraps were filled

with snow, so that the intended body shapes were obtained. The bodies then were placed in the slope.

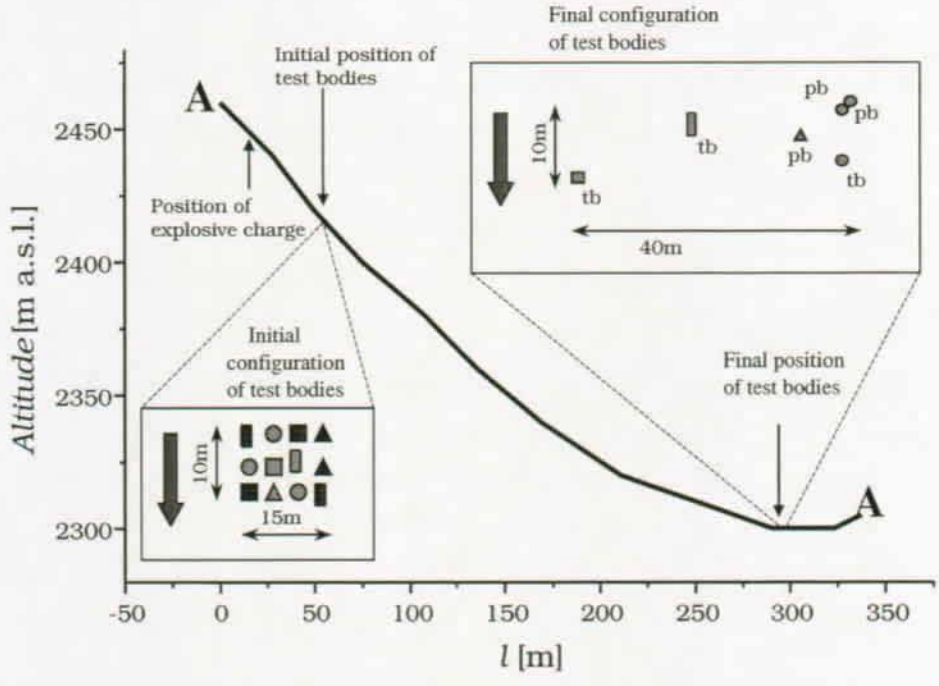

Figure 6.14: *Terrain profile of the Pischa test avalanche along line A-A in Figure 6.13. The initial and final positions and configurations of the test bodies before and after release of the test avalanche are shown. The fat arrows indicate the avalanche flow direction. After the avalanche event, the bodies in the depositional area of the avalanche were either partly buried (pb) or totally buried (tb). Bodies which remained at the initial position after avalanche release are drawn darker than the bodies, which were carried away by the avalanche.*

The initial positions of the bodies were chosen approximately 70 meters downslope the upper edge of the slope in a probable avalanche path. Furthermore, the initial position was situated in the lee of the western limiting ridge, so that northwestern winds could be expected to deposit snow additionally to the deposition by snowfall. The bodies were placed in three rows with each 4 bodies. Every body shape occured once in each row (see also Figure 6.14).

In the two weeks after positioning of the bodies, precipitations were not

sufficient to provide good conditions for avalanche release. The snowfall periods were interrupted by short high pressure periods embedded into a northern weather situation. The interim periods of high pressure (i.e. sunny weather) caused rapid settling of the previously fallen new snow, especially in conection with relatively high temperatures and the increasing radiation from sun due to rising spring. Thus the snow inside the nylon wraps giving them their shape was partly melting. This caused the bodies to freeze at the bottom and lose a part of their volume.

In the interim sunny weather periods, the snow fillings of the bodies were completed again and the frozen bodies were loosened from the bottom. The snow deposited during the previous precipitation periods, which had been partly molten and frozen again, was removed to prevent the bodies to be connected too strongly to the slope. This could have prevented them from being carried away by the test avalanche. The fact, that the snow *inside* the bodies had been molten and frozen again, made the bodies much harder and helped them to keep their shape even under mechanical strain.

Unfortunatedly, the loosening of the bodies from the ground also caused two bodies to slide away approximately 200 m from their initial position into the mid of the test slope. (Nevertheless, they finally were taken away by the avalanche.) From the 13th of March 1998, a period of extensive snowfall prevented any access of the test slope to loosen the bodies, if they would have been frozen to the ground again. Finally, at the 17th of March, an avalanche could succesfully be released.

Avalanche release

In the morning of the 17th of March 1998, thick fog was covering the Pischa area above an elevation of 2300 m a.s.l. Nevertheless, an attempt was made to release an avalanche, because the relatively high temperatures gave rise to the fear that the new snow would rapidly settle down. This would have significantly decreased the possibility for a successful avalanche release. The avalanche was released by an explosive charge of 7.5 kg dynamite, which was attached at a children plastic bob sleigh. The sleigh with the charge was positioned at the position indicated in Figures 6.13 and 6.14 by letting it slide into the slope at a rope, which was fixed, when the sleigh had reached

the demanded position. This had to be done relatively quickly, for the explosives where ignited by a fuse with a burning duration of 1.5 minutes.

Due to the thick fog, the avalanche release only could be observed acoustically: After the detonation of the charge, one could hear the sound of sliding snow and an air draught could be felt, which probably was caused by the avalanche developping a powder part. The only visual observation was obtained by an infrared camera placed on a ridge in 200 m distance in eastern direction from the initial position of the test bodies. Some raw pictures of the charge detonation and the initial avalanche flow were obtained this way. For the weather did not show any tendency to clear up, the recording of experimental results and the recovery of the test bodies could not be performed at the same day as the avalanche release.

Results

The day after, the weather was clear and the effect of avalanche release could be observed: the detonation had released an avalanche with a slab width of 200 m and a mean fracture height of 50 cm. Even in the slope on the other side of the west bounding ridge of the test site, an avalanche had been released. The sliding surface in the release area of the avalanche showed a slate-like structure. A distinct sliding layer could not be determined: the avalanche had been sliding down on many different changing, vertically closely adjacent layers, which can be imagined from Figure 6.15. This picture also shows six test bodies, which had not been taken away by the avalanche.

Obviously, the deeper snow layers had been compressed by repeatingly stepping into the area of initial positions of the test bodies during the preparation of the experiment. For this reason, the lower layers of the snowpack kept lying as a compact slab. In this slab area, only a thin surface layer of snow had been carried away by the avalanche, which could not tear off all test bodies embedded in the slab. The bodies, which were not taken away, probably had been connected to the slab by melting and freezing. Finally loosening them was demanding great mechanical effort. The cube and the cylinder body, which had been sliding away from the initial position before

Figure 6.15: *Initial position of test bodies after avalanche release. Some bodies were not taken away by the avalanche; they kept lying embedded in a slab-like layer of compressed snow.*

avalanche release, nevertheless had been dragged by the avalanche.

The avalanche debris had an approximate width of 300 m and a depth of 1.5-2 m. In the "stauchwall"-region, the debris had a depth of more than 3 m. Figure 6.16 provides an overview over the test site with avalanche slope and debris region. The mean size of snow lumps was about 20-30 cm in the uppermost 50 cm of the debris. In deeper debris layers, mean particle sizes were significantly smaller and the debris was more compact. The limited time of daylight did not allow the recording of a detailed particle size profile of the avalanche debris additionally to recovery and recording work.

Two of the bodies, which had been dragged by the avalanche, were visible at the surface of the avalanche debris even from the upper edge of the test slope. It was the two spherical bodies (see Fig. 6.17). Also the edge of a tedraedrical body was visible on the debris surface, if one was standing closely before it. All other bodies were totally buried and had to be searched employing a Recco^{TM}device (the bodies had been equipped with

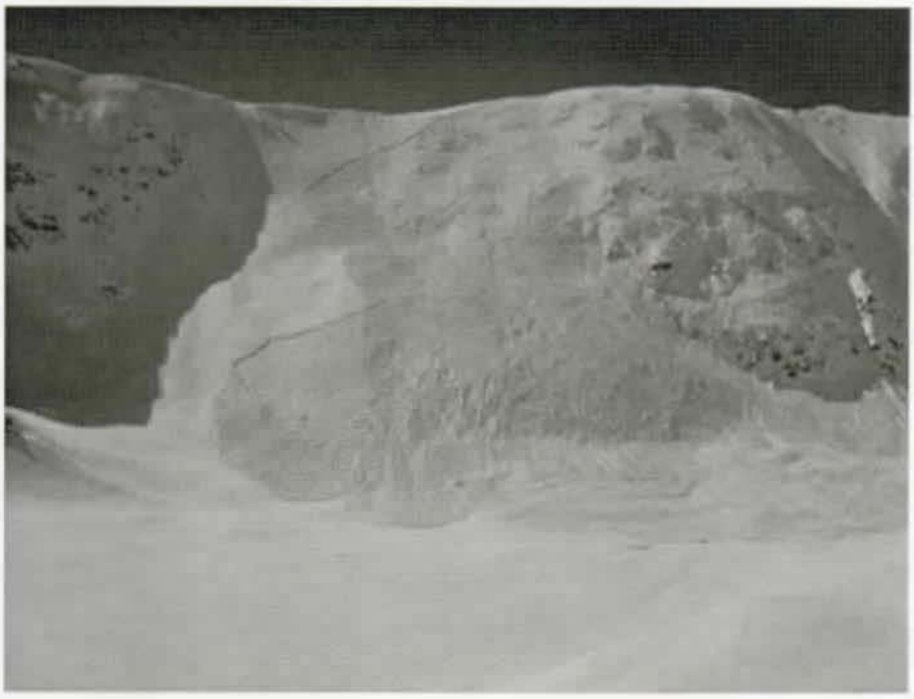

Figure 6.16: *Test slope with debris of the test avalanche.*

Figure 6.17: *Spherical bodies visible at the surface of the avalanche debris.*

Table 6.2: Burial depths of the various test bodies

shape	$\rho_b[\frac{kg}{m^3}]$	$\rho_s[\frac{kg}{m^3}]$	$\phi = \frac{\rho_b}{\rho_s}$	$\frac{\Omega}{\Omega_{sphere}}$	h_b[m]
sphere 1	452	452	1.00	1.00	0
sphere 2	484	452	1.07	1.00	0
sphere 3	462	400	1.156	1.00	0.7
cylinder	447	413	1.08	2.58	0.4
cube	484	347	1.40	2.67	0.46
tetraeder	437	400	1.093	3.20	0.55

Recco^{TM}tranceivers before placing them).

The final positions of the dragged test bodies in and on the debris are sketched in the terrain profile in Figure 6.14. The positions and burial depths of the test bodies were recorded, the latter were measured with respect to the center of mass of each body and were varying from 0 to 0.7 m.

Of course, the evaluation of positions and burial depths of the six bodies dragged by the avalanche does not allow statistically relevant statements. The data provided by the experiment permits, in the best case, some reasonable speculations on the dependency of segregational behaviour from body shape. All statements in the following are subject to this reservation.

Table 6.2 provides the burial depths h_b of the test bodies depending on their surface-volume ratio $\Omega = \frac{A}{V}$ and on the ratio $\phi = \frac{\rho_{body}}{\rho_s}$ of body density and density of the surrounding debris snow. The burial depths were measured with respect to the centers of mass of the bodies. The surface-volume ratios are normalized by the surface-volume ratio of a sphere $\Omega_{sphere} = \sqrt[3]{\frac{36}{\pi}} \approx 2.25$.

In principle, one should regard the ratio of body densities and the density of the *flowing* snow, when examining segregational behaviour depending on density ratios, for segregation only occurs in the flowing avalanche. As the density of flowing snow was not accessible in this experiment, we assume that the (lower) snow densities in the flowing avalanche are proportional to the snow densities in the debris, which now is interpreted as a "frozen mapping" of the flowing avalanche shortly before it had come to rest.

Figures 6.18 and 6.19 show the burial depths h_b of the test bodies depending on the ratio $\phi = \frac{\rho_{body}}{\rho_s}$ of body density and density of the surrounding debris snow and, on the other hand, as a function of their surface-volume ratio $\Omega = \frac{A}{V}$ as listed in Table 6.2. The burial depth h_b of the bodies seems to

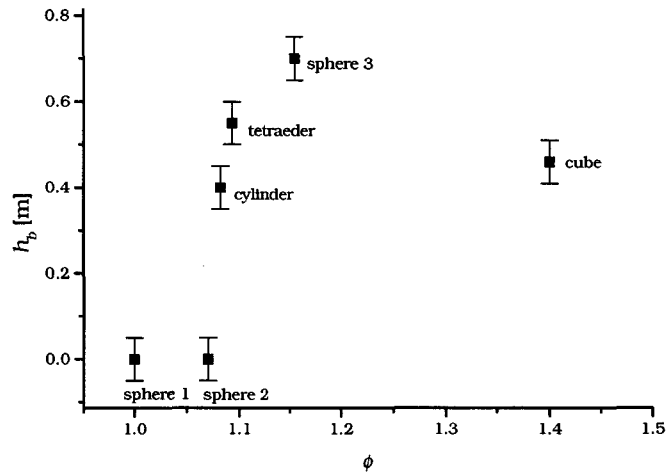

Figure 6.18: *Burial depth of test bodies depending on their ratio $\phi = \frac{\rho_b}{\rho_s}$ of body densities ρ_b and densities ρ_s of surrounding snow.*

increase with increasing density ratio ϕ. Due to the low number of data points, one only can state a raw tendency and, obviously, it is not possible to make any statement about the form of the dependency.

Figure 6.19 shows that the burial depth is also increasing with increasing surface-volume ratio Ω. Intuitively, one would assume an opposite behaviour, as with increasing Ω, also the effective area of the bodies, which external forces can act on, is increasing. If on the relatively small surface of a sphere, enough forces are acting to lift them up to higher flow layers, one would expect that increasing surface area allows even more buoyant forces to act. A possible explanation for the failure of intuition at this point may be the effect of squeeze expulsion as explained in Section 5.4.1, which describes the fact, that larger particles are squeezed out of a layer of smaller particles by imbalanced lateral forces exerted on them by the smaller particles. This effect is similar to a piece of soap sliding out of one's hand when squeezing it. From this point of view, the fact that burial depths are increasing from

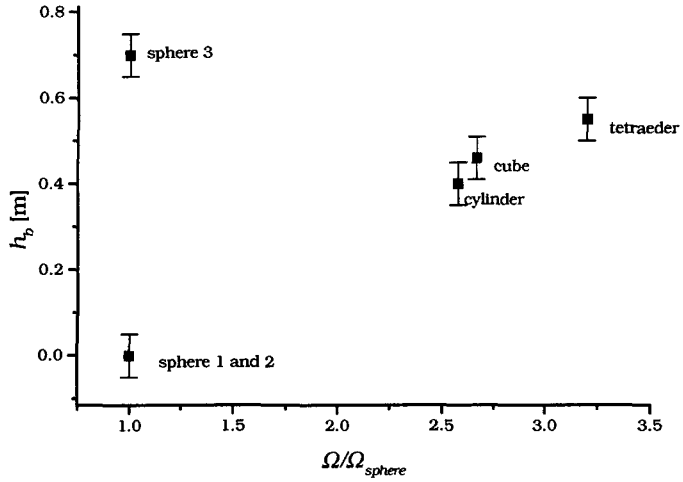

Figure 6.19: *Burial depth h_p of the test bodies depending on their surface-volume ratio Ω.*

sphere to tetraeder via cylinder and cube can be interpreted in that way that the spheres had the best form for showing the squeeze expulsion effect: the more and longer edges and corners a body has, the more it resists to sliding out of a layer due to lateral squeezing.

Anyway, the density ratio ϕ seems to rule the burial depth or the segregational behaviour in a more dominant way than the body shape (i.e. than the surface-volume ratio Ω): Regarding the burial depths of the spherical test bodies, one observes two spheres at the debris surface, and, on the other hand, one sphere having the greatest burial depth of all test bodies - according to its significantly higher density ratio of $\phi = 1.16$ relative to $\phi = 1.0$ and $\phi = 1.07$ of the two visible spheres.

All these attempts of interpretation have to be regarded with respect to the fact that there were only each one cube, cylinder and tetraeder body taken away by the avalanche and deposited in its runout zone: the dependency of burial depth and body shape maybe nothing else than a well-looking product of pure chance. In order to verify or falsify the assumptions made on shape dependency of segregational behaviour, of course, more field experiments are neccessary. Usually, in a test site, conditions are appropriate for avalanche experiments 1 or 2 times each winter.

Second test, January 1999

End of January 1999, the experiment was prepared again. This time, additionally to the test bodies, a dummy (a cylindical bag with approximately human shape and weight), which was connected with an inflated double airbag ABS device, was positioned in the area of initial test body positions. Unfortunatedly, a spontaneous avalanche swept away the test bodies, before an avalanche could be released artificially. As the spontaneous avalanche occured during a snowfall period with extreme wind speeds and considerable avalanche hazard in the test site, the test bodies could not be recovered immediately after the avalanche event. But for a short instance, the view was clearing up and the debris of the avalanche was visible: Three tetraeders, two cylinders, a cube and a sphere body could be observed lying at the surface of the avalanche debris distributed over a range of approximately 30×30m. In addition, the ABS device with its dummy was clearly visible on the surface of the debris. When the debris region of the test site was finally accessible again for the recovery of the test bodies, new snow and debris from other avalanches had been added to the debris of the spontaneous avalanche, which had carried away the test bodies. For this reason the evaluation of burial depths did not make any sense.

Nevertheless, the densities of all bodies which had been observed at the debris surface, were higher than the density of the surrounding debris, indicating that the buoyancy acting on the bodies had been governed by segregation rather than by hydrostatic effects.

The dummy connected to the ABS had been severly damaged, while it had been swept over a rocky wall by the spontaneous avalanche. Also the other body wraps were more or less damaged. As the dummy consisted of a bag filled with plastic granulate, its damage caused considerable pollution of environment, which finally could be cleared up in end of July 1999, when the concerned area of the test site was free of snow again.

6.1.3 Conclusions of field work

Observations in the debris of snow flow avalanches provided some evidence for the occurence of inverse grading in dry and wet snow flow avalanches. Smaller snow particles were found in deeper layers of the deposit than larger snow lumps. In some cases, the fractured snowpack had not been subject to overall mixing, so that the original layering of the snowpack was preserved in the depositional zone of the avalanche debris. Nevertheless, small snow particles were found at the base of the debris, which had obviously diffused through the whole depth of the flowing snow layer. Photographs of the deposit of a wet snow flow avalanche were quantitatively evaluated. The profiles of mean size of the rounded snow lumps, of which the avalanche debris consisted, have a shape which is typical for granular flow subject to inverse grading: the mean particle size is increasing with increasing profile height.

The numerical model used for simulation of inverse grading can only account for spherical particles. Therefore, the dependency of particle shape on the segregational behaviour of large particles was tested in a field experiment. Using equal sized bodies with different geometrical shapes and a common volume of 150 l, an increase of burial depth with increasing surface-volume ratio of the bodies and with increasing ratio of the body density and the density of the surrounding snow could be observed. As only 6 test bodies could reasonably be evaluated, this result is not statistically significant and may be a random effect.

Concluding, one can state that the observations in avalanche depositional zones provide evidence for the occurence of inverse grading both in dry and wet snow avalanches. A field experiment resulted in some hints on the influence of the shape on the segregational behaviour of large bodies in a snow flow avalanche. However, these results are not statistically reliable.

6.2 Laboratory test of collision properties of snow

To relate the numerical simulations of model flows consisting of spherical particles with assumed particle material properties to real snow avalanche flow, the longitudinal restitution coefficient e of snow was measured in a laboratory experiment.

6.2.1 Experimental setup

The longitudinal restitution coefficient e of snow was measured with a simple experimental setup (see Fig. 6.20) which was placed in the cold laboratory of The SFISAR building at Weissfluhjoch, Davos. The setup consisted of a hovercraft track on which sleighs carrying snow samples could move frictionlessly.

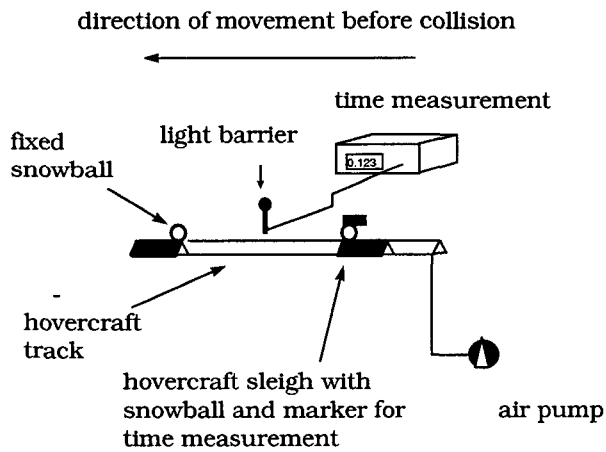

Figure 6.20: *Principle sketch of experimental setup for measurement of the longitudinal restitution coefficient e of snow.*

The hovercraft track had a length of 1 m and a triangular profile. The upper length sides of the track had equidistant little holes, through which compressed air could escape and form an air cushion under the sleigh, which fitted to the triangular profile of the track.

Side- and front views of the hovercraft track with the sleighs are shown in Figures 6.21 and 6.22; Figures 6.23 and 6.24 show photographs of the sleigh and the experimental setup.

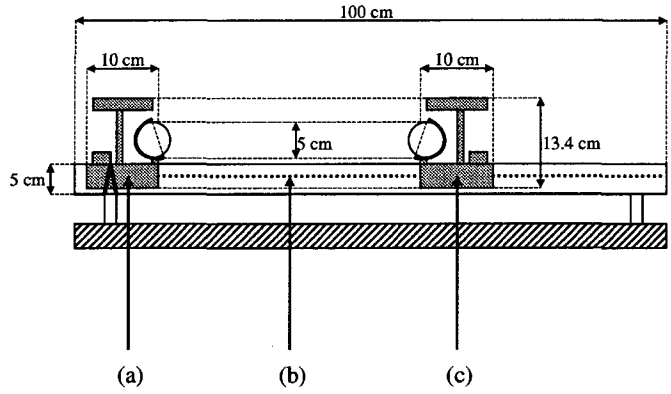

Figure 6.21: *Side view of hovercraft track with sleighs. (a) Fixed sleigh with spherical snow sample, (b) Hovercraft track (c) Moving sleigh with spherical snow sample.*

The compressed air for the hovercraft track was supported by the compressed air support of Weissfluhjoch building, which consists of a 2-cylinder compressor and a mains system which was extended by a branch into the cold laboratory for the present experiment. As the air flow through the hovercraft track was very high, running the hovercraft track over time intervals longer than approximately 10 s caused the air pressure to fall. As a consequence, the hovercraft track could be active only for short intervals, which were just sufficient for the measurement of one single collision event, after which a short break had to be made to let the compressed air system relaxate back to its working pressure.

Spherical snow samples were fixed on hovercraft sleighs, which are shown in Figures 6.22 and 6.23. A sleigh consisted of an inverse V-shaped metal profile of 10 cm length fitting onto the hovercraft track. At one side of the profile, a half sphere with 5 cm diameter was fixed with its open area inclined 20° against the vertical direction. The inner surface of the sphere was equipped with thorns to fix the snow samples. As the snow samples were fixed at one side of the sleigh, their weight had to be compensated by

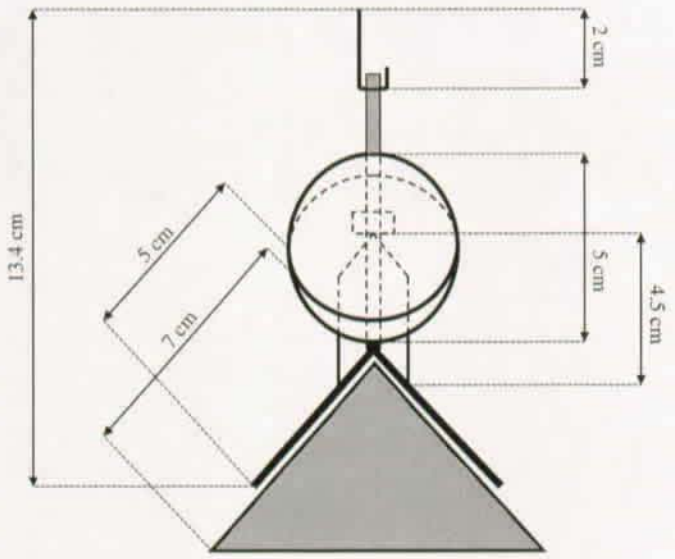

Figure 6.22: *Front view of hovercraft track with sleighs.*

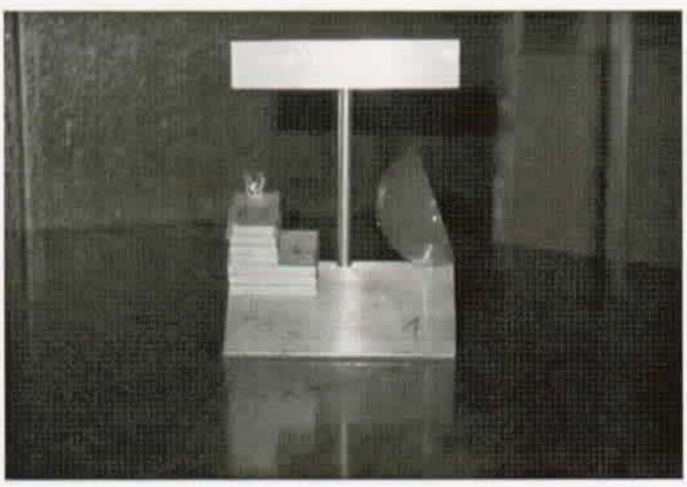

Figure 6.23: *Hovercraft sleigh for carrying snow samples on hovercraft track.*

Figure 6.24: *Experimental setup for measurement of the longitudinal restitution coefficient e of snow.*

an equal weight at the other side to avoid the sleigh getting wedged on the hovercraft track. The compensation was done by little wedge shaped metal pieces, which could be screwed at the other end of the sleigh.

One sleigh with its snow sample was fixed at one end of the hovercraft track with the snow sample heading in the direction of the track. The other sleigh could move freely along the track, so that its sample could collide with the one at the fixed sleigh (see Figs. 6.21 and 6.24).

The velocity of the snowball on the sleigh was measured before and after collision with another snowball of same size and sort of snow on the fixed sleigh at the end of the track. Velocities were determined by measuring the time, which a marker with length l_m needed to pass a light barrier. Passing times could be resolved with a frequency of 1 kHz for times up to 1s, and with 100 Hz for times longer than 1s. For a marker length of $l_m = 10$ cm, this caused a limitation of velocity measurement accuracy to 1%.

The longitudinal restitution coefficient $e = \frac{v_x'}{v_x}$ was determined from the velocity ratio of the velocities v_x and v_x' of the moving snowball before and after the collision with the one on the fixed sleigh. The measurements were performed for different impact velocities. This allowed to measure a dependency of the restitution coefficient from the impact momentum.

6.2.2 Measurement procedure

As explained above, the longitudinal restitution coefficient e was determined as ratio of longitudinal velocities of the snow samples v_x' after and v_x before collision. This would have required the hovercraft track to be perfectly balanced and the sleigh moving perfectly frictionlessly on it. Due to fluctuating air support pressure and slight reminding friction of the sleigh, a perfectly balanced state of the experimental setup could not be maintained over a measurement time period. For this reason, small impact and reflexion velocities, respectively, could result in the sleigh stopping before reaching the light barrier for v_x' measurement. To evade this problem, a small inclination was imposed on the track and corrections to the measured velocities had to be done accordingly.

To do so, the sleigh with the snow sample was placed at x_{impact} at the end of the track, so that the snow ball was in contact with the snowball on the fixed sleigh as indicated in Figure 6.25. Releasing the sleigh from rest caused the sleigh to accelerate slightly in direction to the light barrier and pass it with a velocity $v_{slope} = \frac{l_m}{t_{slope}}$. Here, t_{slope} is the passing time of the sleigh marker with length l_m through the light barrier, which is positioned at $x_{lb} + l_m$, when the sleigh was released from rest at x_{impact}.

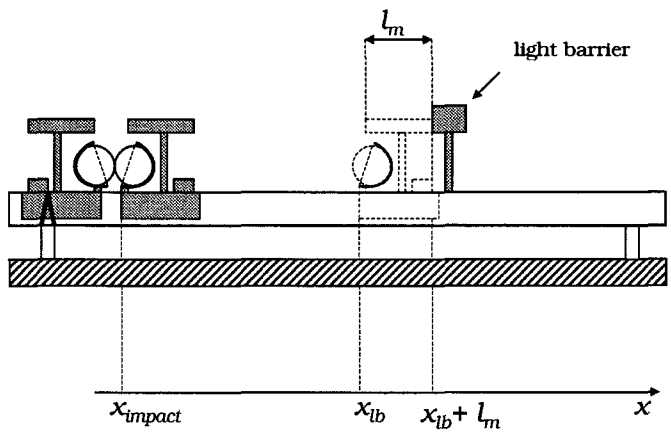

Figure 6.25: *Notation of sleigh positions for measurement procedure.*

The restitution coefficient is then obtained as ratio of velocities of the freely

moving probe sleigh at the collision point $v'_x(x_{impact})$ after and $v_x(x_{impact})$ before the collision of the two snow samples. The velocities after and before collision at x_{impact} can be determined from the sleigh velocities at the light barrier position $v'_x(x_{lb})$ after and $v_x(x_{lb})$ before collision:

$$e_{exp} = \frac{v'_x(x_{impact})}{v_x(x_{impact})} = \frac{v'_x(x_{lb}) - v_{slope}}{v_x(x_{lb}) - v_{slope}} = \frac{\frac{l_m}{t'_{pass}} - \frac{l_m}{t_{slope}}}{\frac{l_m}{t_{pass}} - \frac{l_m}{t_{slope}}}. \tag{6.2}$$

The passing times of the sleigh marker through the light barrier after and before collision are denoted by t'_{pass} and t_{pass}, respectively.

A typical measurement series started with determining v_{slope} by approximately 10-20 releases of the probe sleigh from the collision position. After each release, the system had to be given time for the support pressure to relaxate. Then the sleigh was pushed (by hand) with different initial velocities and t_{pass} and t'_{pass} were recorded for each collision, which were separated by a stop of the air support for pressure relaxation. After each 10 collisions, v_{slope} was determined again to detect an eventual system drift.

As the mass of snow sample and sleigh is much higher than the mass of the snow sample itself, the restitution coefficients were evaluated as functions of impact momentum and not as functions of impact velocity. Maximum impact velocities achieved with the experimental setup were approximately 0.25 ms^{-1}.

Higher velocities caused damage of the snow samples. Regarding the fact that the mass of sleigh and snow sample (aproximately 175g) was about 7 times the typical snow sample mass (typically $\approx$ 25g), this corresponds to an impact velocity of approximately 2.3 ms^{-1} of the snow sample which is in the range of velocity fluctuations observed in the numerical model flows.

6.2.3 Snow samples

Determinations of e were performed in the way described above with different sorts of snow at different laboratory temperatures. The constraint on the snow samples was that they should consist of rather compact snow, which could be put into spherical shape ("snow balls") to get comparable

samples. The snow was formed into spheres by a ladle with the shape of a half sphere with 5 cm diameter. Snow samples were taken from kinds of snow which occur in snow slabs forming avalanches, from avalanche debris and some other kinds of snow for reasons of comparison. Table 6.3 provides a list of snow samples, for which longitudinal restitution coefficients were measured.

6.2.4 Results

All measurements resulted in longitudinal restitution coefficients e_{exp} in the range of $e_{exp} \in [0, 0.3]$ for impact momenta $p_{impact} \in [0, 0.035 \text{ kgms}^{-1}]$, corresponding to a total mass of sleigh and snow sample of ca. 175 g and impact velocities of $v_x \leq 0.25 \text{ ms}^{-1}$. This is equivalent to a snow sample impact velocity of ca. 2 ms^{-1}. Higher impact velocities in general caused the damage of the snow ball sample. In each case, the restitution coefficient was decreasing with increasing impact momentum p_{impact}. The form of the dependency was exponentially decreasing or linear, or, in some cases, undefined. Table 6.4 lists measurement results for the different snow samples.

A plot of the restitution coefficient e of snow sample 8 against its impact momentum is shown in Figure 6.26. The large error bars for low impact momenta are due to the uncertainity in the measurement of v_{slope}, which has an important effect on the reliability of the v_x and v'_x measurement for small values of v_x and v'_x.

Concluding, one can state that the laboratory experiment on the longitudinal restitution coefficient e of snow results in a value of $e_{exp} \approx 0.1...0.3$, which is 3-8 times lower than the value $e = 0.8$ needed in the numerical simulations to obtain stable model flows exhibiting inverse grading. The consequences of this finding will be discussed later on in the course of this chapter. The restitution coefficient of snow is exponentially decaying with the longitudinal impact velocities of the spherical snow probes.

Table 6.3: *Characteristics of snow samples used in the cold laboratory experiment*

Sample	Date of collection	Sort of snow
1	04.12.98	wind packed powder snow from roof of SFISAR building
2	08.12.98	wind packed powder snow from roof of SFISAR building
3	08.12.98	wind packed powder snow from roof of SFISAR building, melted by breathe
4	08.12.98	compacted snow, extracted from footpath to "Gipfeli" near SFISAR building
5	08.12.98	lumps of shovelled wind packed snow, from "Gipfeli"
6	08.01.99	artificial snow, stored for two weeks in cold lab at -11.2C
7	08.01.99	snow lumps from avalanche debris at "Schaafläger", Parsenn ski resort
8	04.02.99	wind packed snow from roof, stored for two weeks at -12 C, slightly molten by breathe before measurement
9	16.02.99	snow lumps of shovelled wind packed snow from roof of SFISAR building
10	17.02.99	very light new snow, formed to snowballs by hand

Table 6.4: *Experimental results for restitution coefficient e of snow balls.*

sample	range of p_{impact} [kgms^{-1}]	range of e_{exp}	shape of decrease of e with p_{impact}
1	$[0, 0.08]$	$[0, 0.35]$	exponential
2	$[0, 0.04]$	$[0, 0.24]$	exponential
3	$[0, 0.02]$	$[0, 0.4]$	linear
4	$[0, 0.05]$	$[0, 0.17]$	undefined
5	$[0, 0.05]$	$[0, 0.15]$	exponential (?)
6	$[0, 0.07]$	$[0, 0.35]$	exponential
7	$[0, 0.03]$	$[0, 0.32]$	exponential (?)
8	$[0, 0.03]$	$[0, 0.27]$	exponential
9	$[0, 0.05]$	$[0, 0.17]$	linear
10	$[0, 0.07]$	$[0, 0.2]$	exponential

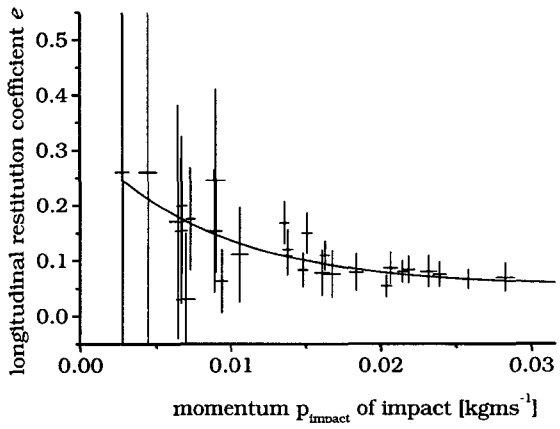

Figure 6.26: *Impact momentum dependency of the longitudinal restitution coefficient of snow sample 8.*

6.3 Interpretation of numerical results in the light of experimental findings

This section deals with the comparison of model results with observations made in real avalanches. Particle size profiles and mean velocities of model flows are compared to the ones of real snow flow avalanches.

6.3.1 Numerically obtained and observed particle size profiles

The numerical simulations of granular flow performed in the current work intended a principle understanding of inverse segregation at a moderate cost of computational resources. This set some limitations on the maximum number of particles involved in the simulations. For this reason, the range of particle radii r was chosen as $r \in [0.18, 0.3]$ m for most simulations. This turned out to be appropriate to study the evolution of inverse grading using a reasonably tractable number of particles.

Two alternative approaches to comparison of particle size profiles in the debris of the Vallée de la Sionne wet snow flow avalanche (see Sect. 6.1.1) with numerically obtained results are described in the following:

- Perform a simulation with a particle size distributions similar to the ones observed in the debris of the real avalanche and compare the simulated particle size profile directly to the observed particle size profiles.
- Compare field observations and simulation results of particle size profiles by normalizing the observed mean particle size ranges and the model particle size range $r \in [0.18, 0.3]$ m to the interval $[0, 1]$.

Similar particle size distributions

The particle size distributions observed in the debris of the Vallée de la Sionne wet snow flow avalanche were approximated by the particle size

distribution of a 1000 particle model flow with a particle size range $r \in [0.03, 0.3]$m. The model size distribution shown in Figure 6.27 is the best approximation to the observed particle size distributions which could be obtained from the `initialisation` algorithm for initial arrangement of particles which is described in Section 5.3.2.

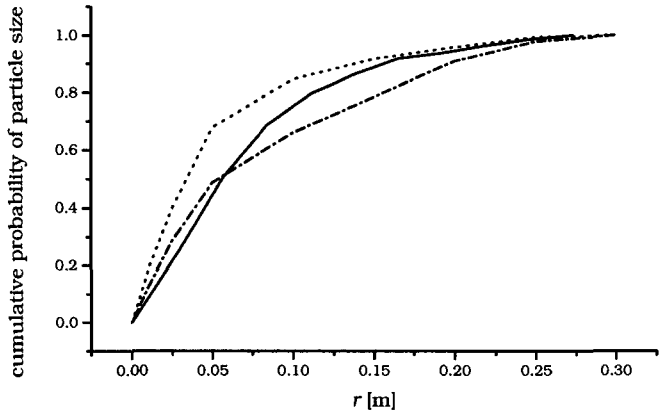

Figure 6.27: *Cumulative particle size distributions. Solid line: Cumulative particle size distribution used in the simulation. Dotted and dash-dotted lines: Cumulative particle size distributions as observed in the profiles of the Vallée de la Sionne wet snow flow avalanche (Fig.6.11).*

The mean particle size profiles observed in the debris of the Vallée de la Sionne wet snow flow avalanche are compared to the results of a simulation with the approximated particle size distribution.

A comparison of the modelled and the observed mean particle size profiles is presented in Figure 6.28. The generic segregational behaviour of the observed mean particle size profiles with particle size increasing with profile height is fairly reproduced. However, there are distinct deviations of the modelled from the observed particle size profiles:

- The observed mean particle size profiles were recorded in the avalanche debris at rest, which is assumed to be a mapping of the size profile of the moving avalanche before standstill. On the other hand, the modelled profile was determined in the moving model flow. The particle assembly in the real avalanche debris is an approximately closest pack-

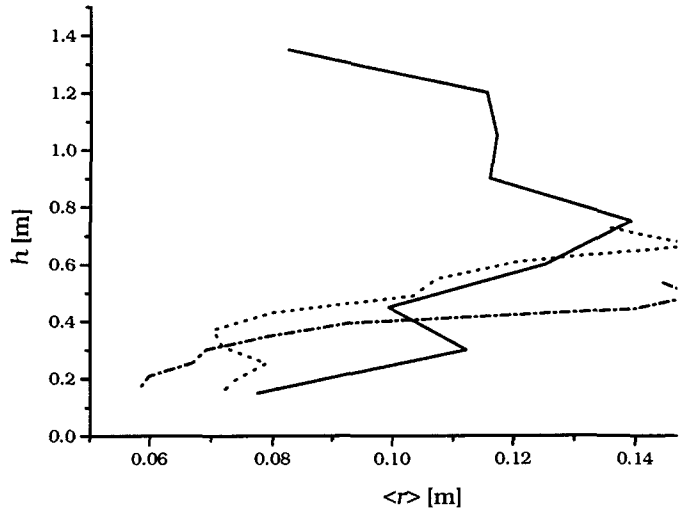

Figure 6.28: *Simulated and observed mean particle size profiles. Solid line: Simulated particle size profile. Dotted and dash-dotted lines: Observed particle size profiles. Line types refer to the ones of the related cumulative particle size distributions in Fig. 6.27. Particle material parameters of model flow: e=0.8, b=0.8, μ=0.4.*

ing of the different sized snow lumps, whereas the model flow is more dilute due to fluctuations inside the moving granular mass. Furthermore, the motion of the model flow generates a dilute "cloud" of small particles bouncing on the surface of the more compact flowing part of the model flow. This cloud is represented by the low mean particle size in the upper part of the simulated profile. Note that the particle number density of the cloud is by an order of magnitude lower than in the dense flow layers exhibiting inverse grading.

- The accumulation of small particles in the lowest flow layers could not be exactly reproduced by the simulation. This may be due to the fact that in the approximate model particle size distribution, small particles are slightly less frequent than in the observed distributions (see Fig. 6.27). Furthermore, the small particles in the "cloud" above the model flow are missing in the lower flow layers. The real wet snow flow avalanche obviously did not generate such a cloud shortly before

standstill.

Different particle size distributions

In the second approach of comparison, the simulation results of flows with a particle size range of $r \in [0.18, 0.3]$ m are compared to the mean particle size profiles observed in the runout zone of the Vallée de la Sionne wet snow flow avalanche. As explained above, the profiles in the granular model are computed in the flowing granular material, but the field measures are taken from the avalanche debris at rest, which results in different profile heights. To allow a comparison between simulated and observed mean particle size profiles, the profile heights were normalized by the maximum profile height h_{max}.

The mean particle size ranges of observed profiles were linearly mapped to the interval $[0, 1]$.

Normalizing and merging the observed particle size profiles 1 and 2 of Figure 6.11 (Vallée de la Sionne avalanche) in one plot, they show a nonlinear (quadratic) increase of normalized mean particle size with height (see Fig. 6.29).

The normalized particle size profiles of simulated segregating model flows with various particle material parameters are presented in Figure 6.30. The profiles show a linear increase of particle sizes with profile height and a steep decrease in the uppest flow layers. One can interpret this effect as a cloud of light, small particles bouncing on the more compact granular flow body, in which the segregation occurs.

The general trend of increase of mean particle size with profile height is well reproduced by the numerical model. The difference in generic profile shapes between measured and simulated segregational particle size profiles can be explained by the fact that the particle size distributions in the avalanche debris are more biased towards lower particle sizes than the model particle size distribution (see Fig. 6.27). Furthermore, comparison of particle size profiles measured in the field with profiles of moving granular model flow is not quite straightforward:

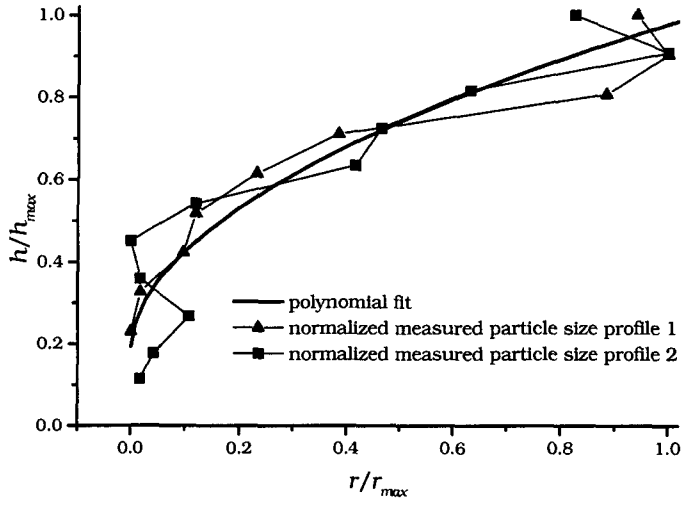

Figure 6.29: *Normalized measured particle radius profiles taken in the debris of the wet snow avalanche in Vallée de la Sionne.*

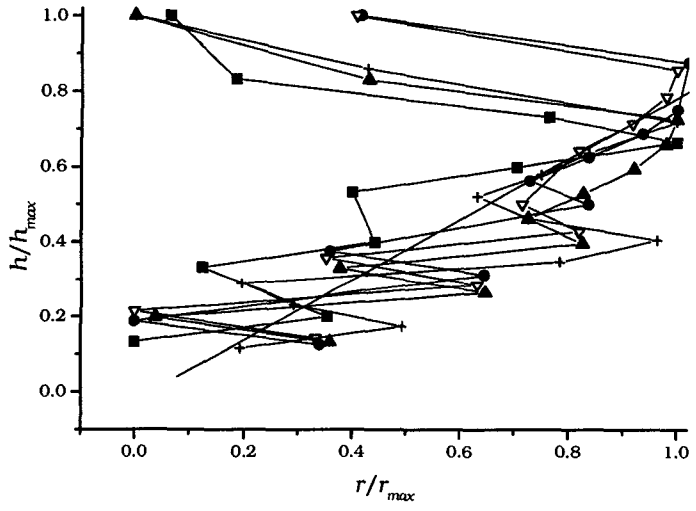

Figure 6.30: *Normalized simulated particle size profiles showing generic linear increase of particle size with height.*

- Comparison of "flowing" model profiles and debris profiles at rest assumes the debris profile to be a frozen snapshot of the flowing avalanche which has, of course, a lower mean particle number density than the debris at rest.

- As explained above, the range of particle radii in the real avalanche is differing from the range of granular model particle radii r, which are lying in a relatively narrow interval $r \in [0.18; 0.3]$ m. The lower bound of particle sizes is much higher than in real avalanches: the particle radii in the real avalanche debris are ranging from 1 cm up to 50 cm. In the simulation, the lower particle sizes are cut off to keep the total amount of particles in the numerical model as low as possible.

6.3.2 Differences of numerically and experimentally obtained restitution coefficients

The laboratory measurement of the longitudinal restitution coefficients e of snow balls resulted in values in the range $e_{exp} = 0.1 \ldots 0.3$. From this result, a severe conflict arises with the findings of the granular model, where steady flows with inverse grading could be produced only for a parameter value of $e \approx 0.8$.

This can be explained by accepting the fact that the granular flow model is not exactly reproducing the dynamics of a snow flow avalanche. Though flow avalanches display the effect of inverse grading, the particle interaction in a flow avalanche is not only of a binary, instantaneous nature. After colliding inelastically, the particles can be in contact over an extended time period and slide or roll along each other with a low dissipation of energy. The used hard sphere model does not account for this behaviour. Instead of a longer contact, the model produces several collisions with a higher coefficient of restitution. That means that the model needs more collisions to reproduce the energy dissipation occuring in one "real" collision with a low restitution coefficient followed by nearly frictionless sliding. For this reason, a power-law type relationship is postulated between the experimentally obtained and the model restitution coefficients e_{exp} and e, respectively.

$$e_{exp} = e^n, \quad n \in \mathbf{N}, \tag{6.3}$$

where n is the number of collisions the hard sphere model produces instead of one particle interaction in a real snow avalanche. In some sense, this

approach resembles the collision-time model of Luding & Mcnamara (1998), which accounts for contacts of several particles over extended time intervals by subsequent elastic collisions. For $e_{exp} = 0.1$ and $e = 0.8$, one yields $n \approx 10$, which is a good approximation of the number of collisions of two model particles while they are passing each other:

To enlighten the motivation of this assumption, regard the time evolution of the time between two collisions (i.e. the time Δt to the next event), in which a large particle ($r = 0.3$) in the model flow is involved. The time Δt between two interactions of the large particle can be regarded as its inverse interaction frequency. Figure 6.31 is a plot of the time intervals Δt between two interactions the large particle encounters during its motion in a model flow with the material parameters $e = 0.8$, $b = 0.8$ and $\mu = 0.4$. The time series of Δt has an intermittent structure showing periods of small Δt corresponding to a high frequency of contacts the large particle is involved in, and, on the other hand, periods with higher values of Δt which correspond to a more undisturbed free motion with less frequent collisions with other particles. The periods of increased interaction frequency can be interpreted as footprints of other particles passing the regarded large particle by bouncing along its surface instead of one inelastic collision followed by sliding along the surface.

From Figure 6.31, the mean of Δt is about $\Delta t \approx 0.01$ during periods Δt_{pass} with higher contact frequency, which have a typical duration of $\mathcal{O}(t_{pass}) = 0.1$s. The model flow was characterized by a mean downslope velocity $\langle v_x \rangle \approx 6\text{ms}^{-1}$ and a mean velocity fluctuation $\langle \delta v \rangle \approx 2.5\text{ms}^{-1}$. Assuming that the mean velocity fluctuation corresponds to the mean velocity at which two particles in the model flow are passing each other during the high contact frequency periods, one can conclude that passing particles bounce a distance $\Delta s_{pass} \approx 0.25$m along each other's surfaces:

$$\Delta s_{pass} = \Delta t_{pass} \cdot \langle v_x \rangle \approx 0.1 \text{ s} \cdot 2.5\text{ms}^{-1} \approx 0.25\text{m}. \tag{6.4}$$

This appears to be a reasonable estimation for the distance, which other snow lumps in a snow flow avalanche slide along a large snow lump with a

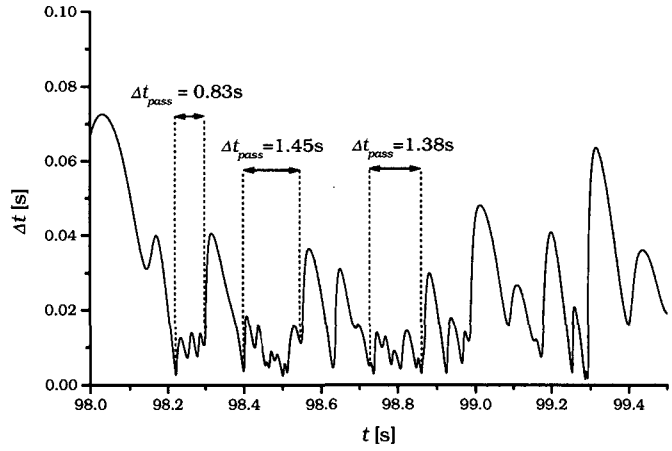

Figure 6.31: *Time evolution of time Δt between two interactions which one single large particle encounters within a model flow with parameters $e = 0.8$, $b = 0.8$ and $\mu = 0.4$. The marked intervals of decreased Δt or increased contact frequency, respectively, are interpreted as generated by passing other particles which are bouncing along the surface of the large particle instead of a contact of longer duration.*

radius of 30 cm after an inelastic ($e \approx 0.1$) collision before separating again. The number n of collisions during the passing is $n = \frac{\Delta t_{pass}}{\Delta t} \approx 10$, which corresponds well to the assumed power-law-type relation (6.3) between the experimentally obtained longitudinal restitution coefficient $e_{exp} \approx 0.1$ and the value of $e = 0.8$ in the simulation of the observed mean particle size profile (see Fig. 6.28).

6.3.3 Flow velocities and velocity fluctuations

The flow velocity of the Vallée de la Sionne wet snow flow avalanche was determined by Schaer & Issler (2000). They obtained a value of 3-5 ms^{-1}, which corresponds well to the mean downslope velocity $\langle v_x \rangle \approx 5\mathrm{ms}^{-1}$ of the simulation which was performed to model the mean particle size profiles of the Vallée de la Sionne wet snow flow avalanche.

As Salm (1982) states, the downslope velocities of dry snow flow avalanches usually lie in the range of $[10, 30]$ ms^{-1}, whereas wet snow flow avalanches reach speeds in the order of magnitude of $[20, 40]$ ms^{-1}. In the frame of the

used hard sphere model, it is easily possible to produce model flows with mean velocities lying in these ranges. However, such model flows turn out to be too dilute to exhibit segregational behaviour. As shown in Figure 6.32, the mean downslope velocities of simulated flows, which exibit inverse grading, are lying in the range of $[2, 10]$ ms^{-1} and therefore hardly match the standard values for avalanche speeds mentioned above.

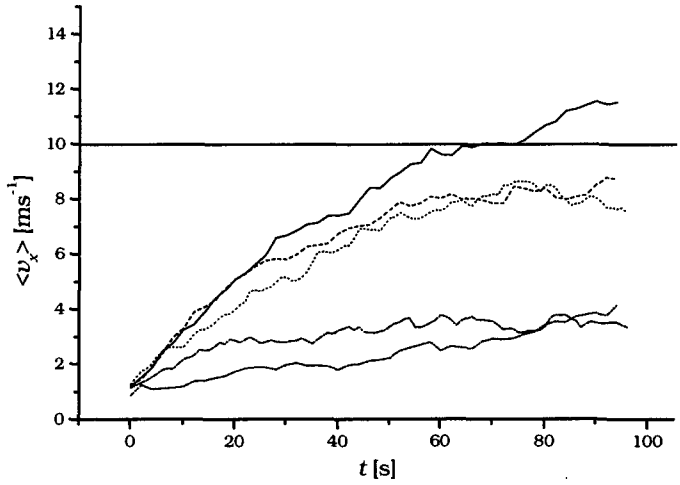

Figure 6.32: *Mean downslope flow velocities of model flows exhibiting inverse grading. The plot shows the time evolution of the mean downslope velocities of the slowest and fastest model flows exhibiting inverse grading. The line* $\langle v_x \rangle = 10\mathrm{ms}^{-1}$ *corresponds to the minimum standard value of flow avalanche speeds.*

The deviation of the mean downslope velocities of simulated and real avalanche flows can be explained by the difference of the restitution coefficients $e_{exp} \approx 0.1 - 0.2$ of snow and the value $e \approx 0.8$ which is necessary to obtain a model flow exhibiting inverse grading:

As stated by Dent (1993), in real snow flow avalanches, the main portion of deformation takes place in a thin layer near the ground which is subject to rapid shearing. Above this thin "active" region, deformation of the avalanche body is reduced by an order of magnitude with respect to the bottom layer: a so-called plug flow with only small velocity fluctuations (say of the order of 10 percent of the mean downslope flow velocity) evolves due to the low elasticity $e_{exp} \approx 0.1 - 0.2$ of snow.

As explained above, the hard sphere model replaces the inelastic particle interactions inside the real avalanche flow by numerous particle collisions with a higher restitution coefficient of $e = 0.8$. This, however, results in a significantly higher ratio $\frac{\sqrt{\langle(\delta v)^2\rangle}}{\langle v_x \rangle}$ of velocity fluctuations and mean downslope velocities. (In the following, the standard deviation $\sqrt{\langle(\delta v)^2\rangle}$ of the mean velocity of the model flow is used as a measure for typical velocity fluctuations occuring in the model flow)

While in the plug flow part of the snow flow avalanche, this ratio is of the order of magnitude of 0.1, in the segregational model flow, it is approximately 0.5, as shown in Figure 6.33. Assuming that the particle velocity fluctuations are dominantly governing the segregational dynamics, a real snow flow avalanche needs to have a mean downslope velocity five times a high as the granular model flow to produce velocity fluctuations of the same order of magnitude. This statement agrees well with the ranges of mean downslope velocities $[2, 10]$ ms^{-1} for simulated and $[10, 40]$ ms^{-1} for real snow flow avalanches. The slow Vallée de la Sionne flow avalanche might have been an exception from this raw rule, for it was consisting of nearly spherical, hard and highly mobile particles, so that the velocity fluctuations have probably been larger than in "normal" snow flow avalanches.

6.3.4 Conclusion of comparison of numerical and experimental results

Simulations of mean particle size profiles provided the same trend as observed in the debris of real avalanches: the mean particle size is increasing with flow height. However, the application of the numerical hard sphere model to field observations of real avalanche behaviour is not straightforward:

Mean particle size profiles of the model flow are computed from the granular model flow in motion, where the field observations of particle size profiles were made in the avalanche debris at rest.

One possibility is to perform simulations of granular flows with a similar particle size distribution as observed in the field. In this case, a dilute

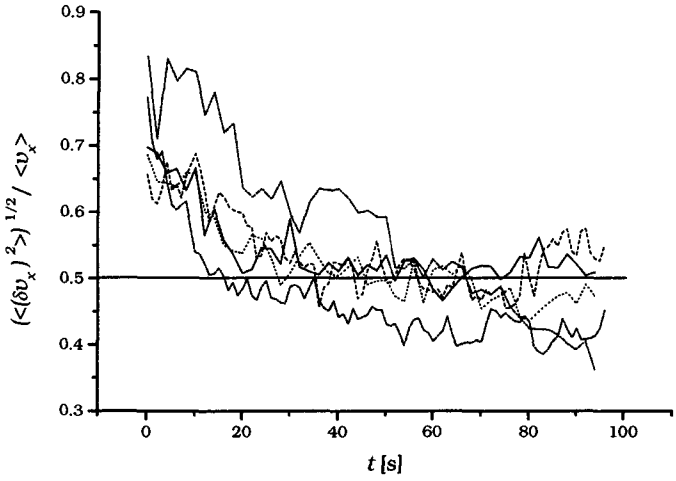

Figure 6.33: *Ratio* $\frac{\sqrt{\langle(\delta v)^2\rangle}}{\langle v_x\rangle}$ *of mean velocity fluctuations and mean downslope velocities for model flows exhibiting inverse grading. After some relaxation time, this so-called fluctuation level tends towards a value of approximately 0.5.*

cloud of small particles evolves above the dense flowing part of the model, which causes deviations of the modelled mean particle size profiles from the observed ones.

In another approach, simulations with particle radii ranging from 0.18 m to 0.3 m were compared with field observations, where the particle radii were ranging from 0.02m to 0.3m. For comparison, the mean particle size ranges and the profiles of both simulated and observed profiles were normalized to the interval [0.1]. This comparison results in a satisfactory qualitative agreement between observation and simulation.

The deviation of the experimentally obtained value $e_{exp} \approx 0.1$ of the longitudinal restitution coefficient of snow from the value $e = 0.8$ required for the simulation of a stable segregating granular flow can be explained by replacing an inelastic collision which is followed by a sliding passing motion of the snow particles by a bouncing motion of particles passing each other in the numerical hard sphere model. This statement is supported by regarding the intermittent time series of the inverse contact frequency of one single particle in the model flow.

The velocity fluctuations inside a granular flow are essential for the evolution of segregational behaviour. Regarding the different velocity fluctuation levels (i.e the ratios of mean velocity fluctuations and mean downslope velocities) in real snow flow avalanches and in the model flow, the deviation of the mean downslope flow velocity of the model flow from the usual standard values of flow avalanche speed can be explained: to achieve velocity fluctuations of the same order of magnitude as the model flow with a velocity fluctuation level of 0.5, a snow flow avalanche with a fluctuation level of 0.1 has to be 5 times as fast as the model flow.

Concluding, one can state that the used hard sphere model can be applied to model inverse segregational behaviour in snow flow avalanches, if the different characters of model and real avalanche flow are taken into account in an appropriate manner.

6.4 Conclusion

Qualitative observations in snow avalanche debris indicate the occurence of inverse grading during avalanche motion.

The shape dependency of burial depth of equal sized bodies in snow avalanche debris was investigated in a field experiment. The recorded data are not statistically significant but encourage the hypothesis that at equal body size, a more rounded body shape with a low surface-volume ratio is supporting the effect of squeeze expulsion which is driving bigger particles into higher flow layers of a granular flow.

Quantitative evaluation of photographs of profiles of a wet snow avalanche debris result in nonlinear particle size decrease with profile depth. On the other hand, simulated segregational particle size profiles show a generic linear decrease of particle sizes with profile depth and a cloud of small particles at the surface of the flow. These differences are due to different particle size ranges in real avalanches and numerical model as well as to the fact, that the simulated profiles have been determined in the flow in motion, where the avalanche profiles were recorded in the avalanche debris at rest. The

debris profiles are supposed to be interpretable as frozen snapshots of flow profiles of flowing avalanches.

The longitudinal restitution coefficient e of the granular particles is the most important material parameter entering the numerical model of the granular flow. Therefore, this parameter was measured for snow particles in a laboratory experiment to get an idea of the relation of the numerical model to real avalanche flows. For snow particles, e_{exp} was approximately a factor 3 lower than the restitution coefficient e leading to steady flow in the numerical model. An inelastic collision with subsequent contact over an extended time interval in the real avalanche flow is replaced by n more elastic collisions in the model flow. This is leading to the assumption of a power-law-type relation between the experimentally obtained value e_{exp} and the value e which is used to generate a stable segregating model flow: $e_{exp} = e^n$. This assumption is supported by regarding the intermittent time series of the contact frequency of one single particle in the model flow.

Observations and the field experiment confirm the occurence of inverse grading in snow flow avalanches. The numerical model is able to reproduce this effect. Assuming that the level of velocity fluctuations (i.e the ratio of mean velocity fluctuations and mean downslope velocity) is mainly governing the evolution of segregational flow behaviour, the differences between typical downslope flow velocities of segregating model flows and real snow flow avalanches can be explained by the fact, that the level of velocity fluctuations in real avalanche flows is approximately by a factor 4-5 lower than in the model flows. This means, that real avalanches have to be a factor 4-5 faster than the model flow to achieve the same level of velocity fluctuations as the model flow.

Finally, one can state that the numerical model is able to reproduce the observed inverse grading in snow flow avalanches, if appropriate measures of comparison are chosen.

Chapter 7

Conclusions

The work will now be summed up from a retrospective point of view. Firstly the considerations of each chapter will be shortly recalled with special emphasis on what has resulted in view of an understanding of inverse grading. It is tried to condense the main results of each chapter into one or two sentences. Then a general summary of the work and an outlook to further work on the integration of granular dynamics into classical snow avalanche dynamics is given.

7.1 Summary of chapters

Snow avalanches and granular flow

A brief historical outline on snow avalanches and an overview of current operational snow avalanche classification are given before describing the development and testing of the avalanche airbag. The functionality of this device cannot be explained by hydrostatic buoyancy in the frame of "classical" avalanche science. It is assumed that the effect of inverse grading in granular flows is the reason why avalanche airbags prevent skiers from sinking down in a flowing avalanche. For this reason, the concept of granular flow with inverse grading as a specific feature is introduced.

The more general concept of granular flow has to replace classical avalanche science in the role of conceptual background against which an understanding of the functionality of the avalanche airbag can be achieved.

Empirical and experimental findings

Field and laboratory observations on aspects of granular flow are reported and discussed in this chapter. The quoted field observations are concerned with the granular flow behaviour such as high mobility and inverse grading in snow avalanches and debris flows. The given examples of laboratory investigations employ chute experiments on free surface flow of granular material. In most cases, field observations are not reproducable, whereas laboratory experiments are and can be designed to be appropriate to capture specific aspects of granular flow. Both field observations and laboratory experiments are limited in the possibility to obtain information about the internal flow structure such as velocity or particle size profiles apart from the boundaries. Especially in the case of inverse grading, such information is of special interest. In the frame of mathematical or numerical models, however, the internal flow structure can easily be obtained.

Field and laboratory investigations are limited in possibilities to access information about the internal structure of granular flow apart from its boundaries which, however, is of special interest for the investigation of inverse grading. Mathematical or numerical models of granular flow can easily provide such internal flow properties.

Mathematical modeling

In this chapter, mathematical and numerical models of snow avalanche and granular flow are enumerated and their validity for the investigation of specific granular flow behaviour, especially of inverse grading is discussed.

Generally speaking, common snow avalanche models are treating avalanches as a continuous fluid. In some sophisticated models, some knowledge of granular flow behaviour is used in the constitutive relations. Nevertheless,

these models do not provide any statements about the specific granular flow structure of avalanches.

Analytical models describe granular flows in terms of kinetic gas theory of massive molecules. They are valid only in very narrow parameter ranges for nearly elastic particles. Though they in principle even can describe segregational processes, they are not appropriate for systematic parameter studies. The same statement holds for a statistical-geometrical approach to inverse grading, which does not take into account the collisional mechanics of the granular particles and therefore does not include any physical material parameters.

Discrete particle models (or discrete element models – DEMs) model the motion of granular material by tracing the motion of each single particle and its interaction with other particles involved in the flow and with the flow boundaries. DEMs can handle granular motion over a broad range of flow and particle properties and therefore are appropriate tools for systematic parametrical studies of granular flow behaviour and inverse grading. The soft-sphere type of DEMs is well suited for slow quasistatic deformation of granular assemblies which are characterized by long term multiple particle contacts, whereas rapid fluctuating flows which are dominated by binary instantaneous collisions of granular particles can be treated by so-called hard-sphere models.

Continuum snow avalanche models use some findings on granular flow behaviour but do not make any statements on specific granular flow behaviour of avalanches. Analytical models describe the principle mechanisms of granular flows but are too restricted in their valid parameter ranges to allow systematic parametrical studies of flow behaviour and inverse grading. Numerical discrete element models are the most appropriate tools for a parametrical investigation of inverse grading in granular flows.

Inverse grading in a hard sphere model

The development and the analysis of results of a hard-sphere model of multidisperse flow of inelastic frictional spheres are reported in Chapter 5. In the

frame of the developed model, granular flow is parametrized by boundary and initial conditions such as slope angle, bottom roughness, initial particle number density and velocities. The granular material itself is parametrized by the longitudinal and tangential restitution coefficients e and b, which describe the particle inelasticity, and by the Coulomb friction coefficient μ of sliding particle contacts. Also the development of statistical evaluation routines which characterize the flow by time averaged profiles of velocity, particle size and other quantities is reported.

In the frame of analysis of model results, a qualitative visual proof of the ability of the model to reproduce inverse grading is given. Limitations of the model lie in the transition regime to quasistatic motion, for which hard-sphere models are not an appropriate description.

Global model flow behaviour and inverse grading were characterized by velocity and particle size profiles. Inverse grading develops only in a distinct range of the parameter space $\{e, b, \mu\}$ related to moderately rapid, nearly steady or slightly accelerating flows. The segregational behaviour breaks down in dense, slow or rapid, dilute flows. Flow and segregational behaviour are sensitive to slight parameter variations in transition regimes of the parameter space. For example, in such a transition regime, a slight increase of the Coulomb friction coefficient μ causes a transition from accelerating to decelerating flow behaviour and lets the segregational behaviour break down.

Stochastic analysis provides a possibility to extract size dependent deterministic segregational dynamics for single particles from single particle motion in the model flow.

It is possible to reproduce the effect of inverse grading in the frame of a hard-sphere model of granular flow. Inverse grading is limited to a distinct regime in the parameter space of the model. Global flow behaviour as well as inverse grading are sensitive to slight parameter variations in the transition regimes of the parameter space. Size dependent deterministic segregational dynamics can be extracted from the model by the method of stochastic analysis.

Experimental work

This chapter reports field and experimental investigations performed in the frame of the current work. Qualitative observations of inverse grading and a field test of shape dependency of segregational behaviour of large bodies in snow avalanches are outlined. A laboratory experiment on the longitudinal restitution coefficient of snow balls states that inelastic properties of snow differ significantly from the model parameter values leading to inverse grading in the hard-sphere model flow. Finally, a comparison of particle size profiles measured in the debris of a wet snow avalanche with numerically obtained particle size profiles is presented, which results in principle qualitative agreement.

Although experimental evidence confirms the assessment that the hard-sphere model approach is a rather far abstraction of real avalanche behaviour, inverse grading observed in snow avalanche debris could be qualitatively reproduced by the numerical simulation.

7.2 General summary

The main goal of this work was to achieve an understanding of the parametrical dependencies of the evolution of inverse grading in granular flow. Investigations started the question after the physical background of the functionality of the avalanche airbag device. Attempts of explanation began in the field of classical avalanche science, which can be regarded as natural "habitat" of the avalanche airbag. An appropriate concept to deal with the problem was found far away from common snow avalanche dynamics, using the effect of inverse grading in granular flows, which can be described in the frame of a numerical hard-sphere-type discrete element model.

A hard-sphere model was developed, which is able to reproduce the effect of inverse grading and allows to investigate the parametrical dependencies of the effect. It turned out that inverse grading could only develop in a distinct range of the parameter space, which is characterized by steady or slightly accelerating global flow behaviour. In transition regimes, global

flow behaviour and the onset of inverse grading were found to be sensitive to slight parameter variations.

It is fascinating that a very simple model of granular flow consisting of different sized spheres can exhibit complex behaviour as the non equilibrium system state of inverse grading is and that it permits principle insight in segregational mechanisms and their parametrical dependencies.

7.3 Outlook

As the laboratory experiments on longitudinal restitution coefficients of snow or observations of real snow flow avalanches indicate, the used hard-sphere model is a far abstraction from real avalanche dynamics, which is much more complicated than the dynamics, which can be described by the numerical model: a snow avalanche does not simply consist of spheres which interact by instantaneous binary collisions.

Furthermore, avalanches are more complicated than the common continuum dynamic avalanche models. A persistent problem, which the latter have to deal with, is that long runout distances of large avalanches are underestimated as well as their deposition heights. This may originate from the fact, that there is no reasonable physical mechanism included in the models, which could account for the erosion and deposition of snow by avalanches moving on the snow cover. The rates of entrainment and deposition (if included in continuum avalanche flow models) are more or less ad hoc estimations. Furthermore, also the physical mechanism underlying the bottom and internal frictional processes is not understood but just lumped together in friction parameters of dry or turbulent friction, which are fitted by comparing the model output with known avalanche models. However, it is difficult to fit simultaneously both runout distances and deposition heights correctly. Besides some attempts to account for granular flow behaviour in the constitutive laws of the avalanche "fluid", the description of friction in operational avalanche models has not changed since the days of Voellmy (1955).

A contemplementary use of granular flow concepts together with common continuum dynamic avalanche models should provide

- principle insight into the inner flow structure of avalanches leading to an understanding of bottom and internal friction processes
- a physically based description of erosion and deposition processes to more realistically account for the mass balance in avalanche modelling

So, beyond the investigation of the specific feature of inverse grading occuring in granular flows outlined in this work, granular dynamics are of great importance for an improved understanding and therefore for a more correct modelling of snow avalanches.

However, the real problem to improve operational avalanche models cannot entirely be handled on the high level of abstraction represented by a hard-sphere discrete element model. It has to be checked, whether due to their ability to account for long term multiple particle contacts, soft-sphere models allow a more realistic description of non fluctuating slow snow avalanche flows.

It is hoped that granular flow concepts also in the field of avalanche dynamics become of the high importance they already have in other fields of geomechanics or industrial processing. Besides the scientific value of deeper insight into the principle snow avalanche mechanics, this will provide more safety for human life and property in alpine terrain.

Chapter 8

Acknowledgements

I would like to express my thanks to Professor Laurent Vulliet for kindly accepting to accompany this work as director and for his encouraging support throughout the time of the work. Dr. Walter Ammann supported the possibility to perform this work at SLF. I wish to thank him for this, for his guidance and for helpful hints concerning the organisatoric and administrative aspects of the work. I am deeply indepted to Dr. Othmar Buser for his constant, friendly support, for many original and helpful ideas and for sharing his enthusiasm for the beauty of physics. Professor Joachim Peinke kindly aggreed in reviewing the work and made very constructive suggestions. I would like to thank him for his persisting interest in this work.

This work would have been impossible without the invaluable support of the members of the SLF to whom I wish to express my heartfelt thanks: Perry Bartelt and all members of the avalanche dynamics team for generously leaving me the time for finishing this work, though there would have been so much work to do; Thank you, Felix Tiefenbacher and Ingo Völksch for filling the voids, Urs Gruber for helping me out in avalanche track topography, Betty Sovilla and Mathieu Fauve and Marcia Phillips for translations; Urs Suter, Christian Simeon, Stephan Frutiger and Gnther Klausegger for their always friendly and effective "doctoral student proof" technical support; Frank Tschirky shared his enourmous know-how on avalanche accidents and

on the avalanche airbag with me. Thank you very much for spending sometimes long and cold hours in the field: Thorsten Baunach, Dani Bühlmann, Peter Gauer, Martin Laternser, Norbert Raderschall, Luki Stoffel, Christoph Tanner, Frank Tschirky, Thomas Wiesinger and Urban. Bruno Gauderon, Andy Stoffel and all of the staff of the IENU section made me forget that computing machines sometimes may cause trouble - thanks a lot for persistent, fast and efficient help! Organisatoric work lost its horrors due to the friendly help of Madeleine Oberhänsli and Christine Berni. And thanks to all of the staff of the SLF for the friendly working atmosphere!

I am indepted to Robert Schaller from the Physics departement of the EPFL for providing the laboratory experimental equipment and to Gilbert Gruaz and Bernard Marguerat from the EPFL soil mechanics laboratory for their help in realizing the experimental setup. Peter Sprecher, Konrad Flütsch, Hans-Jürg Etter and Romano Pajarola from the SOS Parsenndienst in Davos were friendly and competent partners in questions concerning the safety of the field tests and friendly helped out with Recco tranceivers. I want to thank Peter Aschauer from ABS for providing test airbags and for his always quick and effective reaction to technical problems with the avalanche airbags.

The current work has been effected in frame of the project "Burial Prophylaxis with Avalanche Airbags", which was financially supported by the Schweizerische Unfallversicherungsgesellschaft (SUVA), Luzern. This financial support is gratefully acknowledged - the current work would not have been possible without this support.

I wish to say a heartfelt thank you to all friends for companionship troughout sunny and rainy times of the last years. And last but not least, to my parents for their persistent emotional and material support through the long years of my studies.

Appendix A

Notations

A.1 Notations used in Chapters 2 and 3

$e_n = \frac{v'_n}{v_n}$	longitudinal restitution coefficient
g	gravitational acceleration
H	total vertical height difference of a rockfall
L	total horizontal displacement of a rockfall
L_c	chute length
N_p	number of spherical particles involved in a model avalanche
r	particle radius
R	typical radius of bottom roughness
$\mathcal{R} = \frac{r}{R}$	roughness ratio
v_e	steady terminal velocity of a granular model avalanche
$v_{e,s}$	steady terminal velocity of a single particle, of which granular model avalanches consist
v_n	longitudinal particle velocity before collision with bottom roughness
v'_n	longitudinal particle velocity after collision with bottom roughness
v_{cr}	relative creep velocity of a snow layer adjacent to a weak layer
$\bar{v}_x$	steady terminal downslope velocity of a single particle on a rough incline

$\alpha_f = \frac{H}{L}$	"Farböschung" of a rockfall
$\Gamma = \frac{v_c^2}{L_c g}$	structure parameter of model avalanche
$\mu_{ap} = \tan \alpha_f$	apparent friction coefficient of a rockfall
ξ_F	dimensionless downslope position of the leading edge of a granular model avalanche
ξ_R	dimensionless downslope position of the trailing edge of a granular model avalanche

A.2 Notations used in Chapter 4

$\mathbf{a}$	overlap of colliding particles
a_c	cohesion coefficient
A	cross sectional area of avalanche flow
$\underline{\mathcal{A}}$	fourth order viscosity tensor
A_c	total area covered by an avalanche event
b	tangential restitution coefficient of particles
b_{fr}	friction parameter
c_{visc}	viscous damping coefficient
$\mathbf{c}$	particle velocity
$\mathbf{c}_1, \mathbf{c}_2$	velocity of particle 1 and 2, respectively
$\mathbf{c}_{12} = \mathbf{c}_1 - \mathbf{c}_2$	relative velocity of particles 1 and 2
$\mathbf{C} = \mathbf{c} - \mathbf{u}$	velocity fluctuations
D_a	diameter of a particles
D_b	diameter of b particles
$D_c \approx D_v + \bar{D}$	capture diameter
D_v	void sphere diameter
$\bar{D}$	mean particle diameter
$\mathbf{D}$	shear rate tensor
$\hat{\mathbf{D}}$	deviatoric shear rate tensor
$\frac{D}{M}$	mass to drag ratio
e	longitudinal restitution coefficient
$E = \frac{D_v}{D}$	void diameter ratio
E_m	minimum possible void diameter ratio
$f(\mathbf{x}, \mathbf{c}, t)$	single particle velocity distribution function
f'	perturbation of Maxwell velocity distribution function
$f^{(2)}(\mathbf{x}_1, \mathbf{c}_1; \mathbf{x}_2, \mathbf{c}_2, t)$	particle pair velocity distribution function
f_1	decelerating forces by dry friction
f_2	decelerating forces by hydraulic friction
f_n	normal force
f_{slip}	Coulomb frictional force
f_t	tangential force
$f_{t,max}$	maximum tangential force

$\mathbf{f}$	contact force
$\mathbf{f}_{el}$	elastic repulsive force
$\mathbf{f}_{ext}$	external volume forces
$\mathbf{f}_{vis}$	viscous damping force
$\mathbf{F}$	external force acting on one particle
$\mathbf{F}_a$	external force acting on a particles
$\mathbf{F}_b$	external force acting on b particles
g	gravitational acceleration
$g_0(\nu)$	radial distribution function
h	avalanche flow height
h_0	initial flow height of an avalanche
H	height difference travelled by an avalanche
H_D	mean depositional depth
H_{flow}	flow depth in Voellmy block model
h_v	vertical distance of center of mass of an avalanche from the energy line
$i = (a, b)$	index of particle species a and b
$\hat{\mathbf{i}}$	unit vector in x direction
j_y	mass flux in y direction
$\hat{\mathbf{j}}$	unit vector in y direction
$\mathbf{k}$	collisional unit vector
k	coefficient of turbulent friction
$\tilde{k}$	exponent in vicoplastic CEF constitutive law
k_n	normal component of spring constant
k_s	tangential component of spring constant
k_{spr}	spring constant of model repulsive force
k_1, k_2	normal spring constants for approach and rebound
l	index of flow layers
L	- length of runout zone - travel distance of an avalanche - length of sliding avalanche mass, over which resistance forces act
m	mass of particle

m_a	mass of a particles
m_b	mass of b particles
m_{bl}	mass of avalanche block
$\tilde{m}$	coefficient in viscoplastic CEF constitutive law
$n(\mathbf{x}, t)$	particle number density (number of particles per unit volume)
n_a	particle number density of a particles
n_b	particle number density of b particles
n_p	particle number per projected unit area
n_V	number of voids per projected unit area
$\tilde{n}$	exponent in viscoplastic CEF constitutive law
$\mathcal{O}_1, \mathcal{O}_2$	centers of particles 1 and 2, respectively
$\mathbf{p}$	momentum
$P = p_a + p_b$	total pressure of bidisperse granular material
p_a	partial pressure of a particles
p_b	partial pressure of b particles
$p(\mathbf{x}, t)$	instantaneous pressure field
p_e	effective pressure transferred by granular lattice
p_u	pore pressure transferred by ambient fluid
δp_n	normal momentum exchange
δp_t	tangential momentum exchange
q	exponent in viscoplastic CEF constitutive law
$q_{a,net}$	net percolation velocity of a particles
$q_{b,net}$	net percolation velocity of b particles
q_{SE}	squeeze expulsion velocity
$\mathbf{q}$	fluctuating energy flux
$\mathbf{q}_k$	kinetic part of fluctuating energy flux
$\mathbf{q}_c$	collisional part of fluctuating energy flux
Q	mass flow
$\tilde{r}$	exponent in viscoplastic CEF constitutive law
r_a	radius of a particles
r_b	radius of b particles
$R(x)$	curvature radius of avalanche slope
s	downslope position of avalanche center of mass
s_r	downslope runout distance of an avalanche

S_0	accelerating gravitational forces
S_f	accelerating frictional forces
t_c	contact time interval
$\mathbf{t}$	total stress tensor
$\mathbf{t}_a$	species stress of a particles
$\mathbf{t}_b$	species stress of b particles
$\mathbf{t}_k$	kinetic part of total stress
$\mathbf{t}_c$	collisional part of total stress
T	granular temperature
T_x, T_y, T_z	extra normal stresses
$\mathbf{T} = T_{ij}$	stress tensor
$\hat{\mathbf{T}} = \hat{T}_{ij}$	deviatoric stress tensor
$T_0 = \|\mathbf{T}_0\|$	treshold stress intensity
$\mathbf{u}$	bulk velocity
u_r	relative velocity of adjacent flow layers
U_l	region in flow layer l
$\mathbf{v} = v_i = \begin{pmatrix} v_x \\ v_y \\ v_z \end{pmatrix}$	velocity (field) vector
v	velocity of avalanche center of mass
v_p	terminal avalanche velocity
v_t	terminal velocity of avalanche mass
W	frictional work performed by an avalanche
W_0	initial width of avalanche
$\mathbf{W}$	rotation rate tensor
$\mathbf{x} = x_i = \begin{pmatrix} x \\ y \\ z \end{pmatrix}$	spatial position vector
$\mathbf{x}_1, \mathbf{x}_2$	spatial position of center of particle 1 and 2, respectively
$\delta_{ij} = \mathbf{1}$	unit tensor
$\delta_{0\%}$	flow depth, where no small particles occur
$\delta_{100\%}$	flow depth, where only small particles occur

η	dynamic viscosity
$\eta_p(x,y) = \frac{n_b}{n_a}$	particle number ratio
$\eta_{p,0}$	initial particle number ratio
ϕ_a	momentum produced by collisions of a particles
ϕ_b	momentum produced by collisions of b particles
ϕ_e	collision induced change of particle property $\mathbf{\Psi}$ per unit volume
ϕ_{fr}	static internal friction angle
$\mathbf{\Phi}$	collisional transfer
γ	collisional rate of energy dissipation
$\dot{\gamma}$	shear rate
λ_e	thermal conductivity of granular flow
$\lambda_{f,r} = \frac{L^2}{A_c}$	form factor of avalanche runout zone
μ	Coulomb coefficient of friction
$\mu_b = \mu_b(\mu_s)$	shear viscosity term
μ_s	shear viscosity
ν	solid volume fraction
ν_1	coefficient in viscoplastic CEF constitutive law
ν_2	coefficient in viscoplastic CEF constitutive law
ν_1^*	primary normal stress coefficient
ν_2^*	secondary normal stress coefficient
$\psi(x)$	(local) inclination
$\mathbf{\Psi}$	any particle property
$\mathbf{\Psi}_i$	property of particle i before collision
$\mathbf{\Psi}_i'$	property of particle i after collision
ϱ	continuum mass density
ϱ_p	mass density of a particle
σ	uniform particle diameter
$\theta = \tan^{-1}(\mu)$	downslope inclination of the energy line
$\theta(s)$	local inclination of avalanche track
θ_1	inclination of avalanche track
θ_2	inclination of runout zone
$\mathbf{\Theta}$	collisional support
τ	resisting basal shear during avalanche runout
τ_y	yield strength of unconfined debris
ξ	coefficient of turbulent friction

A.3 Notations used in Chapter 5

A_p	frontal area of a particle
a_r	amplitude of bottom roughness
b	tangential coefficient of restitution
b_{slip}	tangential restitution coefficient with respect to slip between colliding particles
b_x, b_y	periodicity of bottom roughness in x- and y- direction
c_w	"cw-value"
$\mathcal{C}, \tilde{\mathcal{C}}$	effective masses for computation of momentum exchange
$d = r_i + r_j$	distance of particle centers of particles i and j in contact
$d^{(i)}(\mathbf{n})$	feret diameter of particle i with respect to unit vector $\mathbf{n}$
$d^{(1)}$	drift coefficient of Langevin Equation
$d^{(2)}$	diffusion coefficient of Langevin Equation
$D^{(1)}$	drift coefficient of Fokker-Planck-Equation
$D^{(2)}$	diffusion coefficient of Fokker-Planck-Equation
D_l	part of connecting line between colliding particles lying in flow layer l
$\mathbf{D} = D_{\alpha\beta}$	deformation rate tensor
D_{II}	effective deformation rate
e	longitudinal coefficient of restitution
E	Mean total energy of flow: $E = T + V$
$F_c = \partial_t \delta p_n$	normal force exerted between particles during collision
$\mathbf{F}_{fr}$	velocity dependent frictional force
F_g	gravitational force
$f_{[e,b,\mu]}$	functional dependence of (rotational) velocities after collision from velocities before collision
f_{factor}	number of events occuring in the flow before storing particle state vectors $\Psi_i(t)$
$g = \|\mathbf{g}\|$	absolute gravitational acceleration

$\mathbf{g} = \begin{pmatrix} g_x \\ g_y \\ g_z \end{pmatrix}$	gravitational acceleration
g_z	z-component of gravitational acceleration in box coordinate system
h	flow height
h_{max}	maximum flow height
i, j	particle indices
i_{next}, j_{next}	indices of the particles colliding next
δh	flow layer thickness for statistical flow evaluation
$\mathbf{k}$	unit vector directing from particle centers j to i
$\mathbf{k}_b$	periodic bottom unit vector defining bottom roughness
l	flow layer index
l_x	periodicity length of periodic boundary conditions in x direction
l_y	periodicity length of periodic boundary conditions in y direction
m_i, m_j	masses of particles i and j
$\tilde{m}$	reduced mass of colliding particles
N	total particle number in the simulation
n_{av}	number of evaluations within regarded evaluation interval
n_r^q	number of particles belonging to size class q in the flow
$n_{r,l}^q$	number of particles belonging to size class q in flow layer l
n_l	number of particles in flow layer l
N_{max}	maximum possible number of particles in the simulation
n_{trial}	maximum number of trials to place a particle into the initial flow configuration
n_x	number of "bottom bumps" in x direction
n_y	number of "bottom bumps" in y direction

$\wp_i$	interaction flag of particle i
$p(\cdot\|\cdot)$	conditional probability distribution function
$\delta\mathbf{p}$	momentum transfer due to collision
δp_n	normal component of collisional momentum transfer
$\delta p_{n,-}$	normal collisional momentum transfer before paroxysm of collision
$\delta p_{n,+}$	normal collisional momentum transfer after paroxysm of collision
$\delta p_{t,-}$	tangential collisional momentum transfer before paroxysm of collision
$\delta p_{t,+}$	tangential collisional momentum transfer after paroxysm of collision
q	index of particle size class
Δr	bin width for particle size statistics
r_{ABS}	radius of tracer particle
r_i	radius of particle i
r_{max}	maximum particle radius
r_{min}	minimum particle radius
s_i, s_j	state (flying/lying) of particle i and j, respectively
$s_{i,next}, s_{j,next}$	states (flying/lying) of particles i_{next} and j_{next}, which will collide next
$S_l^{(2)}(\zeta)$	2nd order structure function of measure ζ in flow layer l
$s_{\alpha\beta}$	stresses produced by one single particle collision
δt	time step for time dependent evaluation
t_{ev}	time point of an event
Δt_{fl}	time step in time dependent evaluation
$t_{i,b}$	time until bottom impact of particle i
$t_{ij,min}$	minimum of collision time table, equivalent to next event time
t_k	kth time step in time dependent averaging
t_{max}	end time point of simulation
t_{min}	start time point of simulation

Δt_c	duration of particle contact during collision
t_-	time from first particle contact to paroxysm of collision
t_+	time from collision paroxysm to reseparation of particles
t_{av}	averaging time interval
t_n	nth time step in flow profile evaluation
T	total kinetic energy of colliding particles
T_i	kinetic energy of particle i
T_{rot}	rotational kinetic energy
T_{trans}	translational kinetic energy
ΔT_{diss}	dissipation of kinetic energy due to one particle collision
t_{ij}	time until collision of particles i and j
t_{win}	averaging time window for time dependent evaluation
$U_\epsilon(\mathbf{x}_i)$	Spherical surrounding of particle i with radius ϵ
U_{start}	region of initial granular assembly
$V(U_{start})$	Volume occupied by initial granular assembly
V_{pot}	mean potential energy of the flow
$\mathbf{x}_i = \begin{pmatrix} x_i \\ y_i \\ z_i \end{pmatrix}$	position of particle i
$\delta\mathbf{x} = \mathbf{x}_i - \mathbf{x}_j$	displacement of particles i and j
$\delta\mathbf{x}^*$	particle displacement of i and j with respect to periodic boundary conditions
$\delta\mathbf{x}_b$	Periodic particle distance vector to bottom
v_{mean}	initial mean downslope flow velocity
$\mathbf{v}_i = \begin{pmatrix} v_{x,i} \\ v_{y,i} \\ v_{z,i} \end{pmatrix}$	velocity of particle i

$\mathbf{v}'_i = \begin{pmatrix} v'_{x,i} \\ v'_{y,i} \\ v'_{z,i} \end{pmatrix}$	velocity of particle i after collision
$\delta\mathbf{v}$	velocity difference of particles i and j at their contact point
$v_{x,0}$	initial mean downslope flow velocity
$w(h_n, t_n; \ldots; h_1, t_1))$	probability of a particle having been elevated at heights $h_1 \ldots h_n$ at times $t_1 \ldots t_n$
$\mathbf{w}_i$	angular rotational velocity of particle i
$\mathbf{w}'_i$	angular rotational velocity of particle i after collision
α, β	indices of spatial coordinates
$\delta\mathbf{v}_t = \mathbf{v}_i - \mathbf{v}_j$	translational velocity difference of particles i and j
ϵ_{ekin}	particles with kinetic energies lower than ϵ_{ekin} are regarded as being at rest
$\epsilon_{distance}$	minimum particle distance numerically resolved within the hard sphere simulation
γ	collisional angle: γ =angle$(\delta\mathbf{v}, \mathbf{k})$
$\Gamma(t)$	δ-correlated noise signal
$\tilde{\kappa}$	reduced momenta of inertia of colliding particles
μ	particle Coulomb friction coefficient
$\bar{\mu}$	macro friction
ν_l	mean particle number density in flow layer l
ν_p	porosity
ν_0	initial mean particle number density of the entire flow
ψ	slope inclination
$\Psi_i(t)$	state vector of particle i
ϱ_{ABS}	density of tracer particle
ϱ_i	particle density
ϱ_{fl}	mass density of ambient fluid
ϱ_{max}	maximum particle density
ϱ_{min}	minimum particle density
$\varrho_{p,s}$	particle mass density

σ_i	particle diameter of particle i
$\sigma_{\alpha\beta}$	stress tensor
σ_{II}	effective stress
τ	time increment
Θ_i	momentum of inertia of particle i
ξ_{colour}	Scaling factor for colour encoding of particle energy in graphic display
$\Delta\xi$	particle distance to next wall
ζ	dummy for any physical measure

A.4 Notations used in Chapter 6

a_{cub}	edge length of cubic test body
a_{tet}	edge length of tetraedrical test body
e	longitudinal restitution coefficient
e_{exp}	experimentally obtained restitution coefficient
h_b	burial depth of test bodies
h_{max}	maximum profile depth
l_m	length of marker of measurement sleigh
n	number of collisions during the passing of two particles in the model flow
p_{impact}	impact momentum of colliding snow samples
r	granular particle radius
r_{cyl}	radius of cylindrical test body
r_{sph}	radius of spherical test body
Δs_{pass}	distance, over which two passing particles are sliding along each other in a snow flow avalanche
Δt	time until a distinct particle in the model flow encounters the next collision
t_{pass}	passing time of measurement sleigh through light barrier
Δt_{pass}	time intervall for passing of two particles in the model flow
$v_{slope} = \frac{l_m}{t_{slope}}$	offset velocity of mesurement sleigh due to inclination of hovercraft track
v_x	velocity of measurement sleigh along hovercraft track before collision of snow samples
v'_x	velocity of measurement sleigh along hovercraft track after collision of snow samples
x_{impact}	collisional position of snow samples
x_{lb}	position of light barrier at hovercraft track
α	height-radius ratio of cylindrical test body
$\mathcal{A}$	surface of test body
$\mathcal{V}$	volume of test body
$\phi = \frac{\varrho_{body}}{\varrho_{snow}}$	ratio of test body density and density of surrounding snow

$\Omega = \frac{A}{V}$	surface volume ratio of test body
ψ	slope inclination
ϱ_{body}	mass density of test body
ϱ_{snow}	mass density of surrounding snow

Appendix B

Curriculum Vitae

name	Kern
first name	Martin Alexander
date of birth	March 24, 1970
place of birth	Marktredwitz, Bavaria, Germany

Education

September 1976 - July 1976	primary school in Naila, Bavaria.
September 1980 - June 1989	Gymnasium Naila, Bavaria.
June 1989	Abitur (baccalauréat), very good (1.3).
June 1989 - October 1990	military service.
November 1990 - July 1996	University of Bayreuth.
July 1996	Dipl. phys. Univ. Bayreuth (very good, 1.4). Diploma thesis: "Measurement of pressure and velocity in a turbulent free jet", directed by PD Dr. J.Peinke.
February 1999 - November 2000	candidat au doctorat at Swiss Federal Institute of Technology Lausanne (EPFL). Thesis: "Inverse grading in granular flow", directed by Prof. Dr. Laurent Vulliet, DGC LMS.

professional work

Summer 1993	external teacher for basics of physics and mathematics at the Professional Education Center of the Bavarian chamber of handicrafts
November 1995 - July 1996	scientific help at the chair of Theoretical Physics II of the University of Bayreuth: tutorial assistance on Electrodynamics and Hydrodynamics.
July 1996-September 1996	scientific assistant at the chair of Experimental Physics II of the University of Bayreuth.
since November 1996	doctoral student at the Swiss Federal Institute of Snow and Avalanche Research: work in the Avalanche Airbag Project.

Bibliography

Adams, M. (1997). Industrial research needs in the development and processing of products having concentrated particulate phases. In R. Behringer & J. Jenkins (Eds.), *Powders and grains*, Rotterdam, pp. 49–52. Balkema.

Advanced Visual Systems Inc. (1992, May). *AVS User's Guide* (Release 4 ed.). Waltham, MA: Advanced Visual Systems Inc.

Ammann, W., Buser, O., & Vollenwyder, U. (1997). *Lawinen.* Basel: Birkhäuser Verlag.

Aschauer, P. (2000, february). Zur Geschichte der Entwicklung des ABS Lawinenballons. private communication.

Bagnold, R. (1954). Experiments on a gravity-free dispersion of large solid spheres in a newtonian fluid under shear. *Proc. Roy. Soc. Lond. A*(225), 49–63.

Barbolini, M. & Nettuno, L. (1998, Dec). Vara one- and two-dimensional models. In C. Harbitz (Ed.), *EU Programme SAME: A survey of computational models of snow avalanche motion*, Oslo, pp. 59–63. IGS.

Bartelt, P. & Gruber, U. (1997). Development and calibration of a voellmy-fluid dense snow avalanche model based on the finite element method. Internal Report 714, Swiss Federal Institute for Snow and Avalanche Research.

Bartelt, P. & Gruber, U. (1998, Dec.). The SFISAR quasi two dimensional model. In C. Harbitz (Ed.), *EU Programme SAME: A survey of computational models of snow avalanche motion*, pp. 39 – 44. IGS.

Bartelt, P., Salm, B., & Gruber, U. (1997). Modelling dense-snow avalanche flow as a criminale - ericksen - filby fluid without cohesion. Internal Report 717, Swiss Federal Institute for Snow and Avalanche Research.

Bideau, D., Ippolito, I., Samson, G., Batrouni, G., Dippel, S., Aguirre, A., Calvo, A., & Henrique, C. (1996). Gravity driven motion of a single sphere on a rough inclined plane. In D. Wolf, M. Schreckenberg, & A. Bachem

(Eds.), *Proc. HLRZ: Workshop on traffic and granular flow*, Singapore. World Scientific.

Bozhinsky, A. & Losev, K. (1998). The fundamentals of avalanche science. Mitteilungen 55, SLF.

Breitfuss, G. & Scheidegger, A. (1974). On a possible mechanism of alpine debris flows. *Annali di Geofisica XXVII*(1-2), 47–57.

Buser, O. & Frutiger, H. (1980). Observed maximum run-out distance of snow avalanches and the determination of the friction coefficients μ and ξ. *J. Glaciol. 26*(94), 121–130.

Campbell, C. (1993). Boundary interactions for two-dimensional granular flows. part 1 and 2. *J. Fluid Mech. 247*, 111–156.

Criminale, W., Ericksen, N., & Filby, G. (1958). Steady shear flow of non-newtonian fluids. *Archive Rat. Mech. Anal. 1*, 410–417.

Cundall, P. & Strack, O. (1979). A discrete numerical model for granular assemblies. *geotechnique 29*(1), 47–65.

Dade, W. & Huppert, H. (1998). *Geology*.

Davies, T. (1985). Mechanics of large debris flows. In *Proc. Int. Symp. on Erosion, Debris Flow and Disaster Prevention*, Tsuhuba, Japan, pp. 215–218.

Dent, J. (1986). Flow properties of granular flows with large overburden loads. *Acta Mechanica 64*, 111–122.

Dent, J. (1993). The dynamic friction characteristics of a rapidly sheared granular material applied to the motion of snow avalanches. *Ann. Glaciol. 18.*

Dent, J., Burrel, K., Schmidt, D., Louge, M., Adams, E., & Jazbutis, T. (1997). Density, velocity and friction measurements in a dry snow avalanche. *Ann. Glaciol. 26.*

Dent, J. & Lang, T. (1983). A biviscous modified bingham model of snow avalanche motion. *Ann. Glaciol. 4*, 42–46.

Dippel, S., Batrouni, G., & Wolf, D. (1996). Collision-induced friction in the motion of a single particle on a bumpy, inclined line. *Phys. Rev. E* (54), 6845 ff.

Dippel, S., Batrouni, G., & Wolf, D. (1997). Motion of a particle on a rough, inclined plane: Comparison of 2 and 3 dimensions. In R. Behringer & J. Jenkins (Eds.), *Powders and grains*, Rotterdam. Balkema.

Dippel, S., Samsun, L., & Batrouni, G. (1996). Motion of a ball on a rough inclined plane. In D. Wolf, M. Schreckenberg, & A. Bachem (Eds.), *Proc. HLRZ: Workshop on traffic and granular flow*, Singapore. World Scientific.

Drake, T. & Walton, O. (1995). Comparison of experimental and simulated grain flows. *J. Appl. Mech. 62*, 131–135.

Eglit, M. (1998, Dec). MSU One- and two-dimensional models. In C. Harbitz (Ed.), *EU Programme SAME: A Survey of Computational Models of Snow Avalanche Motion*, pp. 44 – 47. IGS.

Ennis, B. (1997). Unto dust shalt thou return. In J. Behringer, R.P. & Jenkins (Ed.), *Powders and grains*, Rotterdam, pp. 13–23. Balkema.

Fahnestock, R. (1978). Little Tahoma Peak rockfalls and avalanches, Mount Rainier, Washington, USA. In B. Voight (Ed.), *Developments in Geotechnical Engineering 14A*, Amsterdam, Oxford, New York, pp. 181–196. Elsevier.

Farrell, M., Lun, C., & Savage, S. (1986). A simple kinetic theory for granular flow of binary mixtures of smooth, inelastic spherical particles. *Acta mechanica* (63), 45–60.

Foehn, P., Good, W., Bois, W., & Obled.C. (1977). Evaluation and comparison of statistical and conventional methods of forecasting avalanche hazard. *J. Glaciol. 19*(81), 375–387.

Foerster, S., Louge, M., Chang, H., & Allia, K. (1994). Measurements of the collision properties of small spheres. *Phys. Fluids 3*(6), 1108–1115.

Friedrich, R. & Peinke, J. (1997). Description of a turbulent cascade by a fokker-planck equation. *Phys. Rev. Lett.* (78), 863.

Gramminger, L. (1986). *Das gerettete Leben - Aus der Geschichte der Bergrettung.* Muenchen: Rother Verlag.

Greve, R., Koch, T., & Hutter, K. (1993a). The motion of a granular avalanche in a convex and concave curved chute: Experiments and theoretical predictions. *Phil. Trans. Proc. R. Soc. London A*(342), 573–664.

Greve, R., Koch, T., & Hutter, K. (1993b). Unconfined flow of granular avalanches along a partly curved surface, Part I. *Proc. R. Soc. London A*(445), 399–413.

Gubler, H. (1993). *Swiss Avalanche-Dynamics Procedures for Dense Flow Avalanches.* Davos: AlpuG.

Harbitz, C. (1998, Dec). EU Programme SAME: A Survey of Computational Models of Snow Avalanche Motion.

He, Q. & Huet, C. (1999). On the micromechanical definition of maccroscopic strain and strain-rate tensors for granular materials. *Submitted to J. Fluid Mech.*.

Heim, A. (1882). Der Bergsturz von Elm. *Deutsche Geol. Gesell. Zeitschrift* (34), 74–115.

Heim, A. (1932). *Bergsturz und Menschenleben.* Fretz und Wasmuth.

Herrmann, H. & Luding, S. (1998). Modelling granular media on the computer. *Cont. Mech. Thermodyn.* (10), 189–231.

Hirshfeld, D. & Rapaport, D. (1996). Molecular dynamics studies of grain segregation in sheared flow. *Phys. Rev. E 2*(56), 2012–2018.

Hohenester, J. (1979, april). Lawinenrettungsballon - Rettungshilfe. In *Tagung Elektronik und Lawinen*, Graz, Austria. Institut für Elektronik der Technischen Universität in Graz.

Honerkamp, J. (1990). *Stochastische Dynamische Systeme.* Weinheim: VCH Verlagsgesellschaft.

Hoomans, B., Kuipers, J., Briels, W., & vanSwaaji, W. (1996). Discrete particle simulation of bubble and slug formation in a two-dimensional gas-fluidised bed: A hard-sphere approach. *Chemical Engineering Science 51*(1), 99–108.

Hsü, K. (1978). Albert Heim: Observations on landslides. In B. Voight (Ed.), *Developments in Geotechnical Engineering 14A*, Amsterdam, Oxford, New York, pp. 69–93. Elsevier.

Hungr, O. (1995). A model for the runout analysis of rapid flow slides, debris flows and avalanches. *Canadian Geotechnical Journal* (32), 610–623.

Hutter, K. (1996). Chapter 11: Avalanche dynamics. In V. Singh (Ed.), *The hydrology of disasters*, Dordrecht/Boston/London. Kluwer academic publishers.

Hutter, K. & Koch, T. (1991). Motion of a granular avalanche in an exponentially curved chute: Experiments and theoretical predictions. *Phil. Trans. R. Soc. London A*(334), 93–138.

Hutter, K., Koch, T., Pluess, C., & Savage, S. (1995). The dynamics of granular materials from initiation to runout. Part II : Experiments. *Acta Mechanica* (109), 127–169.

Hwang, H. & Hutter, K. (1995). A new kinetic model for rapid granular flow. *Continuum Mech. Thermodyn.* (7), 357–384.

Irgens, F., Schieldrop, B., Harbitz, C., Domaas, U., & Opsahl, R. (1998). Simulations of dense snow avalanches on deflecting dams. *Ann. Glaciol. 26.*

Irving, G. (1980, June). Avalanche balloon testing lake louise ski area 1979-1980.

Iverson, R. (1997). The physics of debris flows. *Reviews of Geophysics 35*, 245–296.

Iverson, R. & Denlinger, R. (1987). The physics of debris flows - a conceptual assessment. In *Erosion and Sedimentation in the Pacific Rim*, Number 165. IAHS.

Jaeger, H., Nagel, S., & Behringer, R. (1996, Apr.). The physics of granular flows. *Physics Today*, 32–38.

Jenkins, J. (1992). Boundary conditions for rapid granular flow: Flat frictional walls. *J. Appl. Mech. 59.*

Jenkins, J. (1998, Jul.). Kinetic theory for nearly elastic spheres. In *Kinetic and granular continuum thermodynamical approaches to granular and porous media*, Udine. CISM.

Jenkins, J. & Mancini, F. (1987). Balance laws and constitutive relations for plane flows of a dense, binary mixture of smooth, nearly elastic discs. *J. Appl. Mech. 109*, 27–34.

Jenkins, J. & Mancini, F. (1989). Kinetic theory of smooth, nearly elastic spheres. *Physics of Fluids A1*, 2050–2057.

Jenkins, J. & Richman, M. (1985). Kinetic theory for plane flows of a dense gas of identical, rough, inelastic discs. *Phys. Fluids 28*(12), 3485–3494.

Kern, M. (1998, June). Formabhängigkeit der Verschüttungstiefe voluminöser Körper in einer Schneelawine. unpubl.

Koch, T., Greve, R., & Hutter, K. (1994). Unconfined flow of granular avalanches along a partly curved surface, part ii. *Proc. R. Soc. London A*(445), 415–435.

Körner, H. (1976). Reichweite und Geschwindigkeit von Bergstürzen und Fliesschneelawinen. *Rock Mechanics 8*(4), 225–256.

Körner, H. (1980). The energy line method in the mechanics of avalanches. *J. Glaciol. 26*(94), 501–505.

Kosugi, K., Sato, A., Abe, O., Nohguchi, Y., Jamada, I., Nishimura, K., & Izumi, K. (1994). Table tennis ball avalanche experiments. In *Proc. ISSW*, Banff, Canada. ISSW.

Kumar, A. (1994, Sep.). Continuum approach to avalanche dynamics. In *Extended Abstracts, Int. Symp. on Snow and Related Manifestations*, Manali (HP), India. Snow Avalanche Study Establishment.

Lang, R. & Leo, B. (1994). Model for avalanches in three dimensions - comparison of theory and experiments. report 94-5, Cold Regions Research and Engeneering Laboratory.

Lang, R., Leo, B., & Hutter, K. (1989). Flow characteristics of a nonconsrained, non-cohesive granular medium down an inclined, curved surface: preliminary experimental results. *Ann. Glaciol.* (13).

Lian, J. & Shima, S. (1994). Powder assembly simulation by particle dynamics method. *International Journal for Numerical Methods in Engineering 37*, 763–775.

Lin, X. & Ng, T. (1995). Contact detection algorithms for three-dimensional ellipsoid in distinct element modelling. *International Journal for Numerical and Analytical Methods in Geomechanics 19*, 653–559.

Lorig, L., Gibson, W., Alvial, J., & Cuevas, J. (1995). Gravity flow simulation with the particle flow code (PFC). *ISRM News J. 3*(1), 18–24.

Louge, M. (1994). Computer simulations of rapid granular flow of spheres interacting with a flat, frictional boundary. *Phys. Fluids 6*(7), 2253–2269.

Luding, S. & Mcnamara, S. (1998, October). How to handle the inelastic collapse of a dissipative hard-sphere gas with the TC model. http://xxx.lanl.gov/abs/condmat/9810009.

Lun, C. (1996). Granular dynamics of inelastic spheres in couette flow. *Phys. Fluids 8*(11), 2869–2883.

Lun, C. & Bent, A. (1994). Numerical simulation of inelastic frictional spheres in simple shear flow. *J. Fluid Mech. 258*, 335–353.

Lun, C., Savage, S., Jeffrey, D., & Chepurniy, N. (1984). Kinetic theories for granular flow: Inelastic particles in Couette flow and slightly inelastic particles in a general flowfield. *J. Fluid Mech. 140*, 223–256.

Lun, C., Savage, S., Jeffrey, D., & Chepurniy, N. (1986). The effects of an impact velocity dependent coefficient of restitution on stresses developped by sheared granular materials. *Acta Mech. 63*(4), 16–43.

Maeno, N. & Nishimura, K. (1987). Numerical computation of snow avalanche motion in a three-dimensional topography. *Low Temp. Sci. A*(46), 99–110.

Mc Clung, D. & Schaerer, P. (1993). *The Avalanche Handbook.* Seattle, Washington 98134: The Mountaineers.

McClung, D. (1990). A model for scaling avalanche speeds. *J. Glaciol. 36*(126), 188–198.

Munter, W. (1991). *Neue Lawinenkunde.* Bern: Verlag des SAC.

Munter, W. (1997). *Lawinen 3x3.* Garmisch-Partenkirchen: Agentur Pohl & Schellhammer.

Murty, B. & Eswaran, V. (1994a, May). Numerical modelling of avalanches. Report, Snow & Avalanche Study Establishment.

Murty, B. & Eswaran, V. (1994b, Sep.). A shock - capturing scheme for avalanche modelling. In *Extended Abstracts, Int. Symp. on Snow and Related Manifestations*, Manali (HP), India. Snow & Avalanche Study Establishment.

Naert, A., Friedrich, R., & Peinke, J. (1997). A Fokker-Planck equation for the energy cascade in turbulence. *Phys. Rev. E* (56), 6719.

Nakagawa, M. & Imaizumi, T. (1992). Simulation of rapid bimodal granular flows. *Advances in Micromechanics of Granular Materials* (7), 131–140.

Nishimura, K. (1990). Studies on the fluidized snow dynamics. *Contr. Inst. Low Temp. Sci. A*(37), 1–55.

Nishimura, K., Kosugi, K., & Nakagawa, M. (1993). Experiments on ice-sphere flow along an inclined chute. *Mechanics of Materials* (16), 205–209.

Nishimura, K., Nohguchi, Y., Ito, K., Kosugi, K., & Izumi, K. (1996). Snow avalanche experiments at a ski jump. In *Proc. ISSW*, Banff, Canada. ISSW.

Nohguchi, Y. (1989). Three-dimensional equations for mass centre motion of an avalanche of arbitrary configuration. *Ann. Glaciol. 13*, 215–217.

Nohguchi, Y. (1997). Avalanche experiments with styrene foam particles. *Ann. Glaciol. 26.*

Nohguchi, Y., Kobayashi, T., Iwanami, K., Nishimura, K., & Sato, A. (1997). Granulation of snow. In K. Izumi (Ed.), *Snow Engineering: Recent Advances*, Rotterdam. Balkema.

Nohguchi, Y. & Nishimura, K. (1996). Head formation in light granular avalanches. In *Proceedings ISSW*, Banff, Canada. ISSW.

Norem, H., Irgens, F., & Schieldrop, B. (1986). A continuum model for calculating snow avalanche velocities. In *Proceedings of Avalanche Formation, Movements and Effects, IAHS publication*, Number 162, Davos, pp. 363–378.

Norem, H., Irgens, F., & Schieldrop, B. (1989). Simulation of snow avalanche flow in runout zones. *Ann. Glaciol. 13*, 218–225.

Norem, H. & Schieldrop, B. (1991). Stress analysis for numerical modelling of submarine flowslides. report 5220090-10, Norwegian Geotechnical Institute.

Oppenheim, R. (1974). *Die Entdeckung der Alpen.* Frauenfeld: Verlag Huber.

Perla, M. & Martinelli, M. (1976). *Avalanche Handbook.* USDA Agricultural Handbook 489: US Government Printing Office.

Perla, R., Cheng, T., & McClung, D. (1980). A two parameter model of snow avalanche motion. *J. Glaciol. 26*(94), 197–207.

Perla, R., Lied, K., & Kristensen, K. (1984). Particle simulation of snow avalanche motion. *Cold Regions Science and Technology* (9), 191–202.

Quervain, M. (1975). Avalanche formation. In *USDA Forest Service General Report RM-9.*

Reif, F. (1987). *Statistische Physik und Theorie der Wärme.* Berlin, New York: de Gruyter.

Risken, H. (1989). *The Fokker-Planck Equation.* Heidelberg: Springer Verlag.

Rosato, A., Strandburg, K., Prinz, F., & Swendsen, R. (1987). Why the brasil nuts are on the top: Size segregation of particulate matter by shaking. *Phys. Rev. Lett. 58*(10).

Salm, B. (1980). Flow, flow transition and runout distances of flowing avalanches. *Ann. Glaciol. 18*, 221–226.

Salm, B. (1982). *Lawinenkunde fuer den Praktiker.* Bern: Verlag des SAC.

Salm, B., Burkard, A., & Gubler, H. (1990). Berechnung von Fliesslawinen; Eine Anleitung für Praktiker mit Beispielen. *Mitteilungen des Eidgenössischen Intituts fuer Schnee- und Lawinenforschung* (47).

Sampl, P. (1998, Dec). The AVL quasi three- dimensional dense flow model. In C. Harbitz (Ed.), *EU Programme SAME : A Survey of Computational Models for Snow Avalanche Motion*, Oslo, pp. 67–69.

Savage, S. (1979). Gravity flow of cohesionless granular materials in chutes and channels. *J. Fluid Mech.* (92), 53–96.

Savage, S. (1993). Mechanics of granular flow. In K. Hutter (Ed.), *Continuum mechanics in environmental sciences and geophysics*, Number 337 in CISM courses and lectures. International Centre for Mechanical Sciences: Springer, New York, Vienna.

Savage, S. & Hutter, K. (1991). The dynamics of granular materials from initiation to runout. part i : Analysis. *Acta Mechanica* (86), 201–231.

Savage, S. & Lun, C. (1988). Particle size segregation in inclined chute flows of dry cohesionless granular solids. *J. Fluid Mech.* (189), 311–335.

Schaer, M. & Issler, D. (2000, May). Particle densities, velocities and size distributions in large avalanches from impact-sensor measurements. to appear in Ann. Glaciol. 32.

Schild, M. (1967, Jul.). Durch Lawinen verursachte Unfälle und Schäden. In M. de Quervain (Ed.), *Schnee und Lawinen in den Schweizeralpen Winter 1964/65*, Weissfluhjoch/Davos. Eidg. Institut für Schnee- und Lawinenforschung.

Schwarz, O., Horie, Y., & Shearer, M. (1998). Discrete element investigation of stress fluctuation in granular flow at high strain rates. *Phys. Rev. E 57*(2), 603–623.

Sela, N. & Goldhirsh, I. (1998). Hydrodynamic equations for rapid flows of smooth inelastic spheres, to Burnett order. *J. Fluid Mech. 361*, 41–74.

Shimizu, H. (1967, August 14-19). Magnitude of avalanches. In *Physics of Snow and Ice. International Conference on Low Temperature Science*, Sapporo. Hokkaido University.

Shoda, M. (1965). An experimental study on dynamics of snow avalanches. *International Association of Hydrological Sciences Publication* (69), 215–229.

Siefert, M. (1999, October). Routines for analysis of stochastic systems. private communication.

Siegert, S., Friedrich, R., & Peinke, J. (1998). Analysis of data of stochastic systems. *Phys. Lett. A* (243), 275.

Stadler, R. & Buggish, H. (1985). Influence of the deformation rate on shear stress in bulk solids. EFCE publications, Chr. Michelsens Institut.

Tai, Q. & Sadd, M. (1997). A discrete element study of the relationship of fabric to wave propagational behaviour in granular materials. *International Journal for Numerical and Analytical Methods in Geomechanics 21*, 295–311.

Ting, J., Khwaja, M., Meachum, L., & Rowell, J. (1993). An ellipse-based discrete element modell for granular materials. *International Journal for Numerical and Analytical Methods in Geomechanics 17*, 603–623.

Tschirky, F. (2000, July). Bekannte und dokumentierte Lawinenunfälle mit Lawinenballon.

Tschirky, F., Brabec, B., & Kern, M. (2000, August). Avalanche rescue devices: state of development, success and failures. to be published.

Tschirky, F., Meister, R., Ammann, W., & Buser, O. (1995, June). Untersuchungen über die Wirkung des Lawinenballons, Bericht Versuche Winter 1994/95. Internal Report 686, Swiss Federal Institute for Snow and Avalanche Research.

Tschirky, F., Schweizer, J., & Ammann, W. (1996). Avalanche balloons - preliminary test results. In *Proc. ISSW*, Banff, Canada. ISSW.

UNESCO (1981). *Avalanche Atlas. Illustrated International Avalanche Classification.* Paris: UNESCO.

van Kampen, N. (1981). *Stochastic Processes in Physics and Chemistry.* Amsterdam: North Holland Publishing Company.

Voellmy, A. (1955). Über die Zerstörungskraft von Lawinen. *Schweiz. Bauzeitung* (73), 159–165, 212–217, 246–249, 280–285.

Voight, B. e. (1978). *Rockslides and Avalanches 1, Developments in Geotechnical Engineering, vol.14A.* Amsterdam, Oxford, New York: Elsevier Scientific Publishing Company.

Vulliet, L. & Hutter, K. (1988). A set of constitutive models for soils under slow movement. *ASCE Journal of Geotechnical Engineering 114* (9), 1022–1041.

Vulliet, L., Kern, M., & Ammann, W. (2000). Inverse grading in slopes. In *Proc. VIII ISL, 8 th International Symposium on Landslides*, Volume 3, Cardiff, Wales, pp. 1515–1520. Thomas Telford, London.

Walton, O. (1992). Numerical simulation of inclined chute flows of monodisperse, inelastic, frictional spheres. In H. e. a. Shen (Ed.), *Advances in the Micromechanics fo Granular Materials*, pp. 453–461. Elsevier Science Publishers, B.V.

Walton, O. & Braun, R. (1986). Viscosity and temperature calculations for assemblies of inelastic frictional discs. *Journal of Rheology 30*, 949–980.

Wang, Y. & Mason, M. (1992). Two-dimensional rigid-body collisions with friction. *J. Appl. Mech. 9*(59), 635–642.

Williams, J. (1986). Mixing of particulate solids. In J. Uhl, V.W. & Gray (Ed.), *Mixing Theory and Pratice, Vol. 3.* Academic Press, N.Y.

Wolff, Anselm, & Danner (1978, June). Lawinenballon. In *Bericht Nr. EP 018-77*, Ismaning. ALLIANZ Zentrum für Technik GmbH.

Yoshimatsu, H. (1991). Study of the mechanics of debris flow and its simulation modell. *Journal of Japan Landslide Society* (28-2).

Zimmermann, T., Rebora, B., Davalle, E., & Desceudres, F. (1989). A three-dimensional numerical simulation model for rockfalls. *IREM Internal Report 1.*